Intraoperative, Quantitative, and Non-Contact Blood Volume Flow Measurement via Indocyanine Green Fluorescence Angiography

Zur Erlangung des akademischen Grades eines

DOKTORS DER INGENIEURWISSENSCHAFTEN (Dr.-Ing.)

von der KIT-Fakultät für

Elektrotechnik und Informationstechnik

des Karlsruher Instituts für Technologie (KIT)

genehmigte

DISSERTATION

von

Ady Naber, M.Sc.

geb. in Amman, Jordanien

Tag der mündlichen Prüfung:	21. Juli 2021
Referent:	Prof. Dr. rer. nat. Werner Nahm
Korreferent:	Prof. Dr. rer. nat. Ulrich Lemmer

Abstract

Patients suffering from a cerebrovascular disease, which causes the hypoperfusion of the brain, can undergo revascularization surgery as treatment. It is often performed as an open surgery and its goal is to restore the vascular function, in particular the flow of blood. Therefore, an anastomosis (connection of arteries) is installed to augment flow into a hypoperfused area. Complications occur in approximately 10% of the cases, partly related to an insufficient flow augmentation. Hence, the blood flow should be checked intraoperatively to assess the intervention's quality and intervene rapidly to prevent a negative patient outcome.
The current state-of-the-art measurement device is the ultrasonic transit time flow probe. It provides a quantitative flow value but needs to be placed around the vessel. This is cumbersome and holds the risk of contamination, vessel compromise, and rupture.
An alternative method is the indocyanine green (ICG) fluorescence angiography (FA), which is a camera-based method. It is the state-of-the-art method in the high resolution anatomical visualization and it is able to provide the surgeon with a qualitative functional imaging of vessels in the field of view. Approaches to quantify the blood flow via ICG FA failed to obtain trustworthy flow values so far.
This thesis analyzes and improves the capability of ICG FA to provide quantitative values by

1. clarifying on how accurate the measurement can be.
2. proposing methods to improve the accuracy.
3. deriving the existence of a systemic error.
4. proposing a method to compensate for the systemic error.
5. providing an end-to-end workflow from video data input to flow value output.
6. validating the proposed methods and the workflow in an *ex vivo* and *in vivo* study.

The proposed measurement in this thesis is based on the systemic mean transit time theorem for single input and single output systems. To calculate the flow, the transit time of a bolus for a certain distance and the cross sectional area of the vessel need to be obtained. Methods were developed to obtain the blood volume flow, and to identify and quantify the sources of errors in this measurement.

The statistical errors in measuring the transit distance and transit time of the ICG bolus as well as the cross sectional area of the vessel are often neglected in research and thus were quantified in this thesis using *in silico* models. It revealed that the error is too large and requires methods to reduce it.

A method was proposed utilizing the re-continualization of the discrete centerline to significantly reduce the error in the length measurement and decouple its dependency on a structure's angular orientation. Similarly, a method was proposed which re-continualized the obtained indicator dilution curves (IDCs) to reduce the error in the transit time measurement. The propagated statistical error of the flow measurement was reduced to an acceptable and manageable range of 20% to 30%.

The presence of a systemic error of the optical measurement of the blood flow was identified and theoretically derived from the definition of volume flow.
A method to determine and compensate for the error was proposed. It required a fluid flow simulation to obtain the spatio-temporal dye concentration in a blood vessel. The concentration was handed over to a newly developed Fluorescence-Monte-Carlo-Multi-Cylinder (FMCMC) model, which simulated the propagation of photons in a vessel. Thereby, the location of fluorescence events of emitted photons was obtained and the systemic error determined. This enables compensating for the systemic error. It was revealed that the systemic error is independent of the flow as long as the flow is laminar but dependent on the vessel's diameter and the time point at which the error is extracted. Towards earlier time point of extraction of the error, the dependency on the diameter was smaller. Hence, it is advantageous to use the first arrival of the bolus to determine the transit time to decrease the influence of the diameter on the error.

To prove the accuracy of the measurement in an experiment, an *ex vivo* experiment using pig blood and rabbit aortas was designed and set up. It revealed that the obtained flow by the proposed end-to-end workflow agrees with the reference measurement, which was an industrial flow meter. The statistical dispersion of measured flow data agreed with the statistical error margin determined beforehand which also validates the *in silico* approach.

A retrospective *in vivo* study in humans undergoing an extracranial-to-intracranial (EC-IC) bypass surgery was performed. The analysis of the FA data revealed a good agreement with the clinical gold standard method, but with the major advantage of not requiring contact to the tissue. Additionally, it was proven that it can simultaneously provide flow values for multiple vessels in the field of view of the camera.

The presented results are a proof of concept of the suitability of the presented intraoperative, quantitative, and optical measurement of blood volume flow via ICG FA. This thesis paves the way towards the clinical use of this method complementing the current state of the art. It could provide the surgeon with a novel blood volume flow measurement and potentially reduce the risk of complications and increase the patient outcome.

Kurzfassung

In vielen Fällen unterziehen sich Patienten einer Revaskularisationsoperation wenn sie an einer zerebrovaskulären Erkrankung leiden, die eine Hypoperfusion des Gehirns verursacht. Dieser chirurgische Eingriff wird häufig als offene Operation durchgeführt und hat das Ziel, die Gefäßfunktion, insbesondere den Blutfluss, wiederherzustellen. Hierzu wird eine Anastomose (Verbindung von Arterien) angelegt, um den Fluss zu einem hypoperfundierten Gehirnareal zu erhöhen. In ungefähr 10% der Eingriffe treten nach der Operation Komplikationen auf, die zum Teil auf eine unzureichende Durchflusssteigerung zurückgeführt werden. Daher sollte der Blutfluss intraoperativ überprüft werden, um die Qualität des Eingriffs im Operationssaal zu beurteilen und schnell eingreifen zu können. Damit könnte ein negativer Ausgang für den Patienten verhindert werden.

Der derzeitige Stand der Technik in der intraoperativen und quantitativen Blutflussmessung ist die Nutzung der Ultraschall-Transitzeit-Durchflusssonde. Sie gibt einen quantitativen Flusswert an, muss jedoch das Gefäß umschließen. Dies ist einerseits umständlich für den Chirurgen und andererseits birgt es das Risiko von Kontaminationen, Gefäßquetschungen und der Gefäßruptur.

Eine alternative Methode ist die Indocyaningrün (ICG) Fluoreszenzangiographie (FA), welche eine kamerabasierte Methode ist. Sie ist der Stand der Technik in der hochauflösenden anatomischen Visualisierung des Situs und kann zusätzlich dem Chirurgen eine qualitative funktionelle Darstellung der Gefäße im Sichtfeld liefern. Der Stand der Wissenschaft zur Quantifizierung des Blutflusses mittels ICG-FA konnten bisher keine verlässlichen Flusswerte liefern.

Die vorliegende Arbeit analysiert und verbessert die Eignung von ICG FA zu Bereitstellung von verlässlichen und quantitativen Blutflusswerten, indem

1. geklärt wird, wie akkurat die Messung durchgeführt werden kann.
2. Methoden zur Verbesserung der Genauigkeit entwickelt werden.
3. die Existenz eines systematischen Fehlers abgeleitet wird.
4. eine Methode zur Kompensation des systematischen Fehlers entwickelt wird.
5. ein Algorithmus zur Verarbeitung der eingehenden Videodaten für eine Ausgabe eines Durchflusswertes bereitgestellt wird.
6. die Validierung der vorgeschlagenen Methoden und des Arbeitsablaufs in einer *ex vivo* und *in vivo* Studie durchgeführt wird.

Die in dieser Arbeit vorgeschlagene Messung basiert auf dem *systemic mean transit time theorem* für Systeme mit einem Eingang und einem Ausgang. Um den Fluss zu berechnen müssen die Transitzeit eines ICG-Bolus für eine zu bestimmenden Strecke und die Querschnittsfläche des Gefäßes ermittelt werden. Es wurden Methoden entwickelt, um den Blutvolumenstrom zu messen und um Fehlerquellen bei dieser Messung der einzelnen Parameter zu identifizieren, quantifizieren und reduzieren.

Die statistischen Fehler bei der Messung der Transitstrecke und der Transitzeit des ICG-Bolus sowie der Querschnittsfläche des Gefäßes werden in der Forschung oft vernachlässigt. In dieser Arbeit wurden die Fehler mit Hilfe von *in silico* Modellen quantifiziert. Es zeigte sich, dass der Fehler zu groß für eine zuverlässige Blutflussmessung ist und daher Methoden zu seiner Reduzierung benötigt werden.
Um den Fehler bei der Längenmessung deutlich zu reduzieren, wurde eine Methode vorgestellt, welche die diskrete Mittellinie wieder in eine kontinuierliche überführt. Dabei wird der Fehler in der Längenmessung signifikant reduziert und der Fehler von der räumlichen Orientierung der Struktur entkoppelt. In ähnlicher Weise wurde eine Methode vorgestellt, welche die gemessenen diskreten Indikatorverdünnungskurven (IDCs) ebenso in kontinuierliche überführt, um den Fehler in der Laufzeitmessung des ICG-Bolus zu reduzieren. Der propagierte statistische Fehler der Blutflussmessung wurde auf einen akzeptablen und praktikablen Wert von 20 % bis 30 % reduziert.

Die Präsenz eines systematischen Fehlers bei der optischen Messung des Blutflusses wurde identifiziert und aus der Definition des Volumenflusses theoretisch abgeleitet. Folgend wird eine Methode zur Kompensation des Fehlers vorgestellt. Im ersten Schritt wird eine Fluid-Strömungssimulation genutzt, um die räumlich-zeitliche Konzentration des ICG in einem Blutgefäß zu berechnen. Anschließend wird die Konzentration an ein neu entwickeltes Fluoreszenz-Monte-Carlo-Multizylinder (FMCMC) Modell übergeben, das die Ausbreitung von Photonen in einem Gefäß simuliert. Dabei wird der Ort der Fluoreszenzereignisse der emittierten Photonen ermittelt und der systematische Fehler bestimmt. Dies ermöglicht die Kompensation des systematischen Fehlers. Es zeigte sich, dass dieser Fehler unabhängig von dem Volumenfluss ist, solange die Strömung laminar ist, aber abhängig vom Durchmesser des Gefäßes und dem Zeitpunkt der Messung. Die Abhängigkeit vom Durchmesser ist reduziert bei Messungen zu einem früheren Zeitpunkt. Daher ist es vorteilhaft, die erste Ankunft des ICG-Bolus zur Bestimmung der Transitzeit zu verwenden, um den Einfluss des Durchmessers auf den Fehler zu verringern und somit die Messung robuster durchzuführen.

Um die Genauigkeit der Messung in einem Experiment zu beweisen, wurde ein *ex vivo* Experiment unter Verwendung von Schweineblut und Kaninchen Aorten konzipiert und durchgeführt. Es zeigte sich, dass der durch den vorgeschlagenen Algorithmus ermittelte Fluss mit der Referenzmessung (einem industriellem Durchflussmesser) übereinstimmt. Die statistische Streuung der gemessenen Flussdaten durch den Algorithmus stimmte mit der zuvor ermittelten statistischen Fehlerspanne überein, was den *in silico* Ansatz validiert.

Es wurde eine retrospektive *in vivo* Studie an Menschen durchgeführt, die sich einer extrakraniellen-zu-intrakraniellen (EC-IC) Bypass Operation unterzogen hatten. Die Analyse der FA-Daten ergab eine gute Übereinstimmung mit der klinischen Referenzmethode, jedoch mit dem großen Vorteil, dass kein Kontakt zum Gewebe erforderlich war. Zusätzlich wurde gezeigt, dass simultan Flusswerte für mehrere Gefäße im Sichtfeld der Kamera gemessen werden können.

Die vorgestellten Ergebnisse sind ein *Proof of Concept* für die Eignung der vorgestellten intraoperativen, quantitativen und optischen Messung des Blutvolumenstroms mittels ICG FA. Diese Arbeit ebnet den Weg für den klinischen Einsatz dieser Methode in Ergänzung zum aktuellen klinischen Stand der Technik. Sie könnte zukünftig dem Chirurgen eine neuartige Messung des Blutvolumenstroms zur Verfügung stellen und dabei potentiell das Risiko einer Komplikation reduzieren und damit das Wohl der Patienten verbessern.

Acknowledgments

"The strength of the team is each individual member. The strength of each member is the team."

Phil Jackson, Head coach of the legendary 90's Chicago Bulls

Science is teamwork. Many people have contributed in different forms to this work. I would like to sincerely thank all of them.

My sincere gratitude goes to Prof. Werner Nahm for giving me the opportunity to be part of his research group, for supporting me in all instances of the research and for his enthusiasm. I would also like to thank Prof. Uli Lemmer for his engagement in the KSOP, which funded my first 16 months at the KIT by a scholarship, and for refereeing this thesis. I would also like to thank Prof. Gary Steinberg for the very interesting discussions and providing the clinical data.

I would like to thank all my project partners at Carl Zeiss Meditec AG, especially Christoph Hauger for the feedback and input given within the course of the project. I would like to thank Dr. Gunnar Seemann for establishing the contact to the Universitäts Klinikum Freiburg. I would like to thank the whole team in Freiburg, especially Dr. Enaam Chleilat for her support by providing us the biological material.

A big thank goes to all colleagues at the IBT for the great time and support. I want to thank Manfred Schroll for his quick IT support also on weekend and Ramona Modery for her instructions in extracting aortas from rats. A big thanks goes to the guys who read parts of this thesis gave me feedback: Michael Kircher, Simon Hoffmann, Marc Nothstein, Nicolas Pilia, Alexander Anton, Axel Löwe, Deborah Nairn and Maria. A special thank goes to many colleagues: Andreas Wachter for being a great companion from the first day on, Michael Kircher for being the best office mate; Nico Pilia, Yannick Lutz and Steffen Schuler for the fun time in the offices of the fourth floor; Eki for the sweets and the discussion; Marc Nothstein for pushing me at the end of my PhD; Axel Löwe for his professional feedback.

I want to thank all my students who have contributed to my project. Especially: Jesvin Jimmy, Jayson Chaykowski, Leila Meyer-Hilberg, Daniel Berwanger and Simon Hoffmann.

Most importantly, I want to thank my family: My parents, Christine and Sultan, for their unconditional love and support, and shaping me to the person I am now. To my older brother Elias who has been an inspiration to me and always having my back. To Maria, who was always by my side and knew how to cheer me up.

Contents

Abbreviations

ACA	anterior cerebral artery
BA	basilar artery
BFI	blood flow index
CT	computed tomography
EC-IC	extracranial-to-intracranial
FA	fluorescence angiography
FMCMC	Fluorescence-Monte-Carlo-Multi-Cylinder
FMCML	Fluorescence-Monte-Carlo-Multi-Layer
GUI	graphical user interface
ICA	internal carotid artery
ICG	indocyanine green
IDC	indicator dilution curve
laser	light amplification by stimulated emission of radiation
LDRW	local density random walk
MC	Monte-Carlo
MCA	middle cerebral artery
MCMC	Monte-Carlo-Multi-Cylinder
MCML	Monte-Carlo-Multi-Layer
MMD	moyamoya disease
MRI	magnetic resonance imaging
OOF	Optimally Oriented Flux
PCA	posterior cerebral artery
PI	Gosling pulsatility index
RBC	red blood cell
ROI	region of interest
SNR	signal to noise ratio
STA	superficial temporal artery
WBV	whole blood viscosity
WGN	white Gaussian noise

Chapter 1

Introduction

1.1 Motivation

The human brain is an organ with a high energy-density demand. It amounts to only 2% of the entire body mass (or $\approx 1.4\,\mathrm{kg}$) but accounts for about 20% of the total power consumption of a normal adult at rest [1]. Unlike other tissue, the brain has an inefficient anaerobic energy metabolism, and a shortage of oxygen quickly leads to brain cell damage and potentially death [2]. Hence, its sufficient perfusion with blood is crucial to maintain its function. The cardiovascular system must provide the needed amount of oxygenated blood and any disease affecting the supply of blood to the brain must be treated. Some treatments involve revascularization surgery, which has the goal to increase the blood flow into a specific area. It is reported that approximately 10% of the patients have faced complications after surgery due to an ongoing insufficient blood flow [3, 4]. This clinical observation led to the need to develop technologies to monitor the blood flow during surgery. This intraoperative feedback would provide essential information to the surgeon on the quality of the procedure.

The state of the art in intraoperative blood flow measurement is the ultrasonic flow probe. Thereby, the vessel needs to be placed into the probe, which requires space to operate and contact. This holds the risk of contamination, vessel compromise and rupture [5]. An alternative method which could overcome these risks is the optical measurement of the blood flow via indocyanine green (ICG) fluorescence angiography (FA), which is a standard method to monitor the existence of blood in a certain area [6]. This method is commonly used in revascularization surgery to provide the medical staff an anatomical visualization and qualitative functional imaging of vessels in the field of view of the camera [6–12]. This method is nowadays still limited to a qualitative analysis of blood flow. It should be extended to a quantitative analysis to complement the state of the art by a non-contact method and thereby reduce the risks [13].

The overarching goal of this thesis is to develop methods enabling a quantitative measurement of the blood volume flow via ICG FA. Moreover, the accuracy of the developed methods should be analyzed and improved.

The quantitative measurement of blood flow via ICG FA was the subject to research in the past. Thereby, most publications apply the indicator dilution theory[1] to the measurement of the ICG fluorescence emission in a single point. This approach utilizes the fluorescence emission as an optical measurement or surrogate for an analysis of the indicator's absolute concentration. This approach does not comply with the prerequisites of the indicator dilution theory since the emission is not a surrogate for the concentration and moreover, the conservation of mass of the indicator is violated (more details in Section 4.3.1).

Another approach applies the fundamental definition of the volume flow rate (Equation 1.1, with V - volume, t - time, v - mean flow velocity, A - cross sectional area) and the systemic mean transit time theorem for single input and single output systems as defined by Perl et al. [16]. This approach requires an accurate measurement of the cross sectional area and the mean flow velocity.

In this thesis, the approach based on the fundamental definition of the volume flow rate is followed as it is expected to show better results.

$$\dot{V} = \frac{dV}{dt} = \bar{v} \cdot A \tag{1.1}$$

This thesis contributes to the realization of an intraoperative, quantitative, and non-contact measurement of the blood volume flow to complement the state of the art. Thereby, methods for an accurate measurement of spatial distances and temporal delays were developed. Moreover, a systemic error was identified, analyzed and compensated for. Finally, an *ex vivo* and *in vivo* validation of the measurement was performed. Detailed objectives are formulated in the next section.

1.2 Objectives of this thesis

The main focus of this thesis was to develop an intraoperative, quantitative, and non-contact measurement of the blood volume flow using ICG FA. To achieve this, different geometrical of the vessel and temporal parameters of the fluorescence dynamics needed to be extracted from the video signal. Additionally, an analysis of the underlying physical model needed to be performed to ensure its trustworthiness. The developed methods should be applied on *in silico*, *ex vivo*, and *in vivo* data to assess the use case accuracy of the methods.

In detail, this thesis aims to achieve the following objectives:

Analysis of the spatial dimension of the vessel The vessel's length and diameter need to be known to enable the calculation of the flow. They must be extracted from a segmentation.

---

[1] It is based on the findings of Fick [14] and the central volume theorem [15].

The accuracy of both should be determined to asses the reliability of the flow measurement. Therefore, a ground truth is needed and should be generated. Finally, methods to increase the accuracy need to be developed and validated against the provided ground truth.

Analysis of the transit time The transit time of the ICG bolus needs to be determined. It is calculated as the temporal delay between two temporal signals (indicator dilution curves) extracted at two locations. The statistical error in determining the transit time needs to be analyzed. Therefore, a ground truth is needed and should be generated by a computational model. Different methods assessing the transit time should be analyzed.

Generation of a computational model to analyze the systemic error in the flow measurement The underlying physical model of the flow measurement via an optical system should be investigated regarding its validity. For this purpose, a theoretical analysis should be performed and followed by a quantification of the systemic error by a computational model, which simulates the propagation of photons in a vessel.

***Ex vivo* and *in vivo* validation of the method** The measurement of the blood volume flow should be validated first on an *ex vivo* setup to potentially reveal its practical accuracy in a standardized environment and then in an *in vivo* study as a proof of concept of the measurement of blood volume flow in humans.

1.3 Structure of this thesis

Part I introduces the relevant medical and technical fundamentals and includes the state of the art in clinical blood flow measurement.

- **Chapter 2** provides medical fundamentals and underlines the clinical problem and motivation of this thesis. It also provides use cases of revascularization surgery where the blood flow measurement would be beneficial.
- **Chapter 3** introduces the fluorescence angiography.
- **Chapter 4** gives a short overview of the established intraoperative blood flow measurement techniques. It represents the state of the art of commercially available methods to determine the flow and the state of the art in research for the quantification of the blood volume flow via ICG FA.
- **Chapter 5** shows the state of the art in the simulation of the transport of radiation by Monte-Carlo (MC) models. Two propagation models are presented and both are used later in the determination of the systemic error.

Part II presents the necessary steps of the end-to-end workflow to compute the desired flow values from the recorded video input. This includes all pre-processing steps to extract the geometrical and temporal parameters, and the final determination of blood volume flow.

Part III consists of the introduction and analysis of the statistical and systemic error for measuring the geometrical and temporal parameters needed to calculate the volume flow.

- **Chapter 7** introduces the statistical and systemic error. It differentiates both from each other and gives a theoretical analysis of the underlying physical model to calculate the volume flow.
- **Chapter 8** handles the statistical error in determining the length, the diameter of the vessel, and the transit time measurement. It includes an introduction into the problem faced in measuring those parameters, the presentation of the proposed methods and obtained results, and the discussion of the results.
- **Chapter 9** handles the systemic error of the optical measurement of blood volume flow. Similar to Chapter 8, it includes all steps from introducing the problem to the discussion of the results. In this chapter, the simulation of the transport of radiation is addressed and used to determine the systemic error.

Part IV deals with the application of the developed method for measuring the blood volume flow in an *ex vivo* and *in vivo* experiment.

- **Chapter 10** analyzes the performance of the proposed methods in an *ex vivo* experiment. The materials used include pig's blood, aortas taken from rabbits and a self designed setup. This chapter includes all steps from introducing the goals of the experiment to the results and their discussion.
- **Chapter 11** applies the methods to *in vivo* data obtained from revascularization on humans and shows the results and their discussion.

Part V gives an overall conclusion and outlook to the thesis.

- **Chapter 12** concludes all chapters with a focus on the set hypotheses and mainly sets the work into relation to the state of the art in intraoperative blood flow measurement.
- **Chapter 13** summarizes the outlook of the Chapters 8, 9, 10 & 11.

PART I

FUNDAMENTALS

Chapter 2

Medical fundamentals

The human brain is an organ with a high energy-density demand. It amounts to only 2% of the entire body's mass (or $\approx 1.4\,\mathrm{kg}$) but accounts for about 20% of the total power consumption of a normal adult at rest [1]. The brain is supplied with oxygen by the blood. Its perfusion is necessary for the neuronal oxidative metabolism of energy substrates (mostly glucose) [17, 18]. Due to the limited capacity of neurons for anaerobic metabolism (at rest, up to 92% of the adenosine triphosphate in the brain results from oxidative metabolism of glucose), the cerebral blood flow is crucially important for the brain's function and viability [19]. The cerebral blood flow ensures a sufficient delivery of oxygen and energy substrates and the removal of waste products of metabolism. Both hypoperfusion (insufficient flow) and hyperperfusion (excessive flow) can cause brain damage through ischemic injury or the breakdown of the blood–brain barrier, respectively. The latter can cause seizures, headaches, encephalopathy, and both ischemic and hemorrhagic stroke [20].

2.1 Circulatory system

The function of the circulatory system of the blood flow is to ensure a sufficient blood supply to the cells of the whole body. Thereby, nutrients are provided to and waste products are removed from the cells. The circulatory system is also essential for the distribution of hormones, the regulation of body temperature, and many more. It consists of many components, but in this work we will focus on the blood and the vessel system.

2.1.1 Blood

Blood is a suspension that is pumped by the heart through the circulatory system. It consists of blood cells (mainly erythrocytes, leukocytes and thrombocytes) which are suspended in blood plasma. The largest share of the blood cells have the erythrocytes. The volume percentage of red blood cells (RBC or erythrocytes) in the blood is called hematocrit, and its physiological value in humans is around 40% - 50% for males and 35% - 45% for females.

The blood plasma consists of approx. 90% water, 7% proteins and 3% others. The proteins are composed of 60% albumin and 40% globulin (α_1, α_2, β, γ) [21].

One important parameter of blood is its viscosity. Its study, the hemorheology, is complex and a short introduction is given here. Whole blood behaves as a non-Newtonian fluid, which is caused by the RBCs and their deformation [22]. At rest, blood behaves like a solid because RBCs tend to aggregate and form three dimensional structures of rod shaped RBC stacks [22]. To initiate the flow of blood, the internal structural forces have to be overcome by an externally applied force [23]. While flowing, the solid-like structures break into smaller fractions until the RBCs are eventual fully disaggregated [22]. The flow behavior of blood at high shear rates ($> 100\ \mathrm{s}^{-1}$) can be treated as Newtonian with a constant viscosity [24]. At lower shear rates ($< 100\ \mathrm{s}^{-1}$), blood is treated as a non-Newtonian fluid since its viscosity increases exponentially with decreasing shear rate [25]. The viscosity of blood is dependent on the hematocrit, temperature and many more parameters [26–28]. Different models exist to mathematically describe the viscosity of whole blood such as the Casson model, Carreau model or Power Law model. They will not be presented in further detail here, but information on all of them can be acquired in [29].

2.1.2 Cerebral blood vessels

Since this thesis focuses on the arterial vessels, only the arterial cerebral blood vessels will be mentioned.

Arterial blood is brought to each of the cerebral hemispheres by the internal carotid artery (ICA) and the vertebral artery [30]. Thereby, the vertebral arteries enter the skull and unite to form the basilar artery (BA). The BA divides into the two posterior cerebral arteries (PCAs). The ICA divides into two main branches: the middle cerebral artery (MCA) and the anterior cerebral artery (ACA). The PCA, MCA and ACA are mainly responsible for the arterial blood supply of the cerebrum. The inner diameter, vessel wall thickness and blood volume flow of and in these arteries are of interest for this work, since many surgical interventions are performed on them or their distal branches. Table 2.1 shows the mean values of the diameter and blood flow value of certain vessels obtained from various publications [31–36]. The vessel wall thickness of cerebral arteries was reported to be approx. 11% of the outer diameter [37].

A pulsatile pressure and flow is present in the circulatory system. In the cerebral arteries, the amplitude of this pulsatility is more significant than in the veins. Due to the elasticity of arteries (Young's modulus of $E \approx 0.2 - 6\,\mathrm{MPa}$), the pulsatility is lower in distal vessels than in proximal vessels [40–42]. For example, the ratio of systolic to diastolic pressure in the ICA is 117 mmHg / 77 mmHg and drops to 98 mmHg / 62 mmHg in the MCA (MCA is located distal of the ICA, the ICA gets divided into the MCA and ACA) [43].

The pulsatility in flow drops similarly to the pressure. It was shown that the Gosling pulsatility index (PI) (see Equation 2.1 with BFR being the blood flow rate) is significantly reduced from proximal to distal measurements of volume flow in cerebral arteries [44, 45]. A PI of

Table 2.1: This table shows the inner diameter of the major cerebral vessel and the respective blood flow. All values are given as mean ± standard deviation. The diameter values were obtained from almost 10,000 measurements extracted from multiple publications [31–36]. The flow values were obtained from 124 measurement extracted from multiple publications [38, 39].

Vessel	**Diameter** in mm	**Blood flow** in ml/min
ICA	3.99 ± 0.43	287.87 ± 63.81
MCA	2.56 ± 0.37	142.20 ± 43.50
ACA	2.03 ± 0.35	82.00 ± 18.00
BA	3.08 ± 0.46	138.30 ± 42.56
PCA	1.93 ± 0.38	57.51 ± 16.56

zero means that no pulsation is present at all. The PI in the ACA decreases from 0.88 to 0.77 from proximal to distal.

$$PI = \frac{BFR_{systole} - BFR_{diastole}}{BFR_{mean}} \tag{2.1}$$

2.2 Hypo- and hyperperfusion

Hypoperfusion In the case of hypoperfusion organs cannot function properly due to inadequate oxygen supply. The term hypoperfusion describes a reduced amount of blood flow in a certain area, and it can lead to hypoxia/ischemia. Causes for acute hypoperfusion include low blood pressure, heart failure or loss of blood volume and can lead to necrosis of neurons [46]. Chronic cerebral hypoperfusion induces apoptosis in neurons and can lead to cognitive impairment [47, 48]. Chronic cerebral hypoperfusion can be caused by the cerebral small vessel disease such as moyamoya disease, atheroma of arteries, artherosclerosis or aging [47, 49–54]. Hypoperfusion needs to be treated. Most relevant for this thesis is the revascularization surgery (see Section 2.3).

Hyperperfusion Cerebral hyperfusion can occur after treatment of a hypoperfusion and is characterized by various symptoms such as headache, eye and face pain, vomiting, confusion, visual disturbances, neurological deficits, and intracerebral or subarachnoid haemorrhage [55]. Although most patients have mild symptoms, progression to severe symptoms can occur if it is not treated adequately [56]. Because diagnosing cerebral hyperfusion is based on several non-specific symptoms, patients may be misdiagnosed. Knowledge of cerebral hyperfusion among physicians is limited [57]. Some revascularization procedures can cause cerebral hyperfusion such as the mentioned extracranial-to-intracranial (EC-IC) bypass [58].

Summarizing, both conditions, hypo- and hyperperfusion can progress to severe symptoms up to death of the patient. Hence, an adequate control of the blood flow is needed to assess whether one of the conditions is present. A threshold does not exist to define hypo- and hyperperfusion and is depending on the physicians subjective view [57].

2.3 Revascularization surgery

The term revascularization describes the restoration of the vasculature and hence perfusion of an organ. A revascularization surgery can be performed either minimally invasive such as an angioplasty or stenting, or by an open surgery such as installing a bypass. In this work, the latter is of greater importance, especially the EC-IC bypass surgery performed to restore the perfusion of the cerebrum.

EC-IC bypass surgery An EC-IC bypass is a direct artery-to-artery anastomosis. An EC-IC bypass creates an anastomosis between the superficial temporal artery (STA) and a branch of the MCA using micro-surgical techniques and was first introduced by Yasargil and Donaghy in 1969 [59]. Figure 2.1 visualizes the basic principle of the surgery. The expected outcome is an increase of blood flow in the distal branch of the MCA. For more details on the surgical procedure, please see [60].

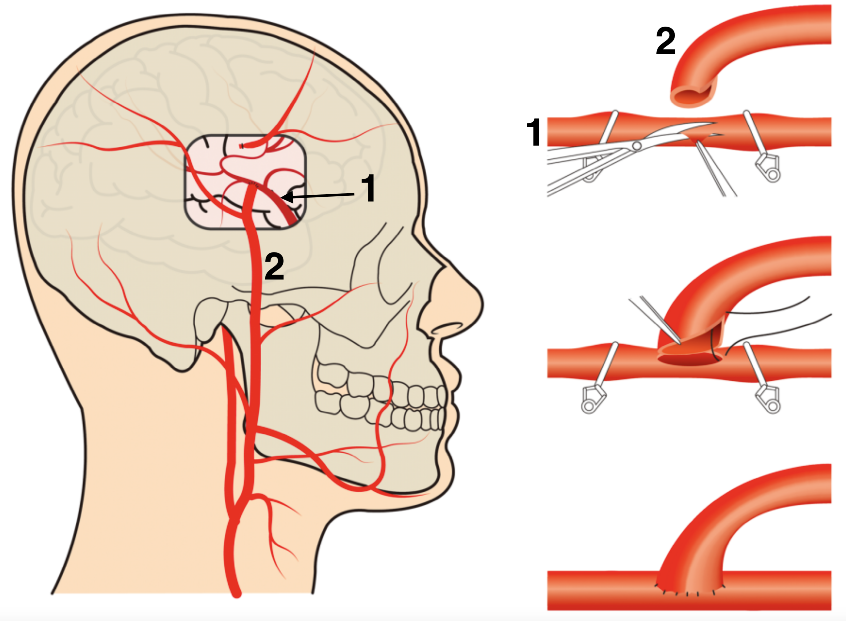

Figure 2.1: An EC-IC bypass is a surgical treatment that requires a cranial trepanation. Thereby, an extracranial artery of the scalp (2) is directed through the opening of the skull and sutured onto an intracranial cortical artery (1). The goal of this bypass is to augment flow to the distal MCA vascular territory. The extracranial artery serves as a donor of blood and the intracranial artery as recipient of blood [60]. The image is adapted from [61] published under the Creative Commons Attribution 4.0 License.

Chapter 3

Fluorescence angiography

3.1 Fluorescence microscopy

Fluorescence microscopy was first introduced in the early 20th century by the companies Carl Zeiss and Carl Reichert [62, 63]. Since then, these microscopes have entered various fields in science and technology and are indispensable in many life science applications. This section will introduce the principle of fluorescence and the setup of a fluorescence microscope.

3.1.1 Fluorescence

The emission of light from a substance is termed as luminescence, and occurs due to the relaxation of excited molecules. Luminescence is divided into two groups: Fluorescence and phosphorescence. We will focus on fluorescence.

The first reported observation of fluorescence was in the 19th century by Sir Frederick William Herschel [64]. It was described in more detail by George Stokes shortly after [65]. Ernst Abbe and Hermann von Helmholtz recognized the potential of fluorescence to yield images with better differentiated and discernible structures when an object emits light by itself [66, 67].

To fluoresce, molecules undergo transition from ground to excited state by absorbing photons of appropriate energy compared to the energy gap between the ground and excited states. Upon excitation, one of the electrons makes a transition to the excited state, in other words: It gains energy by absorbing the photon. Consequently, return to the ground state releases energy in form of the emission of a photon. The process of fluorescence occurs rapidly, the time between excitation and return to ground state is in the scale of nanoseconds. The energy of the emitted photon is lower than the energy of the absorbed photon. Consequently, the emission spectrum is shifted to lower energy than the absorption spectrum, this shift is named Stokes shift (see Figure 3.1) [68].

$$\lambda_S = |\lambda_{emitted} - \lambda_{absorbed}| \tag{3.1}$$

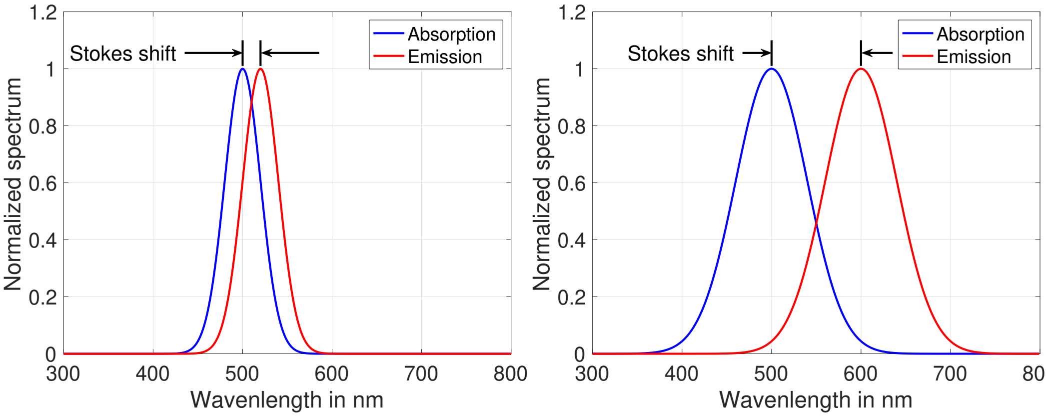

Figure 3.1: Two artificial examples are given on the Stokes shift. In blue the absorption and in red the emission spectra are given. **Left**: An example is shown with a very small Stokes shift. **Right**: An example is shown with a larger Stokes shift. This Stokes shift needs to be taken into consideration in determining the optical filter setup. For the left case, the requirements on the filters are more challenging.

Fluorescence is highly specific either as endogenous autofluorescence[1] of exogenous labeling[2], this enables a broad range on imaging in biology [69]. Thereby, spectral, spatial, and functional information is obtained on the imaged specimen. In this thesis, the exogenous labeling of blood was used. To enable the imaging of a specific dye, specific requirements on an imaging system need to be set and fulfilled.

3.1.2 Setup of a fluorescence microscope

The design of a fluorescence microscope is related to the particular imaging problem. In the case of this thesis, only a frontal illumination and detection are required and will be described in the following. The choice of the correct optical components, such as the filters, relies on the optical properties of the fluorescent dye as given in the previous section.
In this work, the coaxial design for a frontal lighting systems according to the Ploem System is used [70]. The sketch for this setup is shown in Figure 3.2.
It consists of five main components: illumination system, detection system, excitation filter, emission filter and dichroic mirror. They need to be designed according to the (spectral) requirements derived from the used fluorophore. Thereby, the requirements are set to fulfill the following fundamental goals:

1. The light source should emit the needed spectrum to excite the fluorophore.
2. The detector should have a high sensitivity on the spectrum of emission by the fluorephore.
3. Maximum excitation light from the light source should be transmitted to the specimen.

---

[1] Natural fluorescence emission of tissue arising from endogenous fluorophores after exposure to light of a suitable wavelength.

[2] Binding of a non-natural fluorophore to the tissue.

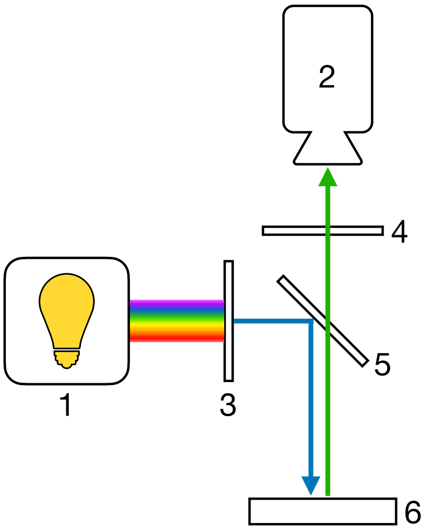

Figure 3.2: This schematic shows the general setup of a coaxial designed fluorescence microscope. It shows in **1**: light source, **2**: camera system, **3**: excitation filter, **4**: emission filter, **5**: dichroic mirror, **6**: specimen. This schematic misses some optical components such as the objective or aperture.

4. Maximum fluorescence emission form the specimen should be transmitted to the detector.
5. No illumination light in the range of the fluorescence emission should be transmitted to the detector.

Commonly, a broad band illumination source is chosen with a band pass excitation filter in front of it to absorb the spectrum which overlaps with the expected fluorescence spectrum. Nevertheless, some systems use laser as an illumination source and therefore do not require an excitation filter [71]. The emission filter should only transmit the expected fluorescence spectrum from the specimen and is mostly designed as a band pass. Although the excitation and emission spectra of some fluorophore overlap, the excitation and emission band pass filter should not overlap. Otherwise, reflections from the specimen or its background could be detected as fluorescence. The dichroic mirror allows a coaxial design by reflecting the excitation light onto the specimen and transmitting the fluorescence light to the detector and should be chosen according to the requirements set on the excitation and emission filters. The choice of the detector depends on factors like the expected fluorescence emission intensity and spectrum, as well as on the required spatial and temporal resolution. The spectral sensitivity of different detector materials is shown in Figure 3.3. For an expected fluorescence around 830 nm, a silicon-based chip is appropriate. The spatial and temporal resolution are connected reciprocally, so a well balanced compromise should be chosen.

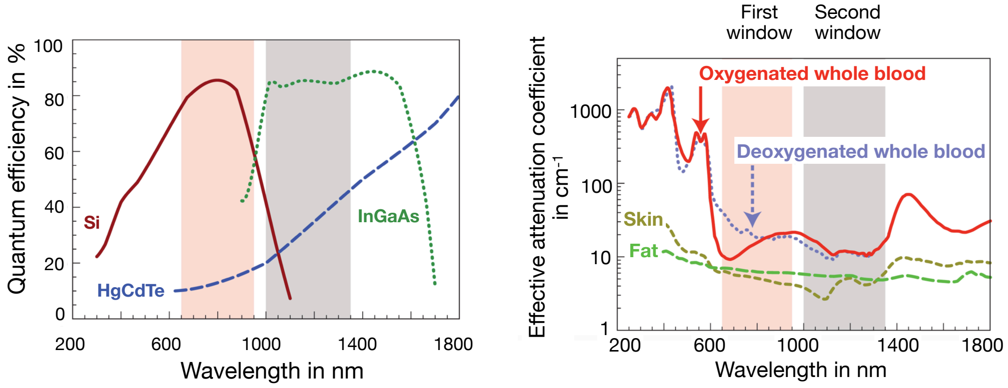

Figure 3.3: Left: This plot shows the quantum efficiency of detectors made from three different materials (Si - silicon, HgCdTe - mercury cadmium telluride, InGaAs - Indium gallium arsenide) in dependency of the wavelength. In the low range of NIR, the Si-based detectors are superior to the others. **Right**: This plot shows the attenuation of light of different wavelength by various tissues. The light red marked area and the grey marked areas are the so-called first and second optical window. Biological tissue attenuates light less in both windows and thus allows a deeper penetration depth. The image is adapted by permission from Springer Nature Customer Service Centre GmbH: Nature Nanotechnology [72] © 2009.

3.2 Indocyanine green

Indocyanine green (ICG) is a tricarbocyanine fluorescent dye with a molar mass of $M_{ICG} = 774.96\,\frac{\mathrm{g}}{\mathrm{mol}}$, which was developed for the near-infrared (NIR) photography by the Kodak Research Laboratories in 1955 [71]. Shortly afterwards, it was clinically used to record indicator dilution curves (IDCs) for the determination of cardiac output and got FDA approved by 1959 [73]. Nowadays, its use has expanded to multiple medical fields such as ophthalmology, neurosurgery, vascular surgery, oncology and many more [7, 74–78]. In the following sections, the relevant information on the pharmacokinetics, binding properties, spectral stability and fluorescence yield are given. Thereby, a focus is set on its dilution in blood in cerebrovascular imaging, whereas properties in other solvents and requirements for other applications are not presented.

3.2.1 Binding properties and pharmacokinetics

ICG is mostly injected intravenously and mainly binds to the plasma proteins in blood. Its binding property depends on its concentration in the solvent (blood). At very low concentrations, it preferably binds to the β-lipoprotein [79, 80]. Otherwise, it preferably binds to the plasma albumin but also binds to the globulin, α_1-lipoprotein and β-lipoprotein [79, 81–84]. The latter bindings are relevant for this work. After being bound, the molecules, made of proteins and ICG, are too large to penetrate the vessel wall, therefore remain intravascularly and can be assumed as a non-diffusable indicator [85]. This property enables the imaging of vessels with a high contrast. ICG has a half-life duration of 2 to 4 min in humans and is rejected by the liver and bile ducts [80, 86–88]. The half-life duration depends on the liver function and can be increased significantly in diseased patients [89, 90]. Nevertheless, the short life time in the circulatory system allows repeated application of ICG in imaging [71]. The administered dose (2.5 mg to 75 mg per patient) of ICG is much lower than the measured lethal dose in animals ($LD_{50} \approx 60\,\frac{\text{mg}}{\text{kg}}$) [91]. It has proven to have a very low toxicity, and the reported incidence of complications is very low [87, 92–96]. The mechanisms responsible for adverse reactions after an ICG injection are unknown. It is hypothesized that most severe complications like an anaphylactic shock are attributed to the iodide component of pulverized ICG [87, 94].

3.2.2 Optical properties

ICG is a fluorescent dye with an absorption and emission maximum at the NIR. Its exact optical properties depend on the solvent and the concentration of ICG. The absorption spectra of ICG in blood plasma shows two peaks (see Figure 3.4). With a variation of the concentration, the prominence of the peaks changes drastically. The first peak is at $\lambda_1 \approx 730\,\text{nm}$ and the second at $\lambda_2 \approx 805\,\text{nm}$. With decreasing concentration, the first peak turns into a shoulder and the second peak gains prominence.

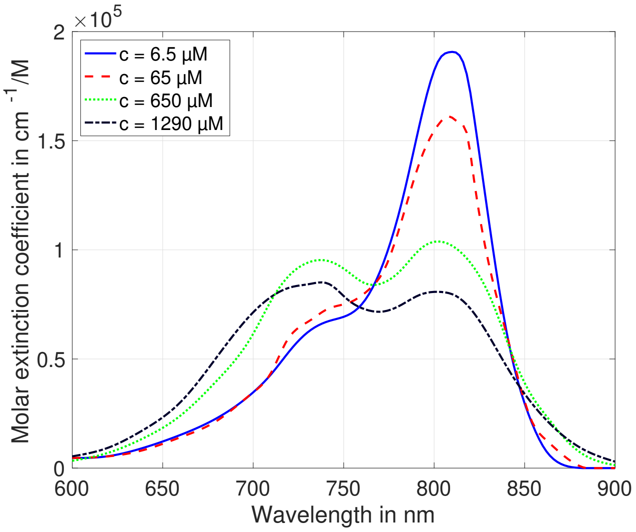

Figure 3.4: The molar extinction coefficient of ICG shows a dependency on the ICG concentration and the wavelength. The concentration has an influence on the absorption of light. The morphology of the spectrum changes drastically, although the peaks and “shoulders” do not shift along the wavelength a lot. The graph is based on the published data by [80] and digitized by [97].

The absorption peaks lie in the so called first optical window where biological tissue has little absorption (see Figure 3.3). Consequentially, this enables a greater depth of penetration and therefore a deeper insight into tissue [72, 75, 98].

The energy of absorbed photons is either transformed into an energy loss such as heat or remitted as a fluorescent photon of lower energy ($\lambda_{absorption} < \lambda_{emission}$). This Stokes Shift is characteristic to the dye, its concentration and the solvent. It is mostly measured as the shift of the maximum in excitation[3] and emission. In the case of blood as solvent, ICG has a Stokes shift of approx. 30 nm [99].

Both spectra, excitation and emission, are shown in Figure 3.5 for a concentration of 0.05 $\frac{\mathrm{mg}}{\mathrm{ml}}$ in whole blood. The emission is depending on the ICG concentaration as shown in Figure 3.5 and shows a non-linear dependency.

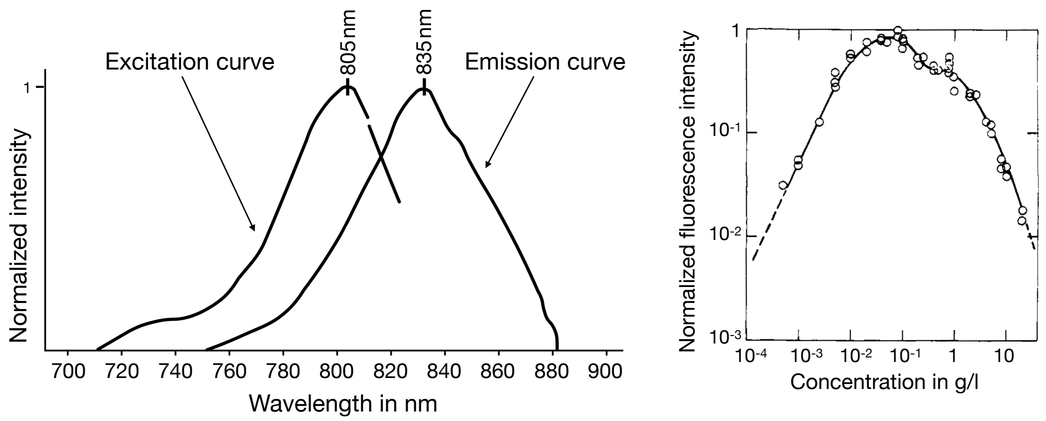

Figure 3.5: Left: The normalized excitation and emission spectra of ICG in whole blood are shown. This image was adapted from [100]. **Right**: The normalized fluorescence intensity of ICG in whole blood is shown. The total fluorescence intensity is dependent on the ICG concentration. This image was adapted from [99], published under the Attribution 4.0 International (CC BY 4.0) Licence.

The fluorescence quantum yield is a characteristic parameter of a dye and depends on the solvent and the concentration of it. It is the ratio of the number of emitted to absorbed photons (see Equation 3.2) and can be interpreted as the probability of an absorbed photon to be turned into a fluorescent photon. In blood, the fluorescence quantum yield is around 1 to 10 % [99, 101]. Interestingly, the absorption and emission spectra of ICG overlap. A re-absorption of emitted fluorescence photons and eventually a remission of a new fluorescence photon is possible [101, 102]. This causes a cascade of re-absorption and remission, which is connected by the fluorescence quantum yield [101].To observe fluorescence of ICG in a solvent, an application tailored set of requirements need to be fulfilled by the imaging device.

$$\Phi = \frac{Photons_{emitted}}{Photons_{absorbed}} \tag{3.2}$$

ICG is mostly stored as a dry powder since it chemically decomposes in most solvents over time and therefore changes its optical properties. Hence, pharmaceutic ICG is available as a powder and needs to be dissolved in a fluid before administration [71]. In clinical practice, it is dissolved in water and sequentially injected intravenously. The spectral stabilization, which means it does not change its optical properties over time, is fastest in distilled water

---

[3] The excitation spectrum is not equal to the absorption spectrum.

and is consistently stable for approx. 7 days [80]. An ICG and water solution mixed with blood reaches spectral stability after 1.5 s [80].

Consequentially, observation by ICG fluorescence imaging of blood are assumed to be trustworthy from the perspective of the spectral stability after 1.5 s from the moment of injection.

Chapter **4**

State of the art in the intraoperative flow measurement

This chapter focuses on the flow measurement during surgery. Measuring the blood flow during surgery has the advantage that the surgeon can rapidly intervene in the case of an insufficient flow. Since the early 20th century, different techniques evolved. In the following chapter, the established magnetic and ultrasound-based methods will be introduced and the current state of the art in research on fluorescence angiography (FA) based methods as well. Other methods that can be utilized for this type of measurement, such as light amplification by stimulated emission of radiation (laser) Doppler, computed tomography (CT) or magnetic resonance imaging (MRI), will not be presented as they either provide a relative measurement or are rather perioperative than intraoperative methods (for more details please see the referenced articles) [103–108].

4.1 Magnetic

One of the first intraoperative blood flow measurement techniques was the electromagnetic flow meter introduced in the late 1937 by Kolin [109]. It is used intraoperatively to asses the blood volume flow in an exposed vessel [110, 111]. It is based on Faraday's law of induction and the Hall effect. The law of induction states that when an electrical conductor move to the lines of force of a magnetic field, a voltage is induced in the conductor. In the context of blood flow measurement: blood is an electrically conductive suspension and its movement (more specifically the movement of the ions in the blood) represents a moving conductor [112]. The Hall effect states that a voltage difference will be generated in an electrical conductor which is facing an electrical current while applying a magnetic field perpendicular to the current.

Electrodes are placed at right angles to the flux and need to be in contact with the vessel wall. Figure 4.1 shows the fundamental setup of a magnetic flow meter. Equation 4.1 shows the dependency of the voltage from the mean flow velocity (U - measured voltage, B - magnetic field, d - distance between the electrodes, $\bar{v}$ - the mean flow velocity and k is a flow medium dependent factor).

$$U = k \cdot B \cdot d \cdot \bar{v} \tag{4.1}$$

The working principle requires a fully closed ring around the vessel. This is inconvenient and thus it was replaced by the flow probes based on ultrasound for the intraoperative use on vessels.

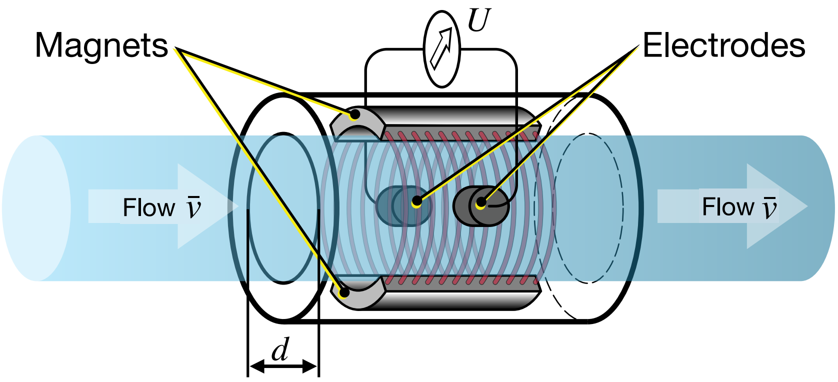

Figure 4.1: The fundamental setup of a magnetic flow meter is shown. A magnetic flow meter consists of an electromagnet, providing a magnetic field perpendicular to the media's flow direction, and at least two electrodes aligned perpendicular to the magnetic field. The blood's ions experience a Lorentz force in dependence of their velocity. This force separates the ions and creates an electrically measurable voltage at the electrodes. This image is adapted from [113].

4.2 Ultrasonic-flow probe

The ultrasound-based measurement of flow can be divided into two approaches: the Doppler flowmetry and the transit time flowmetry. The transit time flowmetry is more accurate in measuring the mean flow velocity and hence more common in intraoperative blood volume flow measurement and is introduced in this section [114].

The transit time flowmetry was introduced by Drost et al. in 1978 to assess the blood volume flow and has nowadays proven to provide significant clinical information [115–119]. The device measures the transit time of an ultrasonic wave upstream and downstream and calculates the flow velocity according to Equation 4.2 ($\bar{v}$ - the mean flow velocity, l is the transit distance, t_1 and t_2 are the transit times of the wave in both opposing directions).

$$\bar{v} = \frac{l \cdot (t_2 - t_1)}{2 \cdot t_1 \cdot t_2} \tag{4.2}$$

The value of $|t_2 - t_1|$ increases with increasing flow velocity and it turns to zero whenever the fluid is not in motion. The design of a probe is shown in Figure 4.2. To perform a

measurement, a signal is emitted, propagates through the vessel, reflected at the acoustic reflector, propagates again through the vessel, is detected and its transit time recorded. The usage of a reflector allows a device design with all bulky component on one side and hence facilitate the use of the device on exposed blood vessels. The ultrasonic beam must cover the whole width of the vessel lumen, so the transducer integrates all velocity components in the vessel. Since stationary parts, such as the vessel wall or gaps within the beam area, do not contribute to the flow velocity, the difference in transit time $|t_2 - t_1|$ is proportional to the volume flow and independent of the shape of the vessel [115, 120]. Nonetheless, to yield accurate results the vessel should fit into the probe's gap well and an acoustic coupler should displace all air. Otherwise, the accuracy decreases [121].
Due to its high accuracy and relatively convenient use, it is the gold standard in intraoperative blood flow measurement, especially in cerebrovascular surgery [121].

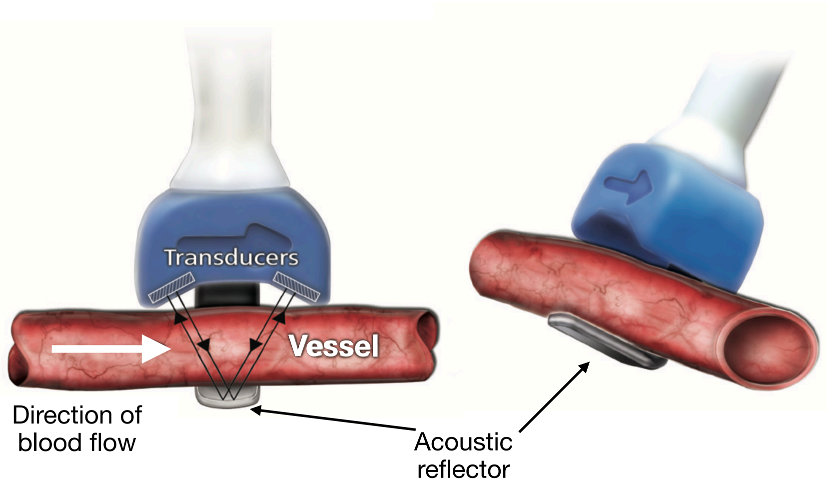

Figure 4.2: The setup of a transit-time-based flow meter consists of two main components. First, a pair of transducers to emit and detect the ultrasonic wave. Second, an acoustic reflector to reflect the wave. This enables a lean design of the probe. It is essential to place an acoustic coupler (e.g. sterile gel) into the gap between the device and the vessel to ensure an accurate measurement. This image is adapted from [122].

4.3 Quantitative fluorescence angiography

The aim of this thesis is the quantification of blood flow via FA. In the following subsections, an overview of the state of the art is given for two fundamentally different approaches to measure the flow via FA: The one point measurement and the two point measurement. Both are presented to reveal differences and motivate the decision on the implemented method for the following studies.

4.3.1 One point measurement - the indicator dilution theory

The one point measurement by the indicator dilution method relies on the findings of Fick back in 1870 [14]. Meier and Zierler first proved and established the central volume theorem [15] which led to the development of the Swan-Ganz catheter (also called Pulmonary artery catheter) in the 1970 [123]. To perform a measurement, an indicator of known quantity needs to be abruptly injected into a vessel and its timewise concentration is measured downstream. This measurement uses one indicator dilution curve (IDC) obtained as single time series (obtained from a point/pixel or as a mean value of a region of interest (ROI)). The volume flow $\dot{V}$ can be determined using Equation 4.3 with m_0 as the administered indicator quantity and $c(t)$ as the timewise concentration of the indicator at a downstream location.

$$\dot{V} = \frac{m_0}{\int_{t=0}^{\infty} c(t)\, dt} \tag{4.3}$$

This approach relies on the conservation of mass of a non-diffusible indicator. Hence, no loss of mass should be present and an absolute measure of the quantities is required. Both requirements are violated in an optical measurement of the IDC in cerebral vessel after an intravenous injection of indocyanine green (ICG). First, the propagation of the ICG bolus faces many junctions at which the bolus is split. It is very likely that only a fraction of the injected quantity m_0 reaches the measurement site. Second, the optical measurement of the concentration of the ICG in the vessel is a complex inverse problem that has not been solved yet. The denominator in Equation 4.3 is strongly affected and the measurements are not accurate [124–128]. Often, researches have observed an overestimation of the blood volume flow by the indicator dilution method with ICG although injection and detection site are close by. Along other reasons for this discrepancy, all publications have in common to suspect the optical properties of ICG as main source of error in these measurements [124, 127–129].

Nonetheless, empirical clinical studies showed that the indicator curve's morphology holds information on the volume flow. Surrogates for the volume flow, such as the blood flow index (BFI) (see Equation 4.4 with ΔICG_{max} as the maximum amplitude, and MTP as the mean time to peak of the signal), evolved [130–132]. It is also applied to ICG FA [133, 134].

$$BFI = \frac{\Delta ICG_{max}}{MTP} \tag{4.4}$$

The BFI is a relative measure of blood flow and is proportional to the absolute flow with an unknown factor. It is only applicable in the case of a constant vessel geometry, injected indicator quantity and detector efficiency [135]. Consequentially, changing the vessel geometry, e.g. installing a bypass, has an influence on the BFI.

4.3.2 Two point measurement

The two point measurement utilizes the fundamental definition of the volume flow rate shown in Equation 4.5 with V as volume and t as the time.

$$\dot{V} = \lim_{\Delta t \to \infty} \frac{\Delta V}{\Delta t} = \frac{dV}{dt} \tag{4.5}$$

Assuming the flow velocity penetrates the cross sectional area perpendicular to it and both are constant, yields Equation 4.6 with v as the flow velocity, A as the cross sectional area, s as the transit distance and t as the transit time. To obtain s and t, two points need to be determined on the geometry e.g. tube, thus the name: two point measurement (see Figure 4.3).

$$\dot{V} = v \cdot A = \frac{s}{t} \cdot A \tag{4.6}$$

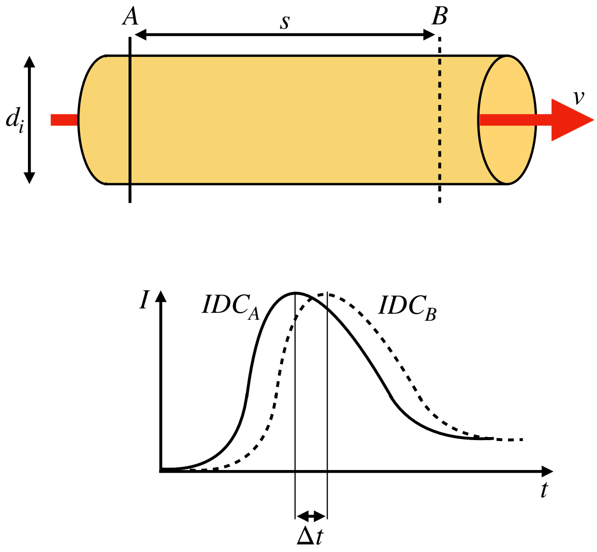

Figure 4.3: Top: a sketch of a vessel with an inner diameter of d_i is shown. The blood has a flow velocity of v. **Bottom**: at the locations A and B, the IDCs were extracted. The distance of both location is s. The transit time is denoted as Δt. The image is taken from [136], published under the Creative Commons Attribution 4.0 License.

In the context of the blood volume flow measurement in vessels, two measurement points on the vessel are set and their geodesic distance determined followed by obtaining two IDCs at these location. The two IDCs are used to determined the transit time as their delay. This two point measurement is based on the systemic mean transit time theorem for single input and single output systems as defined by Perl et al. [16]. This approach relies on the assumption that the two IDCs are of similar morphology.

This approach was used by Weichelt et al. to quantify the blood volume flow intraoperatively by ICG FA [137]. They performed measurements on a phantom and *in vivo* measurements on a human subject (as shown in Figure 4.4). It revealed that the measurement seems to have a systemic dependency on the diameter which was linked to limited penetration depth of the light into the vessels. Table 4.1 shows the measured deviation for the measurement performed on a phantom. The clinical results will not be discussed since only a single patient was involved and the results are not clearly formulated. Anyhow, the paper lacks of many information in the methods part and hence can neither be reproduced nor fully understood. To my best knowledge, no other publications exist regarding the topic of the quantitative measurement of blood volume flow by ICG FA.

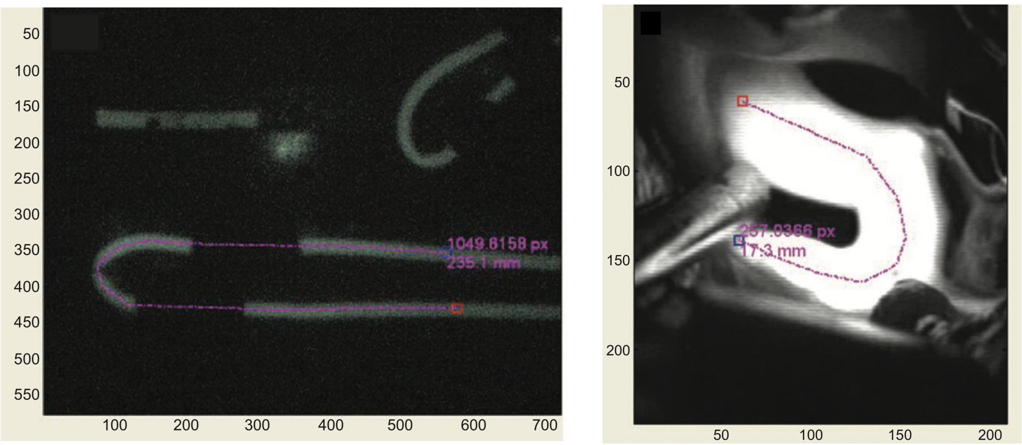

Figure 4.4: Left: this image shows the vessel phantom which was used to assess the volume flow. The axes are in pixels and a manually drawn line depicts the length of the tube. **Right**: this image shows an *in vivo* recorded cerebral vessel of a human subject undergoing revascularization surgery. The manually drawn line depicts the length of the vessel and at its end (blue and red box) the signals were extracted to obtain the delay of the fluorescence at the locations. Both images are taken from [137], published under the Attribution 4.0 International (CC BY 4.0) Licence.

Table 4.1: This table shows the results for the measurement of the volume flow for different diameters. The measured deviation is calculated a the ratio of the via FA determined flow divided by the reference flow. Measuring flow via FA overestimates the flow. Moreover, it depends on the diameter and the flow characteristic [137].

Vessel diameter in mm	**Vessel geometry/ flow characteristic**	**Measured deviation**
1.6	Straight/laminar	1.05-1.09
3.2	Straight/laminar	1.38-1.45
3.2	Straight/non-laminar	1.10-1.12
4.0	Straight/laminar	1.58-1.59
5.0	Straight/laminar	1.48-1.53
5.0	Straight/non-laminar	1.17-1.21

4.4 Summary

Table 4.2 compares the main aspects of an intraoperative measurement of flow based on ultrasound and based on FA as they are the current clinical state of the art in blood flow measurement and the topic of the research in this thesis, respectively.

Table 4.2: A comparison of the intraoperative ultrasound-based and FA-based measurement of blood volume flow.

Aspect	Ultrasound-based	Fluorescence-angiography-based
Contact	Yes	No
Invasive	Only contact	Yes, requires an injection of dye
Immediately repeatable measurement	Yes	No, approx. 10 min between each injection
Multiple simultaneous measurements	No	Yes
Change of instrument	Yes	No
Quantitative measurement	Yes	No
Cost: initial	moderate	high
Cost: per measurement	low	low

Chapter 5

Simulation of the radiation transport by Monte-Carlo models

The simulation of radiation transport in tissues is considered to be a fundamental tool in biomedical optics. It allows the investigation of a large set of possible biomedical applications. Among other approaches, the Monte-Carlo (MC) based methods represent a gold standard in the simulation of forward or inverse problems [138–154].

MC-based methods allow the numerical analysis of complex geometries and media properties. Analytical methods, such as solving the radiative transport equations, are often limited in their capability to analyze complex geometries and complex media properties. The present work utilizes and further develops MC models to solve problems in the field of quantitative fluorescence angiography (FA).

In MC based methods, radiation is modeled by a large set of photons. The wave–particle duality of photons is usually reduced to a solely particle-like treatment of photons. The wave properties as e.g. the polarization are either ignored or simplified (e.g. internal reflection at boundaries is defined as the average of the reflectances of the two orthogonal polarization directions used). Neglecting the polarization of the photons is in the context of this work valid since the photons are multiply scattered and therefore the polarization is quickly randomized.

MC-models simulate the propagation, hence also tracing their paths, of photons in turbid media. Two approaches to compute the paths are established: First, the models that handle photons as a quantum that faces binary decisions, hence named binary propagation. Second, the models that handle photon packages that face weighted decision, hence named weighted propagation (also named scored physical quantities method).

The following sections will introduce both methods separately without going deeper into the choice of geometry, optical parameters or logging of performance parameters. It relates to the work of Wilson et al. and Wang et al. [155, 156].

5.1 Binary propagation

The binary propagation of photons was introduced by [155]. Treating photons as a quantum requires binary decision for interaction with the media or at boundaries, hence the name binary propagation. The general workflow is shown in Figure 5.1.

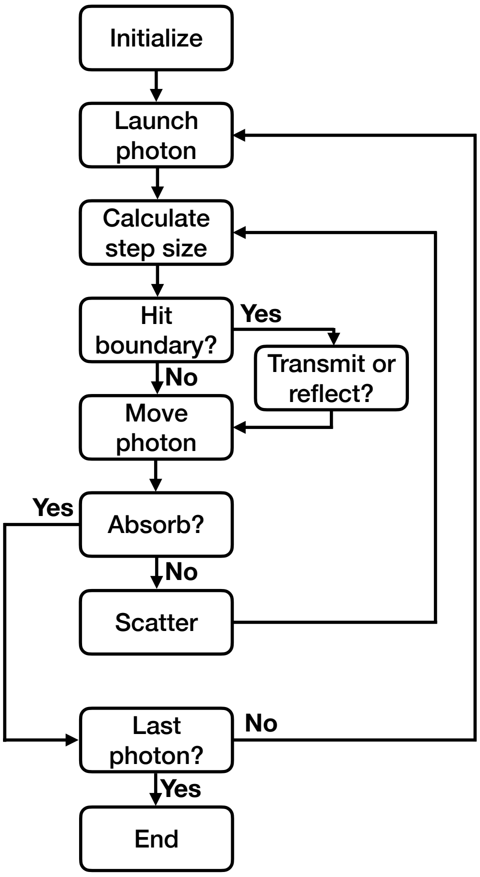

Figure 5.1: The binary propagation model starts by initializing the geometry, the medias optical properties, logging of performance parameters and setting the number of photons to be launched. After launching, the photon step size is calculated (Section 5.1.2 & 5.1.3). The photon will interact with either the media or a boundary upon its propagation (Section 5.1.4 & 5.1.5). At the new location the photon is either scattered (the direction is updated and then a new step size is calculated) or absorbed. The photon will be terminated in case it exits the geometry or is absorbed by the media and a new photon is launched (Section 5.1.6). This is repeated until the desired number of photons were launched and terminated. The scheme is based on [155, 157].

5.1.1 Geometry and coordinate system

The photons propagate through a geometry that has certain optical properties. The geometry can be composed of different materials and hence have a heterogeneous structure. In the MC-based simulation, four material parameters are used to simulate the propagation.

- n - refractive index: defined as the relative velocity of a photon in the material (reciprocal relative to the velocity in vacuum).
- μ_a - absorption coefficient: defined as the probability of a photon absorption event per unit infinitesimal path length.
- μ_s - scattering coefficient: defined as the probability of a photon scattering event per unit infinitesimal path length.
- g - scattering anisotropy: defined as the average of the cosine value of the deflection angle.

The MC model propagates photons in three dimensions. Therefore, a Cartesian coordinate (x, y, z) system is used. The geometries are not bound to fit this coordinate system and can be defined e.g. as cylinders as presented later (chapter 9).

5.1.2 Launching a photon

A photon always has a current position $S = \begin{pmatrix} x \\ y \\ z \end{pmatrix}$ and a propagation direction $M = \begin{pmatrix} \mu_x \\ \mu_y \\ \mu_z \end{pmatrix}$. The number of photons launched depends on the particular application. Generally, a trade off between computation time and reliability of the results for the performance parameter must be done. The reliability of the results is ensured by performing a convergence analysis with an increasing number of launched photons. This needs to be performed in a separate study. The launching position and direction of the photons determines the type of illumination (e.g. spot vs. homogeneous or diffuse vs. direct illumination).

5.1.3 Calculate step size and relocate photon

A photon's current position and propagation direction is known, hence its future position E can be determined as shown in Equation 5.1.

$$E = S + sz \cdot M \tag{5.1}$$

To do so, a step size sz is needed. It is calculated as shown in Equation 5.2. The step size depends on the probability of interaction in the media μ_t (as the interaction coefficient, see Equation 5.3) and on the random number $\xi \in [0, 1]$.

$$sz = -\frac{ln(\xi)}{\mu_t} \tag{5.2}$$

The interactions include absorption, determined by the absorption coefficient μ_a and elastic scattering, determined by the scattering coefficient μ_s (all in cm^{-1}) [158]. The step size represents the mean free path length between two interaction sites. It is based on the sampling of the probability distribution for a photon's free path (for more details please refer to [156]).

$$\mu_t = \mu_a + \mu_s \tag{5.3}$$

Please note that μ_t is the sum of all absorption and scattering coefficients of the current media the photon is located in.

5.1.4 Interaction at the new location

After propagating the photon to its new position, it interacts with the tissue. It is either absorbed or scattered. The probability being absorbed or scattered are

$$P_{absorb} = \frac{\mu_a}{\mu_t} \tag{5.4}$$

$$P_{scatter} = \frac{\mu_s}{\mu_t}, \tag{5.5}$$

respectively. To determine which interaction will be performed, a random number ξ is generated. If $\xi \leq P_{absorb}$, the absorption is performed, else the photon is scattered.

Absorption In the case of absorption, the photon is terminated at its location E. This location can be logged and used for further analysis.

Scattering In the case of scattering, the photons propagation direction M is updated. The scattering properties of the media is determined by the size and distribution of the scattering objects in it. Blood is a cell suspension, and its cell components are dominating its scattering properties. There will be a deflection angle $\theta \in [0, \pi)$ and an azimuthal angle $\psi \in [0, 2\pi)$ to be sampled statistically. The scattering can be modeled by different phase functions such as the McCormick phase or Henyey-Greenstein function [159–161]. For this work, the latter was used for the blood and vessel wall since it proved to perform best [162, 163]. The cosine of the deflection angle $cos\theta$ is shown in Equation 5.6 and the azimuthal angle ψ is given in Equation 5.7.

$$cos\theta = \begin{cases} \frac{1}{2 \cdot g}\left(1 + g^2 - \left(\frac{1-g^2}{1-g+2 \cdot g \cdot \xi}\right)^2\right) & \text{if } g > 0 \\ 2 \cdot \xi - 1 & \text{if } g = 0 \end{cases} \tag{5.6}$$

$$\psi = 2 \cdot \pi \cdot \xi \tag{5.7}$$

The parameter $g \in [-1, 1]$ is the scattering anisotropy. A value of 0 indicates isotropic scattering and values close to 1 a forward directed scattering. Values of -1 indicate backwards scattering but are not of interest in this work since tissue has a positive g.

After obtaining $cos\theta$ and ψ, the propagation direction can be updated as shown in Equations 5.8 to 5.10.

$$\mu'_x = \frac{sin\theta}{\sqrt{1-\mu_z^2}} \cdot (\mu_x \cdot \mu_z \cdot cos(\psi) - \mu_y \cdot sin(\psi)) + \mu_x \cdot cos(\theta) \tag{5.8}$$

$$\mu'_y = \frac{sin\theta}{\sqrt{1-\mu_z^2}} \cdot (\mu_y \cdot \mu_z \cdot cos(\psi) - \mu_x \cdot sin(\psi)) + \mu_y \cdot cos(\theta) \tag{5.9}$$

$$\mu'_y = -\sqrt{1-\mu_z^2} \cdot sin(\theta) \cdot cos(\psi) + \mu_z \cdot cos(\theta) \tag{5.10}$$

5.1.5 Interaction at boundaries

During the propagation, a boundary to a different media might be hit. The photon can either be reflected or transmitted and refracted. First of all, the photon is moved to the hit point H. The remaining step size is stored and used later. At H, neither absorption nor scattering will be regarded.

The probability of the photon of being reflected or transmitted needs to be determined. It depends on the angle of incidence α_i and angle of transmission α_t (orthogonal incidence: $\alpha_i = 0$). It is calculated using Fresnel's formulas for internal reflection $R(\alpha_i)$ as shown in Equation 5.11. It is an average of the reflectances of the two orthogonal polarization directions.

$$R(\alpha_i) = \frac{1}{2} \cdot \left(\frac{sin^2(\alpha_i - \alpha_t)}{sin^2(\alpha_i + \alpha_t)} + \frac{tan^2(\alpha_i - \alpha_t)}{tan^2(\alpha_i + \alpha_t)} \right) \tag{5.11}$$

The photon is reflected in the case of $R(\alpha_i) \geq \xi$ and else it is transmitted. The angle of transmission α_t is calculated using Snell's law (Equation 5.12 with n_i and n_t as the refractive indices of the medium of incidence and transmission, respectively).

$$n_i \cdot sin(\alpha_i) = n_t \cdot sin(\alpha_t) \tag{5.12}$$

In case of internal reflection, the remaining step size is propagating towards the updated propagation direction, which follows the law of reflection in respect to the tangential plane at H. At the end of this propagation, the photon is absorbed or scattered.

In case of transmission, the propagation direction changes according to Snell's law. Also, the remaining step size needs to be updated, because the medias properties might change. The updated remaining step size is given by Equation 5.13 with $\mu_{t,1}$ and $\mu_{t,2}$ as the interaction coefficient of the media of incidence and transmission, respectively.

$$sz'_{remain} = sz_{remain} \cdot \frac{\mu_{t,1}}{\mu_{t,2}} \tag{5.13}$$

5.1.6 Photon termination

A photon is terminated either by absorption or by exiting the geometry into the ambient media, where a further propagation and tracking is possible but often not required. Nonetheless, the exiting point and the propagation direction of the photon can be used for further analysis such as ray tracing.

5.2 Weighted propagation

The weighted propagation of photon packages was introduced by Wang et al. to improve the efficiency of the MC simulation [156]. Treating weighted photon packages instead of single (binary) photons is a simple variance reduction technique, which leads to a rapid convergence of the simulation. The weighted propagation is an acceleration of the binary propagation and is used when absorption patterns are of interest and not single absorption points [156]. The weighted propagation considers many photons in a photon package. While propagating, a fraction of this package is absorbed. This remaining rest keeps on propagating and faces scattering. The weight is a measure for the 'surviving' fraction of photons after each step. Setting the initial weight to unity allows a convenient handling of the absorbed and surviving fraction.
The general workflow is shown in Figure 5.2.

5.2.1 Geometry and coordinate system

The geometry and the coordinate system are set and treated identically in the binary and weighted propagation models.

5.2.2 Initialization, step size and relocation of photon

Initialization The photon package initialization in the weighted model is identical to the binary model with the addition that a weight $W_{Ph,init} = 1$ is added as an attribute for each photon independently.

Step size and relocation of photon The calculation of the step size and the relocation of the photon are handled identically to binary propagation (see Section 5.1.3).

5.2.3 Interaction at the new location

After the propagation of the photon package to its new position, it interacts with tissue in form of absorption and scattering. The absorption affects the weight of the package, which results in the checking of the weight to decide whether it is terminated or not. The scattering is performed identically to the binary model (see Section 5.1.4).

Absorption A fraction of the photon's weight will be absorbed. The quantity of it is given by Equation 5.14. Hence, the updated weight is $W' = W - \Delta W$.

$$\Delta W = W \cdot \frac{\mu_a}{\mu_t} \tag{5.14}$$

Due to the dependency of ΔW on W, the updated weight will never be zero. Therefore, a roulette is introduced to terminate photon packages that have a very small weight. A package enters the roulette if its weight is under a certain threshold. This threshold was set to $W_{thres} = 10^{-4}$. Hence, $1 - 10^{-4}$ was already absorbed upon the propagation of the package and a further propagation was neglected to save computational time. The roulette gives the package a change of $1/m$ to survive, else it is terminated. Simply terminating the packages in the roulette would violate the conservation of energy (or number/weight of photons). Therefore, the weight of surviving packages is increased by m (see Equation 5.15).

$$W = \begin{cases} m \cdot W & if\ \xi \leq \frac{1}{m} \\ 0 & if\ \xi > \frac{1}{m} \end{cases} \tag{5.15}$$

In this work, $m = 10$ was used. After updating the photon package's location and weight, it is scattered and its propagation direction is updated as well.

5.2.4 Interaction at boundaries

The interaction at boundaries can be treated in two ways. Either identical to the binary propagation as binary decision, so the whole package is either reflected or transmitted, or the weight is split into a reflected and transmitted package. For the latter, the reflected weight is $W'_{refl} = W \cdot R(\alpha_i)$ and the transmitted weight is $W'_{trans} = W \cdot (1 - R(\alpha_i))$. The drawback of this approach is that the number ob photon packages that need to be tracked increases exponentially and is therefore very computationally costly. The binary handling shows very similar results and can be compensated by launching more photons at the beginning [156]. For this work, the binary handling at boundary hits was used.

5.2.5 Photon termination

A photon package is either terminated by the roulette or by exiting the geometry to the ambient medium.

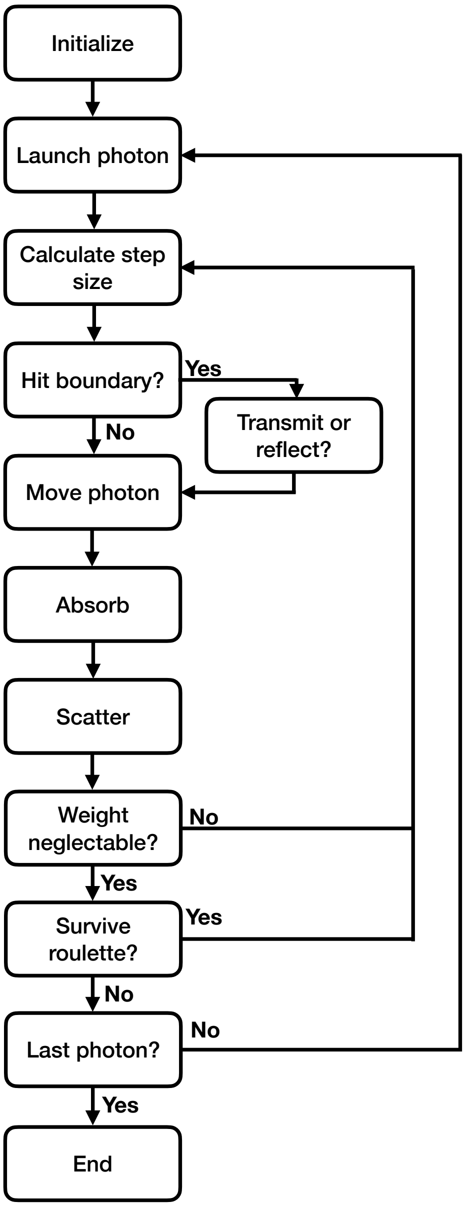

Figure 5.2: The weighted propagation model starts by initializing the geometry, the medias optical properties, logging of performance parameters and setting of the number of photon packages to be launched. After launching the package, the step size is calculated (Section 5.2.2). It interacts with either the medium or a boundary upon its propagation (Section 5.2.3 & 5.2.4). At the new location, the weight of the package is reduced due to absorption and is followed by scattering. In the case that the package is not terminated, a new step size is calculated. The photon package is terminated in case it exits the geometry or does not survive the roulette and a new package is launched (Section 5.2.5). This is repeated until the desired number of photon packages were launched and terminated. The scheme is based on [156].

PART II

FROM VIDEO INPUT TO FLOW OUTPUT

Chapter 6

Workflow

The overarching goal of this work is to develop, analyze, and validate a processing chain to extract blood volume flow information from recorded fluorescence angiography (FA) videos or image sequences.[1] In this chapter, the workflow is presented. Its single components including input and output are visualized in Figure 6.1.

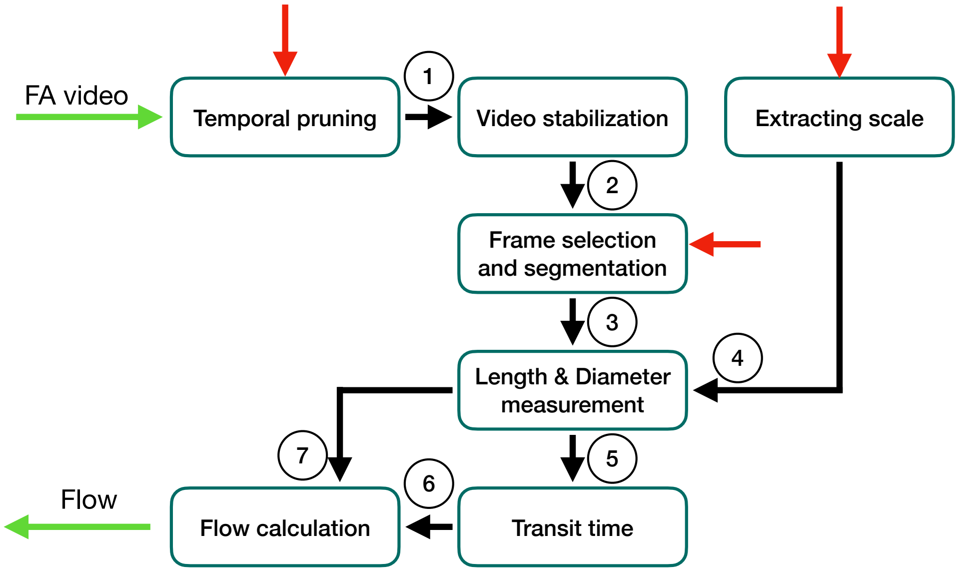

Figure 6.1: In this overview, all components and information passed among the single steps of the algorithm are visualized. Green arrows indicate the general input and output. Red arrows indicate user interaction and will be described in the corresponding section. The black arrows indicate automated handovers from one step to the next. Handovers consist of: 1 the temporally shortened video, 2 the motion compensated video, 3 the segmentation of the automatically selected frame, 4 the image's scale, 5 the obtained centerline which is used to calculate the transit time of the bolus from the video (2), 6 the calculated transit time, 7 the length and diameter of the vessel.

---

[1] Note that in this chapter a video and image sequences will be named video for the sake of readability.

6.1 Requirements on the clinical data

To be compatible with the proposed algorithm, the data should comply with the following requirements.

1. FA video:
    a) It must contain the dye's inflow and washout phase into the vessel (recirculation is not required).
    b) The vessel of interest must be permanently in the image and no instruments obstructing the view.
    c) The vessel of interest must be in the focal plane.
    d) The microscope's settings (zoom, focus, illumination, etc.) must be kept constant.
    e) The microscope's gain value must either be kept constant or must be tracked for each frame.
    f) The microscope must be kept stationary.
    g) At one time, a ruler must be in the image but should not violate point 1b and should also be in the focal plane.
    h) The vessel should be homogeneously illuminated.

2. Reference measurement via e.g. ultrasonic flow probe
    a) A reference measurement of the blood volume flow at the vessel must be taken shortly before or after recording the video data (time scale of a few minutes). Preferably, multiple measurements should be taken.[2]
    b) The location of the measurement should be marked (e.g. snapshot image or post-operative annotation).

6.2 Video pre-processing

The videos recorded in a lab or during surgery will need two pre-processing steps. First, a temporal pruning of the data to exclude irrelevant sequences. Second, a video stabilization to compensate for the relative movement of the patient and camera system.

Temporal pruning The recorded videos will include data/passages that are irrelevant or troublesome for the analysis: for example the frames that are recorded before the fluorescent dye has reached the camera's field of view do not consist any information on the dye's dynamics. Therefore, two criteria for the pruning are derived:

1. Sequences before the dye has reached the field of view will be excluded.
2. Sequences where the recirculation of the dye is prominent will be excluded.

---

[2] The mean flow or temporally resolved.

To assess whether any of the criteria are met, the average grey value of each video frame is calculated and analyzed over time. An examples where the two criteria are met is shown in Figure 6.2. The frames in between the two red dotted lines will be passed to the next processing step.

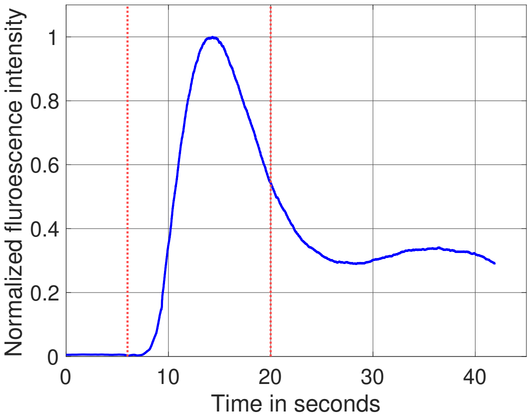

Figure 6.2: This normalized fluorescence intensity curve was measured *in vivo*. The time to the arrival of the bolus is clearly visible ($t < 7\,\mathrm{s}$) and violates the first criterion for pruning. This is indicated by the left red dotted line. The second red dotted line indicates the violation of the second criterion. The recirculation of the bolus is clearly visible with a peak at approx. $t = 35\,\mathrm{s}$. The outflow of the first bolus and the inflow of its recirculation overlap, and the point of the violation of the second criterion is annotated manually.

Video stabilization Since relative movement between the vessel of interest and the camera occurs, a compensation for this movement is needed. The relative movement can be induced by the heartbeat and respiration of the patient or by the operation of the surgical microscope by the staff. Both can cause deterministic and transient, high and low frequency movement. It is crucial to perform this compensation since the upcoming analysis is an Eulerian and not a Lagrangian approach.[3]

A registration of each frame to its consecutive frame is needed. The transformation matrix of this registration is used to match both frames spatially. Thereby, only translational motion was allowed. This is justified since scaling is excluded by the requirements for recording the data (no change in the zoom was allowed) and the relative axial motion of the patient and camera were assumed to be negligible. Rotational motion is also excluded by the requirements and negligible motion is expected. To register the images an image similarity metric needs to be maximized. The inter-frame mean squared error was used as a metric since the frames are recorded by the same device/modality and no major changes of grey values are expected from frame to frame (see Equation 6.1 with I_1 & I_2 being the two images

---

[3] Eulerian approach: The observed site (pixel or pixel group within a frame) remains stationary and changes of features are tracked only within it. Lagrangian approach: The observer follows the spatial movement of a feature and thereby changes constantly site.

of the size N by M pixel).

$$MSE(\Delta n,\Delta m) = \frac{1}{N \cdot M} \sum_{n=1}^{N} \sum_{m=1}^{M} (I_1(n,m) - I_2(n+\Delta n, m+\Delta m))^2 \tag{6.1}$$

The regular step gradient descent method is used to find the maximum similarity, hence minimum MSE. It performs efficiently and proved to be suitable in a preliminary test. It is an iterative method that in contrast to the normal gradient descent methods has a constant step s until the gradients direction ($\nabla MSE(\Delta n,\Delta m)$) changes. Starting from a random initial position X_0, the steps are calculated as shown in Equation 6.2 (L as the learning rate and ∇ as the gradient) and update the position as shown in Equation 6.3 (k is a counter of the number of steps taken).

$$s = L \cdot \nabla MSE(\Delta n,\Delta m) \tag{6.2}$$

$$X_{k+1} = X_k - s \tag{6.3}$$

This iterative process stops whenever either the maximum allowed number of iterations k_{max} or a threshold for the gradients magnitude (G_{min}) or a threshold for the steps length (s_{min}) is reached. The latter two indicate a convergence of the algorithm. The following parameters were set: $L = 0.5$, $k_{max} = 100$, $G_{min} = 10^{-4}$, $s_{min} = 10^{-5}$.

The resulting translational motion (depicted by the Δn & Δm) between both images I_1 & I_2 is used to derive a transformation matrix to match both images best. This is done for each frame of the video and thereby a motion compensated video is available in the end. The image format should be kept constant. So, in case of a translational compensation black pixels were added to the image as shown in Figure 6.3 at the bottom of the image.

6.3 Frame selection

A frame needs to be selected and extracted from the video and passed to the segmentation process. The frame should show a high contrast of the vessel of interest compared to the background. The data was recorded using a high magnification of the recording system. This hold the advantage that mostly the vessel of interest is omnipresent in the image. Whenever the dye flows into the vessel, the fluorescence intensity increases significantly. At the time point where the whole vessel is filled with the dye, a maximum intensity is reached. Thus, it has a large contrast to the background. Identifying this frame is done by calculating the mean intensity of each image and selecting the image with the maximum intensity. Figure 6.3 shows an example of a resulting frame.

6.4 Segmentation

Segmenting an image is an indispensable step in many computer vision applications. The purpose is to binarize the image into a foreground and background. The foreground should

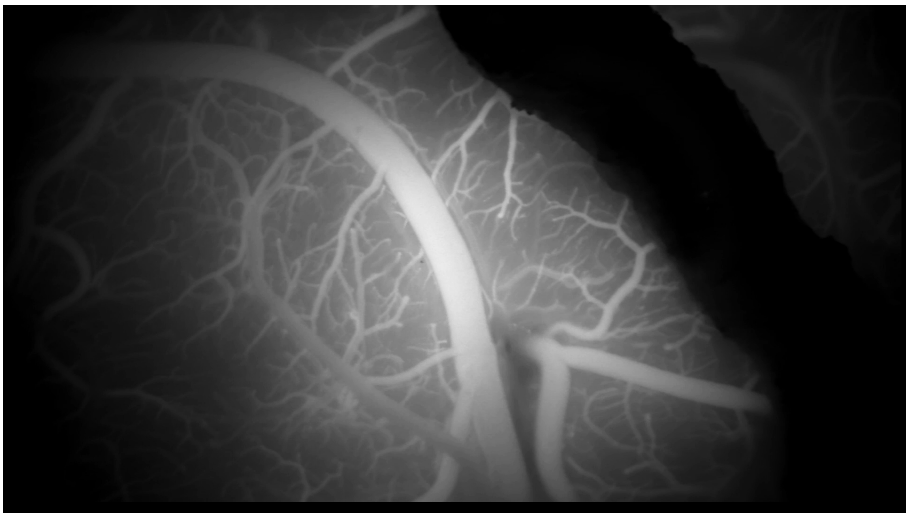

Figure 6.3: This frame is taken from a video of a cerebrovascular intervention. It is not the first frame and therefore the video stabilization was performed on it. The black horizontal line at the bottom is a result of aligning this frame to the consecutive ones. This frame is as well selected by the frame selector to be suitable for the segmentation process. The vessel of interest has a good contrast towards the background and is clearly visible.

be the vessel of interest and the background all the rest. As Figure 6.3 indicates, often multiple vessels are in the field of view. A segmentation by Otsu's method yields a good results for the segmentation of vessels in general and is performed [164]. Afterwards, the vessel of interest needs to be determined robustly. This was ensured by allowing the user to pick it. Often, pruning the segmentation is needed since branches exist and should not be included in the further analysis. The user can decide where to prune the segmentation. Both steps involve an interactive graphical user interface (GUI). The segmentation's border after pruning is shown in Figure 6.4. Since the fluorescent light passes a scattering media (vessel wall) on its path to the detector, the segmentation might not represent the inner structure of the vessel. A refinement of the segmentation is performed to ensure it depicts the inner structure of the vessel. A spatial-gradient-based segmentation method is used which showed plausible results in a clinical setting [165]. It relocates the border of the initial segmentation towards the minimum of the second derivative of the intensity values perpendicular to the border. This relocation is not visible in a figure but has an effect on the segmentation. Hence, also on the diameter measurement in the next step, as shown in literature (for more details on the segmentation please see the given reference) [165].

6.5 Length and diameter measurement

The spatial dimension of the vessel of interest needs to be determined. The geodesic length and the cross sectional area of the vessel are in focus. Since a 3D object was projected into a 2D plane, the width of the segmentation is used as a surrogate for the diameter. This

Figure 6.4: This image shows the segmentation's border in red after the user has picked the vessel of interest and has cut off the irrelevant region of the mask. Here, the top and bottom of the vessel was excluded due to the presence of branches. The branches would affect the flow measurement since the flow would split at the branches and therefore no constancy of mass is given.

assumption is valid as long as the vessel has a circular cross section. As long as the blood pressure is larger than the ambient pressure, which is in an open brain surgery the case, it is very likely to be valid unless a pathology is present.

First, the centerline of the segmentation is computed. The centerline is a one pixel thin line which represents the medial axis of the segmentation. Its length can be determined by different methods. The description of the centerline extraction methods and their resulting errors can be found in Section 8.2.1. Then, the diameter value is obtained for each pixel of the centerline and transferred into a local cross sectional area. The mean cross sectional area along the centerline is used for the final calculation. The description of methods to obtain the diameter and their resulting errors can be found in Section 8.2.1. Figure 6.5 shows the centerline in blue[4] and indicates the maximum diameter by a green circle.

6.6 Extraction of scale

The length and diameter of the structure are given in pixels. This needs to be turned to a metric value. Hence, a scale is needed. In the present data, it is not possible to calculate the scale since the optical parameters of the recording system are not known. Therefore, a ruler is required to be in the image (see Section 6.1). Such a ruler is shown in Figure 6.6 and the user needs to interactively select two points of known distance on the ruler to calculate the scale within the image. The scale is then used to transfer the length and diameter values from pixels to millimeter. It is crucial to image the ruler in the focal and it should not tilted (relative to the focal plane). Otherwise, an scaling error is introduced.

---

[4] For visualization purposes, the one pixel thin centerline was dilated to a 3 pixel thin line.

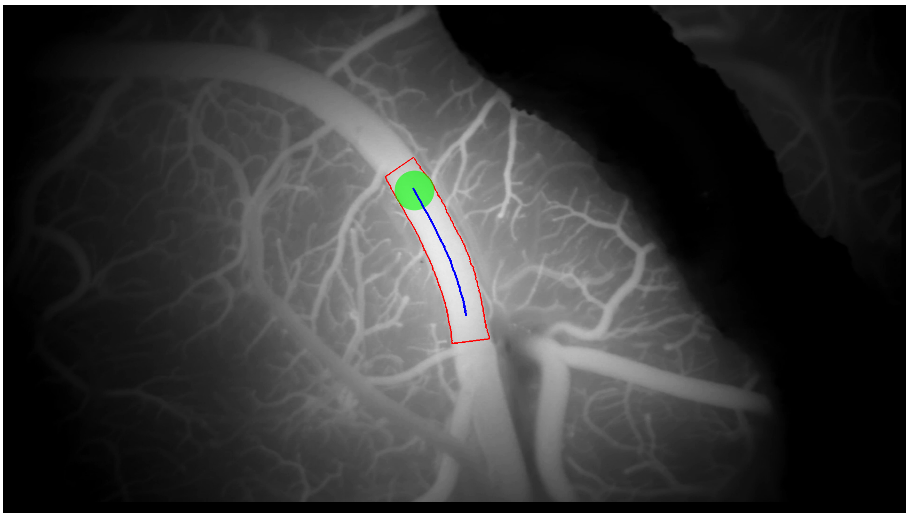

Figure 6.5: The segmentation is used to determine the vessel's medial axis: the centerline. It is indicated in blue. For each element of the centerline a diameter value was calculated. In green, the maximum diameter of this structure is visualized.

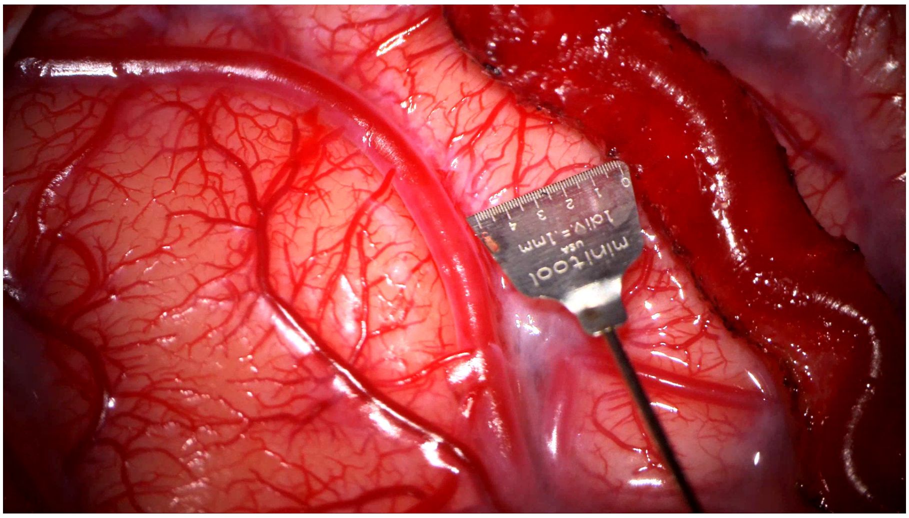

Figure 6.6: An example of a ruler used to calculate the image's scale.

6.7 Transit time measurement

The transit time was defined as the delay of a signal relative to another signal obtained from a different location within the same vessel. This definition is valid according to the systemic mean transit time theorem for single input and single output systems as defined by Perl et al. [16]. Thereby, multiple features can be used such as the temporal shift of the maxima. In the respective chapters, details on the particular features are given.

In this work, the ends of the centerline were chosen as the defined measurement locations.

Obtaining a signal from temporal intensity variations from a single pixel involves strong noise. Defining a region of interest (ROI) at the measurement locations and using the mean value of it is beneficial since it suppresses uncorrelated noise. Thus, taking the mean of an ROI intrudes a spatial smoothing and the size of it should be chosen with care. The ROI was chosen to be as large as a third of the diameter of the vessel which provides sufficient noise reduction but does not apply too strong spatial smoothing. Figure 6.7 shows an example of the obtained signals.

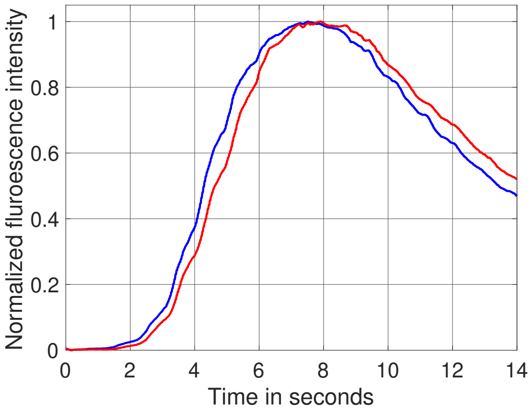

Figure 6.7: This plot shows the normalized fluorescence intensity of two signal obtained at the ends of a centerline (signals are obtained from the case also shown in Figure 6.5). Blue is obtained proximal and red distal. Both are of similar morphology but shifted relatively to each other. This shift needs to be determined.

The systemic mean transit time theorem by Perl et al. is defined for the measure of absolute concentrations [16]. In this investigation, the absolute concentration is not known and cannot be derived accurately by the fluorescence intensity. The fluorescence intensity is strongly linked to the concentration but is not equal. Moreover, the dynamic changes of the fluorescence intensity is depending on the flow profile and the fluorophore's distribution in the regarded volume. Hence, a systemic error ε_{sys} is introduced, derived and analyzed in Chapter 7.2 & 9. The calculated ε_{sys} is included into the calculation of the volume flow as shown in Equation 6.4 (more details in Chapter 7.2).

$$\dot{V}_{corrected} = \frac{\dot{V}_{observed}}{\varepsilon_{sys}} \tag{6.4}$$

6.8 Determination of blood volume flow

The blood volume flow is calculated by adapting the beforehand proposed Equation 6.4.

$$\dot{V}_{corrected} = \frac{\bar{v} \cdot A}{\varepsilon_{sys}} = \frac{s \cdot A}{t \cdot \varepsilon_{sys}} \tag{6.5}$$

PART III

STATISTICAL AND SYSTEMIC ERROR ANALYSIS

Chapter 7

Sources of error

Metrology suffers from a basic dilemma. Due to technical reasons each measuring process is affected by a measurement error such as the quantization of the continuous input signal or the influence of thermal noise. A measurement is influenced by so-called random errors, as introduced by C.F. Gauss. Due to the possibility to describe random errors with descriptive statistics, errors of stochastic nature are called statistical errors in this work and are discussed in Chapter 7.1. Besides statistical errors, systemic errors are present and discussed in the Chapter 7.2.

7.1 Statistical errors

The goal of determining the volume flow depends on the measurement of multiple parameters (as shown in Equation 7.1). Each parameter's measurement error contributes to the overall flow measurement error with its magnitude and by error propagation. The error propagation will be introduced in the following.

$$\dot{V} = \frac{\pi \cdot d \cdot s}{4 \cdot t} \tag{7.1}$$

Error propagation The calculation of the blood volume flow has a limited accuracy due to the statistical errors in measuring the diameter and length of the vessel and the transit time of the bolus. In this work, the accuracy is calculated with a conservative approach using the error propagation of uncorrelated variables according to the DIN standard 1319 specification [166, 167]. The error ε of a function $f(x_i)$ is described as

$$\varepsilon_{f(x_i)} = \sum_{i=1}^{n} \left| \frac{\partial f}{\partial x_i} \right| \cdot \varepsilon_{x_i} \tag{7.2}$$

with x_i being the variables and n the number of variables.
In this work the $f(x_i)$ is $\dot{V}(s,d,t)$ and the error propagation yields

$$\varepsilon_{\dot{V}} = \left| \frac{\partial \dot{V}}{\partial s} \right| \cdot \varepsilon_s + \left| \frac{\partial \dot{V}}{\partial d} \right| \cdot \varepsilon_d + \left| \frac{\partial \dot{V}}{\partial t} \right| \cdot \varepsilon_t \tag{7.3}$$

, hence

$$\varepsilon_{\dot{V}} = \frac{\pi \cdot d^2}{4 \cdot t} \cdot \varepsilon_s + \frac{2 \cdot \pi \cdot_d \cdot s}{4 \cdot t} \cdot \varepsilon_d + \frac{\pi \cdot d^2 \cdot s}{4 \cdot t^2} \cdot \varepsilon_t. \tag{7.4}$$

To compute the relative error ε_{rel} of $\dot{V}$, Equation 7.4 needs to be divided by $\dot{V}$ and for all variables the absolute error must to be substitute with their relative error. This results in Equation 7.5.

$$\varepsilon_{rel,\dot{V}} = \varepsilon_{rel,s} + 2 \cdot \varepsilon_{rel,d} + \varepsilon_{rel,t} \tag{7.5}$$

In Section 8 the errors in measuring the variables are determined. To assess whether the determined errors are suitable for the analysis of blood volume flow is not motivated by the clinically relevant accuracy but by the accuracy of the current gold standard. Therefore, the state-of-the-art ultrasonic flow probe by Transonic® was used as reference. It claims to have an accuracy of ±10% to ±20%, depending on the size, configuration and type of the flow probe [168]. The clinically relevant accuracy will not be taken into account (although it would allow a larger error margin).
In this work, a statistical error of $< \pm 20\%$ is considered as comparable to the gold standard method.

7.2 Systemic error

Systemic errors appear in different shapes and are often unknown. Dealing with unknown errors is complicated and therefore requires an extensive analysis [167].
Detecting systemic errors in a model requires questioning its assumptions and checking whether all of them are valid. In this work, the equation used to calculate the blood volume flow is examined. Other systemic errors also appear in different shapes in this work and will not be further investigated, but discussed in the respective chapter. To name an example, the scale of an image is extracted from a recorded ruler. Is the ruler tilted, a systemic error will be involved in the following calculations. To avoid such a systemic error, requirements were set in the respective chapter of this thesis.
The proposed calculation of the volume flow by

$$\dot{V}_{true} = A \cdot \bar{v} = \frac{\pi \cdot d^2 \cdot s}{4 \cdot t} \tag{7.6}$$

assumes $\frac{s}{t} = \bar{v}$. Equation 7.7 shows the general definition of volume flow in a rigid circular pipe with $v_{abs}(r, \phi)$ as the spatially resolved absolute flow velocity along the cross section of the pipe.

$$\dot{V}_{true} = \int_A v_{abs}(r, \phi)\, dA \tag{7.7}$$

The volume flow measurement via fluorescence angiography (FA) requires excitation light to penetrate and propagate in the vessel until it faces a fluorescence event and then propagate back out of the vessel into a detector. Thereby, the penetration depth will be limited in both directions, excitation and fluorescence emission. Hence, the flow velocity profile of the blood is neither represented completely nor equally weighted in the recorded signal by the detector. So, the general definition of volume flow in Equation 7.7 is erroneous. Therefore, in this work a novel approach is proposed. An optical weight is introduced to Equation 7.7 as shown in Equation 7.8.

$$\dot{V}_{observed} = \int_A w(r,\phi) \cdot v_{abs}(r,\phi)\, dA \tag{7.8}$$

The optical weight represents the spatial probability density of the origin of a detected fluorescent photon. Section 9 gives details on how to obtain $w_{r,\phi}$ and will not be further discussed here. Since the $v_{abs}(r,\phi)$ is not known, it is replaced by $v_{rel} = \frac{v_{abs}}{\bar{v}}$. This substitution holds the advantage that $\bar{v}$ is independent and can be written in front of the integral (see Equation 7.9). The integral is calculated in respect to the cross sectional area. From here on, it is turned into two integrals in respect to r and ϕ separately. Since the cross sectional area does not change linearly with r, the Jacobian determinant must be included and results in $dA = dx\,dy = r\,dr\,d\phi$.

$$\dot{V}_{observed} = \bar{v} \cdot \int_r \int_\phi w(r,\phi) \cdot v_{rel}(r,\phi) \cdot r\, d\phi\, dr \tag{7.9}$$

Assuming laminar flow in the pipe and neglecting gravitational forces, $v_{rel}(r,\phi)$ is of parabolic shape. Since the flow profile is axisymmetric, it can be expressed by Equation 7.10 with R as the radius of the inner lumen of the vessel (for $r < R$) [169].

$$v_{rel}(r) = 2 \cdot \left(1 - \left(\frac{r}{R}\right)^2\right) \tag{7.10}$$

Non-laminar flow in cerebral vessels might appear at bifurcation or at pathologies such as aneurysms. These cases might not be suitable for an analysis of the systemic error as performed here. Nonetheless, in most cases laminar flow can be assumed [24, 170].
Afterwards, the term $\frac{A}{A}$ is added and yields Equation 7.11.

$$\dot{V}_{observed} = A \cdot \bar{v} \cdot \int_r \int_\phi w(r,\phi) \cdot v_{rel}(r) \cdot \frac{1}{A} \cdot r\, d\phi\, dr \tag{7.11}$$

The term in front of the integral can be substituted by $\dot{V}_{true}$ (see Equation 7.6) and results in

$$\dot{V}_{observed} = \dot{V}_{true} \cdot \int_r \int_\phi w(r,\phi) \cdot v_{rel}(r) \cdot \frac{1}{A} \cdot r\, d\phi\, dr. \tag{7.12}$$

Finally, the systemic error in the blood volume flow measurement via FA is

$$\varepsilon_{sys} = \frac{\dot{V}_{observed}}{\dot{V}_{true}} = \int_r \int_\phi w(r,\phi) \cdot v_{rel}(r) \cdot \frac{1}{A} \cdot r\, d\phi\, dr. \tag{7.13}$$

In Chapter 9 the method to obtain $w(r,\phi)$ is presented. For the calculation of the systemic error ε_{sys} the angular components of $w(r,\phi)$ are averaged, hence yield $w(r)$ and simplify the equation above to

$$\varepsilon_{sys} = \int_{r=0}^{R} w(r) \cdot v_{rel}(r) \cdot \frac{2 \cdot \pi}{A} \cdot r\, dr. \tag{7.14}$$

Since $w(r)$ will be obtained at discrete values of r, the integral needs to be converted to a sum with R being the inner radius of the vessel and n the number of bins.

$$\varepsilon_{sys} = \lim_{n\to\infty} \sum_{i=1}^{n} \left(w(r_i) \cdot v_{rel}(r_i) \cdot \frac{2 \cdot \pi}{\pi \cdot R^2} \cdot r_i \cdot dr \right) \tag{7.15}$$

By approximating the integral with a sum of finite bins, the dr is turned into the finite size of each bin $\frac{R}{n}$.

$$\varepsilon_{sys} \approx \sum_{i=1}^{n} \left(w(r_i) \cdot v_{rel}(r_i) \cdot \frac{2}{R^2} \cdot r_i \cdot \frac{R}{n} \right) \tag{7.16}$$

$$\varepsilon_{sys} \approx \sum_{i=1}^{n} \left(w(r_i) \cdot v_{rel}(r_i) \cdot \frac{2}{R \cdot n} \cdot r_i \right) \tag{7.17}$$

The r_i used to calculate the ε_{sys} is the mean value of the inner and outer boundary (radius) of the respective bin (also used in Equation 7.10).
Equation 7.17 will be used in Chapter 9 to calculate the systemic error.

Chapter 8

Statistical error

The goal of determining the volume flow depends on the measurement of multiple parameters. Each parameter's measurement error contributes to the overall flow measurement error with its magnitude and by error propagation (see Section 7.1 and Equation 7.4).

The goal of this chapter is to quantify the magnitude of the statistical errors in the measurement of the geometrical (s, d) and temporal ($t_{transit}$) parameters and propose methods to reduce them. In order to adequately quantify and potentially reduce temporal and geometrical parameter measurement errors, it is necessary to know the ground truth of the measurand. Obtaining a ground truth in a clinical or even lab setting is often not possible due to the lack of a trustworthy reference.

In this work, the measurands are obtained by a computational model and therefore a ground truth is known.

Geometrical and temporal errors are addressed separately in the following sections.

Some sections of this chapter were published in multiple publications by myself and were reused here [136, 171, 172]. The method used to reduce the error in length measurement is filed as a patent application under the number DE102020102683.8 and US17/166,945.

8.1 Introduction

8.1.1 Measurement of geometric parameters

Measuring an objects length and diameter is often addressed in the application of optic and photonic technologies such as fluorescence microscopy or X-ray computer tomography. These geometrical parameters provide crucial information in multiple medical fields such as ophthalmology, otolaryngology, and oncology but their measurement accuracy are rarely critically discussed [173–178]. The errors in the geometrical measurement also exist in non-medical applications, where an object is projected onto a detector grid and therefore holds a source for errors mainly due to discretization [179].

The error introduced by the discritization of a continuous object onto a grid (camera chip) will be quantified, reviewed and if needed a re-continualization method will be introduced to reduce this error. Two hypotheses are formulated:

1. The length measurement error due to discretization is reduced by a re-continualization of the object's discrete centerline.
2. The error depends on the angle in respect to the rectangular grid of the pixels in a camera chip and this dependency can be reduced by a re-continualization of the discrete centerline. For example, a line which is projected at an angle of 0°, 45°or 90°onto the rectangular grid should show a minimum error in length due to its perfect fit to the grid. Intermediate angles will show a higher error

To quantify the geometrical measurement errors and asses the performance of the proposed method a large data set containing a trustworthy ground truth is required. Since obtaining the ground truth from clinical data is difficult and often not possible, we propose to compute this data set using an *in-silico* model. The generation of the data set is described in Section 8.2.1.1. Then the extraction of the centerline is shown in Section 8.2.1.2. The measurement of the discrete geodesic length s and diameter d are shown in Section 8.2.1.3.

8.1.2 Measurement of the bolus transit time

The transit time $t_{transit}$ of an indicator bolus to pass the distance s needs to be determined. To calculate it, two indicator dilution curves (IDCs) are obtained by monitoring the spatio-temporal propagation of the indicator at two distinct locations along the vessel of interest (see Figure 4.3). The transit time is expressed by the temporal shift of the two IDCs. This procedure is according to the systemic mean transit time theorem for single input and single output systems as defined by Perl et al. [16]. This approach relies on the assumption that the two IDCs are similar in their morphology. The expected morphological changes of the IDCs are negligible (in the Appendix A.5 the magnitude of change is shown). Three general assumptions are set as well. First, the bolus transit time equals the mean blood volume transit time. Second, the real fluorescence intensity curve equals the simulated indicator bolus curve. Lastly, the simulated indicator bolus curve equals the realistic indicator solution curve in a cerebral vessel. This section focuses on the evaluation of the performance of different methods measuring $t_{transit}$ and their quantitative statistical error in the presence of different noise levels. As mentioned in Section 7.2 a systemic error is expected but is not included in this section (for the analysis of the systemic error please see Section 9). In order to perform the specified evaluation, data sets containing two corresponding IDCs with a know ground truth of $t_{transit}$ are needed. Although *in vivo* IDCs are monitored frequently in clinical routines and are thus widely available, they lack a sufficient and trustworthy ground truth of the transit time [180].

Creating a ground truth by simply shifting an *in vivo* IDC would result in identical samples having identical noise, which is also unintended. Additionally, *in vivo* IDC contain temporally correlated and uncorrelated noise that cannot be separated from the desired signal (described by the additive noise model $m(t) = s(t) + n(t)$ with $m(t)$ as measured, $s(t)$ as desired signal and $n(t)$ as noise). Therefore, making the analysis of the influence of the noise is impossible. The state-of-the-art surgical microscopes have a maximum sampling frequency of $f_{sampling} = 60\,\mathrm{Hz}$, which is sufficient to discretize the continuous IDC (according to the Nyquist-Shannon sampling theorem) but strongly limits the detectable shifts. Creating artificial sub-samples (reasonable samples in between the measured ones) would be a simple method to increase the number of samples and allow shifting of one IDC. To obtain sub-samples a mathematical model is used, which interpolates the signal. The model applies bias to the performance of methods measuring the time shift which introduces a systemic error to the ground truth and is undesirable. Consequentially, a credible performance evaluation of methods measuring the transit time $t_{transit}$ based on *in vivo* IDCs cannot be assured by merely duplicating and delaying an IDC for these three main reasons (lack of a reference, inseparable noise and relatively low sampling rate).

Therefore, a method is proposed to compute highly adaptable data sets of two corresponding and differently sampled IDCs with a ground truth transit time $t_{Ground\,truth}$ using an *in silico* model. Even though an *in vitro* flow phantom could provide a similar data set, *in silico* generated data sets are low-cost, accurate and easily configurable to the desired field of application [181]. The generated data sets will be used to evaluate and enhance methods measuring the transit time $t_{transit}$, thereby increasing its temporal accuracy which is not yet suitable for clinical studies [137, 182]. Achieving a higher temporal accuracy by increasing the sampling rate of the measuring device is possible. In a noise-free signal the maximum error of an ideal measurement is equal to half of the quantization interval, in our case, equal to $\frac{1}{2 \cdot f_{sampling}}$. In a noisy signal, the accuracy will decrease drastically with a decreasing signal to noise ratio (SNR). Furthermore, an increase in the sampling rate is limited since the noise level is often coupled reciprocally to the integration time of the A/D-Converter. Therefore, a method was proposed to fit mathematical models to the data points to interpolate and re-continualize the signal. This can enhance the accuracy in the temporal detection of events [183]. The proposed models are commonly used in the IDC-based measurement of blood volume and cardiac output to suppress noise, artifacts and increase the accuracy of the measurement [15, 184–187].

Two hypotheses were set up:

1. Using mathematical models to re-continualize the dilution curves, decreases the error in the transit time measurements compared to using the measured discrete data.
2. A sub-frame rate accuracy can be accomplished by combining a suitable configuration of a mathematical model, extracted features and pre-processing of the input data.

The generation of the data sets is described in Section 8.2.2.1. The methods used to obtain the transit time and quantify the measurement error are described in Section 8.2.2.2.

8.2 Methods

8.2.1 Measurement of geometric parameters

8.2.1.1 Generation of a synthetic data set

The *in silico* model needs to represent a broad variety of possible vessel geometries and contain an accurate ground truth on the length and diameter of the particular geometry. Generally, the model needs to fulfill the listed requirements below to ensure its suitability for the evaluation of the error in the length and diameter measurement. The model needs to

- generate binary images.
- mimic cerebrovascular scenes, short vessel parts with very few or no bifurcations.
- restrict the shape to mathematically expressible forms (such as straight lines, simply bend lines, multiply bend lines and combined structures with a bifurcation).
- be able to apply constant as well as changing diameter values.
- provide the ground truth (as reference and allows the reproduction of the images).
- allow the generation of a large and diverse set of data.

We propose to model a vessels geometry with the help of mathematical functions. The main advantage is that the mathematical functions allow an accurate length measurement in the continuous space by calculating the arc length of a section of the function. These functions will be mapped onto a grid (mimicking a camera chip). This one pixel thin line will be the centerline of the vessel. By dilating each centerline pixel by a diameter value a vessel segmentation is mimicked. Figure 8.1 visualizes the workflow for the generation of one image.

To my knowledge, there is no publication available describing vessels by mathematical functions. Therefore, multiple functions with a high variability are used to ensure that the data set is divers and represent a broad variety of possible vessel geometries. The used mathematical functions and their parametric limitations are shown in Table 8.1. Thereby, the parameter m is the window width in the image whereas the function will be placed into (m is chosen randomly within the limit of [65 350]). The applied diameter profiles were constant, monotonic narrowing to a diameter value of one pixel, monotonic narrowing to a randomly smaller diameter from one end to the other, non-uniform narrowing, non-uniform widening and random narrowing/widening (handcrafted for single centerlines as a set of linear functions).

The output of the model is a set of binary images and corresponding meta-information that include the ground truth length and diameter. The general framework was set to be a 720 x 576 pixel binary image, this corresponds to the PAL(DV) standard which is widely spread in optical fluorescence angiography (FA) systems. The resolution can be easily changed.

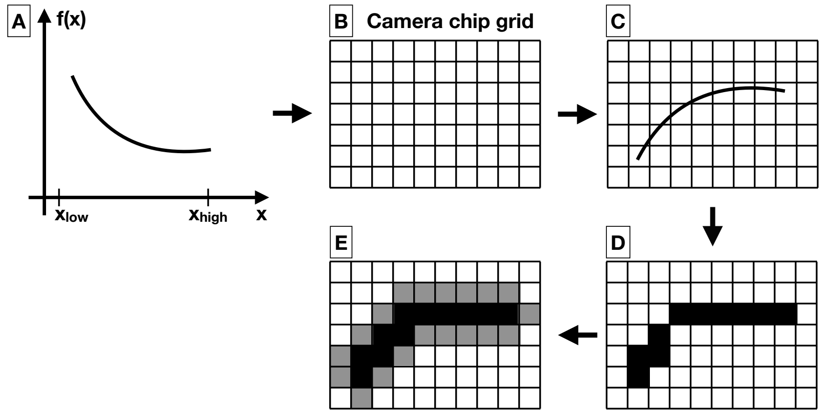

Figure 8.1: **A**: a function from Table 8.1 was picked randomly. x_{low}, x_{high} and the functions coefficients were also randomly chosen within the respective limits. **B**: an artificial camera chip grid was generated. **C**: Its position and rotation on the grid were chosen randomly and projected onto the grid. It was ensured that both ends of the function are in the middle of a pixel. In the shown case, the function was rotated by 180°. **D**: the continuous function was discretized. Hence, the ground truth discrete centerline for the vessel is obtained. **E**: the centerline is dilated by a diameter value (grey). This binary image will be used for the analysis of the performance of methods measuring the length and diameter of the structure.

8.2.1.2 Centerline extraction

Two centerline extraction methods were used in this work. Both methods differ fundamentally, are commonly used for the extraction of a centerline and will be presented in the following paragraphs. Afterwards, the necessary post-processing steps are presented.

Erosion The centerline extraction by erosion is well established and used in various medical and non-medical application [188, 189]. Erosion is a fundamental and iterative nonlinear operation in morphological image processing and belongs to the family of median filters [190]. A termination condition needs to be set to preserve a closed line. Its iterative use results in a thinning of a foreground structure (logical 1) to a one-pixel thick line or even a dot in case of a circular structure. The erosion process takes the elements in the neighborhood of a pixel in consideration and decides whether to eliminate the pixel or not. This set of elements was defined as all pixels in a 3 x 3 cross neighborhood of the pixel under investigation being in the center. The termination condition was set to an asymmetrical vertical and horizontal check of the neighbors to ensure a one pixel thick centerline.

Voronoi diagram The Voronoi diagram is in contrast to the erosion is not an iterative or morphological method [191]. It is a method derived from set theory which partitions a n-dimensional space into Voronoi cells. Each Voronoi cell is defined by a center point. The cell includes all points with minimal (Euclidean-) distance to this center point. If a point has an equal distance to two center points, then this point belongs to a Voronoi edge, which separates two Voronoi cells. Each point of the set belongs exclusively to one cell or edge. A

Table 8.1: Mathematical function, their formula and variables (inv.=inverted, freq. = frequency)

Function type	Detailed type	Formula	Variables' limit
Straight lines		$f(x) = \tan(\theta) \cdot x$	$\theta = [-45°, 45°]$ x is arbitrary
Parabolas	Left arm	$f(x) = a \cdot x^2$	$a = [1,2]$ $x_{low} = [-\sqrt{2m}, -2]$, $x_{high} = [x_{low}+2, 0]$
	Right arm		$a = [1,2]$ $x_{low} = [0, \sqrt{2m}-2]$, $x_{high} = [x_{low}+2, \sqrt{2m}]$
	Vertex		$a = [1,2]$ $x_{low} = [-\sqrt{2m}, -1]$, $x_{high} = [1, \sqrt{2m}]$
	Left arm inv.		$a = [-1,-2]$ $x_{low} = [-\sqrt{2m}, -3]$, $x_{high} = [x_{low}+2, 1]$
	Right arm inv.		$a = [-1,-2]$ $x_{low} = [1, \sqrt{2m}-2]$, $x_{high} = [x_{low}+2, \sqrt{2m}]$
	Vertex inv.		$a = [-1,-2]$ $x_{low} = [-\sqrt{2m}, -2]$, $x_{high} = [2, \sqrt{2m}]$
Polynomials		$f(x) = \sum_{k=4}^{n} a_k \cdot x^k$	$n \leq 15$, $x = [-5,5]$
Sinusoids	Low freq.	$f(x) = a \cdot \sin(f \cdot \pi \cdot x)$	$a = [0.2m, 0.7m]$, $f = [1,2]$ $x_{low} = [0, 2\pi]$ $x_{high} = [x_{low}+0.5\pi, x_{low}+2\pi]$
	High freq.		$a = [0.1m, 0.1 + \frac{m}{2f}]$, $f = [1.5, 7]$ $x_{low} = [0, 2\pi]$ $x_{high} = [x_{low}+0.5\pi, x_{low}+2\pi]$
Curved Waves	Quadratic	$f(x) = q \cdot x^2$ $+ a \cdot \sin(2 \cdot \pi \cdot f \cdot x)$	$q = [-10, 15]$ $a = [0.05m, 0.15m]$, $f = [0.5, 2]$ $x_{low} = [-3, 3]$ $x_{high} = [x_{low}+2, x_{low}+6]$
	Cubic	$f(x) = c \cdot x^3 + q \cdot x^2$ $+ a \cdot \sin(2 \cdot \pi \cdot f \cdot x)$	$c = [-15, 10]$, $q = [-15, 30]$ $a = [0.1m, 0.3m]$, $f = [0.5, 2]$ $x_{low} = [-3, 3]$ $x_{high} = [x_{low}+2, x_{low}+6]$
Bell curves	Gaussian	$f(x) = a \cdot e^{-\frac{x^2}{2\sigma^2}}$	$a = [0.2m, m]$, $\sigma = [0.2, 3]$ $x_{low} = [-5, 1]$, $x_{high} = [1, -5]$
	Gaussian inv.		$a = [-0.2m, -m]$, $\sigma = [0.2, 3]$ $x_{low} = [-5, 1]$, $x_{high} = [1, -5]$
	Polynomials	$f(x) = a \cdot 16$ $\cdot (x^4 - 2 \cdot x^3 + x^2)$	$a = [0.2m, m]$ $x_{low} = 0$, $x_{high} = 1$
	Polynomials inv.		$a = [-0.2m, -m]$ $x_{low} = 0$, $x_{high} = 1$
Bifurcations		Combination	

Voronoi diagram is the representation of all Voronoi edges. They can be used to extract a centerline in 2D and 3D data sets and it was shown that it complies strongly with the Medial Axis Transformation [192]. In Figure 8.2 an example of a centerline extraction by a Voronoi diagram is shown. The obtained centerline is shown in red and the Voronoi edges in blue. The set of Voronoi center points is defined as all border pixels of the segmentation mask. Two types of Voronoi edges appear, first the edges separating two neighboring Voronoi cell center points (along the segmentation border line) and second the edges separating two opposing Voronoi cell center points. These edges resulting from opposing center point represent the centerline of the given mask.

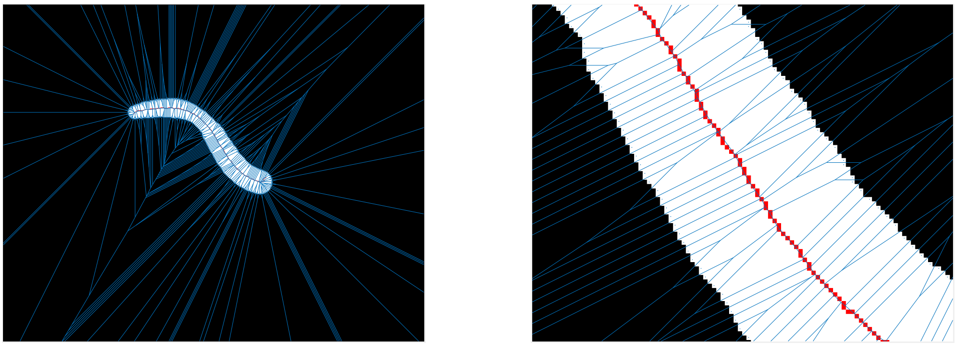

Figure 8.2: To the left the Voronoi diagram of a segmentation mask, to the right a zoom into a section of this diagram - blue are the Voronoi edges, red the centerline extracted from the Voronoi edges. Both images are adapted from [172] published under the Creative Commons Attribution 4.0 License.

Post-processing The post processing of the centerline is required before handing it over to the length measurement. Artifacts such as centerlines with a break of one pixel or single foreground pixels are fixed by detecting and filling (using morphological closing) or eliminating those. Afterwards a crucial step needs to be done, connections as stairway like steps are adjusted into exclusively diagonal connections. This is done by template matching. Since a limited number of stairway like connection occur, each one is assigned an exclusively diagonal connections (see example in Figure 8.3). This is necessary due to the overestimation of the measured centerline in case of the appearance of orthogonal step connections as shown in Figure 8.3.

Finally, spurs (unwanted parasitic branches) were removed. A detailed description of the method to identify spurs is described in the Appendix A.2. To identify spurs the centerline orientation was compared to the orientation of the structure for each element of the current centerline. The centerline orientation was obtained by matching the 3x3 neighborhood of a centerline pixel with predefined templates. The structures orientation was measured using the Optimally Oriented Flux (OOF). The OOF computes two eigenvalues and eigenvectors for each pixel of the centerline. The eigenvector belonging to the eigenvalue closer to zero determines the orientation of the structure for that pixel. If both orientations are above a threshold of 45°then the pixel will be excluded from the centerline.

Figure 8.3: To the left a stairway like connection and to the right its correction is visualized. The left figure is used as template to detect stairway like connection in the raw centerline. To the left an incorrect measurement due to a step-like connection with a distance of 2, to the right the corrected centerline with a measured distance of $\sqrt{2}$. Both images are adapted from [172] published under the Creative Commons Attribution 4.0 License.

8.2.1.3 Length and diameter measurement

This section describes the derivation of the ground truth length from the mathematical functions. Also, the methods used to obtain the discrete length of the centerline and the diameter of the structure are described in the following.

Ground truth length The final binary images were based on mathematical functions. The ground truth of the length was extracted from the mathematical function $f(x)$ as the arc length $l_{Arc}(f(x))$ of the function $f(x)$ from x_{start} to x_{end} (Equation 8.1). $f'(x)$ is the differentiated function.

$$l_{Arc}(f(x)) = \int_{x_{start}}^{x_{end}} \sqrt{1 + f'(x)^2} dx \tag{8.1}$$

Some curves were described as parametric curves by $\mathbf{c}(u) = \begin{pmatrix} x(u) \\ y(u) \end{pmatrix}$ which had the advantage that also bifurcations and other complex functions can be easily analyzed. The arc length was calculated as shown in Equation 8.2.

$$l_{Arc}(\mathbf{c}(u)) = \int_{u_{start}}^{u_{end}} \sqrt{x'(u)^2 + y'(u)^2} du \tag{8.2}$$

Ground truth diameter A diameter value was assigned to each centerline pixel while generating the data set. Those values were documented and used as the ground truth diameter values.

Discrete length The discrete length of the obtained centerline was calculated as the sum of Euclidean distances of each pixel to its neighbor as seen in Equation 8.3, $l_{discrete}$ is the discrete length of the centerline, i is the index of the sorted pixels along the centerline, i_{max} is the number of elements of the centerline and $\mathbf{cl}$ represents the centerline.

$$l_{discrete} = \sum_{i=1}^{i_{max}-1} \|\mathbf{cl}(i+1) - \mathbf{cl}(i)\|_2 \tag{8.3}$$

Re-continualization of the centerline by polynomial model A set of points can be approximated by a polynomial function. To avoid ambiguous function values due to non-negative integer exponentiation of the variable (as they would appear in a circle) the $x_{cl}(i)$ and $y_{cl}(i)$ (paired coordinate of the elements of the centerline) were treated independently. A polynomial of the order 10 and all elements of $x_{cl}(i)$ and $y_{cl}(i)$ are used. The order 10 was chosen due to its versatility and adaptability since it can depict a broad range of geometries and showed good results in an explorative preliminary study. The functions' coefficients are determined using the least squares method by QR decomposition of the Vandermonde Matrix [193]. Afterwards both polynomials ($x_{poly}(u)$ & $y_{poly}(u)$) can be used to calculate the arc length of the approximated centerline (see Equation 8.4).

$$l_{poly} = \int_{u_{start}}^{u_{end}} \sqrt{x_{poly}'(u)^2 + y_{poly}'(u)^2} du \tag{8.4}$$

Re-continualization of the centerline by Bézier curves In contrast, Bézier curves are parametric curves with Bernstein polynomials ($B_{n,i}$) as basis [194]. The ith Bernstein polynomial of the order n is defined as:

$$B_{n,i}(u) = \binom{n}{i} \cdot u^i \cdot (1-u)^{n-i} \tag{8.5}$$

with $u \in [0,1]$ and

$$\binom{n}{i} = \frac{n!}{i! \cdot (n-1)!} \tag{8.6}$$

A Bézier curve is a linear combination of Bernstein polynomials of the order n, weighted by the control points P as input. n equals the number of control points P_i. This results in the following function with $u \in [0,1]$:

$$Bezier(u) = \sum_{i=0}^{n} \binom{n}{i} \cdot u^i \cdot (1-u)^{n-i} \cdot P_i \tag{8.7}$$

The Bézier curve is used to approximate the reconstructed discrete centerline by a continuous function. Therefore, all elements of the centerline are used as control points for a set of k Bézier curve elements. Each curve was calculated from at least four control points, where two consecutive curves share exactly one point. A collinearity condition at the transition of two segments enforces a C^1 Bézier spline (continuously differentiable). Both (having at least four control point, sharing one and collinearity condition) avoid too strong spatial smoothing compared to the input of all control points at once and still matches the requirement of constantly differentiable function due to the tangential property of Bézier curves in general. The length of each curve is determined by the parametric Bézier curve elements ($x_B(u)$ & $y_B(u)$) and summed up to calculate the length of the centerline (Equation 8.8).

$$l_{Bezier} = \sum_{B=1}^{k} \int_0^1 \sqrt{x_B'(u)^2 + y_B'(u)^2} du \tag{8.8}$$

Discrete diameter The centerline and the segmentation are needed to perform the measurement of the diameter. The diameter measurement needs to be done for each pixel of the obtained discrete centerline. The used method dilates a circle C which is centered at the designated centerline pixel $p_{center} = \begin{pmatrix} x_c \\ y_c \end{pmatrix}$ until it hits the segmentation's boundary. Hence, the circle C is characterized as shown in Equation 8.9.

$$C\left(\begin{pmatrix} x_c \\ y_c \end{pmatrix}, d\right) = \left\{\begin{pmatrix} x_c \\ y_c \end{pmatrix} \in \mathbb{R}^2 | \ || \begin{pmatrix} x - x_c \\ y - y_c \end{pmatrix} || \leq \frac{d}{2}\right\} \tag{8.9}$$

In the discrete space the centering pixel p_{center} has a dimension of 1 x 1 pixel. Hence, only diameter with an odd number of pixels will be computed ($d = 2 \cdot r_{max} + 1$ with $r_{max} \in \mathbb{N}^1$ and being the maximum radius until the circle hits the boundary). To overcome this limitation we need to check whether the circle hits the segmentation's boundary single or double sided. The first case indicates an even and the second case an odd diameter value. To determine the correct diameter, the circle is dilated by one more pixel after it hits the boundary. The center of gravity p_{grav} of all pixels that exceed the segmentation is calculated. It should be close the p_{center} if the excess is symmetric or close to the boundary if the excess is single sided (see Figure 8.4). A threshold is needed to decide whether the calculated distance $dist_{center-grav} = ||p_{center} - p_{grav}||$ is small enough to indicate an odd diameter value. The threshold was set to $dist_{thresh} = \frac{r_{max}}{\sqrt{2}}$. This threshold divides the circle into an inner circle and an outer ring, which have exactly the same area (a randomly picked element of the circle has the same probability to be in one of the two areas). Is $dist_{center-grav} < dist_{thresh}$, then the diameter value is set to $2 \cdot (r_{max} - 1) + 1$ (-1 to compensate for the additional dilation after hitting the boundary). In all other cases a second step is needed. The center of the circle will be shifted away from the p_{grav} by one pixel. If a single sided excess is detected (on the opposite side), the diameter value is set to $2 \cdot r_{max}$. In the case that a double sided excess is detected, the diameter value is set to $2 \cdot (r_{max} - 1) + 1$. If the circle lays completely in the segmentation, then an erroneous centerline pixel is present. This pixel will then be ignored for the further analysis.

Laboratory measurement: length and diameter To support the findings from the *in silico* simulation an experiment was set up. The possibilities *in silico* were very broad and easily scalable. As a proof of concept the results of the linear functions and straight silicone tubes were compared regarding the error in the geodesic length measurement. The silicone tubes had a thin wall and were filled with a solution containing the dye Indocyanine Green and the blood analog to ensure a high contrast while imaging with a camera and illumination setup. They were placed on a rotational plate as seen in Figure 8.5 and images were taken at different angles (0° to 90° in 15° steps always starting at 0°). The rotational positioning accuracy of the plate was $\pm 0.5°$. The relative position of the plate and the recording system were not changed throughout all experiments. The size of the tubes were varied as shown in the Table 8.2. Markers were placed on the tubes to indicate the distances at which the

---

[1] $\mathbb{N}$ according to the DIN-Norm 5473:1992-07

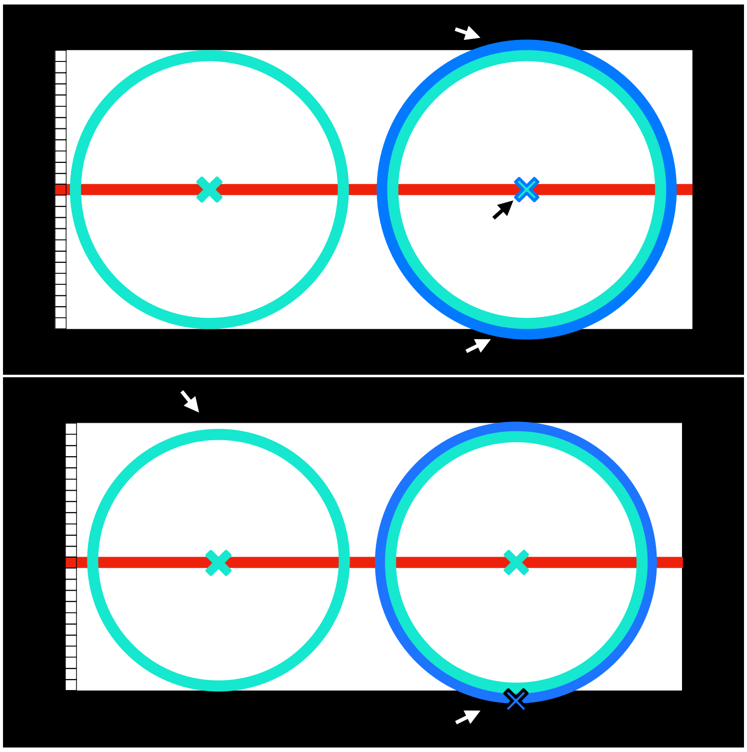

Figure 8.4: In the top and bottom image the centerline is depicted in red and the segmentation in white. In cyan the dilated circles are shown that first touch the segmentation's border. In dark blue the further dilatation by one pixel is shown. For visualization purposes the circle are not discretized. The cyan cross depicts the center of the circle p_{center} and the dark blue cross the center of gravity p_{grav} of the pixels exceeding the segmentation's border. **Top**: A segmentation with an odd number diameter value (in pixels). The dilated circle hits the segmentation's border double sided (white arrows) and hence a further dilatation results in a p_{grav} matching p_{center} (black arrow). **Bottom**: A segmentation with an even number diameter value (in pixels). The dilated circle hits the segmentation's border single sided (white arrows) and hence a further dilatation results in a p_{grav} afield of p_{center} (right white arrow).

measurement was performed. Multiple measurements with a caliper were performed to obtain the ground truth. In total 56 images were recorded and then processed the same way as the *in silico* images.

The setup included the following items:

- Surgical microscope PENTERO® 900 (Carl Zeiss Meditec AG, Oberkochen, Germany)
- Silicone tubes RCT THOMAFLUID® (Reichelt Chemietechnik Gmbh + Co., Heidelberg, Germany)
- Rotational plate PR01(/M) (Thorlabs GmbH, Munich, Germany)
- Blood analog:
  - 52,4 ml demineralized water
  - 41,5 ml Glycerin (99,5%) (WHC GmbH, Hilgertshausen-Tandern, Germany)
  - 6,7 g protein powder Impact Whey Protein (MyProtein Hut.com Ltd., Northwich, England)
- indocyanine green (ICG) (PULSION Medical Systems SE, Munich, Germany)

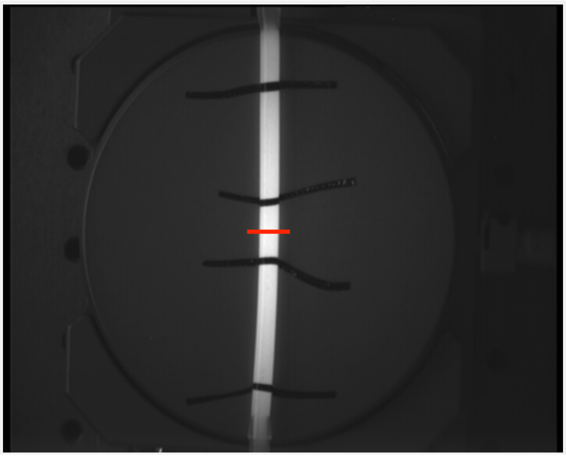

Figure 8.5: An exemplary image of a silicone tube filled with ICG and blood analog. It was fixed to a rotational board and the red line indicates 0° of rotation. This image is adapted from [172] published under the Creative Commons Attribution 4.0 License.

Table 8.2: Tubes used in the experiment. The manufacturing tolerance is according to the DIN ISO 3302-1 E2.

Inner diameter incl. tolerance in mm	**Wall thickness** in mm
1 ± 0.35	1
2 ± 0.35	0.5
3 ± 0.4	0.5
4 ± 0.4	0.5
5 ± 0.5	0.5
6 ± 0.5	1
7 ± 0.7	1
8 ± 0.7	1

Evaluation The relative error in the length measurement will be used for the evaluation of the methods. The relative error is calculated in reference to the continuous ground truth length (see Eq.8.10) for the *in silico* data.

$$\varepsilon_s = \frac{l_{measured}}{l_{Arc}} - 1 \tag{8.10}$$

Eight values need to be tracked for each image:

1. Continuous ground truth length l_{Arc}
2. Discrete ground truth length without any centerline reconstruction $l_{discrete}$
3. Discrete length with the centerline reconstruction by erosion $l_{discrete,erosion}$
4. Discrete length with the centerline reconstruction by Voronoi diagram $l_{discrete,Voronoi}$
5. Continuous length with the centerline reconstruction by erosion and interpolation by Bézier $l_{Bezier,erosion}$

6. Continuous length with the centerline reconstruction by erosion and interpolation by polynomial approximation $l_{poly,erosion}$
7. Continuous length with the centerline reconstruction by Voronoi diagram and interpolation by Bézier $l_{Bezier,Voronoi}$
8. Continuous length with the centerline reconstruction by Voronoi diagram and interpolation by polynomial approximation $l_{poly,Voronoi}$

The relative error in the diameter measurement will be determined analogously to Equation 8.10. Thereby, the denominator will be the preset diameter value which was set at the generation of the data sets.

For the laboratory experiment the equivalent measures to the above listed will be used. The ground truth of the length is the mean of multiple measurements with a caliper and the ground truth of the diameter is taken from Table 8.2.

8.2.2 Measurement of the bolus transit time

Two IDCs with a ground truth temporal shift are needed to perform an evaluation of the measurement of the time shift. The generation of them is based on a fluid simulation which is presented in Section 8.2.2.1. The section also includes the post-processing of the curves as noise will be applied. Afterwards, the measurement of the shift is in focus in Section 8.2.2.2.

8.2.2.1 Generation of a synthetic data set

The following requirements were set for the data sets of two corresponding IDCs:

- The computed curves should mimic IDCs.
- The curves' morphology should be highly configurable.
- The ground truth transit time of the two curves in a data set must be known.
- The samples of the curves should be shifted relative to each other (so using two curves with not identical samples ensuring the depiction of 2 curves taken at two different locations).
- Different noise levels should be applicable.

The finite element-based software COMSOL Multiphysics (version 5.4) with the packages Computational Fluid Dynamics (laminar flow) and Chemical Reaction Engineering (transport of concentrated species and transport of diluted species) was used for this *in silico* model. The *.mph* file to reproduce the results is available and can be handed out. The calculation of the motion of the fluid is based on the Navier-Stokes equation and the continuity equation (see Equation 8.11 & 8.12 with $\mathbf{u}$ as the fluid velocity, p the pressure, ρ the density, μ the dynamic viscosity, $\mathbf{F}$ external forces and the nabla operator ∇ that indicates the coverage of all spatial dimensions).

$$\rho\left(\frac{\partial\mathbf{u}}{\partial t}+\mathbf{u}\cdot\nabla\mathbf{u}\right)=-\nabla p+\nabla\cdot\left(\mu(\nabla\mathbf{u}+(\nabla\mathbf{u})^T)-\frac{2}{3}\mu(\nabla\cdot\mathbf{u})\mathbf{I}\right)+\mathbf{F} \tag{8.11}$$

$$\frac{\partial\rho}{\partial t}+\nabla\cdot(\rho\mathbf{u})=0 \tag{8.12}$$

Assuming laminar flow, an incompressible fluid and no external forces (such as gravity) the continuity equation yields

$$\nabla\cdot\mathbf{u}=0, \tag{8.13}$$

and the terms $-\frac{2}{3}\mu(\nabla\cdot\mathbf{u})\mathbf{I}=0$ and $\mathbf{F}=0$ for Equation 8.11.

The dye will spatially diffuse due to its concentration gradient. Hence, the direction of the diffusive flux can be normal to the fluid flow direction. This is expressed by the convection–diffusion equation (Equation 8.14 with c being the species' concentration, $\mathbf{J_{Diff}}$ being the diffusive flux and $\mathbf{R}$ describing sources or sinks of c). The diffusive flux can be approximated by Fick's first law (Equation 8.15 with D as the diffusion coefficient). Since no sources or sinks are present, $\mathbf{R}=0$.

$$\frac{\partial c}{\partial t}+\nabla\cdot\mathbf{J_{Diff}}+\mathbf{u}\cdot\nabla c=\mathbf{R} \tag{8.14}$$

$$\mathbf{J_{Diff}}=-D\nabla c \tag{8.15}$$

The equations are fully coupled and solved by the PARDISO (PARallel DIrect SOlver) solver which is based on the LU decomposition (Lower–Upper). The relative tolerance in the calculation of each measuring point is set to 0.1%.

The modeling in this work is performed using COMSOL Multiphysics as a tool for numerical simulation. Alternatively, other software can be used analogously (Ansys, OpenFOAM or similar). This numerical approach enables the implementation and calculation of more complex geometries and the ability to calculate spatially resolved concentrations. This is advantageous for future applications. In this work, the used geometry and properties are simplified and not realistic representatives of the circulatory system and therefore merits of the methods used for computing are irrelevant.

The fluid was modeled as a homogeneous liquid. A rotationally symmetric geometry was defined. It was divided into a section containing blood analog (water with glycerol and protein powder) and a section containing a homogeneous concentration of the indicator (ICG) dissolved in the blood analog (see Figure 8.6, the used geometry mimics an in-house flow phantom. The geometry, COMSOL settings and the defined parameters are attached in the Appendix A.3). Consequentially, the indicator concentration is a rectangular function at $t=0$ and mimics an abrupt injection. Lastly, multiple lateral locations were defined where the mean indicator concentration across the cross-sectional area was measured. Thereby, different morphologies were computed depicting increasing degrees of dilution. We used a distance of 50 cm between the three different measurement locations. The distance from

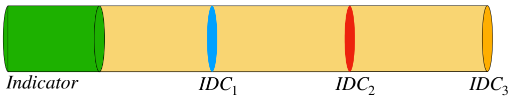

Figure 8.6: Sketch of the rotationally symmetric geometry with a section containing a homogeneously distributed indicator (green area) and a blood analog (yellow area). After applying a laminar flow, concentration curves are obtained as the mean concentration at the pipe's cross-sectional area at the three marked locations (blue, red and orange). The corresponding dilution curves are shown in Figure 8.7. Please note that the scale of the figure does not represent the scale used in the *in silico* model. This image is adapted from [136] published under the Creative Commons Attribution 4.0 License.

the heart to the brain is approx. 50 cm, which would mimic an injection via a central venous catheter and the other distances peripheral injections (e.g. arm of the patient) [195].

The following input parameters, properties and boundary conditions were defined:

- Inner radius: $r_i = 2\,\mathrm{mm}$
- Outer radius: $r_o = r_i$
- Rigid vessel wall: $E = 0$
- Applied volume flow: $\dot{V} = 150\,\frac{\mathrm{ml}}{\mathrm{min}}$
- Inflow modeled as a ramp function reaching the designated volume flow in 1 second.
- Open outlet with pressure: $p = 1\,\mathrm{atm}$
- Laminar fluid flow and convection (Re - Reynolds number): $Re \approx 600 < Re_{critical}$
- Incompressible fluid: $\rho = constant$
- Non-Newtonian fluid behavior modeled by the Casson-model (see Appendix A.3)
- No wall slip: $\mathbf{u}(r = r_i) = 0$
- No external pressure or hydrostatic pressure
- No gravitational force

The volume flow is chosen based on reports on physiological values of cerebral arteries of this size. Thereby, a linear regression of the weighted average (weighted on the sample size of each report) is performed and the value for the chosen diameter is rounded to the closest multiple of 25 $\frac{\mathrm{ml}}{\mathrm{min}}$ [31, 36, 38, 39, 196]. The modeled volume flow is continuous and not pulsatile. This simplification can be assumed as valid in distal arteries. It was shown that the Gosling pulsatility index (PI) is significantly reduced from proximal to distal measurements of volume flow in cerebral arteries [44, 45].

For the simulation of the flow and the evaluation of the mean indicator concentration, a fine mesh with 175176 elements was built. Each mesh element consisted of triangles with a radially decreasing side length ranging from $10^{-4}\,\mathrm{m}$ to $10^{-6}\,\mathrm{m}$. To obtain the three IDCs with different morphologies, the time frame of the simulation was set from 0 s to 12 s with a sampling rate of $f_{sampling} = 1200\,\mathrm{Hz}$. Therefore, each computed data set consisted of $1200\,\mathrm{Hz} \cdot 12\,\mathrm{s} = 14400$ samples. The sampling frequency is related to the frame rate of common surgical microscopes of 25 Hz and 60 Hz. As a result of this sampling process with 1200 Hz, we obtained $\frac{1200\,\mathrm{Hz}}{25\,\mathrm{Hz}} = 48$ and $\frac{1200\,\mathrm{Hz}}{60\,\mathrm{Hz}} = 20$ different sub-samples at 25 Hz and 60 Hz, respectively. This held the advantage that it also increases the variability in shifting the curve. The raw IDCs are shown in Fig. 8.7. After computing the raw IDCs, the data sets were imported into MathWorks MATLAB R2019b.

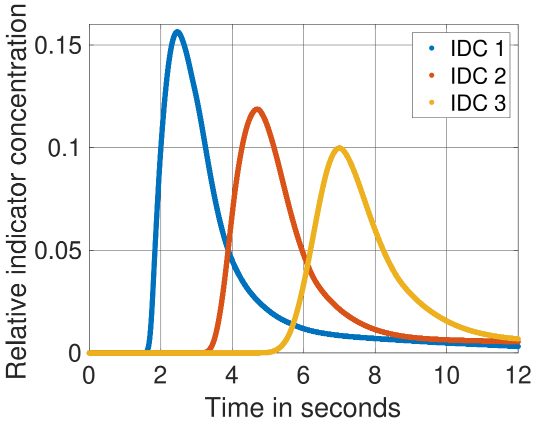

Figure 8.7: The three IDCs obtained from the fluid flow model with a sampling rate of 1200 Hz. The relative concentration is normalized to the input concentration c_{ICG}. The blue, red and orange curves show the IDCs in a distance of 50 cm, 100 cm and 150 cm to the injection side as sketched in Figure 8.6, respectively. This image is adapted from [136] published under the Creative Commons Attribution 4.0 License.

The goal was to obtain two IDCs mimicking a measurement from locations with a short distance in between. The following steps were applied to fulfill the requirements mentioned at the beginning of this section (pipeline is shown in the Figures 8.8A - 8.8C):

- Duplication of one IDC (see Figure 8.8A).
- Temporal shift of one IDC by a known value (ground truth) ranging from 1 frame to 4 frames in the case of 25 Hz (2 frames to 8 frames in case of 60 Hz; see Figure 8.8A).
- Different sub-sampling to the desired sampling rate (e.g. 25 Hz or 60 Hz; see Figure 8.8B).
- Application of white Gaussian noise (WGN) to both curves to represent noise such as Johnson–Nyquist noise (SNR ranges from 8 dB to 20 dB; see Figure 8.8C).

The motivation of duplicating one raw (noise-free) IDC is strongly linked to the expected temporal shift. The field of view in cerebrovascular surgery is approx. 3x3 cm^2, the mean flow velocity is approx. $10-50\,\frac{\mathrm{cm}}{\mathrm{s}}$ and a typical exposed length of a vessel is $1-2\,\mathrm{cm}$ [38, 39, 197, 198]. The expected morphological changes of the IDCs are negligible and for the sake of the computational effort ignored (in the Appendix A.5 the magnitude of change is shown). Therefore, the computed IDCs are duplicated and shifted by the proposed range which relies on the expected clinical circumstances.

Different sources of noise will appear in the measurements e.g. thermal noise from the recording device and patient related noise such as the heart rate. Johnson–Nyquist noise was represented in the data set by additive WGN due to its similar characteristic. Additive WGN is described by the probability density function shown in Equation 8.16 of a Gaussian

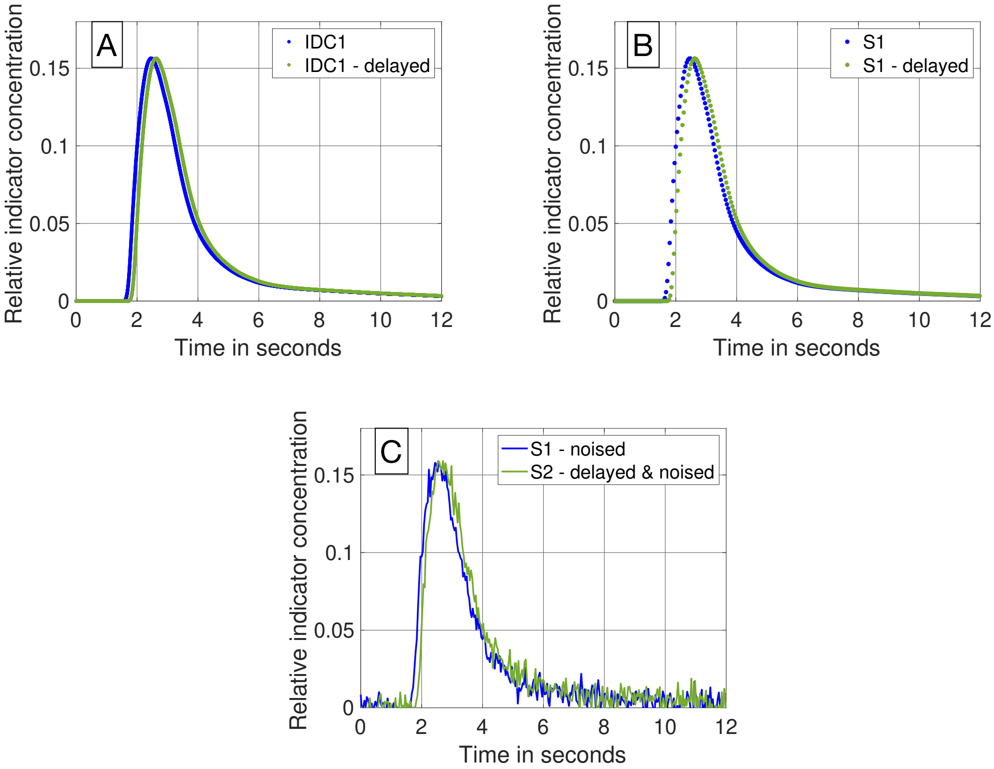

Figure 8.8: A: IDC1 in blue without any manipulations. In green the same curve delayed by a transit time $t_{transit} = 160\,\text{ms}$. Both are sampled with $1200\,\text{Hz}$. **B:** Sub-sampling of the two curves from Figure A. Both curves are sub-sampled to $25\,\text{Hz}$. **C:** Final data set containing two differently sub-sampled curves, one of them temporally shifted by the ground truth transit time $t_{Groundtruth}$. WGN is applied to both IDCs ($SNR = 20\,\text{dB}$). All images are adapted from [136] published under the Creative Commons Attribution 4.0 License.

random variable n with μ as the mean value and σ as the standard deviation.

$$f(n) = \frac{1}{\sqrt{2\pi\sigma^2}} e^{-\frac{(n-\mu)^2}{2\sigma^2}} \tag{8.16}$$

μ was set to zero and σ is calculated using the definition of the SNR (Equation 8.17).

$$SNR = 10 \cdot log_{10}\left(\frac{P_{Signal}}{P_{Noise}}\right) \text{dB} \tag{8.17}$$

With the relation

$$P_{Noise} = 2\sigma^2 \tag{8.18}$$

of the noise power P_{Noise}, the standard deviation σ and the approximated signal power

$$P_{Signal} = \sum\nolimits_t |s(t)|^2 \tag{8.19}$$

of the noise-free IDC samples $s(t)$, the standard deviation σ can be calculated as

$$\sigma = \sqrt{\frac{P_{Signal}}{2 \cdot 10^{\frac{SNR}{10 \cdot \text{dB}}}}} \tag{8.20}$$

No other noise was added due to the lack of information on its characteristic since mostly the separation of desired signal and noise is not possible. Additionally to WGN, you could consider to include shot noise. The quantum fluctuation of the photons hitting the detector are dependent on the scattering, absorption and fluorescence events in a tissue slab which are stochastically determined processes. Hence, they can be interpreted as shot noise. Following the central limit theorem, the uncertainties of the interaction of a photon relies on the superposition of multiple randomized events and therefore shot noise can be assumed as normally distributed and modeled by additive WGN [199]. Other influences of noise are excluded in this investigation. WGN noise tests the robustness of the proposed mathematical models against disturbance. This is rather in focus of this investigation than the ideal realistic representation of all sources of noise.

The application of noise is done for each data set independently. Hence, each time a new noise set is generated and added to the signal. The application of noise on the signal assumes that the error in the transit time measurement is linked to amplitude noise and is therefore an appropriate representation of disturbing influences on the measurement. Since no publication is known to me that states the typical expected SNR value for cerebrovascular FA, the chosen SNR range is related to observations in *in vivo* data obtained by project partners.

Summarizing, different raw IDCs were simulated in COMSOL Multiphysics and imported to MathWorks MATLAB R2019b to compute different sub-samples, apply a temporal shift and noise. In total, 12096 data sets were computed:

- 3 raw IDCs with different morphology
- 2 sampling rates: $f_{sampling,1} = 25\,\text{Hz}$ & $f_{sampling,2} = 60\,\text{Hz}$
- 12 different sub-sampling combinations
- 7 different SNR levels (8 dB to 20 dB in 2 dB steps)
- 6 independent realizations for each noise level
- 4 different temporal shifts (transit times)

As a result, a large amount of diverse data sets, each containing two corresponding IDCs ($c_1(t)$ and $c_2(t)$) with a known ground truth transit time are given and ready for the following evaluation of different methods measuring the transit time $t_{transit}$. In the case that methods are applied to both curves, $c_1(t)$ and $c_2(t)$ are named $c(t)$ for simplicity.

8.2.2.2 Evaluation of methods measuring the transit time Δt

MathWorks MATLAB R2019b was used for the following evaluation and analysis.

Typical analysis of transit time is based on feature-based methods such as peak to peak distances or using the cross-correlation of both signals as a tool to determine the transit time [182]. Using artificial up-sampling, these methods are able to compute sub-frame rate transit times. Artificial up-sampling does not add information to the data and can provoke artifacts that manipulate the analysis in a negative manner.

Therefore, we propose to fit established and physiologically motivated mathematical models

to the data sets of both IDCs $c_1(t)$ and $c_2(t)$ and then compute the transit time as the shift of those two mathematical functions. This investigation takes four models into consideration: The parabola function, the local density random walk (LDRW), the gamma variate function and the mono-exponential function. The parabola function is chosen due to its simplicity and robustness of fitting; it takes only the data points around the peak into account. The LDRW function is based on the theory of diffusion of the indicator by drift models. It regards the indicators movement as a longitudinal diffusion superimposed on a linear convection and is valid for an instantaneous injection, which fits our problem [200, 201]. The gamma variate function is derived from modeling an unidirectional constant flow as a series of multiple mixings in sequential compartments of the same volume with only one input and output, which fits our problem as well [202, 203]. Both the LDRW and gamma variate function take the whole curve into account. However, both are not able to represent recirculation. The mono-exponential function describes the washout of the indicator and only takes the descending arm of the curve into account. It was developed to extrapolate the dilution curve on the descending arm to estimate the curves course without recirculation [184].
Different features will be used to extract the transit time $t_{transit}$ from two fitted mathematical functions. Each feature is function specific and will be described in detail in the corresponding section.

Post-processing of the data Before fitting mathematical models to the two curves of a data set, a pre-processing step is needed. Each IDC needs to be cut to ensure a robust fitting. Two examples: First, prior to the arrival of the indicator zeros are recorded. Including them into the fitting algorithm does not make any sense and can cause problems. Second, fitting the parabola model to the whole signal does not make sense either, therefore the peak is detected and only data points surrounding it are considered for fitting.
Addressing the problem of the first example, the data points prior to the appearance of the indicator should be removed since they contain no information and are basically zeros with noise applied to it. Equation 8.21 has shown to be empirically appropriate to find this cut point t_{cut1} on the abscissa representing the appearance of the indicator despite of the impact of noise (c_{max} is the maximum concentration, t_{up} only considers the data points left of the peak and t_{down} only considers the data points right of the peak). The subscript of t_{up} and t_{down} shows at which values of c_{max} the t value is chosen. Example: $t_{down,20\%c_{max}}$ is the t value on the right side of the peak at 20% of the maximum concentration. To determine the needed parameters of the equation, a moving average with a window length of 20 samples is used to reduce the impact of noise on the signal. The length of 20 samples was chosen to ensure a low pass filtering without affecting the morphology of the IDC too much. To ensure unambiguity the search for the parameters on the up slope are performed from left to right and on the down slope from right to left. This pre-processing is applied on all data sets independently to the further processing.

$$t_{cut1} = t_{up,20\%c_{max}} - 0.1 \cdot \left[t_{down,50\%c_{max}} - t_{up,50\%c_{max}}\right] \tag{8.21}$$

Addressing the problem of the second example, it is reported that cutting the data as a pre-processing step enhances the robustness and accuracy of the fit. Seven different levels of cutting are introduced: they range from $t_{20\%c_{max}}$ to $t_{80\%c_{max}}$ in steps of 10%. Further, it is reported that an unequal cutting to the left compared to the right of the peak is favorable due to different information content in the data (e.g. exclusion of recirculation) [204]. For this purpose, 3 cutting methods are additionally introduced and depicted in Figure 8.9.

1. No further cutting left of the peak and variable cutting levels right of the peak.
2. Cutting left of the peak at half the value of the variable cutting to the right of the peak.
3. Variable but identical cutting left and right of the peak.

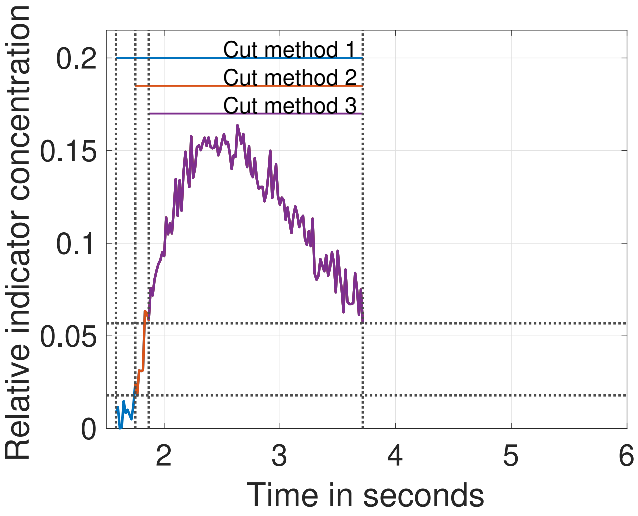

Figure 8.9: Visualization of the three different pre-processing (cutting) methods on the data. The cut level is set to 40 % of the maximum. After applying cut method 3, the purple curve remains. Applying cut method 2 results in the curve consisting of purple and red. Application of cut method 1 results in the curve of all three colors purple, red and blue. This image is adapted from [136] published under the Creative Commons Attribution 4.0 License.

Summarizing, 21 different variations (3 cut methods and 7 cut levels) to cut the IDC as a pre-processing step are possible and will be evaluated in this analysis.

Mathematical models The mathematical models are described in the following sections as well as the initial estimation of their parameters $\mathbf{p_{init}} = (p_{1,init}, p_{2,init}, \dots, p_{n,init})$. The initial estimation is needed to run a least squares optimization algorithm to determine the function's parameters $\mathbf{p}$ which fit the data best. Since indexed variables are easier to handle, the input data $c(t)$ is described as the set of data points $(t(k), c(k))$ with $\forall k \in [1, K]$ (K being the number of data points). Therefore, we solve the problem

$$\min_{\mathbf{p}}\{F_{fit}(\mathbf{p})\} = \min_{\mathbf{p}|p_i \in [p_{lb}, p_{ub}]}\{\textstyle\sum_{k=1}^{K} |f_{model}(\mathbf{p}, t[k]) - c[k]|^2\} \tag{8.22}$$

with p_{lb} being the lower bound and p_{ub} the upper bound of the respective parameters p_i. To solve Equation 8.22, different algorithms like the 'trust-region-reflective' or the 'Levenberg-Marquardt' algorithms are suitable. The 'trust-region-reflective' algorithm is used in this study [205].

The time shift of the functions can be determined after fitting the mathematical models to the pre-processed (cut) input data (two IDCs). The features used to determine the time shift are specific to the mathematical models and described in the corresponding following sections. For all mathematical models the following notation are used:

$$\begin{aligned} c_{max} &= max\, c(t) \\ t_{c_{max}} &= arg\, max\, c(t) \end{aligned} \tag{8.23}$$

t_0 is the time point of the beginning of the data after cutting. t_{end} is the last time point data after cutting (or recording).

Parabola model The parabola model is defined as shown in Equation 8.24. This model is fitted to the data points around the peak (according to the cutting method specified at the beginning of this section) of the IDC.

$$f_{Parabola}(\mathbf{p},t) = -p_1 \cdot (t - p_2)^2 + p_3 \tag{8.24}$$

The parabola has a distinct morphology which facilitates setting up $\mathbf{p}$. The input $c(t)$ was smoothed by a sliding rectangular window with a window size of 20 samples to ensure $p_{2,init}$ and $p_{3,init}$ are determined robustly. $\mathbf{p}$ was determined as shown in the following equations.

$$p_{1,init} = \frac{c(t_{end}) - c_{max}}{(t_{end} - t(c_{max}))^2} \tag{8.25}$$

$$p_{2,init} = t_{c_{max}} \tag{8.26}$$

$$p_{3,init} = c_{max} \tag{8.27}$$

No boundaries are needed for the optimization of the parameters $\mathbf{p}$ of the parabola.

To determine the shift of the two fitted parabolas of one data set, the maximum of each parabola is used as feature.

Local density random walk (LDRW) model The LDRW model is defined as shown in Equation 8.28. This model can be fitted to the whole IDC.

$$f_{LDRW}(\mathbf{p},t) = p_1 \cdot \left(\frac{e^{p_2}}{p_3}\right) \cdot \sqrt{\frac{p_2 \cdot p_3}{2\pi(t - p_4)}} \cdot e^{-\frac{p_2}{2}\cdot(\frac{p_3}{t-p_4}+\frac{t-p_4}{p_3})} \tag{8.28}$$

According to the approach of Mischi et al. and Bogaart et al., the parameters are calculated as shown in the following equations [186, 206]. $p_{1,init}$ represents the total amount of injected dye. Consequentially, it can be expressed as the integral of $c(t)$ or in the discrete case as a sum of the products. $p_{2,init}$ represents the slope of the ascending arm. $p_{3,init}$ represent the abscissa coordinate of the maximum. $p_{4,init}$ represents the zero time of the distribution and is in our case slightly shifted away from the distributions maximum to be sure to not prune the distribution at the beginning because our function is defined only for positive values of $t - p_4$ and therefore optimization will be only performed for $t > p_4$.

$$p_{1,init} = \frac{1}{2} \cdot \sum_{i=0}^{N} (t_{i+1} - t_i) \cdot [c(t_i) + c(t_{i+1})] \tag{8.29}$$

$$p_{2,init} = \frac{1}{2} \cdot \frac{|t_{c_{max}} - t_0|}{c_{max}} \tag{8.30}$$

$$p_{3,init} = \frac{1}{2} \cdot (t_{end} - t_0) \tag{8.31}$$

$$p_{4,init} = t_0 - \frac{1}{5} \cdot |t_{c_{max}} - t_0| \tag{8.32}$$

The boundaries for **p** were set as $(p_1, p_2, p_3, p_4) \in ([0,\infty), [0,\infty), [\frac{p_{3,init}}{100}, \infty), [0, t_0])$.
To determine the shift of two fitted LDRW functions, the maximum as well as the maximum and minimum of the first and second derivative of each LDRW function are used as features. Further, the cross-correlation of the two LDRW functions is used to determine the time shift. It is applied to the two LDRW functions and their first derivative, as well as to the functions and their first and second derivative with an additional linear temporal interpolation with a factor of 100 (the functions are continuous but MATLAB is a vector and matrix-based software and the calculation of the cross-correlation requires a discrete input and therefore the functions are sampled with a sampling rate 100 times higher than the input sampling rate for the fitting, e.g. $f_{sampling} = 25\,\text{Hz}$, then the input for the calculation had a $f_{sampling} = 2500\,\text{Hz}$. We assume this accuracy with maximum error of $\frac{1}{50}$ of a frame is sufficient).

Gamma variate model The gamma variate model is defined as shown in Equation 8.33. This model can be fitted to the whole IDC.

$$f_{Gamma}(\mathbf{p}, t) = p_1 \cdot (t - p_4)^{p_2} \cdot e^{-\frac{t - p_4}{p_3}} \tag{8.33}$$

According to the approach of Madsen and Mischi et al., the parameters are calculated as shown in the following equations [187, 207]. $p_{1,init}$ and $p_{2,init}$ represent the coordinates of the maximum (obtained by differentiating the function and setting it equal to zero). $p_{3,init}$ represents the slope of the decreasing arm of the function. $p_{4,init}$ represents the zero time of the distribution and is in our case slightly shifted away from the distribution's maximum.

$$p_{1,init} = \frac{e^{p_{2,init}} \cdot c_{max}}{(p_{2,init} \cdot p_{3,init})^{p_{2,init}}} \tag{8.34}$$

$$p_{2,init} = \frac{t_{c_{max}} - p_{4,init}}{p_{3,init}} \tag{8.35}$$

To calculate $p_{3,init}$ a moving average with a window size of 20 samples is applied to the signal and the endpoint $(t_{SW,n}, c_{t_{SW,end}})$ of the signal is used.

$$p_{3,init} = -\frac{t_{SW,end} - t_{c_{max}}}{ln(c_{t_{SW,end}})) - ln(c_{max})} \tag{8.36}$$

$$p_{4,init} = t_0 - \frac{1}{5} \cdot |t_{c_{max}} - t_0| \tag{8.37}$$

The boundaries for $\mathbf{p}$ were set as $(p_1, p_2, p_3, p_4) \in ([0, \infty), [0, \infty), [\frac{p_{3,init}}{100}, \infty), [0, t_0])$.
To determine the shift of two gamma variate functions, the same features and methods are used as for the LDRW function.

Mono-exponential model The mono-exponential model is defined as shown in Equation 8.38. This model is fitted to the descending arm of the data set. Thereby, the descending arm is defined as the data points $t > t_{c_{max}}$ after running a moving average on $c(t)$ with a window size of 20 samples.

$$f_{MonoEx}(\mathbf{p}, t) = p_1 \cdot e^{p_2 \cdot (t - p_3)} \tag{8.38}$$

According to Brands et al., the parameters are calculated as shown in the following equations [208]. To determine $p_{1,init}$ and $p_{3,init}$, the smoothed data is used. $p_{1,init}$ and $p_{3,init}$ represent the coordinates of the maximum of the function, hence the start of the defined sector of the mono-exponential function. $p_{2,init}$ represents the slope of the function.

$$p_{1,init} = c_{max} \tag{8.39}$$

$$p_{2,init} = \frac{1}{t_{end} - p_{3,init}} \cdot ln\left(\frac{c(t_{end})}{p_{1,init}}\right) \tag{8.40}$$

$$p_{3,init} = t_{c_{max}} \tag{8.41}$$

No boundaries are needed for the parameter optimization of the mono-exponential model.
Determining the shift of two Mono-Exponential functions is not trivial since their maxima and minima depend solely on the sections of $c(t)$ to which they are fitted to. So, no maximum or minimum of the function can be used. Therefore, a feature was introduced which describes the euclidean distance of the normalized function to a defined point. Both axes were normalized, $c(t)$ to c_{max} and t to $t_{end} - t_{c_{max}}$. Finally, the cost function f_c (see Eq. 8.42) was minimized to obtain a time stamp t_{eucl} for each IDC. The transit time can be calculated as the difference of both time stamps t_{eucl} of one data set.

$$f_c(t_{eucl}) = \sqrt{\left(\frac{f_{model}(t_{eucl})}{c_{max}}\right)^2 + \left(\frac{t_{eucl} - t_{c_{max}}}{t_{end} - t_{c_{max}}}\right)^2} \tag{8.42}$$

Control group A control group is added to enable the assessment of the performance of the proposed methods. Using the peak of the raw data relies on a single sample point in each IDC and is very noise sensitive. The cross-correlation of the IDCs relies on a larger set of sample points, is less noise sensitive and therefore used for this performance assessment. The cross-correlation is applied to the raw input data $c(t)$, its first derivative $\Delta c(t)$ (discrete sample to sample difference), the linear interpolated input data $c_{interpolate}(t)$ and to the interpolated first derivative $\Delta c_{interpolate}(t)$. A linear interpolation with a factor of 100 is applied to enhance the accuracy.

Performance parameter In total, 22 combinations of mathematical models and features as well as 4 control groups are used to assess the transit time error on all 12096 *in silico* generated data sets. The performance parameter used to compare different methods measuring the transit time was defined as the absolute difference between the measured transit time t_{calc} of two IDCs of one data set and the ground truth transit time $t_{Groundtruth}$. It will be represented as ε_{frames} in frames to emphasize whether a sub-frame rate accuracy is accomplished or not. The calculation of the absolute error $\varepsilon_{t_{transit}}$ and error in frames ε_{frame} is shown in Equation 8.43.

$$\varepsilon_{frame} = \varepsilon_{t_{transit}} \cdot f_{sampling} = |t_{calc} - t_{Groundtruth}| \cdot f_{sampling} \tag{8.43}$$

The mean value μ and standard deviation σ of ε_{frame} will be used for the evaluation. The μ and σ are calculated using 12096 data sets

- 3 morphologically different IDCs
- 7 different SNR levels
- 6 cycles for each SNR level
- 4 different transit times $t_{transit}$
- 2 different sampling rates $f_{sampling}$
- 12 different combinations of sub-sampling

for each combination of methods and pre-processing (546 in total)

- 26 combinations of different mathematical models, features and control group
- 3 methods of cutting the data
- 7 levels of cutting the data.

The absolute error at a certain SNR $\varepsilon(SNR)$ should decrease with an increasing sampling rate. The ratio of decrease in $\varepsilon(SNR)$ is the same as the ratio of the increase in sampling rate. An aspect that is not considered in this evaluation is the increasing effect of noise on the measured signal due to a shortened integration time (exposure time) at higher sampling rates at the detector. This effects the SNR by a factor of the square root of the ratio of the two sampling rates. This assumes uncorrelated noise and a linear decrease of integration time with increasing sampling rate and will be only discussed at the end.

8.3 Results

The results are split into the results of the analysis of the geometrical, with a focus first on the length and then the diameter measurement, and temporal parameters.

8.3.1 Measurement of geometrical parameters

Figure 8.10 shows two examples of vessel segmentations generated by the *in silico* model. 1204 such images were generated and more examples are given in the Appendix A.1. The centerline extraction, the length, and diameter measurement methods where then applied on these 1204 images.

Figure 8.10: *In silico* simulation of two vessel segmentations. **Left**: Section of a parabola with a stenosis, **right**: Bifurcation including sections of two Gaussian bells and a sinusoidal. Both images are adapted from [172] published under the Creative Commons Attribution 4.0 License.

8.3.1.1 Measurement of length

***In silico* model** Table 8.3 shows the discretization error of the mathematical functions, which is due to the projection onto the grid. No centerline reconstruction methods were used here, and all errors are positive (overestimation). Furthermore, the quantity of images in each set is shown.

Table 8.4 shows the comparison of the spatial interpolation methods for the centerline extraction by erosion for all used mathematical functions. It should be noted that the mean error due to discretization after the centerline extraction is 7.0 % and the best interpolation method (Bézier) reduces this error to 2.7 %.

Table 8.5 shows the comparison of the spatial interpolation methods for the centerline extraction by Voronoi diagrams for all used mathematical functions. The mean error due to discretization after the centerline extraction is 7.9 % and the best interpolation method (Bézier) reduces this error to 4.7 %.

Table 8.3: Mean relative error of the discrete length measurement with no centerline reconstruction compared to the continuous ground truth [171].

Function type	Relative error	Quantity in the set
Straight lines	2.3%	184
Parabolas	7.2%	312
Polynomials	6.3%	168
Sinusoids	6.8 %	132
Curved Waves	7.6%	102
Bell curves	8.5 %	108
Bifurcations	6.7 %	198
Mean of all	6.3%	

Table 8.4: Mean relative error of the length measurement methods in % after centerline extraction by erosion compared to the continuous ground truth. Significance was proven for the reduction of the error compared to the discrete length for each function type **** p<0.0001.

	Discrete $\mu \pm \sigma$	Bézier $\mu \pm \sigma$	Polynomial $\mu \pm \sigma$
Straight lines	5.2 ± 3.8	2.6 ± 1.8 ****	2.1 ± 1.6 ****
Parabolas	7.5 ± 4.0	2.4 ± 1.5 ****	1.9 ± 1.3 ****
Polynomials	6.5 ± 4.8	3.9 ± 6.2 ****	7.2 ± 7.5 ****
Sinusoids	8.5 ± 5.8	4.2 ± 7.8 ****	6.6 ± 12.6 ****
Curved waves	7.6 ± 2.6	2.5 ± 1.4 ****	2.6 ± 2.2 ****
Bell curves	10.4 ± 3.2	3.1 ± 1.7 ****	1.9 ± 1.4 ****
Bifurcations	6.1 ± 5.4	2.1 ± 5.3 ****	2.6 ± 5.1 ****
Mean of all	7.0 ± 4.8	2.7 ± 4.5 ****	3.2 ± 5.8 ****

Table 8.5: Mean relative error of the length measurement methods in % after centerline extraction by Voronoi diagrams compared to the continuous ground truth. Significance was proven for the reduction of the error compared to the discrete length for each function type **** p<0.0001.

	Discrete $\mu \pm \sigma$	Bézier $\mu \pm \sigma$	Polynomial $\mu \pm \sigma$
Straight lines	5.1 ± 5.8	3.3 ± 5.8 ****	3.2 ± 6.0 ****
Parabolas	8.6 ± 7.0	4.2 ± 8.5 ****	4.5 ± 8.7 ****
Polynomials	9.1 ± 8.5	7.7 ± 11.0 ****	11.2 ± 11.3 ****
Sinusoids	8.6 ± 5.0	5.6 ± 7.8 ****	8.9 ± 12.8 ****
Curved waves	8.3 ± 4.5	4.5 ± 7.0 ****	5.7 ± 7.5 ****
Bell curves	8.2 ± 4.2	3.4 ± 5.1 ****	3.4 ± 5.6 ****
Bifurcations	7.9 ± 11.2	4.6 ± 11.6 ****	5.9 ± 11.2 ****
Mean of all	7.9 ± 8.1	4.7 ± 9.2 ****	5.9 ± 10.0 ****

The mean run time for the combination of the two centerline reconstruction and interpolation methods is shown in Table 8.6. The erosion method with polynomial approximation was the quickest and the Voronoi diagram in combination with the Bézier curve the slowest. The difference was approximately a factor of ten. The measurement of the discrete length was neglected due to an unacceptable performance. The run time was determined on a computer with an Intel i5-Quad-Core Processor with 3.4 GHz with no parallel computing.

Table 8.6: Mean run time of the different combination of the methods in seconds for a single image.

	Erosion	**Voronoi**
Bézier curve	13.08 s	21.09 s
Polynomial approximation	2.33 s	10.34 s

Laboratory experiment The deviation in the measurement of the ground truth with the caliper was in the magnitude of 0.1 % or less of the length of the segments in all cases. The experiments on the silicone tubes resulted in the mean length errors which are shown in Table 8.7. Please note that these errors represent the mean error for all angles.

Table 8.7: Mean relative error of the length measurement methods in % after the centerline extraction by both methods and the spatial interpolation compared to the ground truth for the experimental data set (mean also over all angles). Significance was proven for the reduction of the error compared to the discrete length for each function type **** p<0.0001. Angle resolved relative errors are given in Table 8.8 & 8.9.

	Discrete $\mu \pm \sigma$	**Bézier** $\mu \pm \sigma$	**Polynomial** $\mu \pm \sigma$
Erosion	4.7 ± 3.0	$1.9 \pm 1.3^{****}$	$1.6 \pm 1.6^{****}$
Voronoi	5.0 ± 3.0	$2.0 \pm 1.3^{****}$	$1.5 \pm 1.5^{****}$

The tubes were set up as lines in different angles. Table 8.8 & 8.9 and Figure 8.11 show the relative error in dependency to the angle (relative to the resolution grid). The discrete centerline shows, as expected, a clear dependency on the angle with the minimum error at 0, 45 and 90 degree where the centerline best fits into the camera chip grid.

8.3.1.2 Measurement of diameter

***In silico* model** Table 8.10 shows the error in the diameter measurement in dependency of the function type and the centerline reconstruction method. The centerline reconstruction by erosion yields better results. The mean run time to obtain the diameter values for a single image was 0.025 seconds.

Laboratory experiment Table 8.11 shows the errors relative to the ground truth for both centerline extraction methods and for different angles. The ground truth of the tubes' diameter and their tolerance are shown in Table 8.2. The tolerance was ignored in computing the values in Table 8.11.

Table 8.8: Mean relative error of the length measurement methods in % after the centerline extraction by erosion and the spatial interpolation compared to the ground truth for the experimental data set. Significance was proven for the reduction of the error compared to the discrete length as indicated *:p<0.05, **: p<0.01, ***: p<0.001 ****: p<0.0001.

	Discrete	**Bézier**	**Polynomial**
Angle	$\mu \pm \sigma$	$\mu \pm \sigma$	$\mu \pm \sigma$
0 °	2.4 ± 1.3	1.8 ±1.5 *	1.5 ± 1.5 ***
15 °	7.0 ± 2.4	2.3 ± 1.0 ****	1.7 ± 1.6 ****
30 °	6.6 ± 2.3	1.9 ± 1.3 ****	1.6 ± 1.6 ****
45 °	2.2 ± 1.7	1.6 ± 1.6 *	1.6 ± 1.7 *
60 °	7.0 ± 2.3	1.8 ± 1.3 ****	1.4 ± 1.6 ****
75 °	5.8 ± 2.6	2.1 ± 1.2 ****	1.9 ± 1.7 ****
90 °	1.9 ± 1.3	1.7 ± 1.6	1.6 ± 1.7

Table 8.9: Mean relative error of the length measurement methods in % after the centerline extraction by Voronoi diagrams and the spatial interpolation compared to the ground truth for the experimental data set. Significance was proven for the reduction of the error compared to the discrete length as indicated *: p<0.05, **: p<0.01, ***: p<0.001 ****: p<0.0001.

	Discrete	**Bézier**	**Polynomial**
Angle	$\mu \pm \sigma$	$\mu \pm \sigma$	$\mu \pm \sigma$
0 °	2.4 ± 1.6	1.8 ±1.3	1.5 ± 1.4 *
15 °	7.4 ± 2.3	2.6 ± 1.0 ****	1.6 ± 1.2 ****
30 °	6.8 ± 2.2	2.1 ± 1.3 ****	1.7 ± 1.6 ****
45 °	2.5 ± 1.5	1.6 ± 1.5 **	1.5 ± 1.6 ***
60 °	7.1 ± 2.2	1.9 ± 1.1 ****	1.5 ± 1.5 ****
75 °	6.4 ± 2.2	2.3 ± 1.0 ****	1.5 ± 1.6 ****
90 °	2.3 ± 1.7	1.7 ± 1.5	1.5 ± 1.6 **

8.3.2 Measurement of the bolus transit time

The following two sections show the results for the generation of the data sets containing two corresponding IDCs with a ground truth of the transit time $t_{Groundtruth}$ (Section 8.3.2.1) and their analysis (Section 8.3.2.2) separately.

8.3.2.1 Generation of a synthetic data set

An example of the results of the generated data is shown in Figure 8.12A. The generated IDC has a similar morphology as the clinically obtained *in vivo* IDC in Figure 8.12B. The *in vivo* data is obtained during an extracranial-to-intracranial (EC-IC) bypass installation by a surgical fluorescence microscope in high definition resolution, with a sampling frequency of 60 Hz. The Pearson's correlation coefficient is 0.93. Since the *in silico* model does not include a circulatory flow, no recirculation appears in the generated data set compared to the *in vivo* data set. Figure 8.13 shows the power spectral density for the *in vivo* and *in silico* data set. The frequency is cut off after 5 Hz because it does not contain any significant changes.

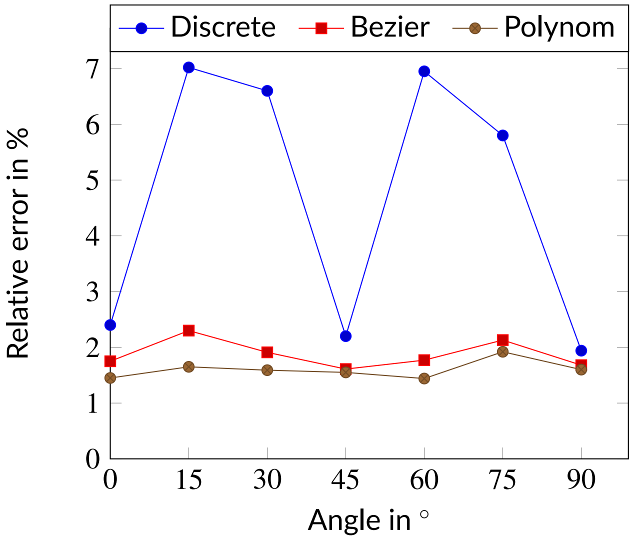

Figure 8.11: Relative length error using the erosion method in dependency on the angle for straight silicone tubes. The angle is measured to the horizontal pixel grid structure. This image is adapted from [172] published under the Creative Commons Attribution 4.0 License.

Table 8.10: Mean and standard deviation of the relative error of the diameter measurement in % in dependency of the analyzed structure after centerline extraction by the two proposed methods.

	Erosion $\mu \pm \sigma$	**Voronoi** $\mu \pm \sigma$
Straight lines	3.5 ± 4.8	4.5 ± 5.7
Parabolas	3.6 ± 5.5	4.2 ± 6.4
Polynomials	4.3 ± 5.8	5.4 ± 7.2
Sinusoids	3.4 ± 1.9	4.4 ± 2.6
Curved Waves	3.5 ± 1.5	3.7 ± 1.6
Bell curves	3.4 ± 1.8	3.5 ± 1.8
Bifurcations	4.0 ± 1.6	4.7 ± 1.6
Mean of all	3.7 ± 4.2	4.4 ± 5.0

8.3.2.2 Evaluation of methods measuring the transit time Δt

The mean computation time from the input of two IDCs to the output of the transit time error was approx. 0.298 s. This includes the initial estimation of the mathematical functions' parameters p_{init} for both IDCs, the optimization of the parameters and finally the determination of the temporal delay t_{calc} as well as the comparison to the ground truth transit time $t_{Groundtruth}$ to evaluate the temporal accuracy $\varepsilon_{t_{transit}}$ and ε_{frame}.
Visualizing all 8036 combinations of methods measuring the shift of two IDCs is not appropriate. To facilitate the visualization of the results, a 7x7 matrix is used to show the mean ε_{frame}. The values for the mean ε_{frame} are determined for the values labeled at the axis, the space in between is interpolated. Each matrix is specific for a combination of a mathematical function, feature, cutting method and sampling frequency $f_{sampling}$ and shows

Table 8.11: Mean and standard deviation relative error of the diameter measurement in % in dependency of the angle after the centerline extraction by both methods.

	Erosion	**Voronoi**
	$\mu \pm \sigma$	$\mu \pm \sigma$
0 °	2.4 ± 3.0	2.5 ± 2.2
15 °	3.0 ± 2.7	2.4 ± 2.6
30 °	3.3 ± 2.8	2.3 ± 2.3
45 °	3.5 ± 2.3	2.7 ± 2.1
60 °	2.5 ± 1.6	2.4 ± 1.7
75 °	3.3 ± 1.5	2.2 ± 1.4
90 °	3.4 ± 2.8	2.7 ± 1.4
Mean of all	3.1 ± 2.3	2.5 ± 1.8

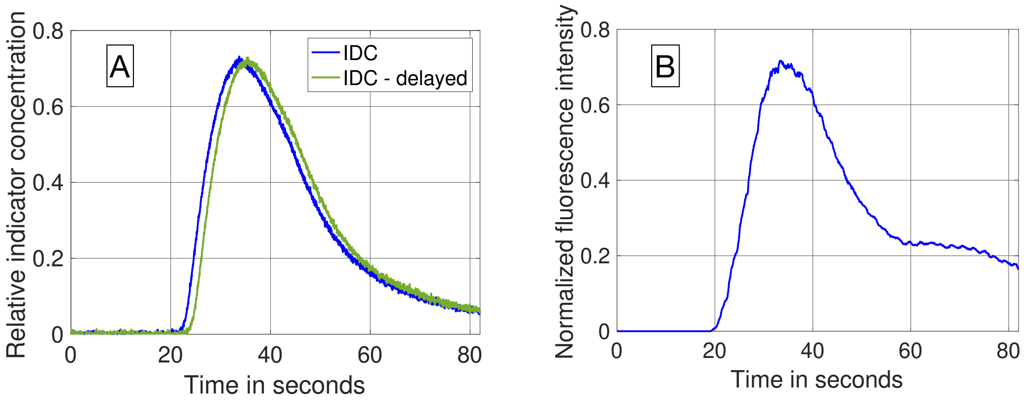

Figure 8.12: A: An example of a synthetically computed data set. It shows two IDCs with a delay of $1.5\,\mathrm{s}$ and a SNR of $37\,\mathrm{dB}$. **B:** An *in vivo* IDC obtained from a cerebrovascular EC-IC bypass surgery by ICG FA. The signal is obtained by averaging an area of 10 x 10 pixel which corresponds to a third of the vessel's diameter. Both images are adapted from [136] published under the Creative Commons Attribution 4.0 License.

the mean ε_{frame} in dependency of the preformed cutting levels as a pre-processing step and the SNR. The color code in Figure 8.14 - 8.17 shows the errors in frames (ε_{frame}). Errors larger than 1 are presented in yellow. The performance of the cross-correlation on the raw data set with $f_{sampling} = 25\,\mathrm{Hz}$ is shown in Figure 8.14A as benchmark for the proposed methods. The linear interpolation of the raw data already shows a decrease of the error (Figure 8.14A - 8.14B). The best performance from the control group at $f_{sampling} = 25\,\mathrm{Hz}$ was the cross-correlation of the linearly interpolated data set with the cutting method 2 (cutting at half the value left of the peak compared to the variable cutting to the right of the peak) and is shown in Figure 8.14B. The results of the three best combinations of mathematical functions and features measuring the transit time with the data set at $f_{sampling} = 25\,\mathrm{Hz}$ are shown in Figures 8.15A - 8.15C. They all perform similarly well and show a strong decrease of error compared to the usage of the raw data (8.14B). The results at $f_{sampling} = 60\,\mathrm{Hz}$ are shown in Figures 8.16 - 8.17 and show a similar performance compared to the lower sampling frequency. The methods that perform best at 25 Hz also tend to perform best at 60 Hz.

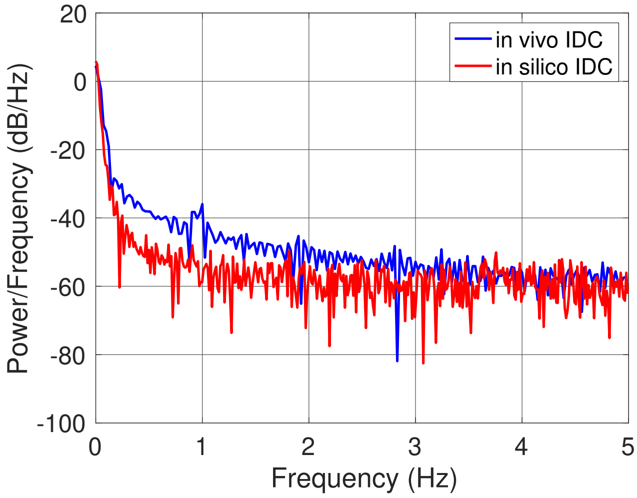

Figure 8.13: Power spectral density of the *in vivo* and *in silico* data in the spectral rang of up to 5 Hz. Image adapted from [136] published under the Creative Commons Attribution 4.0 License.

In the Appendix A.4 the corresponding values for μ and σ are shown in tabular form, which were used to compute Figures 8.14A to 8.17C.

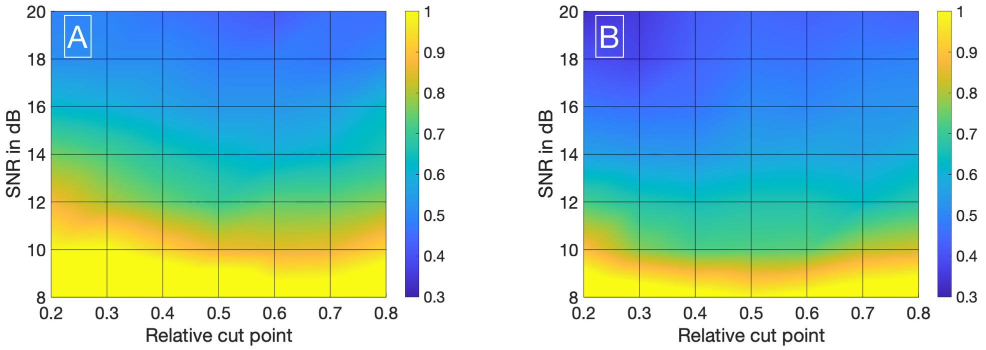

Figure 8.14: The colors in both plots show the errors in frames (ε_{frame}). Errors larger than 1 are presented in yellow. Very low error appear in blue/green. **A:** Mean ε_{frames} using the raw data sets ($f_{sampling} = 25\,\mathrm{Hz}$) with no mathematical fits. To obtain the transit time the cross-correlation is computed after applying the cut method 3. **B:** Mean ε_{frames} using the linearly interpolated data sets ($f_{sampling} = 25 \cdot 100\,\mathrm{Hz}$) with no mathematical fits. To obtain the transit time the cross-correlation is computed after applying the cut method 2. Both images are adapted from [136] published under the Creative Commons Attribution 4.0 License.

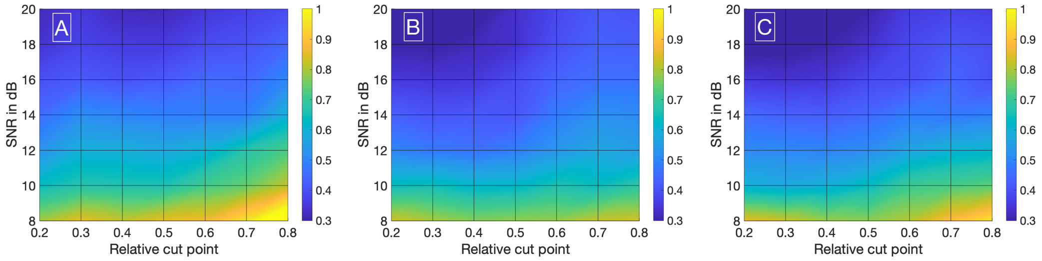

Figure 8.15: The colors in all plots show the errors in frames (ε_{frame}). Errors larger than 1 are presented in yellow. Very low error appear in blue/green. **A:** Mean ε_{frames} using the gamma variate model on the data sets ($f_{sampling} = 25\,\mathrm{Hz}$). Before fitting the model, cut method 3 is applied to the data set. To obtain the transit time the cross-correlation is computed. **B:** Mean ε_{frames} using the gamma variate model on the data sets ($f_{sampling} = 25\,\mathrm{Hz}$). Before fitting the model, cut method 1 is applied to the data set. To obtain the transit time the cross-correlation of the first derivative is computed. **C:** Mean ε_{frames} using the LDRW model on the data sets ($f_{sampling} = 25\,\mathrm{Hz}$). Before fitting the model, cut method 1 is applied to the data set. To obtain the transit time the cross-correlation of the first derivative is computed. All images are adapted from [136] published under the Creative Commons Attribution 4.0 License.

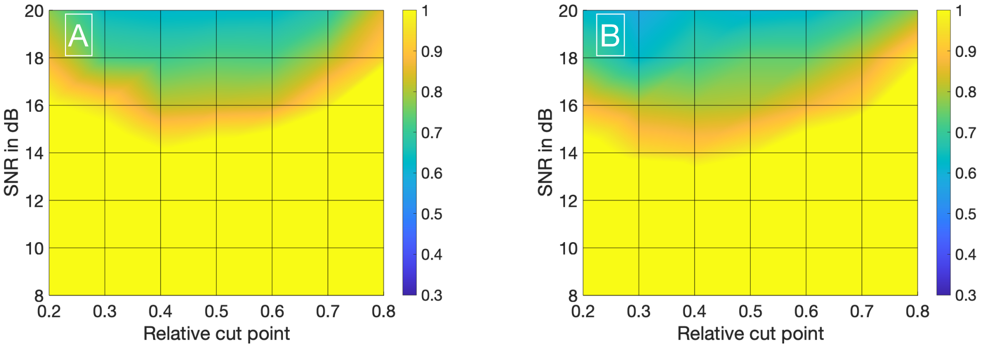

Figure 8.16: The colors in both plots show the errors in frames (ε_{frame}). Errors larger than 1 are presented in yellow. Very low error appear in blue/green. **A:** Mean ε_{frames} using the raw data sets ($f_{sampling} = 60\,\mathrm{Hz}$) with no mathematical fits. To obtain the transit time the cross-correlation is computed after applying the cut method 2. **B:** Mean ε_{frames} using the linearly interpolated data sets ($f_{sampling} = 60 \cdot 100\,\mathrm{Hz}$) with no mathematical fits. To obtain the transit time the cross-correlation is computed after applying the cut method 2. Both images are adapted from [136] published under the Creative Commons Attribution 4.0 License.

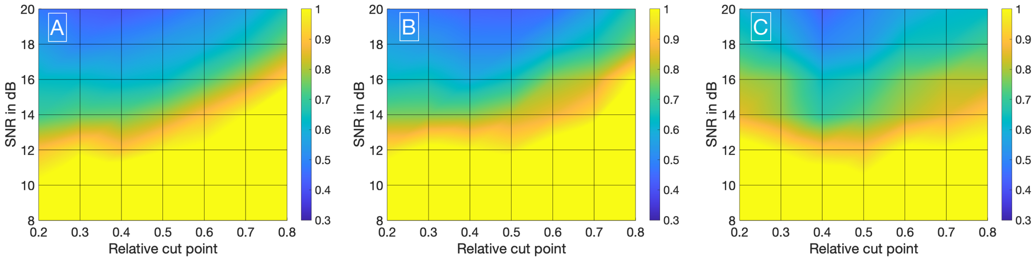

Figure 8.17: The colors in all plots show the errors in frames (ε_{frame}). Errors larger than 1 are presented in yellow. Very low error appear in blue/green. **A:** Mean ε_{frames} using the gamma variate model on the data sets ($f_{sampling} = 60\,\mathrm{Hz}$). Before fitting the model, cut method 3 is applied to the data set. To obtain the transit time the cross-correlation is computed. **B:** Mean ε_{frames} using the LDRW model on the data sets ($f_{sampling} = 60\,\mathrm{Hz}$). Before fitting the model, cut method 3 is applied to the data set. To obtain the transit time the cross-correlation is computed. **C:** Mean ε_{frames} using the LDRW model on the data sets ($f_{sampling} = 60\,\mathrm{Hz}$). Before fitting the model, cut method 1 is applied to the data set. To obtain the transit time the cross-correlation of the first derivative is computed. All images are adapted from [136] published under the Creative Commons Attribution 4.0 License.

8.4 Discussion & conclusion

8.4.1 Measurement of geometrical parameters

The proposed model is able to generate a large number of images mimicking pre-segmented cerebral vessels with a mathematically defined ground truth. The multitude of shapes including bifurcations depict a large variety of possible vessel structures. To my knowledge, there is no publication available describing vessels by mathematical functions. Therefore, some of the proposed functions and their parameters' limits might be suitable and others unsuitable to describe a vessel's geometry. The functions used in this model can be considered separately and therefore the findings derived from the results as well. Validation of the model and the used functions requires a large *in vivo* data set. Nevertheless, the model is designed to depict an extensive range of vessel geometries and a retrospective containment is possible.

8.4.1.1 Length

The focus of this section is the discussion of the measurement of the geodesic length along the centerline. The error due to discretization of the ground truth centerline is +6.3% (Table 8.3). No centerline reconstruction method was involved in this step and the simulation is set up with the PAL(DV) standard. This error is also always positive. The error of the discrete centerline reconstructed by the erosion and voronoi diagrams method increased to 7.0% and 7.9%, respectively (Table 8.4 & 8.5). This is intuitive, since the error due to the reconstruction adds up to the discretization error. According to Equation 7.5, the propagated error from the length measurement is directly forwarded as an element of the sum. Assuming the same error for the diameter measurement, the relative error in the flow measurement would result in 21.0% and 23.7% for the erosion and Voronoi method. In fact, the error is even higher because the model does not account for segmentation errors or projection errors of a 3D structures onto a 2D plane. This projection error is strongly dependent on the angle between the vessel segment and focal plane. It can be described by a cosine function $cos(\alpha) = \frac{l_{projection}}{l}$. Small changes in α result in small projection errors and are tolerable. A tilt angle of approx. ± 16 ° would equalize the positive effect of the re-continualization by the proposed methods. In a clinical context a tilt angle of 16 ° is not expected. The depth of field in typical neurovascular surgery is smaller than 2 mm (at a magnification of >7) [209]. Consequentially, any vessel larger than 7 mm would be partially blurry. Nevertheless, requirements on the measurement's workflow can be derived to ensure that the projection error does not equalize the gained accuracy in the improved length measurement.

These propagated error values due to discretization are already too high. For comparison, sonographic contact intraoperative flow meters have an accuracy of $\pm 10\%$ [168]. This emphasizes the need for an improved geodesic length assessment method to enable a reliable optical volume flow measurement. One option is changing the hardware and using a camera with a higher spatial resolution. Unlike the coastline paradox, where the length of a fractal object is prolonged towards infinity with increasing resolution, we expect a convergence of the measured geodesic length towards the true length with increasing resolution [210]. This is due to the decreasing discretization error. It relies on the assumption that a vessel is a non-fractal object. This assumption is most likely valid for vessels (probably not for the capillary system). The upgrade of the recording system is costly and cannot be easily performed on systems already in use and therefore it is not the prioritized solution. Another option is using software-based methods to enhance the length measurement. Re-continualization methods such as spatial interpolation to ensure in the prevalent cases a smooth centerline is the preferred choice since they can be easily installed to all systems. The length measurement of discrete objects has shown to be longer than the continuous ground truth due to the angular characteristic of the pixels as a grid. In some outlier cases the length has been underestimated. Either the reconstruction or the spatial interpolation of the centerline introduces a negative error. We have observed that the reconstruction of the centerline can provoke negative errors due to an erroneous spurs removal at the ends of the centerline, especially in the case of bifurcation. Whether the spatial interpolation introduces a negative error is checked by applying it to the discrete ground truth centerline (no reconstruction involved) and comparing the resulting length with the continuous length of the centerline. This showed a mean relative error of $< 0.05\,\%$ for the Bézier curves method, which emphasizes its suitability to properly re-continualization a discrete centerline without too strong spatial smoothing. The polynomial approximation showed a mean relative error of approx. $-2\,\%$. This implies a strong spatial smoothing caused by the limited capability of polynomial functions to represent different and versatile structures. Here the order of the polynomial has a large influence since a small order could provoke a strong smoothing and a large order could introduce spikes and therefore lengthen the centerline. Taking into account that a centerline consists of hundreds of elements a global fitting approach (as the polynomial fit) is prone to extensive smoothing effects, compared to a local piecewise fitting function. Therefore, the proposed method using Bézier curves is more robust.

All proposed centerline extraction methods and their combination with spatial interpolation methods show a significant decrease in the relative error in length measurement. This verifies the first hypothesis and validates the proposed approach. Especially the centerline extraction by erosion in combination with the Bézier curve interpolation shows a significant decrease in error from 7.0 % to 2.7 % (compared with the discrete centerline obtained by reconstruction). The run time of approx. 13 seconds per image on average is acceptable since the operation is not required to be in real time. Furthermore, the code runs on MATLAB and not on an optimized processor and solver, so a further decrease in run time is possible. The run time was tracked to evaluate the methods relatively to each other and not in an absolute manner.

The evaluation of the recorded images of silicone tubes comply with the *in silico* simulation and show similar errors with their respective counterpart (straight lines). The laboratory experiments are prone to several sources of errors. First, the positioning accuracy of the sample in the field of view contains errors. The translational displacement was avoided by fixing the imaging system and the rotational plate. The rotational positioning was set by a rotational plate with an accuracy of ±0.5°. A value of this magnitude induces a minor error in the length measurement even at the most sensitive angle changes (see Figure 8.11). Second, the manual measurement of the ground truth length with a caliper introduces errors. The caliper has an indication accuracy of 10 µm which introduces a small error. The measured segments yield lengths from 12 - 75 mm and are much larger than this error. Furthermore, the repeated measurement with the caliper showed a good reproducibility with a deviation of 0.1 % or less. In conclusion, all errors are small and do not have a large impact on the measurement and therefore the results of the laboratory experiments are assumed trustworthy. The results of this investigation also verifies the second hypothesis. The rectangular grid of the detection array leads to an angle dependent error which is reduced by re-continualization. The angular measurements (Table 8.8 & 8.9 and Figure 8.11) show a clear dependency of the error in length in case of a discrete measurement. The measurements also show that the re-continualization by spatial interpolation significantly reduces this error in nearly all cases. The reduction is more significant in the cases of angles which do not fit the grid (15 °, 30 °, 60 ° & 75 °). This implies that the dependency of the error to the angle is reduced. It is not possible to recreate all *in silico* categories with silicone tubes since the geometry of the tubes changes when they are bent. 3D printed structures could overcome this drawback but an investigation of the tolerances of the printers is required. The results of this research are of great importance for applications where small changes in the measurement have a significant impact on the outcome. Especially in medicine and life science errors can have fatal consequences for the patient. Facilitating a non-contact flow measurement with an acceptable accuracy would fit into the surgical workflow. It would also increase the quality of the procedure and could decrease the recurrence rate. Further, the results are also applicable in all fields where geodesic distances of discretized images are requested with a high precision.

8.4.1.2 Diameter

This section focuses on the discussion of the measurement of the diameter. Unlike in the measurement of the geodesic length the diameters' ground truth is not continuous. So, the ground truth diameter is always a natural number ($d \in \mathbb{N}^{*2}$) and the measured diameter as well. Hence, the absolute difference is always a natural number. The influence of this quantization is especially large in small diameter values since the relative error difference will be very high. Therefore, the maximum of the relative errors reaches up to 50 % (e.g. ground truth diameter of 2 pixels and measured diameter of 3 pixels). This explains the deviations of the results from the *in silico* model and laboratory experiment. The *in silico* model included images of vessels with narrowing diameters (similar to a stenosis) which could not be reproduced in the laboratory experiment. The tubes were of uniform shape and diameter. Nonetheless, the magnitude is the same. Important is as well that in contrast to the length measurement no dependency on the angle was proven. With a mean relative error of 3.7 % and 3.1 % for the *in silico* model and laboratory experiment respectively it is acceptable

---

[2] $\mathbb{N}^*$ According to the DIN-Norm 5473:1992-07

(see Section 7.1). Since the presented method does not include any re-continualization, improvement is possible (e.g. as presented by [211–213]). Please note that the segmentation error is excluded and would influence the diameter measurement directly.

8.4.2 Measurement of the bolus transit time

Obtaining the ground truth transit time of two corresponding IDCs is a challenge. A method was proposed and implemented simulating adjustable IDCs with a known ground truth of the transit time in a statistical relevant quantity. Thereby, a high degree of freedom in the variation of the signal's morphology, sampling rate, sample positioning, transit time and noise level is given. This allows a versatile use of the *in silico* model to mimic different signals obtained from different organs. As an alternative to COMSOL Multiphysics, other numerical simulation tools can be used as well to simulate the presented IDCs. Without depending on advanced simulation software, analytic methods such as the Taylor-Aris approach exist and need be adapted to the setup by introducing additional perturbation terms as presented by Alizadeh et al. [214, 215].

8.4.2.1 Data set generation

The presented IDCs were generated using an in-silico model. The model incorporated the fluid dynamic properties and chemical interactions, such as diffusion, of the used indicator. The model should be transferable to mimic different non-diffusible indicator types. Note, diffusion occurs in non-diffusible indicators within the solvent media but not with the surrounding tissue (e.g. a thermal indicator diffuses into the surrounding tissue and is therefore a diffusible indicator, ICG remains intravascularly, has nearly no diffusion into surrounding tissue and is therefore a non-diffusible indicator). The chosen diffusion coefficient for ICG D_{ICG} (see Appendix A.3) is set equal to the diffusion coefficient of the protein. Since ICG binds to the proteins and is at the initial state of the study in equilibrium, it is assumed that it will have the same diffusion coefficient. The proposed *in silico* model uses a laminar flow of a homogeneous liquid in a rigid vessel. In contrast, blood is a cell suspension containing the liquid plasma and the solid cells. Since the indicator of interest (ICG) binds primarily to the proteins in the blood plasma, it will be affected by a heterogeneous distribution of cells [71]. To reduce the computational effort in this model, this heterogeneous distribution was not taken into account and a simplified homogeneous distribution assumed. The assumption of a rigid vessel wall does not have a significant influence on the model since a continuous flow, thus pressure, was applied. Assuming a continuous volume flow is motivated by a significantly decreasing PI from measurements taken proximal and distal on certain cerebral vessels [44, 45]. This significant decrease does not imply the disappearance of the pulsatility and therefore limits the results of this study to distal cerebral arteries. The geometry of the setup represents the *in vitro* flow phantom build in our facility (details to this phantom are given in the Appendix A.6). The generated IDCs match well the measured IDC in the phantom (Pearson's correlation coefficient of 0.98-0.99, Appendix A.6). This proves its validity and also validates the second assumption given in Section 8.1.2. An extensive comparison with *in vivo* data is not possible due to the lack of data. Nonetheless, the presented case shows a high accordance with the simulated data (Pearson's correlation coefficient of 0.93). Both, *in vivo* and *in vitro* comparisons prove the similarity of the IDCs: see Section 8.3.2.1 and Section A.6 in the Appendix. The *in silico* setup represents the vessel with an open end and no recurrence of the bolus, thus limiting the reliability of data points on the curve's descending side where recirculation does not appear (in Figure 8.12A, no bump is present after the peak as in Figure 8.12B). Nevertheless, in most methods measuring the transit time $t_{transit}$, the dilution curve is cut off after its concentration has decreased to 30 % - 50 % of the respective peak, which excludes most influences by the recirculation [180, 186, 216]. Further on, in the measurement of blood volume flow in cerebrovascular bypass surgery the distance of both measurement location is very short ($< 2\,\mathrm{cm}$). Thus, the influence by recirculation will be nearly identical in both signals, equally influencing the two mathematical fits and thereby not influencing the transit time measurement. Modeling the injection as a rectangular input function assumes an ideal abrupt injection. In clinical practice the anesthetist will inject the indicator and an inter- and intra-individual variability will occur. Choosing the rectangular input function facilitates and standardizes the study design to ensure a comparability of the results. WGN is applied to the data set's two corresponding IDCs to represent sources of noise such as Johnson–Nyquist noise. However, WGN only approximates limited sources of noise and does not cover all sources of noise and/or artifacts observed in the *in vivo* measurements. Adding other noise sources such as shot noise and artifacts such as the spatial exclusion of the dye by blood cells requires a more profound investigation on *in vivo* data. Nonetheless, the robustness of the proposed algorithms can be evaluated using WGN. The example in Figure 8.12B shows distinctive noise/artifacts in the area of the peak concentration which seems to not be reproduced by WGN. Since the presented *in vivo* signal is extracted as the averaged signal within the area of 10x10 pixel, uncorrelated noise, such as WGN, is reduced. Correlated noise and artifacts will remain present in the signal. The ripples on the signal shown in Figure 8.12B are at a frequency of approx. 1 Hz and might be the patient's pulse which is a correlated noise source. This cannot be verified since no vital monitoring data is available. Nevertheless, the simulated curves and their power spectral density (Figure 8.13) show a high accordance with the clinically obtained *in vivo* data from intraoperative FA measurements. Performing an objective comparison is possible but is not expedient since the morphology of the available *in vivo* data is limited. The transfer function from the dye's concentration to the optically measured fluorescence is not known and has an influence on the optically measured signal since it affects the signals morphology. Generally, the focus of this investigation was the measurement of the statistical error and the effect of the transfer function was assumed as negligible. The presence of a transfer function would induce a systematic error to the measurement which can be separated from this investigation but is in focus in Chapter 9. Therefore, these data sets are suitable for the evaluation of methods measuring the transit time of optically measured IDCs.

8.4.2.2 Evaluation of the error in the transit time measurement

The performance of different methods measuring the transit time with varying complexity was evaluated. Thereby, the transit time was calculated according to the systemic mean transit time theorem for single input and single output systems as defined by Perl et al. [16]. This theorem assumes that the shape of the curve does not change significantly and is valid in this investigation due to the short distance between the measurement sites (Appendix A.5). The first hypothesis that using a mathematical model decreases the error in measuring the transit time can be verified with some limitations. Obviously, not all combinations of mathematical models and features are suitable for the enhanced measurement of the transit time of an indicator bolus. Especially the mono-exponential function showed a bad performance, probably due to a complex feature-based metric measuring the delay. The parabola model showed better results than the mono-exponential model but inferior to the gamma variate and the LDRW model. The gamma variate and the LDRW model performed equally well. Both are suitable to verify the hypothesis especially using the cross-correlation which takes all data points into account and not solely the peak to peak distance. Verification of the second hypothesis that a sub-frame rate accuracy can be accomplished by using a suitable configuration of mathematical function and pre-processing in combination with a feature, is also limited. For a sampling frequency of 25 Hz the configuration: gamma variate, cross-correlation of the first derivative using an up-sampling factor of 100 and cut method 1 performed best. It showed a mean value for ε_{frame} of less than 0.85 for all SNR (8 dB – 20 dB) and cut levels (see Figure 8.15B). The Figures 8.18A & B also underline its robustness. In case of a $f_{sampling} = 25\,\mathrm{Hz}$, a sub-frame rate accuracy was accomplished in all cases as soon as the noise level was above a $SNR \geq 14\,\mathrm{dB}$. Accomplishing a sub-frame rate accuracy with a higher sampling frequency is harder since the absolute time tolerance decreases. The appearance of a lower performance in case of a higher sampling rate is misleading. The reduction of the absolute time error $\varepsilon(SNR)$ has a mean value of approx. 26 % lower at 60 Hz than in 25 Hz (see Table 8.12). Assuming no noise the accuracy should increase by the ratio of the sampling rates, here $1 - \frac{25}{60} = 60.3\,\%$. This shows that noise has a clear influence on the sampling rate dependent decrease of $\varepsilon_{t_{transit}}$. Nevertheless, the influence of a decrease of SNR with increasing sampling rate (so decreasing integration time) is not included in this evaluation and therefore the reduction of the error by 26 % is an optimistic calculation. The evaluation of more and different mathematical models, such as the log-normal and lagged-normal model, is possible and could reveal more suitable models [217].

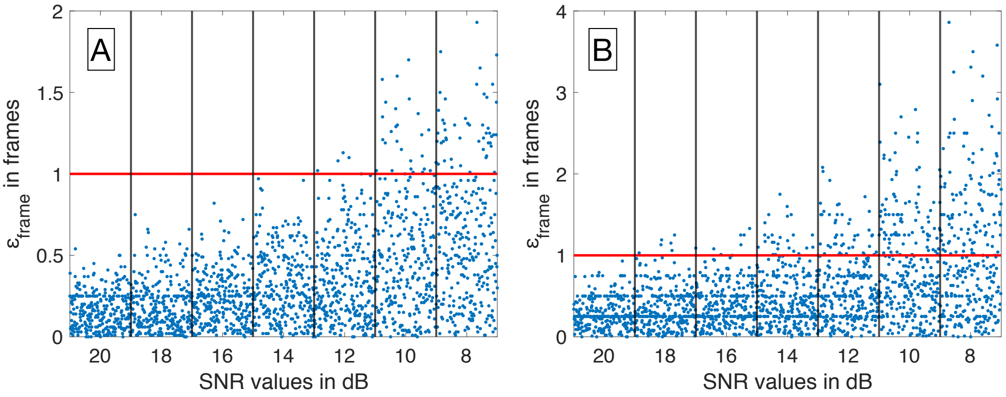

Figure 8.18: A: The relative error of all data sets ($f_{sampling} = 25\,\mathrm{Hz}$) is shown in relation to the SNR. The red line indicates the relative error of one frame. The blue dots show the single results obtained by the fitting the LDRW model to the data cut at $40\,\%$ by the cut method 1 and using its first derivative as input for the cross-correlation. The distribution of the dots within a column is irrelevant. All data sets had a relative error of less than one frame for SNR larger than $12\,\mathrm{dB}$. **B:** The relative error of all data sets ($f_{sampling} = 60\,\mathrm{Hz}$) is shown in relation to the SNR. The red line indicates the relative error of one frame. The blue dots show the single results obtained by the fitting the LDRW model to the data cut at $40\,\%$ by the cut method 1 and using its first derivative as input for the cross-correlation. The distribution of the dots within a column is irrelevant. All data sets had a relative error of less than one frame for SNR larger than $18\,\mathrm{dB}$. Both images are adapted from [136] published under the Creative Commons Attribution 4.0 License.

Table 8.12: Mean absolute error $\varepsilon_{t_{\mathrm{transit}}}$ and its standard deviation for two sampling frequencies f_{sample} in dependency of the SNR. The ground truth transit time was evenly distributed ranging from $40\,\mathrm{ms}$ to $160\,\mathrm{ms}$ for $f_{\mathrm{sample}} = 25\,\mathrm{Hz}$ and from $33\,\mathrm{ms}$ to $133\,\mathrm{ms}$ for $f_{\mathrm{sample}} = 60\,\mathrm{Hz}$.

SNR	$25\,\mathrm{Hz}$	$60\,\mathrm{Hz}$
20 dB	10.0 ms ± 7.1 ms	7.2 ms ± 5.3 ms
18 dB	12.1 ms ± 7.9 ms	8.3 ms ± 6.4 ms
16 dB	13.9 ms ± 9.5 ms	10.7 ms ± 8.8 ms
14 dB	16.8 ms ± 12.1 ms	11.4 ms ± 9.4 ms
12 dB	19.9 ms ± 15.1 ms	15.3 ms ± 12.0 ms
10 dB	23.9 ms ± 18.5 ms	18.5 ms ± 13.7 ms
8 dB	31.3 ms ± 22.9 ms	23.5 ms ± 16.9 ms

8.5 Outlook

8.5.1 Measurement of geometrical parameters

The proposed model depicts a broad range of vessel geometries. Its validation requires a sufficient *in vivo* data set. Its validation on different images could help to clarify which mathematical functions are the most suitable for length analysis. This also leads into an application tailored model (e.g. retinal vessel have different geometries than cerebral vessels). So far, this model does not account for the projection errors of a 3D object onto a 2D plane. Adding a dimension to the mathematical functions is possible. This would not only enable the inclusion of projection errors into the investigation, it would also enable 3D length analysis (for example of 3D - computed tomography (CT) or magnetic resonance imaging (MRI) data sets).

The evaluation of the performance of the proposed length measurement techniques could be extended by a systemic and quantitative displacement analysis. In this work, the focus was on the length and diameter measurement.

The proposed diameter measurement was taken as sufficient. Other methods can be considered and an investigation of their performance performed.

The developed model can be used to determine the performance of hardware-based methods to lower the discretization error. Changing the resolution in the model is easy and a follow up study can be performed to assess the benefits of increasing the resolution. Requirements on the resolution could be derived from this assessment and the required applicative specifications.

8.5.2 Measurement of the bolus transit time

The proposed hypotheses are verified with some limitations regarding the methods used and present noise level in the signal. The investigated mathematical models and features represent a fraction of the possible methods. Therefore, more mathematical models and features can be implemented and tested on the generated data set. The investigated noise levels are chosen reasonably according to our experience but could be expanded to a larger range and finer gradation. A reduction of the noise has a large impact on the accuracy in measuring the transit time, so different noise reduction techniques should be considered and evaluated. Nevertheless, care should be taken since the cross-correlation is depending on the data sets' morphology and obviously the morphology is affected by temporal filtering and thereby might affect clinical decision making [218]. The absolute error $\varepsilon_{t_{transit}}$ in the transit time measurement decreased with increasing sampling frequency. So, increasing the frame rate increases the accuracy but at some point, the benefit will be eliminated by an increased noise level (noise is mostly coupled reciprocally with the integration time). Therefore, we hypothesize that there is a recording modality and purpose specific optimum of the sampling rate in regards of the error in the transit time measurement. Additionally, it was assumed that the transfer function from the dyes concentration to the optical measurement is negligible. This transfer function should be obtained and added to the error propagation assessment as a source for a systemic error. Finally, the investigation of methods on *in silico* data is linked to assumptions which reduce the complexity of *in vivo* data to a manageable level. Therefore, *in vivo* data should be obtained to check the robustness of these methods in real life scenarios.

Chapter 9

Systemic error

In Section 7.2 the presence of a systemic error in the optical measurement of blood volume flow was suspected and its presence theoretically derived. In the following chapter, methods are proposed to quantitatively assess this systemic error in dependency of the volume flow and diameter.

9.1 Introduction

As derived in Section 7.2 the systemic error ε_{sys} is described by

$$\varepsilon_{sys} = \int_A v_{rel}(r,\phi) \cdot w_{opt}(r,\phi) \cdot \frac{1}{A}\, dA \tag{9.1}$$

with A as the cross section of the vessel's inner lumen, r as radius, ϕ as the angle, v_{rel} as the normalized flow velocity and w_{opt} as the optical weighting function (probability density function).

It was assumed that the flow in the vessel is laminar, which is very probable in physiological cases and also in many pathological cases (not valid in geometrical irregularities such as in large Aneurysms) [24, 170]. Therefore, v_{rel} can be assumed to be of axisymmetric parabolic shape, thus independent of ϕ, as given in Equation 9.2. Thereby, R is the radius of the inner lumen of the vessel.

$$v_{rel}(r) = 2 \cdot \left(1 - \left(\frac{r}{R}\right)^2\right) \tag{9.2}$$

The optical weighting function $w_{opt}(r,\phi)$ should represent where the spatial origin of the photons reaching the detector was (only photons which were emitted by fluorescence from the dye). To obtain $w_{opt}(r,\phi)$, a Monte-Carlo (MC) model was developed, verified and used. The following general requirements to the model were set:

- It should be of cylindrical shape mimicking a vessel.
- It should have at least two concentric layers. Inner cylinder as blood volume and outer hollow cylinder as vessel wall.
- It should include a homogeneous illumination.

- It should include a detector model.
- Fluorescence events should be incorporated.
- It should be able to track the location of the fluorescence events.

Since fluorescence events should be incorporated, the concentration of the dye needs be known. The propagation of the bolus is dynamic and therefore the dye's concentration is a function of the location r and ϕ, and time t. To obtain the concentration of the dye a fluid flow simulation is performed prior to the optical MC simulation.
The work flow to obtain ε_{sys} is shown in Figure 9.1.

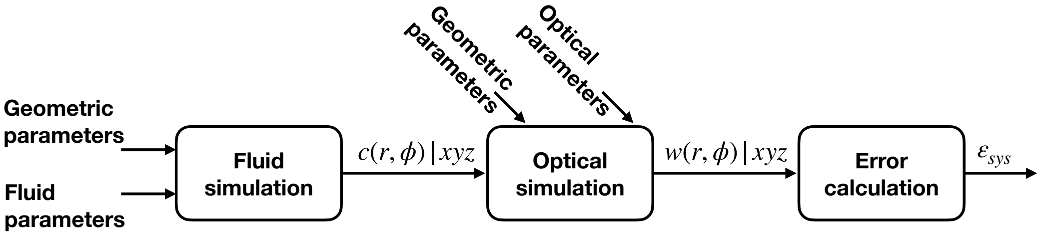

Figure 9.1: The workflow to obtain ε_{sys} started with setting up the geometric parameters, such as diameter and length, of a pipe and fluid parameters, such as viscosity and diffusion coefficient, of the liquid with indocyanine green (ICG) dissolved in it. A fluid simulation using COMOSL Mulitphysics was utilized to obtain the spatio-temporal concentration of indocyanine green (ICG) $c_{ICG}(r,\phi,t)$ within a cross section of the pipe. It was handed over to the optical simulation utilizing the developed Fluorescence-Monte-Carlo-Multi-Cylinder (FMCMC) model. The diameter, and the optical properties of the blood, vessel's wall and indocyanine green (ICG) were used to obtain the spatio-temporal probability density function $w(r,\phi,t)$ of the origin of fluorescent photons hitting a detector. This was finally used to calculate the systemic error $\varepsilon_{sys}(t)$.

As reported by Weichelt et al., the systemic error is expected to be diameter dependent. Moreover, it should be time dependent since the flow profile is a function of the radius and an early appearance of indicator is expected at the area of higher velocities. There is no reason to expect a flow dependency of the systemic error as long as the flow is laminar.
Therefore, two hypotheses were set up:

1. The systemic error ε_{sys} is dependent on the diameter and time point at which it is extracted.
2. The systemic error ε_{sys} is not dependent on the volume flow as long as it is in laminar regime.

9.2 Preparatory work: calculation of the dye's concentration

The overarching goal of this section was to obtain the spatially and temporally resolved concentration of indocyanine green (ICG) for multiple geometries and flow values.
This section includes the methods and results.

9.2.1 Method

A fluid flow simulation was already introduced in Section 8.2.2.1. The calculations were done analogously in COMSOL Multiphysics (version 5.4) using the physics packages: Computational Fluid Dynamics (laminar flow) and Chemical Reaction Engineering (transport of concentrated species and transport of diluted species). In contrast to the method used in Section 8.2.2.1, not the averaged concentration across the cross section of the pipe was extracted but the spatially resolved concentration over the cross section.

Geometry and fluid flow The general design did not change but the diameters were varied from 1 mm to 5 mm. The applied volume flow was varied as shown in the Table 9.1. Those values represent physiological and pathological flow values in human arteries (see Section 2.1.2). The performed investigation included 17 different simulations combining different diameters and flows. An individual time frame was needed for each simulation to ensure a sufficient temporal resolution and time range but limiting the computational time to a manageable amount (see Table 9.1).

Table 9.1: The simulated diameter with the respective applied blood flow values are shown in this table. The requirements on the temporal scope and resolution of each set were different and are given as well.

Diameter in mm	**Flow** in ml/min				**Range of simulation and resolution** in s (start:step size:end)			
1	25	50	65	80	0:0.01:1.8	0:0.01:2	0:0.01:1.5	0:0.01:1.5
2	50	80	120		0:0.01:7	0:0.01:5	0:0.01:4	
3	120	150	180		0:0.02:7	0:0.02:5	0:0.02:4	
4	150	250	350		0:0.1:20	0:0.1:20	0:0.05:20	
5	250	300	350	400	0:0.05:20	0:0.05:20	0:0.05:20	0:0.05:20

The measurement position was defined at 60 cm behind the injection site. This value relied on the mean distance from the heart to the cerebral arteries [195, 219–221]. This distance was not a realistic representation since in clinical routine the injection is intravenously in the periphery. It was assumed that the indicator will be homogenized in the hearts chamber and afterwards ejected into the aorta as a rectangular input function with each heartbeat. Therefore, also a rectangular input function was chosen. Both assumptions facilitate and standardize the study design to ensure the comparability of the results. Furthermore, the chosen distance was larger than the length which is needed to ensure a fully developed parabolic laminar flow profile (see Equation 9.3 according to [24, 222] with Re being the Reynolds number).

$$l_{laminar} = \left[0.619^{1.6} + (0.0567 \cdot Re)^{1.6}\right]^{\frac{1}{1.6}} \cdot 2 \cdot R \tag{9.3}$$

Blood's viscosity The flow media was blood. Its viscosity was described by the Power-Law model as

$$\eta = m \cdot \dot{\gamma}^{n-1} \tag{9.4}$$

with η being the apparent viscosity, $\dot{\gamma}$ the shear rate, m and n are the Power-Law constants. The constants used in this simulation were $m = 14.67\,\mathrm{mPa} \cdot \mathrm{s}^n$ and $n = 0.7755$. These values were based on the Best Three Variable Model (B3VM) proposed by Walburn et al. for physiological human blood (hematocrit = 45% at 25°C) [223]. It proved to provide the best description of blood rheology in the shear rate range of $\dot{\gamma}$ from $0.031\,\mathrm{s}^{-1}$ to $120\,\mathrm{s}^{-1}$, which is sufficient for all configurations of this analysis [224, 225].

Blood's density The blood's density is not constant. It depends on the hematocrit, protein concentration in the plasma and others [226]. Various studies have confirmed that the density of blood and distilled water are nearly equivalent [227]. A constant blood density of $\rho_{blood} = 1050\,\frac{\mathrm{kg}}{\mathrm{m3}}$ was assumed.

ICG: diffusion coefficient & initial concentration The macroscopic diffusion of ICG in the human body is well studied but no publication exist revealing the microscopic diffusion of ICG in whole blood. Nonetheless, 98% of the ICG is bound to the plasma proteins and lipoproteins [85]. Therefore, the diffusion coefficient of those proteins in whole blood was used as the diffusion coefficient of ICG. The diffusion coefficient was set to $D_{ICG} = 7.6 \cdot 10^{-7}\,\frac{\mathrm{cm}^2}{\mathrm{s}}$ [228, 229]. The initial concentration was set to $c_{init,ICG} = 6.4519\,\frac{\mathrm{mmol}}{\mathrm{m}^3}$ $(= 0.005\,\frac{\mathrm{g}}{\mathrm{l}})$.

9.2.2 Results

The overarching goal was to obtain the spatially and temporally resolved concentration of ICG for multiple vessel geometries and volume flow values. Showing all of them here is not expedient. Two examples are shown in Figure 9.2. All six plots show the relative ICG concentration colorcoded as indicated by the colorbars in dependency of the spatial (radial) location. Note, each plot has its own colorbar to enhance the contrast.

Finally, the obtained concentration distribution of ICG for each diameter and volume flow value was used as input for the simulation of the photon's propagation in the following section.

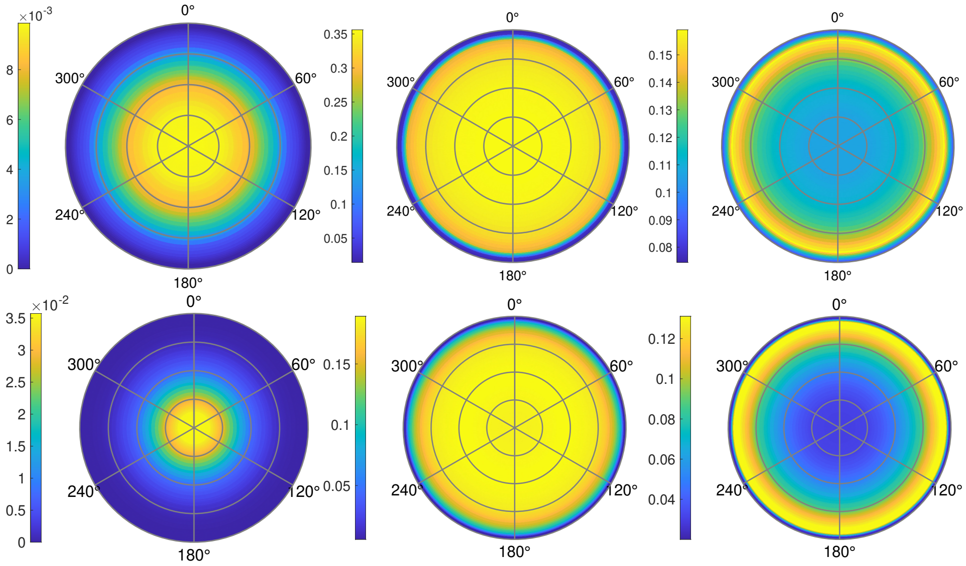

Figure 9.2: In all six plot the local concentration of ICG relative to the initial concentration is shown. Note that the colorbar changes from plot to plot. Since the geometry was axisymmetric and no gravitational forces were included, the concentration is axisymmetric as well. The top row was computed using a diameter of $3\,\mathrm{mm}$ and volume flow of $120\,\frac{\mathrm{ml}}{\mathrm{min}}$; the bottom row using a diameter of $5\,\mathrm{mm}$ and volume flow of $400\,\frac{\mathrm{ml}}{\mathrm{min}}$. The plots to the left refer to the inflow phase and hence the bolus' first arrival. The plots to the right refer to the outflow phase where the ICG is mostly concentrated at the vessel's wall. The middle plots are taken temporally from in between the other two and represent the phase where the ICG concentration is close to being homogeneous within the vessel. The gray circles in the plot indicate 0.25, 0.5, and 0.75 of the radius. It is clearly visible that the ICG first arrives in the most inner circles and is concentrated at the most outer circle during washout.

9.3 Methods

The calculations done in Section 9.2 to determine the dye's concentration via a fluid flow simulation were used as input for the following method. The methods used to obtain $w_{opt}(r, \phi)$ by an optical simulation are in focus in this section. All methods were implemented in MathWorks MATLAB R2019b.

9.3.1 Fluorescence Monte-Carlo-Multi-Cylinder simulation

The Fluorescence-Monte-Carlo-Multi-Cylinder (FMCMC) simulation was based on the general MC approach of Wang et al. to simulate a photon's path in turbid media [156]. Their approach consisted of a multi-layer geometry and a focused illumination beam. Multiple improvements needed to be done (those are only the most relevant changes, minor changes will not be listed here):

- Convert the multi-layer to a multi-cylinder geometry to allow the modeling of a vessel.

- Implement a spatially homogeneous illumination to mimic the illumination by a microscope.
- Implement a simplified detector system.
- Incorporate fluorescence events.
- Incorporate the tracking of the location of fluorescence events.

Details on the points of improvement are given in the following paragraphs.

Converting the multi-layer geometry to a multi-cylinder geometry Figure 9.3 illustrates the change in geometry. The proposed conversion from a multi-layer to a multi-cylinder geometry affected the calculation of a photon's behavior at the interface of two media. The calculation of the step size, absorption, scattering were not be affected by the conversion. In contrast to the Monte-Carlo-Multi-Layer (MCML) geometry which is only finite in the z dimension, the Monte-Carlo-Multi-Cylinder (MCMC) geometry had infinite long and concentric cylinders in the y dimension. The origin of the Cartesian coordinate system was placed in contrast to the MCML geometry not on the surface of the slab but in the symmetry axis of the concentric cylinder. The boundaries of the concentric cylinders were defined by a mathematical function for circles centered on the symmetry axis (see Equation 9.5). Thereby, its location on this axis in y-direction was irrelevant and by definition $y \overset{!}{=} 0$.

$$r = \sqrt{x^2 + z^2} \tag{9.5}$$

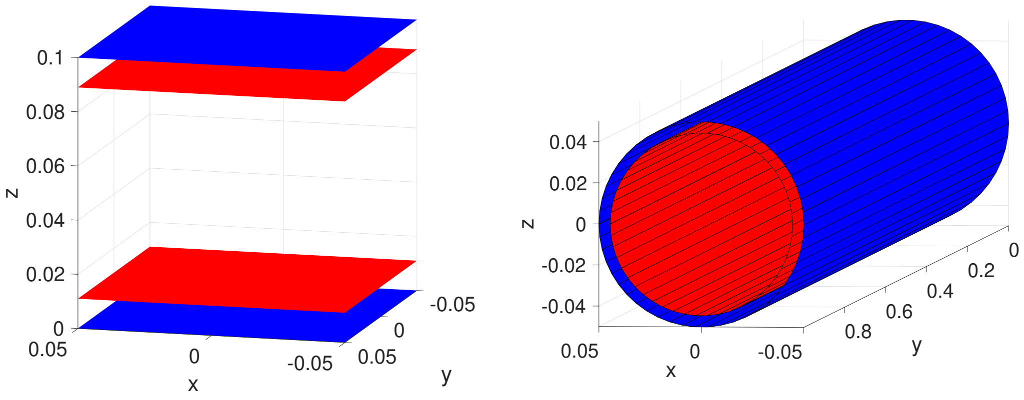

Figure 9.3: For both plots: in red the borders of the blood volume and in blue the borders of the vessel wall are shown. **Left**: the MCML geometry is shown which is finite in z and infinite in the xy-plane. **Right**: the MCMC geometry is shown which is a better representation of a vessel. It was composed of two concentrically aligned cylinders with infinite length in y.

Generally, the geometry was composed of two main layers: the blood volume in the middle surrounded by the vessel wall. The blood volume contained a heterogeneous concentration of the dye (ICG), which is axisymmetric. So, the blood volume was again composed of many layers with identical properties of the blood but different concentrations of ICG and hence different fluorescence properties. It was assumed that the properties of blood are not affected by the concentration of ICG, this is valid for small concentrations of ICG (which is the case in this investigation) [71]. The number of layers within the blood volume was depending on the diameter of the geometry and was 19, 30, 41, 56, 67 layers for the diameters 1mm, 2mm, 3mm, 4mm, 5 mm, respectively. The different and increasing number of layers were a result of the meshing process in the fluid flow simulation (see Section 8.2.2.1). The thickness of the layers was varying and therefore the thickness was also given as input into the FMCMC model.

Detecting boundary hits in the MCMC geometry Detecting a boundary hit of a photon upon its propagation path was different in the MCMC geometry compared to the MCML geometry. A photon's step was defined by a start S_{photon} and endpoint E_{photon}. In the MCML a simple check of the z coordinate was sufficient to asses whether a boundary was crossed. In the MCMC, simply calculating the r coordinate of S_{photon} and E_{photon} and checking it does not work out as illustrated in Figure 9.4. Determining whether a boundary hit was present or not was done in the orthogonal projection into the xz-plane since the y-coordinate was irrelevant for this. So, this investigation was performed in the $\mathbb{R}^2$. The extraction of all boundary hit points was a 2-dimensional analytic problem of extracting the intersection of a line (limited by S_{photon} and E_{photon}) and a circle. The line was defined as given by Equation

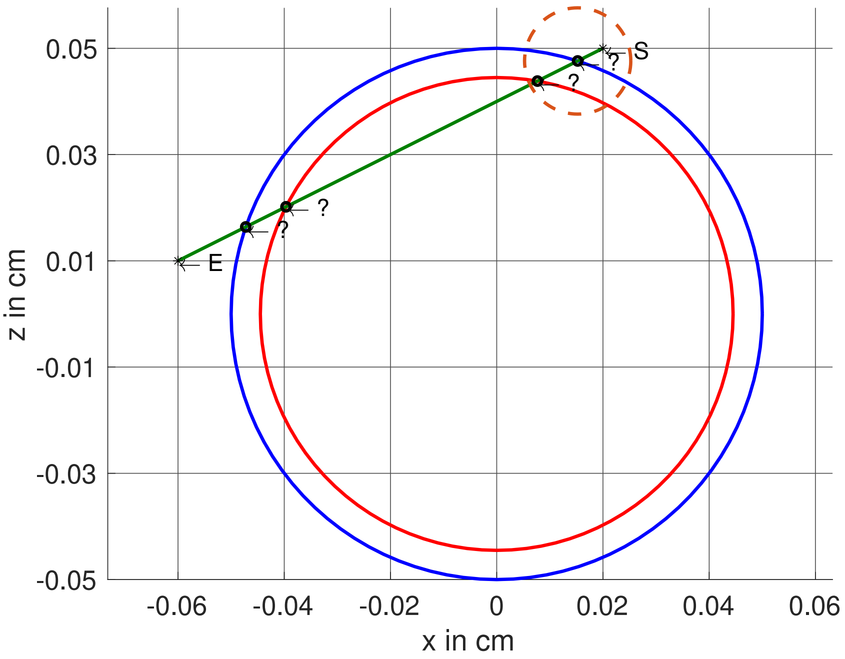

Figure 9.4: This is a projection of the MCMC geometry into the xz-plane. The boundary of the blood volume and vessel wall are shown in red and blue, respectively. S and E mark the start and end position of the photon's step. Checking the radius at S and E does not provide sufficient information on whether a boundary was hit or not. By using linear algebra, multiple potential boundary hit points were determined as indicated by the question marks. The hit point which was used for the boundary interaction is the one closest to S (indicated by the dotted circle).

9.6 (deriving m and n from S_{photon} and E_{photon} was trivial and will not be specified here).

$$z = m \cdot x + n \tag{9.6}$$

The two possible x-coordinate were determined by setting Equation 9.5 and 9.6 equal resulting in

$$x_{hit_1,hit_2} = \frac{-m \cdot n \pm \sqrt{(m^2+1) \cdot r^2 - c2}}{m^2+1}. \tag{9.7}$$

The z coordinate was determined by inserting x_{hit_1,hit_2} in one of the used equations. These boundary hit points were named H_{photon}. The H_{photon} which was closest to the S_{photon} was extracted since the photon will interact there first and probably change direction. All other hit points were ignored. Afterwards, H_{photon} should be in between S_{photon} and E_{photon}. If not, it was ignored as well. Finally, the y-coordinate was again added to the remaining hit point. In the rare case that E_{photon} was exactly on the boundary of the circle, then the step size needed to be shortened by $1 \cdot 10^{-5}$ cm. This also was true when the distance of E_{photon} to the boundary of the circle was smaller than the numerical accuracy of MATLAB.

Interaction at boundary hit points Once a photon hits a boundary it will interact. It is either reflected or transmitted. This decision was performed as introduced in Section 5.1.5 and 5.2.4 using the angle of incidence and refraction. The angle of incidence was calculated using the directional information of the photon (μ_{photon}) and the normal to the circle. The angle of refraction was calculated according to Snell's Law (Equation 5.12). Once the decision was made, the new E_{photon} was calculated (see Section 5.1.5 & 5.2.4), H_{photon} will replace S_{photon} and the step size was updated according to Equation 5.2. Figure 9.5 illustrates the case of transmission and refraction or reflection. Please note, whenever S_{photon} was updated, a new iteration starts, so multiple hits were possible within one step size sz.

Homogeneous illumination The initialization of the photons at the surface of the object is interpreted as the illumination setting. The Dirac-beam illumination of the MCML can be turned into a homogeneous one, by spatial superposition of the results. In the MCMC this was not possible since the geometry was a cylinder. Therefore, the initialization of the photons needed to be adapted to mimic a homogeneous illumination. Idealized parallel illumination was assumed (the angular deviation of the rays in a clinical setting less than 1°at the minimal working distance of 200 mm and the maximum vessel size 5 mm and therefore this assumption valid [230]). So, the initial direction $(\mu_x, \mu_y, \mu_z) = (0, 0, -1)$ of the photons was identical. The starting coordinates of the photons was $(x, y, z) = (x, 0, \sqrt{r^2 - x^2})$ with $x \in [-r, r]$. The location of the photon is y is not as important and hence a homogeneous line illumination was sufficient to obtain the relevant parameters. To ensure a homogeneous illumination, x was randomly generated using the random number $\xi \in [0, 1]$ as shown in the following equation.

$$x = (2 \cdot \xi - 1) \cdot r \tag{9.8}$$

The initialized photons will face different angles of incidents due to the curved surface of the cylinder. Hence, it needed to be determined whether a photon was transmitted and refracted or reflected at the very first step before entering the geometry.

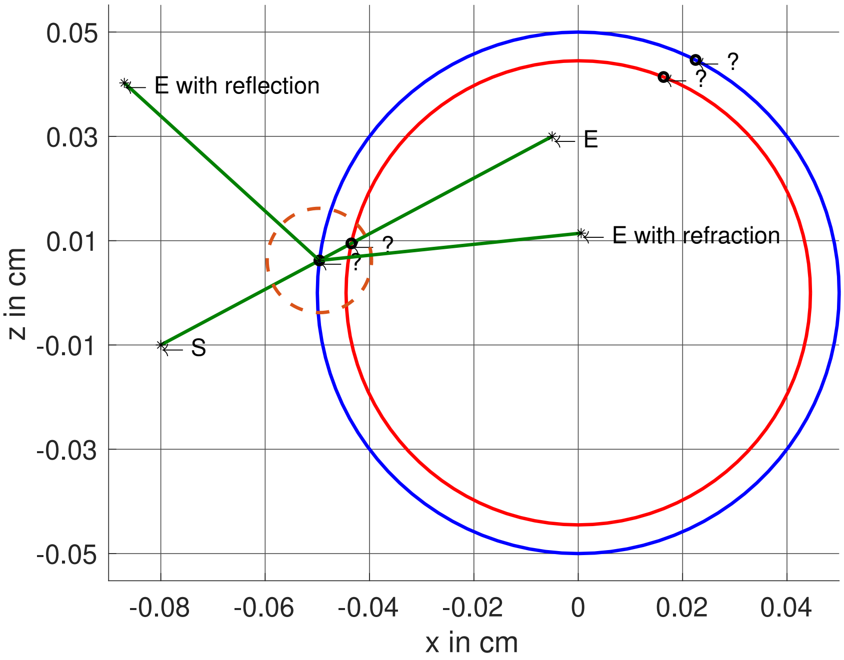

Figure 9.5: The MCMC geometry was projected into the xz-plane. The photon faced an interaction with a boundary at the middle of the dotted circle. It was either reflected, or transmitted and refracted. Depending on the decision a new E_{photon} was determined. In the shown case another boundary hit will be present if transmitted and refracted.

Simplified detector The MCML model represents the detector as an infinite large detector in the xy-plane with infinite sensitivity. Since the implementation of a camera model with optical components is very extensive and would increase the computational time, a simplified detector model was implemented for the MCMC model. Thereby, a finite large detector ($1\,\mathrm{cm}^2$) was tangentially centered over the vessel in a distance of 1 cm. Whenever a photon exited the vessel, it needed to hit this detector and its exiting point from the vessel needed to be located in the upper half of the cylinder ($z > 0$). Figure 9.6 illustrates the setting for a vessel with a diameter of 5 mm.

Incorporating fluorescence Multiple approaches were published proposing methods to handle fluorescence events in MC models [157, 231–233]. For this work, the efficient and accurate determination of the location of fluorescence was important. Therefore, most approaches cannot be used. The method proposed by Welch et al. was the most appropriate [157].

The implemented method included two separate propagation regimes. The propagation of excitation photons was calculated using the binary propagation model (see Section 5.1). As soon as this photon was absorbed, a fluorescent photon package was launched at this location and its propagation will be calculated using the weighted propagation model (see Section 5.2). Figure 9.7 visualizes the transition from one regime to the other. The communication be-

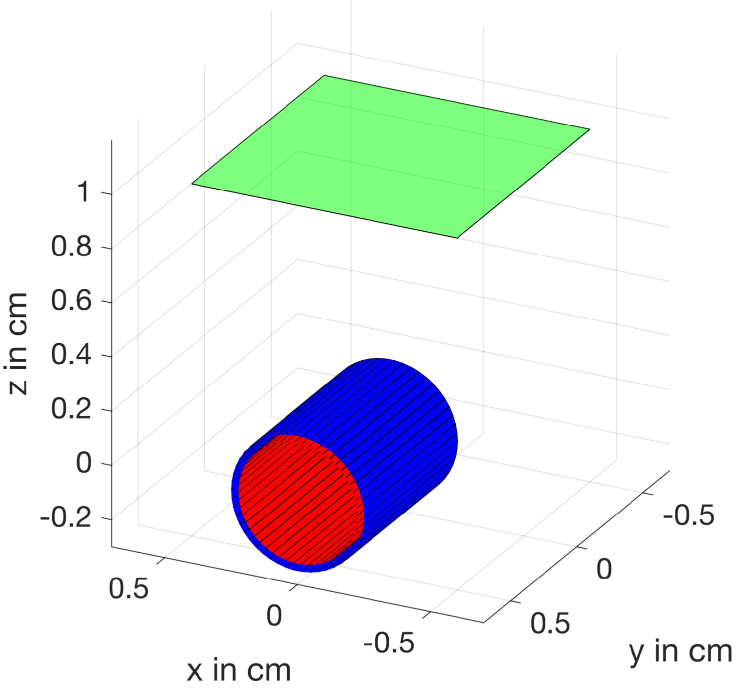

Figure 9.6: The green rectangle is the simplified detector model. It was positioned above the multi cylinder geometry in a distance of 1 cm.

tween both was bidirectional and both were initialized with the same geometry and optical properties.

Two initial propagation properties of the fluorescent photon package needed to be determined: initial propagation direction and the weight of the photon package. Fluorescence was interpreted similar to an isotropic scattering and hence the initial propagation direction of the fluorescent photon package was random. The weight was depending on the absorption coefficient of the non-dye components and the absorption coefficient of the dye and its quantum yield. It was calculated as shown in Equation 9.9 (with $\mu_{A,ICG}$ as the absorption coefficient of the ICG, $\mu_{A,non-ICG}$ as the sum of all absorption coefficient else than ICG and QY as the quantum yield of ICG - all values were determined according to the regarded wavelength of 830 nm. The background of the formula was as following. A photon needed to be absorbed by the fluorophore and not by the other components, hence the ratio of both absorption coefficients was calculated. Then, a factor (QY) needed to be multiplied to account for the quantum yield of the fluorophore.

$$W_{fl} = \frac{\mu_{A,ICG}}{\mu_{A,non-ICG} + \mu_{A,ICG}} \cdot QY \tag{9.9}$$

The absorption coefficient of ICG was dependent on its concentration and was calculated according to Yuan et al. as shown in Equation 9.10 [102]. This linear relationship of the absorption coefficient is only valid for $c_{mol,ICG} \in [0, 0.6\,\mu\text{M}]$ with $c_{mol,ICG}$ as the molar concentration of ICG. For higher concentrations a non-linear relationship is present [80]. The molar concentration is derived form the concentration c_{ICG} in $\frac{\text{g}}{\text{l}}$ and the molar mass M_{ICG} of

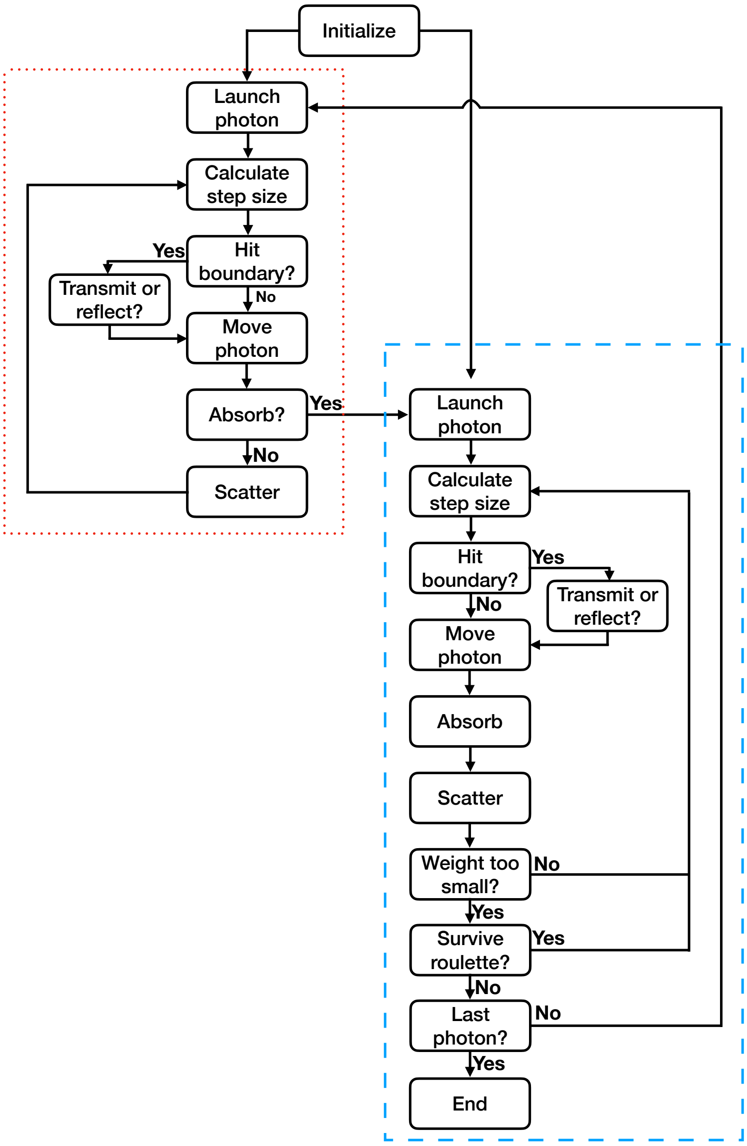

Figure 9.7: In the red dotted box the binary propagation of the excitation photons is visualized. In the blue dashed box the weighted propagation of the fluorescent photon packages is visualized. Both were initialized with the same parameters and properties. Whenever an excitation photon was absorbed, an isotropic scattered photon package was launched with the weight according to Equation 9.9. Whenever this package was terminated, a new excitation photon was launched. This loop was performed until the desired number of excitation photons were launched.

ICG (see Section 3.2) by Equation 9.11. The molar mass of ICG M_{ICG} is a constant and c_{ICG} was computed by the fluid flow simulation presented in Section 9.2. All concentrations in this work were in the range of $[0, 0.6\,\mu\mathrm{M}]$ and thus a linear relationship was valid.

$$\mu_{A,ICG} = 3.43 \cdot 10^5 \cdot c_{mol,ICG} \frac{1}{\mathrm{cm} \cdot \mathrm{M}} \tag{9.10}$$

$$c_{mol,ICG} = c_{ICG}/M_{ICG} \tag{9.11}$$

ICG has a nonlinear fluorescence quantum yield versus its concentration [71]. Nonetheless, for low concentrations, its convergence towards a constant is proven [234]. For the concentrations used in this work, a constant quantum yield was assumed. The overarching goal of obtaining the spatial probability density of a photons fluorescence event location obviously included the normalization of the obtained weights. Hence, the effect of the quantum yield was negligible [157]. Therefore, and for the sake of computational time, the quantum yield was set to 1.

All needed properties of the photon package were computed and it was launched at its position. The position of this fluorescence event was temporary stored and a binary flag $F_{fluorescence}$ was set to true, this indicates that it was a fluorescent photon. It was propagated as presented in Section 5.2.

Logging grid for the results A photon needed to fulfill three requirements to be registered in a logging grid:

1. It must have faced a fluorescence event ($F_{fluorescence} = true$).
2. It must hit the detector.
3. It must have left the vessel from its upper half (H_{photon} has positive z).

In the case a photon fulfilled the three requirements above, its weight was added into the grid at the coordinates where the photon had faced a fluorescence event. Logging those photon weight's into a Cartesian grid (x, y, z) was problematic since the geometry was cylindrical and a voxel could contain a boundary and thereby two different layers. Therefore, cylindrical coordinates (r, ϕ, y) were used. For the determination of the systemic error the y coordinate was not considered and thus the logging was projected into the $r\phi$-plane. After launching all photons, the grid contained the accumulated weight of all fluorescent photons that hit the detector. Please note: the location of the fluorescence event was logged and not the location where the detector was hit. The grid had 100 bins in r and 500 bins in ϕ (and a single y bin). The relative flow profile $v_{rel}(r)$ (see Section 7.2) was axisymmetric and hence independent of ϕ. Therefore, to determine the systemic error, the ϕ coordinate was not of interest and the photons' weight that hit the detector was logged as $w_{FMCMC}(r)$. Finally, the accumulated weight in each bin was normalized, first to the total amount of accumulated weights in all bins (Equation 9.12) and second to the ratio of the bin's area to the total area (Equation 9.13). The first normalization step was needed since the probability of a fluorescent photon's origin was of interest. The second normalization step was needed to account for the variable bin size in a polar coordinate system.

$$w_{bin}(r_i) = \frac{w_{FMCMC}(r_i)}{\sum_{i=1}^{n} w_{FMCMC}(r_i)} \tag{9.12}$$

$$w(r_i) = \frac{w_{bin}(r_i)}{\sum_{i=1}^{n} w_{bin}(r_i) \cdot \frac{A(r_i)}{\sum_{i=1}^{n} A(r_i)}} \tag{9.13}$$

9.3.1.1 Validation of the FMCMC model

The developed FMCMC model was based on the method proposed by Welch et al. [157]. This model is often used and validated. The in-house implementation needed a validation to ensure its correct function and emphasize the trustworthiness of its results. Therefore, a comparison with another established simulation or an experiment should be performed. In this work, the latter was chosen. The experiments performed by Liu et al. were suitable for this analysis [235]. They provide all input parameters needed for the simulation and additionally, the range of parameters is large. In the following, the methods they have used are described. The FMCMC model is valid if the normalized fluorescence remittance matched the experiment. The location of the fluorescence events in the FMCMC was assumed to be correct, a validation of this was neither possible with this experiment nor with other published data.

Experimental setup and study by [235] The experiment was performed to provide a systematic validation of MC modeling of fluorescent light propagation in tissues. The samples were cylinders with homogeneous properties (single layered). Thereby, two sets of samples were produced: in one set the concentration of scattering particles was fixed and absorption particles varied, in the other set the concentration of absorption particles was fixed and scattering particles varied. Details on the production of the phantoms and the detailed optical properties are given in their manuscript and will not be detailed here [235]. The illumination and recording system consisted of an optical fiber device with different geometries. One geometry was chosen and its results taken for the validation process. The geometry is shown in Figure 9.8. The other geometries are more complex but do not add any value to the analysis.

The fiber was placed on the flat top of the cylinder and the remitted fluorescence intensity measured. Three measurements were performed and the mean calculated for each sample.

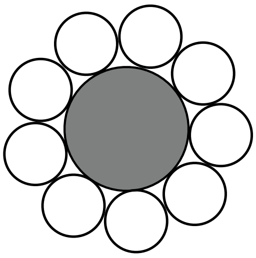

Figure 9.8: The fiber optic probe had a central illumination fiber with a core /cladding diameter of 200 /245 µm. It was surrounded by a concentric ring of nine collection fibers each with a core/cladding diameter of 100 /130 µm. The distance between the center of the illumination fiber and the each collection fiber was 187.5 µm. The numerical aperture NA of all fibers was 0.22.

Simulational study The optical properties of the samples used in the experiment were taken as input for an adaption of the FMCMC model. The experimental setup used the flat top surface of the cylinders for the measurements. This was not possible in the FMCMC since the cylinders are infinitesimally large in y direction. Hence, a Fluorescence-Monte-Carlo-Multi-Layer (FMCML) was derived from the FMCMC geometry and used to ensure a flat surface. The detector of the remitted fluorescence were analogously realized to the experimental fiber probe geometry in Figure 9.8. They were implemented as multiple circles of identical size and relative location to the illumination area. All fluorescence photon packages exiting the model from the circles were accumulated and tracked. The initial position of the photons launched in the illumination area was randomized. Their initial direction was also randomized but restricted in semi-sphere-coordinates facing into the geometry. The coordinates were converted to Cartesian-coordinates. In total 5,000,000 photons were launched. The weight of the remitted fluorescent photons was tracked for each geometry/sample separately.

To enable a comparison of the fluorescence intensity from the experiment with the weights obtained from the model, a normalization step was required. Each experimental data point was normalized by the sum of all experimental data points of its set, and each simulation data point was normalized by the sum of all simulation data points of the respective set. This method of normalization, sets the area under the curve to unity and facilitates the comparison of the both results.

To quantify the results, the cross correlation and the Root Mean Square Error (RMSE) of the experiment and simulation were calculated

9.3.1.2 Obtaining the systemic error

The following section describes the methods used to obtain the systemic error mentioned in Section 7.2. The proposed FMCMC model in Section 9.3.1 was utilized. The computed concentrations of ICG in Section 9.2 were used as input for the model.

Convergence Before starting a large trail, a convergence analysis was performed. It included launching 10 million photons in 1 million steps. Thereby, the change of the performance parameter ε_{sys} was regarded.

Study settings The study included 17 different sets of combinations of diameter and flow values. Table 9.2 shows an overview of the diameter, flow value and the number of computed layers in the blood volume. The concentration of ICG in each layer was time dependent (see Section 9.2). Therefore, for each configuration of diameter and flow value 34 time steps were simulated to obtain a time dependent w_{opt}. The 34 time steps were not distributed equidistantly, they were empirically determined. Generally, time steps were more dense at the inflow phase since greater changes were expected and required a higher sampling frequency.

Table 9.2: The inner diameter was set, the outer diameter was determined by adding the mean vessel wall thickness of cerebral arteries to it (see Section 2.1.2). The flow values were chosen according to physiological and pathological values for the arteries of the respective size. The number of layers within the blood volume were determined by the fluid flow simulation (see Section 9.2).

Inner diameter in mm	**Outer diameter** in mm	**Flow** in ml/min				**Number of layers in the blood volume**
1	1.28	25	50	65	80	19
2	2.56	50	80	120		30
3	3.85	120	150	180		41
4	5.13	150	250	350		56
5	6.41	250	300	350	400	67

The optical properties were set as shown in Table 9.3. Since in literature a variation of the properties is reported, the mean of multiple publications was used [163, 236–244].

Table 9.3: Optical properties of the blood, vessel wall and ICG are shown. Note, it was assumed that ICG did not change the blood's properties. The μ_{A} of ICG was dependent on the molar concentration of ICG $c_{\mathrm{mol,ICG}}$ and $\frac{1}{\mathrm{M}}$ is a unit.

	Blood	**Vessel wall**	**ICG**
μ_{A} in cm^{-1}	7.38	2.25	$3.43 \cdot 10^5 \cdot c_{\mathrm{mol,ICG}} \cdot \frac{1}{\mathrm{M}}$
μ_{S} in cm^{-1}	713	200	-
g	0.99	0.99	-
n	1.38	1.44	-

The initialization and propagation of the photons was performed for each time step of each configuration of diameter and flow as described in Section 9.3.1. Afterwards, the obtained w_{opt} were used to calculate the systemic error as given in Equation 7.17 in Section 7.2. Hence, the systemic error was time dependent.

9.4 Results

9.4.0.1 Validation of the FMCMC model

The comparison of the experimental and simulational data is shown in Figure 9.9. Qualitatively, the simulational results agree with the experimental results. This is reflected in the cross correlation of 0.991 and 0.997 for the variation of the absorption and scattering coefficient, respectively. The absolute error of the computed and measured normalized fluorescence emission ranged from approx. 2% to 3% for the variation of the absorption coefficient and is approx. 1% for the variation of the scattering coefficient. The computational time to obtain a single data point was approx. 5 days.

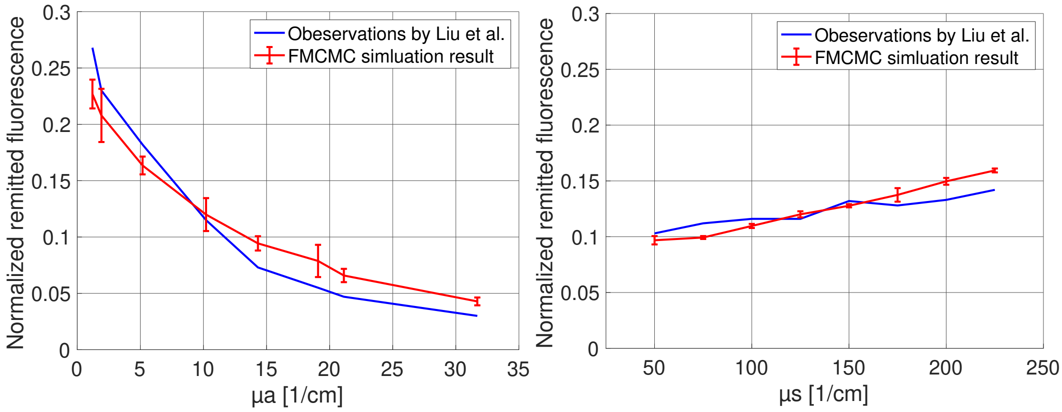

Figure 9.9: **Left**: the comparison of the experimental and simulational data for a fixed scattering and varying absorption coefficient is shown. **Right**: the comparison of the experimental and simulational data for a fixed scattering and varying absorption coefficient is shown. The error bars for the observation by Liu et al. are negligible. The bars for the simulational results indicate the minimum to maximum range of the results for different runs of the FMCMC model.

9.4.0.2 Obtaining the systemic error

Convergence analysis The convergence analysis revealed that generally little changes were present (<0.5%) in the whole range (see Figure 9.10) which indicates that launching one million photons is sufficient. In Figure 9.10 to the right the number of absorbed excitation photons and the weight of the detected fluorescence photons is shown. This was meant to be a plausibility check. Since the geometry did not change, it was expected to show a linear increase which it clearly does and the results are plausible.
To be on the safe side 3 million photons were assumed as suitable for usage in the upcoming analysis.

Study The performed study had multiple purposes. It was implemented to obtain the time dependent w_{opt} and hence also ε_{sys}. It should clarify on the dependency of ε_{sys} of the diameter, time and the predefined volume flow.
In Figure 9.11 the w_{opt} for a diameter of 3 mm and flow of 120 $\frac{\text{ml}}{\text{min}}$ is shown, to the left the w_{opt} at inflow is given and moving to the right later time points are visualized. For early time point, high values in w_{opt} are clearly closer to the center but it is also visible that the attenuation of the light is present the deeper it penetrates the vessel. For later time points, the high values in w_{opt} are shifted towards the outer radii. This is due to the shift of the ICG towards outer radii.
In Figure 9.12 the timewise course of $\varepsilon_{sys}(t)$ and the remitted fluorescence are shown for the same diameter and flow configuration as used for Figure 9.11. $\varepsilon_{sys}(t)$ is steadily declining and seems to converge for late time points. This result partly validates the first hypothesis. The remitted fluorescence shows a slightly steeper increase than decrease. It seems to converge as well.

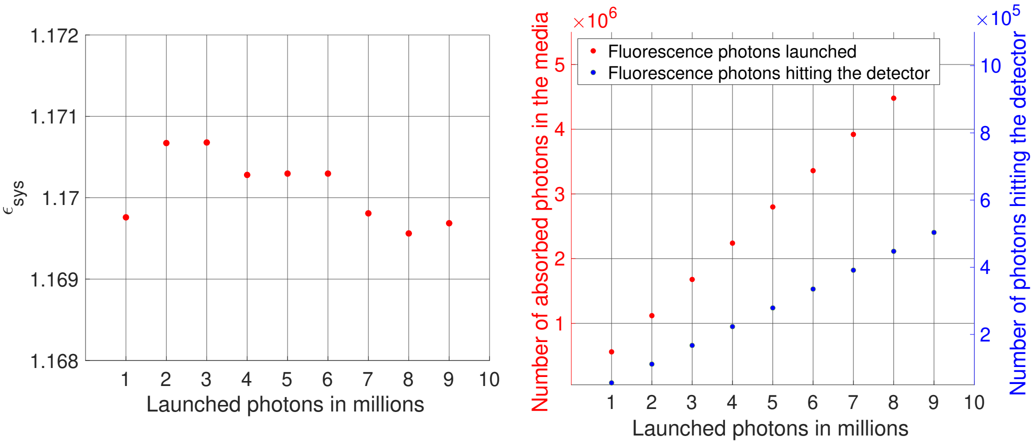

Figure 9.10: **Left**: the systemic error in dependency of the number of launched photons is shown. It does not deviate a lot for the whole range of launched photons. This implicates convergence already at a small number of photons. **Right**: the number of absorbed photons in the blood volume (red) and the number of photon packages hitting the detector (green) are shown in dependency of the launched photons. Both should increase linearly since the geometry and its optical parameters did not change. The results are plausible.

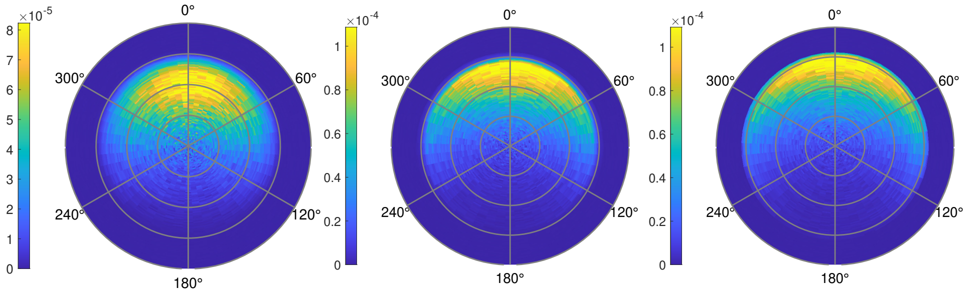

Figure 9.11: The $w_{opt}(r,\phi)$ for three time points are visualized. **Left**: at the inflow phase of the ICG. **Right**: at the outflow phase of the ICG. **Middle**: at a time point between inflow and outflow of the ICG. Timewise, a clear shift of high values of w_{opt} towards the outer radii is visible.

Figure 9.13 shows the dependency of ε_{sys} on the diameter d and volume flow at three characteristic points on the emission's course. Thereby, the maximum, the 30 % and 5 % of the maximum were chosen. The value at the emissions maximum was chosen because it is a characteristic point in each course of $\varepsilon_{sys}(t)$. The 5 % and 30 % of maximum were chosen because they represent the very first appearance of the dye and the rapid increase of the dye, hence the maximum slope of the increase (30 % of maximum showed empirically to correlate with the maximum slope of the signal). Using the 5 % and 30 % of maximum seems to not be robust for large geometries, this can be traded back to a too low temporal resolution.

The mean values for each diameter are shown in Table 9.4. For each diameter value, the ε_{sys} is increasing the closer it gets to the time point of initial inflow of the ICG. The span of each ε_{sys} for all diameter values decreases the closer it gets to the time point as well.

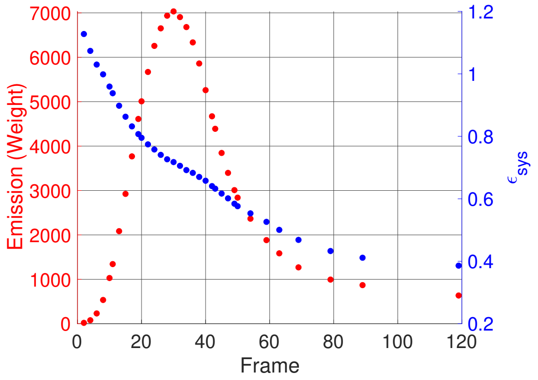

Figure 9.12: The fluorescence emission is shown over time (frames) in red. To each sample point in this plot, a corresponding $w_{opt}(r,\phi)$ (similar to Figure 9.11) was obtained and used to calculate the $\varepsilon_{sys}(t)$, shown in green.

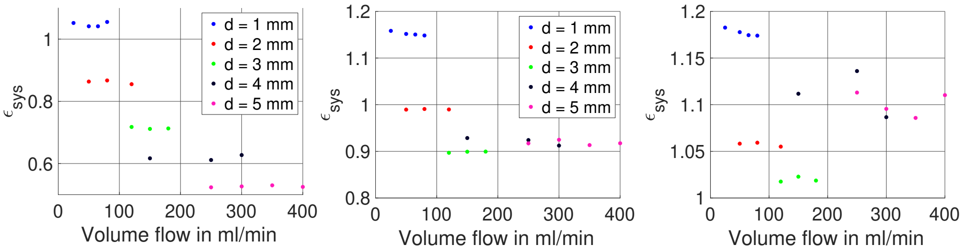

Figure 9.13: All three plots show the systemic error in dependency of the volume flow and diameter. The left plot used the ε_{sys} obtained at the time point of maximum emission. The middle plot used the ε_{sys} obtained at $30\,\%$ of the maximum emission. The right plot used the ε_{sys} obtained at $5\,\%$ of the maximum emission. Note that the ordinate axis labels are different between the plots. The right plot uses the color notation of the diameters.

Table 9.4: The mean value of ε_{sys} for each diameter is given. Thereby, ε_{sys} was measured at the time point of the maximum of the remitted fluorescence and 30% and 5% of the maximum.

Diameter	$\varepsilon_{\text{sys,max}}$	$\varepsilon_{\text{sys,30\%}}$	$\varepsilon_{\text{sys,5\%}}$
1 mm	1.05	1.15	1.18
2 mm	0.86	0.99	1.06
3 mm	0.71	0.90	1.02
4 mm	0.62	0.92	1.11
5 mm	0.62	0.91	1.10

9.5 Discussion & conclusion

9.5.1 Validation of the FMCMC model

The FMCMC showed qualitatively similar results to the experiment. An exponential decrease in remittance with increasing absorption and a linear increase of remittance with increasing scattering (see Figure 9.9) was observed in both. Quantitatively, the cross correlation is with > 0.99 very high and the error is very low with a maximum of 3%. The results for the variation of the absorption coefficient has a distinct behavior. For low absorption coefficients the simulation underestimates the remittance and for high absorption coefficients it overestimates the remittance. These small deviations can be provoked by simplifications done in the modeling. The model is in contrast to the physical samples perfectly homogeneous. The optical fibers (illumination and detector fibers) were modeled as an ideal flat and circular surface, which is an approximation of its real geometry. Nonetheless, taking those minor deviations into account the total fluorescence emission modeled by the FMCMC is valid. It is assumed that the location of the fluorescence events is correct since this cannot be evaluated but is used for the determination of the systemic error.

9.5.2 Obtaining the systemic error

Convergence analysis MC models require a high number of repetitive calculations to provide reliable results. In theory, an infinite number is required to obtain the correct expected value of the performance parameter. Hence, a convergence analysis was needed to determine the number of repetitions at which little changes in the performance parameter will occur to make a trade-off between the computational time and trustworthiness of the result. The performance parameter in this work was the systemic error ε_{sys} which was derived from w_{opt}. With a relative change of less than 1% the convergence analysis indicated convergence of ε_{sys} already at one million launched photons. The relative change of less than 1% is sufficient since other influencing factors such as the reported and used optical properties of the blood, vessel wall and ICG have a large range. Moreover, a value of less than 1% is relatively small compared to the statistical errors presented in Section 8.

According to Noebauer et al. the smoothness of $w_{opt}(r,\phi)$ is a measure of convergence as well [245]. The smoothness is obviously dependent on the used grid. Figure 9.11 visualizes $w_{opt}(r,\phi)$ and subjectively seems to not being smooth which is contradictory to the results of the convergence analysis discussed in the previous paragraph. Visualizing $w_{opt}(r,\phi)$ is misleading because to calculate ε_{sys}, the relative flow profile $v_{rel}(r)$ (see Equation 9.2) was weighted by $w_{opt}(r)$. Since $v_{rel}(r)$ is axisymmetric and independent of ϕ, $w_{opt}(r,\phi)$ was projected into $w_{opt}(r)$. Figure 9.14 shows such a projection which is in contrast to Figure 9.11 smooth.

Although launching one million photons would have been acceptable, three million photons were launched to ensure a convergence of the results. The computational time for this threefold was with one day for small and one week for large geometries acceptable.

For obtaining the systemic error a detector of a finite size was placed in a specified distance. To test the influence of the detector's size, its size was varied. Changing it from a $1\,\mathrm{cm}^2$ to $1\,\mathrm{mm}^2$ had very little influence on the systemic error (<1% deviation) but an increased number of launched photons would have been required to converge. Therefore, the chosen detector size was used.

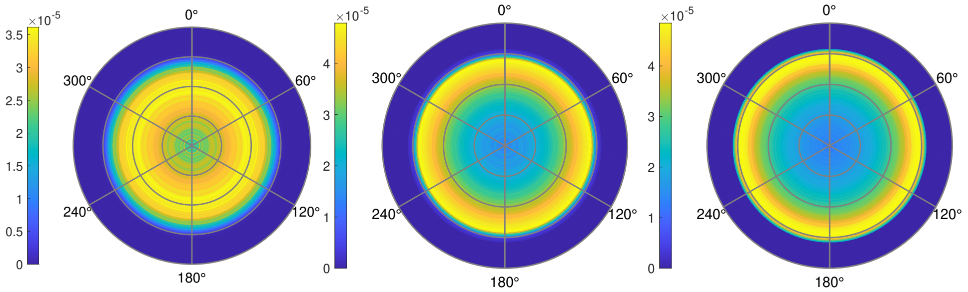

Figure 9.14: All three plots show the $w_{opt}(r)$ as the mean over ϕ of $w_{opt}(r, \phi)$ for the same setting as given in Figure 9.11. A shift of the high values of $w_{opt}(r)$ towards the outer radii with increasing time (from left to right) is clearly visible.

Study The performed investigation should quantify the systemic error and reveal its dependencies. Therefore, a FMCMC model was developed to obtain the probability density function of the fluorescence location of remitted fluorescent photons. The correctness of the fluorescence event location cannot be validated but the model yields a valid total remission of fluorescent photons (see Section 9.5.1). Here, a single fluorescence event was allowed at the propagation a photon (and photon package). In reality, the overlapping absorption and emission spectra of ICG allow the fluorescent photon to be absorbed and remitted as fluorescent photon again. Thus, the location might change. Hence, the correctness of the fluorescence location is an assumption and its validation is a task for future work.

The model neglects the change of the optical properties of the material in dependency of the wavelength. This assumption is based on the minor changes of the optical properties for this wavelength range [163, 236–244]. Yet, an implementation of variable optical properties of the blood and vessel wall could set the model closer to reality. The fluid flow simulation models blood in a macroscopic manner. But in a microscopic manner, the optical properties (scattering and absorption) of RBC are dependent on their orientation [246, 247]. Including the RBC as particles of non-spherical shape into the fluid flow simulation could enable a measurement of their orientation. This would be followed by a spatially variable optical property of blood in the FMCMC model.

The timewise course of the systemic errors $\varepsilon_{sys}(t)$ were obtained for each geometry and flow configuration. For all cases the results are plausible in the sense that they are below the value of 2 and do converge for large t. The maximum value below 2 was expected since the maximum local flow velocity in the flow profile is twice the mean velocity. A convergence at large t was expected since a no slip condition was set for the fluid flow model and thus mostly only diffusion was present close to the border of the vessel and a convergence for large t towards a small value was expected. Characteristic to all obtained $\varepsilon_{sys}(t)$ was a plateau-like course at the time points where the maximum fluorescence emission was recorded. This can be explained by the local distribution of the ICG concentration, which was at that time points homogeneous. The homogeneous distribution did not change a lot for some consecutive samples and therefore the $\varepsilon_{sys}(t)$ was not changing as well. Generally, the steadily declining $\varepsilon_{sys}(t)$ is plausible since the faster local flow velocities in the middle of the pipe arrive first at the measurement site and only slower components will add up to it. Hence, a decline of $\varepsilon_{sys}(t)$ is expected (this would change if recirculation would be integrated into the fluid flow model).

The analysis of $\varepsilon_{sys}(t)$ for the different configurations revealed that the systemic error
- ○ is dependent on the diameter.
- ○ is not dependent of the volume flow.
- ○ is dependent on the time point at which it is extracted.

Thereby, both hypotheses stated in Section 9.1 are valid. The diameter dependency is plausible since the penetration depth of the excitation and fluorescent photons is limited. For the diameter range relevant for neurovascular surgery, the systemic error was decreasing with increasing diameter.[1]

A dependency on the volume flow was not proven. The flow was varied within the limitation of laminar flow, and pathological-physiological flow value. Hence, for non-laminar flows the dependency will be different. Non-laminar flow in cerebral vessels can appear at bifurcation or at pathologies such as aneurysma. These cases are not suitable for an analysis of the systemic error as performed here. A sophisticated and personalized fluid flow and optical model is required to enable an analysis of those cases. Nonetheless, in most cases laminar flow can be assumed [24, 170].

The systemic error has a characteristic dependency on the diameter. Additionally, this dependency also depends on the time point at which the systemic error was extracted. The magnitude of the dependency on the diameter decreased towards early t for values of $t < t_{max}$. Consequentially, it makes more sense to analyze the inflow phase for the transit time analysis than using the maximum of intensity. Thereby, the dependency is lowered and a more robust calculation is ensured.

Proposed systemic error values The overarching goal was to obtain the systemic error ε_{sys}. It was revealed that the systemic error is time and diameter dependent. Therefore, multiple functions are needed to define ε_{sys}. Equations 9.14 to 9.16 are derived from the results shown in Figure 9.13. $\varepsilon_{sys,max}(d)$, $\varepsilon_{sys,30\%}(d)$, $\varepsilon_{sys,5\%}(d)$ represent the diameter dependent systemic error at the point in time of maximum fluorescence emission, 30% of maximum emission and 5% of maximum emission, respectively.

$$\varepsilon_{sys,max}(d) = \begin{cases} -0.186 \cdot d + 1.233 & \text{for } d \in [1\,\text{mm}, 2\,\text{mm}] \\ -0.148 \cdot d + 1.158 & \text{for } d \in (2\,\text{mm}, 3\,\text{mm}] \\ -0.096 \cdot d + 1.000 & \text{for } d \in (3\,\text{mm}, 4\,\text{mm}] \\ -0.092 \cdot d + 0.988 & \text{for } d \in (4\,\text{mm}, 5\,\text{mm}] \end{cases} \tag{9.14}$$

$$\varepsilon_{sys,30\%}(d) = \begin{cases} -0.162 \cdot d + 1.314 & \text{for } d \in [1\,\text{mm}, 2\,\text{mm}] \\ -0.092 \cdot d + 1.173 & \text{for } d \in (2\,\text{mm}, 3\,\text{mm}] \end{cases} \tag{9.15}$$

---

[1] Note that the error is not equal to the deviation. The error is decreasing and thereby turning from overestimation to underestimation with increasing diameter. Hence, the error is changing its sign and a minimal deviation is present for a certain vessel diameter.

$$\varepsilon_{sys,5\%}(d) = \begin{cases} -0.120 \cdot d + 1.297 & \text{for } d \in [1\,\text{mm}, 2\,\text{mm}] \\ -0.038 \cdot d + 1.133 & \text{for } d \in (2\,\text{mm}, 3\,\text{mm}] \end{cases} \tag{9.16}$$

9.6 Outlook

The implemented FMCMC model was based on the approach of Welch et al. [157]. It was a trade-off between fulfilling the requirements and limiting the computational time. Its main characteristic is the simulation of the excitation photons in the binary model and the fluorescence photons in a weighted model. Thereby, a photon can only face a fluorescence event once. In reality the absorption and emission spectra of ICG overlap [71]. Hence, allowing only a single fluorescence event is erroneous although it is often assumed [231, 233]. The inclusion of self-absorbance of fluorescent photons should be investigated. The approach by Liebert et al. propagates all photons using the weighted model [232]. Hence, a photon could face multiple fluorescence events. This approach is more complex and computational costly. Implementing it and performing the 17 studies would have taken more resources since multiple fluorescent photon packages needed to be launched and tracked. Nonetheless, performing a comparison of both models would give great insights into the effects of the simplification done in this work.

The scattering of a photon was determined using the Henyey-Greenstein phase function because it is reported to be well suited for the simulation of blood [162]. It is also reported that the McCormick phase function is also well suited for the simulation of blood [163]. Both publications agree that for physiological blood the difference between the both phase functions is small. Nonetheless, controversial statements are present and an investigation is needed to find the optimal phase function for the simulation of blood.

Fluorescence includes the change of the wavelength of the photon. This is not taken into account in this work and justified by the little change of the optical properties of blood and vessel wall. The wavelength dependent properties should be obtained and incorporated into the model. It is not expected to increase the computational time since it only changes the pointer at a look-up table of the properties.

The total remittance of fluorescence calculated by the FMCMC model was validated using the experimental data of Liu et al. [235]. This validation did not include the location of fluorescence events. In this work, the location was assumed to be correct. This assumption should be validated in a future experiment. So far, no publication is known to the author that proposes a suitable experiment for the validation of this assumption.

The used detector model is not a realistic representation of a camera and its optical components. Modeling the camera and its optics is favorable. Each photon exiting the geometry has a defined location and propagation vector. Both can be extracted and used for ray tracing (including a more complex optic). This would also enable the generation of an image of the object simulated.

Once a realistic camera model is incorporated, a new phantom should be used to validate the simulations (multi-cylinder geometry). A cylindrical multi-layered fluorescent phantom with known optical properties would be needed (see [248–252]). The validation of the fluorescence event location might be possible with a phantom with heterogeneous dye concentrations but will most probably be limited to macroscopic effects.

The used fluid flow simulation to obtain the spatio-temporal concentration of ICG in the pipes had some limitations that were mentioned in Section 8.2.2.1. At this point, one assumption is of great interest. The assumption of blood as a homogeneous fluid. In fact, blood is a cell suspension. ICG mostly binds to components of the plasma. The cells displace the plasma. Hence, a heterogeneous distribution of cells would influence the distribution of the plasma and also the diffusion of ICG. The distribution of cells in flowing blood is heterogeneous with an aggregation in the center of the vessel. It depends on many factors such as the oxygen saturation, shear rate, osmolarity and more [163, 246, 247, 253–259]. Moreover, the orientation of the RBC influences the optical properties of blood which is not regarded in the model since RBC are not modeled in a microscopic manner [246, 247]. Hence, the heterogeneous distribution of the blood cells can be included in future simulations to perform a sensitivity analysis. The inclusion of a heterogeneous distribution is similar to including the Sieve effect[2] into the investigation [163, 260].

Finally, the findings on the systemic errors should be used in the blood flow measurement to compensate for the systemic error.

---

[2] The Sieve effect is also known as absorption flattening. When photons pass through a suspension of absorbing particles, such as blood, photons that do not encounter cells pass unattenuated by absorption. As a consequence, the transmission is higher than it would be if all cells were uniformly dispersed in the solution. Hence, the amplitude of the maxima in an absorption spectrum for a heterogene solution are reduced relative to those for a homogeneous solution of the same average concentration.

PART IV

EX VIVO AND IN VIVO STUDY

Chapter 10

Ex vivo experiment

The overall topic of this work is the measurement of blood volume flow via fluorescence angiography (FA). In the previous Chapters 8 and 9, the errors in the measurement were determined in an *in silico* setup. The observations and analysis indicated that the volume flow measurement should be applicable to practice. The experiment performed in this chapter used the previously introduced work flow and methods to validate the blood volume flow measurement in an *ex vivo* environment. *Ex vivo* (Latin: “out of the living”) means that the experiment is performed on biological tissue outside of its donor’s body. In this case, the vessel and the blood were taken from animals and used in an experimental setup to assess the performance of the proposed blood flow measurement.

10.1 Introduction

Ex vivo studies allow the investigation of physiological and pathological cases under standardized conditions. Thereby, the control of the degrees of freedom is the main advantage which allows an isolated analysis and profound conclusions. Nonetheless, the *in vivo* use case has to be depicted as good as possible to ensure the transferability of these findings into the surgical hall.

The conducted experiments involved the pumping of pig blood through a tube system into an extracted aorta from a rabbit. The flow was measured by a reference system and the proposed method via FA. Those two measurements were compared to assess the accuracy of the proposed method.

Thereby, two hypotheses were formulated:

1. The mean volume flow for different aortas has a smaller deviation from the reference for the measured cases (60, 120, 150, 180, 200 $\frac{\mathrm{ml}}{\mathrm{min}}$) than the determined propagated statistical error in Chapter 8.
2. The stepwise increasing flow leads to a stepwise increasing flow measurement with the proposed method. Here, all measurements of a designated flow for one aorta are averaged to calculate the step size and compared with the reference step.

10.2 Materials and methods

10.2.1 Biological material

As mentioned earlier, two biological materials were used in the *ex vivo* experiment. As substitute for human blood, pig's blood was used and to represent the human cerebral vessels, an aorta extracted from a rabbit was used.

Blood The blood used for the experiments had to fulfill two requirements: it should
1. be available in a large quantity.
2. mimic the rheological properties of human blood.

The quantity needed to conduct the experiments was in the magnitude of tens of liters. The rheological properties can be compared using key indicators of blood. The whole blood viscosity (WBV), hematocrit, red blood cell deformability and aggregation are common key indicator of blood which impact the flow [261, 262]. For this work, the key indicator WBV was mainly used. Table 10.1 shows the WBV and hematocrit of different animals in comparison to human, note that small animals (rat and rabbit) were already excluded due to the restrictions in availability [261, 263].

Table 10.1: Comparison of the hematocrit and the whole blood viscosity at different shear rates for different animal models. The data is adapted from [263].

Animal model	Hematocrit in %	WBV at $0.7\,\mathrm{s}^{-1}$ in $\mathrm{mPa\cdot s}$	WBV at $2.4\,\mathrm{s}^{-1}$ in $\mathrm{mPa\cdot s}$	WBV at $94\,\mathrm{s}^{-1}$ in $\mathrm{mPa\cdot s}$
Horse	35	38	20	5
Pig	33	25	15	5
Cattle	30	7	6	5
Sheep	33	7	6	4
Human	42	33	19	6

Cattle and sheep blood were excluded due to their large difference in WBV. Furthermore, horse blood was excluded since the local slaughterhouses were not able to provide it regularly. Pig blood was available in large quantities and matches the rheological properties of human blood well and was therefore chosen for the *ex vivo* experiments. The anticoagulant fibrisol (trisodium citrate E331 and salt) was added to the blood in a concentration of $10\,\frac{\mathrm{g}}{\mathrm{l}}$ to prevent the blood from clotting. The blood was bought at Rachele Fleisch & Wurst in Karlsruhe, Germany.

No ethics vote was needed since the animals were killed for other purposes than research and hence were not included in the animal protection law (§4 TierSchG).

Vessel The vessel model had to match the size and mechanical properties of human cerebral arteries (see Section 2.1.2). The availability of the vessel was an important aspect. Two animal models were available in the vicinity of the facility. At the Institute for Applied Biosciences- Department of Genetics, rats (Rattus norvegicus, Stamm Fischer 344) were available. The aorta of the rat is of the size (length and diameter) of small cerebral arteries. At the University Medical Center Freiburg, the heart of New Zealand White rabbits were used for a Langendorff setup and the remaining of the rabbit were available. The aorta of the rabbits is of the size of large cerebral arteries. The rat's aorta were extracted but due to their size and fragility, their handling was challenging and showed insufficient quality.
Multiple publications confirm that the rabbit's aorta is a good match to human cerebral arteries in terms of mechanical properties and surgical handling [264–270]. For this work, 11 aortas of the New Zealand White rabbits were extracted by Dr. Enaam Chleilat (University Medical Center Freiburg, Group of Prof. Peter Kohl). The ethical approval was obtained from the local institutional animal care and use committees (Regierungspräsidium Freiburg, file number: X-16/10R). The aortas were stored according to the protocol as suggested by van Doormaal et al. in a mixture of the following reagents at -18°C between extraction and the usage of the aorta [264].

- 10% Dimethyl sulfoxide DMSO purity $\geq$ 99.5% (Carl Roth GmbH+Co.KG, Karlsruhe, Germany)
- 90% Roswell Park Memorial Institute 1640 solution ROTI$^{®}$Cell RPMI-1640 (Carl Roth GmbH+Co.KG, Karlsruhe, Germany)

10.2.2 Experimental setup

The experimental setup had to fulfill two main requirements. It had to provide

1. a clear image of the fluorescence bolus flowing through the vessel.
2. a ground truth of the flow.

To achieve those requirements, multiple evolutions of the setup were developed according to the V-model of the VDI 2206 [271]. In this section, the final setup used for the experiments is introduced. An overview of the experimental setup is shown in Figure 10.1. The shown components are explained in detail in the following paragraphs. The camera and illumination systems is shown separately in Figure 10.7, because otherwise, most of the experimental setup would have not been visible. The flow phantom's design included different single design features from published phantoms, which were utilized in this phantom, yet its combination of different features is unique [134, 272–278].

Blood reservoir and stirrer The blood reservoir and stirrer had to keep the blood at a constant temperature of 25°C and prevent the cellular components of the blood from sedimentation. Hence, the stirrer required a heat management system. The temperature of 25 °C was chosen according to the room temperature and is a common temperature at

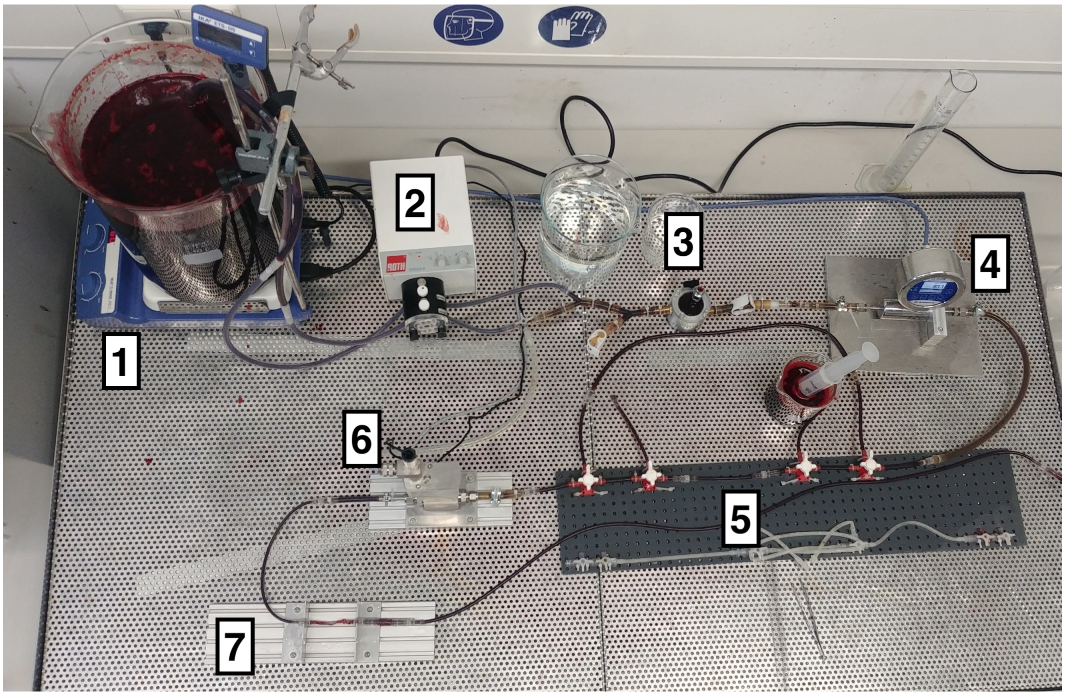

Figure 10.1: The experimental setup (excluding the camera and illumination system): 1: blood reservoir and magnetic stirrer and heater; 2: peristaltic pump; 3: air trap; 4: industrial flow meter; 5: bolus injection system; 6: pressure gauge; 7: vessel and hence measurement site for the proposed method. The devices are connected by silicone tubes and the blood is disposed in a sink not visible in this image. The camera and illumination system were placed above the vessel holder.

which the bloods properties are known. Using 37°C was not feasible due to the necessary heating of all pipes and component, which would have required a disproportionate effort. The components used were:

- 10 liter beaker ROTILABO® short 10000 ml (Carl Roth GmbH+Co.KG, Karlsruhe, Germany)
- Heater and magnetic stirrer C-MAG HS 7 (Carl Roth GmbH+Co.KG, Karlsruhe, Germany)
- Magnetic bar ROTILABO® cylindrical 10 mm diameter and 70 mm length (Carl Roth GmbH+Co.KG, Karlsruhe, Germany)

The blood was provided in bags or large canisters at 3°C - 4°C by the slaughterhouse. Before pouring it into the beaker, it was shaken to ensure the blood cells were homogeneously distributed. Approx. 9 liters were poured into the beaker. The beaker was placed on the stirrer and the stirring intensity was stepwise increased to a value of 5 out of 6. Setting up a high stirring intensity from beginning on did not work since the viscosity of blood at cold temperatures is higher and the magnet did not manage to rotate constantly. The temperature was set to 25°C. It took approx. 4 h to heat up the blood.
Blood was refilled into the beaker as soon as the blood level fell below 5 l. The experiment was then paused until the blood has reached 25°C again.

Pump A pump was needed to move the blood and ensure a sufficient flow. The flow range needed was set by the size of the rabbit aorta (approx. 2.5-3 mm). The used pump and tubes were the

- Peristaltic pump Roth Cyclo II with six roller and two channels (Carl Roth GmbH+Co.KG, Karlsruhe, Germany)
- Tubes for peristaltic pumps 1.6 mm inner diameter and 4.8 mm outer diameter (Carl Roth GmbH+Co.KG, Karlsruhe, Germany).

The flow was set to match the required values. These values are introduced in Section 10.2.3. If necessary, the second channel of the pump was used.

Connectors and tubes To enable a quick modification and reorganization of the elements of the setup, Luer taper connectors were used as interface. All devices had a male connector at the input and female connector at the output. The Luer connectors had a barbed nozzle attached to the silicone tubes as interface to the devices. The tube's size and hence also the size of the Luer connector were chosen according to the devices specification. The following connectors and tubes were used.

- Barbed nozzle of different sizes - Luer to barbed nozzle (Drifton A/S, Hvidovre, Denmark)
- Silicone tubes RCT THOMAFLUID® (Reichelt Chemietechnik Gmbh + Co., Heidelberg, Germany)

Air trap Since air could be introduced into the blood due to stirring in the blood beaker or a misplacement of the tubes (that suck the blood out of the reservoir), a convenient method of trapping and releasing the air was required. Further on, the peristaltic pump applied a pulsatile flow (the pulse amplitude is very small - magnitude of 1% to 2%). By intentionally leaving a small air compartment in the air trap, these pulsations were attenuated. Thereby the air trap acted as a low pass filter. Since no such air traps are commercially available, it was designed by me and manufactured in the in-house workshop (responsibles: Eric Hoffner and Patrik Narewski). Figure 10.2 shows its design. It consisted of a sealed hollow cylinder and had a flow inlet, flow outlet and a valve. The inlet was placed higher than the outlet to ensure that no air bubbles reach the outlet. The valve was manually operated and required the user to open and close it whenever needed. The topside of the air trap was made from Plexiglas® so the user could see into the air trap. The following materials were used

- Mini ball valve $\frac{1}{8}$ inch (ESSKA GmbH, Hamburg, Germany)
- Barbed nozzle 10 mm barbed outlet from brass (Landefeld Druckluft und Hydraulik GmbH, Kassel, Germany)
- Aluminum for the cylindrical corpus
- Plexiglas® 9 mm
- O-ring to seal the contact of the aluminum and Plexiglas®

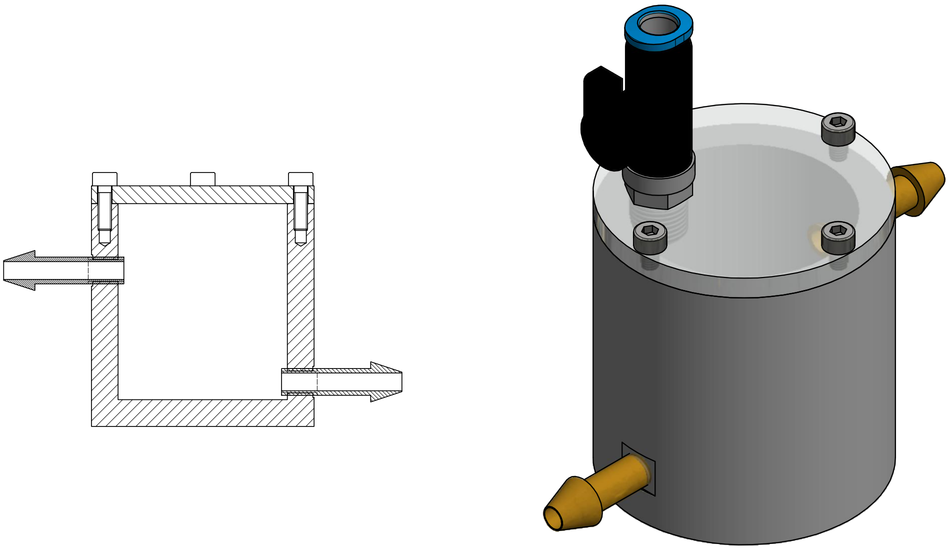

Figure 10.2: Technical sketch of the air trap. **Left**: a cutaway drawing of the air trap is shown. The inflow of blood (left) was placed higher than the outflow (right) to prevent air bubbles from getting into the outflow. **Right**: The isometric view of the airtrap. The top plate was made from Plexiglas® to allow the user to see how much air is in the air trap. The manual valve was placed off-center in the top plate. Hence by tilting the air trap, the trapped air accumulates at the valve. The valve was operated manually.

Flow meter and pressure gauge To obtain the ground truth value for the flow, an industrial flow meter was used. It had to be suitable for the flow rates and pressures planed. Furthermore, the pressure needed to be recorded to ensure the arteries were neither over- nor under-pressurized. The following devices were used:

- Flow meter ES113I (BRONKHORST HIGH-TECH B.V., Ruurlo, Netherlands)
- Pressure gauge IN-PRESS P-502Cl (BRONKHORST HIGH-TECH B.V., Ruurlo, Netherlands)

The flow meter was chosen due to its high accuracy of $\leq \pm 0.8\,\%$, a sufficient measurement range of $2\,\frac{\text{ml}}{\text{min}}$ to $200\,\frac{\text{ml}}{\text{min}}$, an ingress protection of IP66 and its approval for food contact according to EC1935/2004 (nevertheless, blood needs to be washed out properly). It had a 6 mm connector (outer diameter, compression type). The flow meters accuracy was measured for water at 25°C. Therefore, before starting the experiments its accuracy was checked by pouring the blood into a measuring cylinder (accuracy of $\pm 0.5\,\text{ml}$) for one minute and integrating the respective recording of the device for the same time. The accuracy was approved also for blood (for flows from $60\,\frac{\text{ml}}{\text{min}}$ to $200\,\frac{\text{ml}}{\text{min}}$).
The pressure gauge was chosen due to its high accuracy of $\leq \pm 0.5\,\%$, sufficient measurement range of 2 mbar to 2 bar (approx. 1.5 mmHg to 1500 mmHg), ingress protection of IP65 and its FDA and USP Class VI approved compounds. It had a 6 mm connector similar to the flow meter.

Additionally to the flow and pressure, the temperature of the blood can be tracked by both devices. Both devices were connected to a computer and the timewise course of flow, pressure and temperature was monitored and recorded with the Software BRONKHORST FLOWPLOT. The sampling frequency was set to $f_{sample} = 100\,\text{Hz}$. The data was saved as a .txt and imported into MathWorks MATLAB R2019b for further analysis.

Injection system The indocyanine green (ICG) needed to be injected into the flow. The procedure had to be standardized and have a low influence on the flow. Therefore, a direct injection of ICG by a syringe into the flow stream was excluded.
To inject the dye, a method introduced by Weichelt et al. was adapted [273]. For this, the dye was already dissolved in an additional blood reservoir in a concentration of $c_{init,ICG} = 0.005\,\frac{\text{g}}{\text{l}}$. A bypass system had two independent routes for the blood: one route for the application of the ICG bolus and one to keep the blood in motion while refilling the first route. A syringe was used for the refilling process. Please note that the ICG was not injected into a flowing stream. The stream was stopped in this section of the injection system. The injection system is shown in Figure 10.3.
Route A (colored dark-green) contained the ICG solution, route B (colored red) was the bypass. The section of route A between the two green arrows contained the ICG solution. It was refilled with a syringe attached to either one of the connectors at C and turning the selector valve 2 and 3. For the refilling process, selector valve 1 and 4 were directing the blood flow through route B. Whenever the refilling was completed, selector valves 2 and 3 were set for a continuous flow from left to right and then selector valves 1 and 4 were turned to redirect the blood flow through route A. Thereby, a standardized injection of a rectangular bolus was ensured. The turning of the valve pairs needed to be done synchronously to avoid disturbances of the flow. The minimal distance to the measurement site had to be larger than the distance needed to develop a constant and laminar flow profile (see Equation 9.3 in Section 9.2.1). The following materials were used for the injection system:

- Indocyanine green ICG-PULSION (Pulsion Medical Systems SE, Feldkirchen, Germany)
- Three-way selector valves nominal width 4 mm (Bürkle GmbH, Bad Bellingen, Germany)
- Barbed nozzle of different sizes - Luer to barbed nozzle (Drifton A/S, Hvidovre, Denmark)
- Syringe MEDIWARE Luer Lock 50 ml (mediparts GmbH, Oberhausen, Germany)
- Perforated plate polyethylene (in-house production)
- Cable ties

The perforated plate was used to fix the three-way valves with cable ties to it. This ensured a mechanical stability while turning the valves.

Vessel preparation and integration The rabbit's aorta needed to be free of leakage. Due to the nature of the aorta, it has multiple branches. Large branches (e.g. towards the kidney)

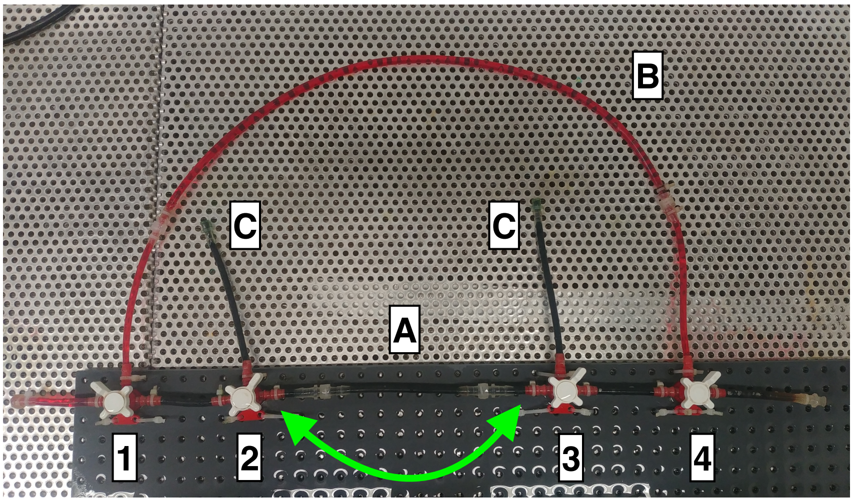

Figure 10.3: The injection system is shown. It can be operated with a flow from left to right or vice versa. Route B was used in normal flow condition to refill the ICG or just before the bolus was released. While route B was active, valves 1 & 4 were set to direct the flow in a 90° angle into route B. Meanwhile, the ICG can be filled into the section marked by the green arrow in route A via the connectors at C. To do so, valves 2 & 3 were set at a 90° angle towards each other. With this settings, the ICG flowed in from one of the connectors C and flowed out through the other. It was always ensured that no bubbles were introduced by the refilling process. Once the bolus was refilled, valves 2 & 3 were set to an exclusively straight flow through route A. Finally, valves 1 & 4 were also set to an exclusively straight flow. Thereby, route B was excluded and route A activated and the bolus was accelerated.

were closed with a ligature. Small branches were glued with cyanacrylat (superglue - Henkel AG & Co. KGaA, Düsseldorf, Germany). An image of a ligature is shown in Figure 10.4 on the top. An image of a glued branch is shown in Figure 10.4 on the bottom.

Afterwards, the aorta needed to be connected to the tubes. This was realized by wrapping the aorta on a barbed nozzle (same as mentioned in the previous paragraph). To prevent the aorta from slipping off the nozzle and to seal the connection, an o-ring and cyanacrylat was used as shown in Figure 10.5. Finally, the vessel was placed in an in-house built vessel holder with variable distance as shown in Figure 10.6.

Outlet and cleaning The used blood was directed into a sink and disposed. After finishing the experiments, the whole systems was flushed with cold water. All components needed to be cleaned properly. Therefore, a non-foaming chlorine alkaline cleaning agent was used. These type of agents are particularity suitable for removing organic deposits as blood [279]. The cleaning agent ALU CLEANER SX (WIGOL® W.Strache Gmbh, Worms, Germany) was used.

The solution of cleaning agent and water was circulated in the system for 30 minutes. Afterwards, the used and with organic residuals contaminated solution was stored in a separate canister and disposed at the waste management facility of the KIT. Finally, the whole system was flushed with cold water for 30 minutes to be sure that all the cleaning agent was removed.

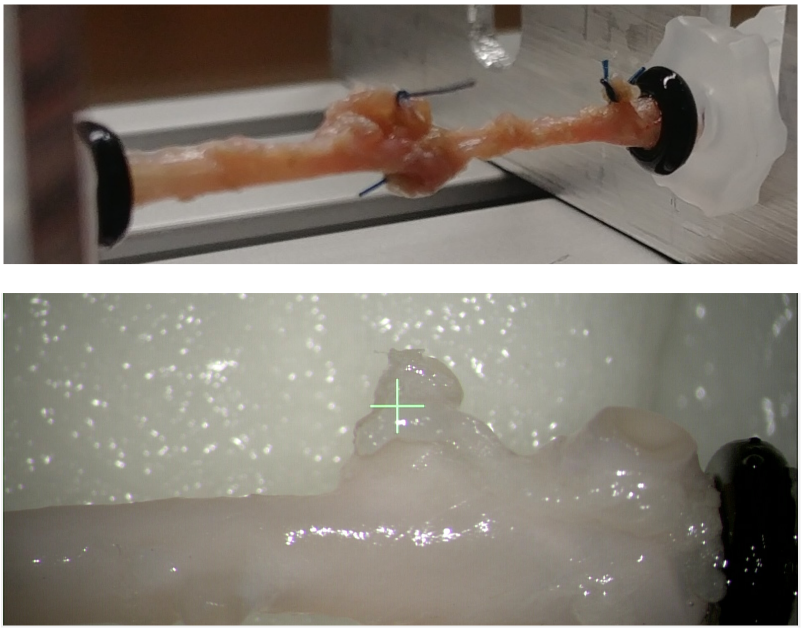

Figure 10.4: In the images, the two methods to seal a vessel are shown. **Top**: An aorta from a rat, the green threads/sutures are the ligatures set at the kidney branches (mid) of the aorta and another unknown branch (right). A ligature shuts off the flow through the branches. **Bottom**: A section of an aorta of the rabbit, at the green cross a branch was glued and hence closed. Right to the glues branch, a so far not closed branch is visible. Setting a ligature at those branches in not possible since they are too short.

Illumination and recording system The illumination and recording system was placed above the vessel holder (which was holding the rabbit's aorta). To ensure mechanical stability, the camera and the collimator of the illuminating system were mounted to a frame as shown in Figure 10.7. The used components were:

- System profile ITEM profile 5 20x20 mm and accessories (item Industrietechnik GmbH, Solingen, Germany)
- Black plastic panels KAPA®graph 5 mm (3A Composites GmbH, Singen, Germany)
- Xenon light source ASA MAX 350 W with a mirror module for a wavelength of 750 nm to 1050 nm (Mountain Photonics GmbH, Landsberg am Lech, Germany)
- Optic fiber ASA HLG-1000 (Mountain Photonics GmbH, Landsberg am Lech, Germany)
- Collimator ASA RLQL80-1 (Mountain Photonics GmbH, Landsberg am Lech, Germany)
- Excitation band-pass filter with a center wavelength $\lambda_c = 769\,\text{nm}$ and bandwidth $\lambda_B = 41\,\text{nm}$ (Edmund Optics GmbH, Mainz, Germany)
- NIR enhanced monochromatic camera Basler acA2000-165um-NIR (Basler AG, Ahrensburg, Germany)
- Camera objective 35 mm KMP-IR XENOPLAN 35/1.9 (Schneider Kreuznach, Bad Kreuznach, Germany)

Figure 10.5: The aorta was attached to a barbed nozzle. It was pulled on it and then an o-ring was put over it to firmly press on it. A small amount of glue was dispensed on the aorta behind the o-ring to glue it to the connector. Both steps (o-ring and glue) prevented leakage and provided mechanical stability so the aorta cannot detach from the connector.

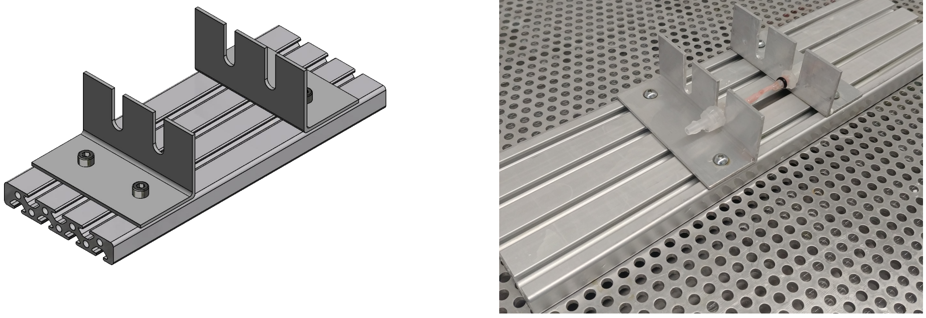

Figure 10.6: The vessel holder is shown. **Left**: the isometric view of the designed vessel holder. The screws on the L-shaped slide allowed the variation of the distance between both slides. **Right**: the realized vessel holder is shown. The connectors which were attached to the aorta (Figure 10.5) were placed in the holder into the opening of the slide.

- Emission band-pass filter with center wavelength $\lambda_c = 832\,\mathrm{nm}$ and bandwidth $\lambda_B = 37\,\mathrm{nm}$ (Edmund Optics GmbH, Mainz, Germany)

The collimator ensured a homogeneous rectangular illumination of the whole field of view (160 x 85 mm) of the camera system. The focal plane was fixed to the middle of the vessel and the aperture of the objective was open to its maximum to ensure a high sensitivity. The depth of field was less than 1 mm. Since the vessel was smaller than the field of view of the camera, the field of view was limited to 1088 x 448 pixels. The gain was set to 12 dB and the exposure time was set to 35 ms, hence a frame rate of 28.5 Hz was recorded. The recording time was set to 30 s to ensure that the washout of the ICG was also included in the

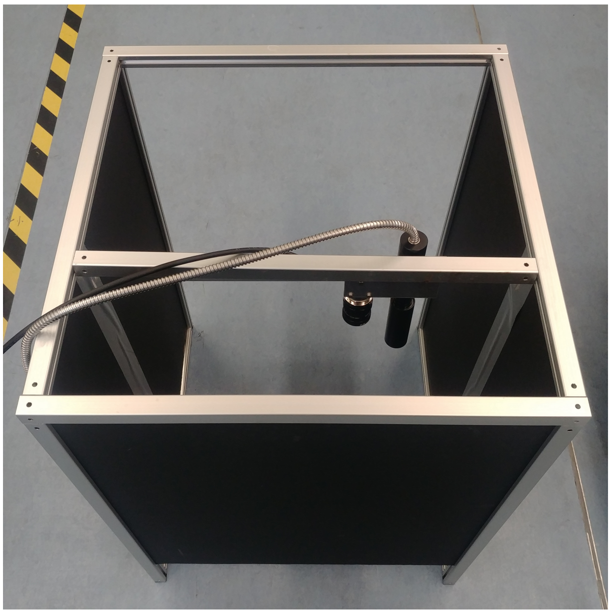

Figure 10.7: The camera and collimator for the illumination were attached to a frame. The camera was connected to a computer via a USB 3.0 cable. The collimator was connected to the xenon light source via an optic fiber. Black plastic panels were included into the frame to minimize the influence of stray light on the experiments. The panels also prevented blood from spattering across the lab in case of a malfunction of a connector.

data sets. The video was recorded as a sequence of single .tiff images with a bit depth of 12 bit (lossless compression). After recording, the image sequence was checked for dropped out frames.

The software pylon Viewer 6.2.0 was used to obtain the image sequences.

10.2.3 Flow configurations

The set values for the volume flows at the pump needed to match the expected blood flows of human cerebral vessels of the size similar to the rabbit's aorta. The rabbits' aortas had an inner diameter of approx. 2.5 mm to 3 mm. The volume flow was set to $60\,\frac{\text{ml}}{\text{min}}$, $120\,\frac{\text{ml}}{\text{min}}$, $150\,\frac{\text{ml}}{\text{min}}$, $180\,\frac{\text{ml}}{\text{min}}$, $200\,\frac{\text{ml}}{\text{min}}$. This volume flow range depicts physiological and pathological flow values for human cerebral arteries (see Section 2.1.2). In total, a minimum of 15 measurements for each flow value were performed and five different aortas were used (the other aortas showed insufficient quality).

10.2.4 Flow measurement by the proposed method

The optical measurement of the blood volume flow was carried out as proposed in Chapter 6 and 10.2.3. The feature used for the determination of the transit time was the mean delay of the two indicator dilution curves (IDCs) at 2%, 3%, 4%, 5%, 7% and 10% of maximum fluorescence intensity. This feature holds the least amount of diameter dependent deviations based on the findings in Chapter 9. The systemic error was set to $\varepsilon_{sys} = 1.02$ according to the findings in Chapter 9. The observed volume flow was corrected according to Equation 6.4.

10.2.5 Evaluation

The volume flow was extracted from the image sequences as proposed in Section 6. To each image sequence, a corresponding reference flow measurement was given. Both were compared.

First, the mean flow for each designated flow value were assessed and put into perspective to the propagated statistical error from Chapter 8 to validate the first hypothesis stated in Section 10.1.

Second, five aortas were used and each was measured three times at each designated flow value. For each aorta and designated flow value, the three measurements were averaged and then compared to the other averaged values for the three measurements of the same aorta. This enabled the comparison of the response of the measurements to an increase of flow (stepwise) at the input. It was expected to show a corresponding variation in both step direction and size.

The propagated errors from Chapter 8 were used to set the measured deviations into relation to the expected deviation. The errors in the measurement of the geometrical parameter were $\varepsilon_d = 3.5\%$ (Chapter 8.3.1.2) and $\varepsilon_s = 2.5\%$ (see Chapter 8.3.1.1). Both were determined based on the assumption that the vessels are straight objects and hence the obtained error for straight lines were used. The error in the measurement of the bolus transit time $\varepsilon_{t_{transit}}$ was not determined for the selected feature in this chapter. For the calculation of the propagated error, a conservative approach was used. The lowest error was used for the comparison with the obtained results. To determine $\varepsilon_{t_{transit}}$, the signal to noise ratio (SNR) and $t_{transit}$ must be known. $t_{transit}$ was measured. The SNR was not known (also the signal's and noise components were not known). A SNR of 20 dB was assumed based on subjective experience. It results in a $\varepsilon_{t_{transit}} = 10.4\%, 12.4\%, 20.5\%, 22.9\%$ for the flow values of $60\,\frac{\text{ml}}{\text{min}}$, $120\,\frac{\text{ml}}{\text{min}}$, $180\,\frac{\text{ml}}{\text{min}}$, $200\,\frac{\text{ml}}{\text{min}}$, respectively. The propagated expected statistical error for the volume flow measurement is shown in Table 10.2.

Table 10.2: Since the transit time of the bolus depends on the flow velocity, each flow value got assigned an own propagated expected statistical error for the volume flow measurement. The values were determined based on the fundamentals given in Chapter 7.1 and findings in Chapter 8.

Flow value	$60\,\frac{\text{ml}}{\text{min}}$	$120\,\frac{\text{ml}}{\text{min}}$	$180\,\frac{\text{ml}}{\text{min}}$	$200\,\frac{\text{ml}}{\text{min}}$
Propagated error	19.9%	21.9%	30.0%	32.4%

10.3 Results

Figure 10.8 shows a sequence of the images recorded for a rabbit's aorta. Figure 10.9 shows an aorta with a well visible source of leakage. In the shown case due to an insufficiently glued branch. The evaluation of such images was often not possible as the conservation of mass principle was not obeyed in the vessel. Moreover, background illumination by the leaked blood interfered with the segmentation. This was the case for six out of eleven aortas.

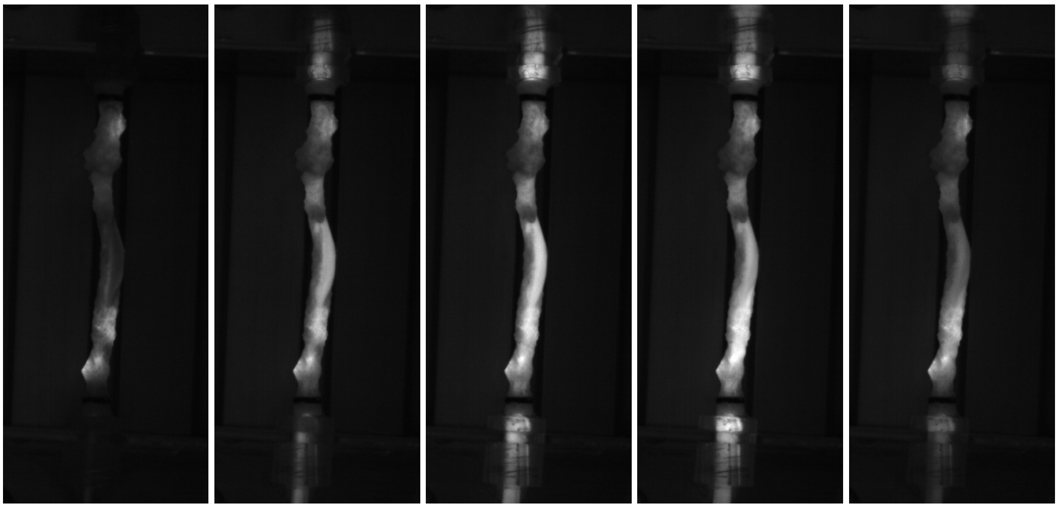

Figure 10.8: An image sequence of the transit of the ICG bolus through a rabbit's aorta. The time is increasing from left to right. The first image shows the vessel before the arrival of the bolus. The second to forth image show the increasing fluorescence intensity and hence the inflow of the bolus. The fifth image shows the wash-out of the bolus.

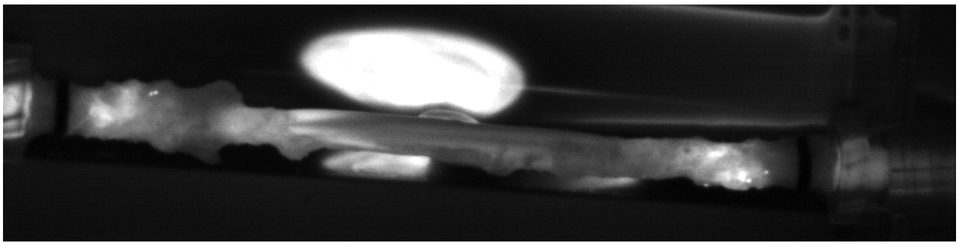

Figure 10.9: This aorta had a source of leakage due to an insufficiently glued branch in the middle of the vessel. In the background, the leaked fluorescent blood remained and disturbed the analysis of this recording. Moreover, the flow meter was placed before the location of the leakage, hence the net volume flow varied within this section. Such data was excluded from the analysis.

Table 10.3 shows the results of the volume flow measurement by the reference and the proposed method. It also shows the blood's temperature and the pressure close to the artery.

Furthermore, the relative propagated error is shown to put the spread of the values measured by the proposed method into perspective of the expected spread. It addresses the first hypothesis in Section 10.1. Using the Mann-Whitney-U-test for significance resulted in a $p < 0.05$ between all measured flows by the proposed method and hence a change in the input was followed by a significant change at the output.

Table 10.3: All measured values in this table are given as mean value ± standard deviation. The reference flow, pressure and temperature were obtained from the industrial flow meter and pressure gauge. The proposed method measuring the flow optically via FA yielded a deviation given in the table. The deviation was calculated as the fraction of the flow value obtained by the proposed method divided by the reference method. The relative propagated error was determined based on the fundamentals given in Chapter 7.1 and findings in Chapter 8.

Reference in $\frac{\mathrm{ml}}{\mathrm{min}}$	**Proposed method** in $\frac{\mathrm{ml}}{\mathrm{min}}$	**Deviation**	**Relative error** (propagation)	**Pressure** in mmHg	**Temperature** in °C
59.2 ± 0.4	75.7 ± 20.4	1.28	± 0.20	26.2 ± 0.7	23.0 ± 0.2
122.1 ± 0.2	130.0 ± 42.2	1.06	± 0.22	58.0 ± 0.7	23.1 ± 0.2
183.9 ± 0.7	187.6 ± 47.1	1.02	± 0.30	81.0 ± 1.3	24.4 ± 0.3
205.6 ± 0.5	207.9 ± 31.0	1.01	± 0.32	96.8 ± 1.7	24.0 ± 0.3

Table 10.4 shows the response of the proposed method to a stepwise increase of flow. It addresses the second hypothesis in Section 10.1.

Table 10.4: This table shows in the first column the ratio of the ground truth. The other columns show the ratio of measured flow values related to the measurement at 60 $\frac{\mathrm{ml}}{\mathrm{min}}$. A1 to A5 indicate the different aortas used to obtain the measurements. It is visible in Table 10.3 that the reference is very close to the designated flow values. Hence, the designated values were chosen as reference for the purpose of simplification.

Ratio	**A1**	**A2**	**A3**	**A4**	**A5**
120/60=2.00	1.04	1.67	1.53	2.22	1.76
180/60=3.00	1.75	3.02	2.34	2.88	3.06
200/60=3.33	1.84	3.27	2.91	3.44	3.06

10.4 Discussion & conclusion

The utilization of *ex vivo* experiments are a necessary step prior to conducting *in vivo* studies to ensure the work flow and accuracy of the algorithms are suitable. In the following paragraphs, the single aspects of the experimental setup are discussed. The results of the experiments and the hypotheses are discussed at the end of this section.

Biological material Although the blood contained anticoagulants, it still had formed clots occasionally. Clotting is problematic for multiple reasons. First, it can obstruct the flow or even clog the pipe. Within all experiments, nine occlusions happened and were followed by a drastic increase of pressure in the devices and tubes. In three cases, the connectors detached and blood spatter happened. The flow meter was identified as the main occlusion area and a meter with a larger diameter might not solve this issue but rather shift it (the flow meter was placed at the beginning of the stream, see Figure 10.1). Second, clots interfere with the measurements as they disturb the flow in general. Moreover, if a clot is formed and enters the bolus a displacement of the blood with ICG happens and appears as a dark spot in the timewise course of intensity.

Although clotting happened rather rarely, preventing them would increase the efficiency and accuracy of the setup. It was observed that clots mostly formed in the reservoir or even in the containers as delivered by the slaughterhouse. Therefore, placing a filter or sieve in front of the intake could reduce the amount of clots in the system. Its condition should be checked regularly because it affects the flow due to a higher resistance at the intake with increasing obstruction of the filter.

The temperature of the blood influences the blood's viscocity [263]. The blood was warmed up to 25°C but the tubes and devices were influenced by the ambient room temperature. Controlling the ambient temperature by either installing a sophisticated room temperature management or tempered tubes (e.g. placing them in a tempered water reservoir) and devices could reduce the influence of the ambient temperature.

Blood is a natural product and was obtained in different batches from a slaughterhouse. Its hematological profile and hence properties face a significant and systemic variability linked to age, food composition and physiological status [280]. The variations of the blood's properties were not analyzed in this work and were assumed to be constant for all experiments.

Vessel The aorta abdominalis of the rats was extracted and its use was intended to mimic small human cerebral vessels. The extraction requires expertise and is challenging for a non-specialist. Due to its small size, installed ligatures or glue to close branches were disturbing the view on the vessel too much. Moreover, attaching the aorta to the connector resulted in the rupture of the tissue or non-concentric alignment of both which negatively influenced the flow behavior.

The aorta abdominalis of the rabbits was extracted by professionals at the University Medical Center Freiburg. Its branches are larger and hence easier to detect and close. Nonetheless, some aortas could not be sealed properly, which resulted in blood leaking underneath the glue and potentially the development of a residual volume. In Figure 10.10 at the red arrow, a residual volume is present. In five cases, a non-concentric alignment between the aorta and the connector was visible. In those cases, the aortas were not used for the experiments. Generally, working with the rabbit's aorta was more convenient and less penalizing than working with a rat's aorta. Using a different arterial model with less branches than an aorta should be considered to reduce the amount of manipulation of the artery.

Experimental setup The experimental setup worked well but had some aspects that can be improved.

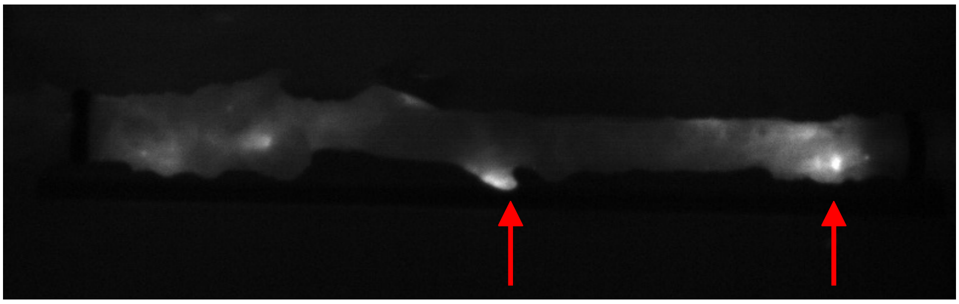

Figure 10.10: After a washout time of five minutes, the shown aorta still had remaining ICG containing blood. The vessel was sealed by gluing and the vessel was leakage-free. Nonetheless, a branch might not have been closed but rather covered with glue. Hence, a residual volume between vessel and cover was present and yielded remnant fluorescence.

The peristaltic pump was able to provide all necessary flow values for the experiments. The nature of these type of pumps yielded a pulsatile flow. The air volume in the air trap and the elasticity of the tubes acted as a low-pass filter and hence dampened the pulsatility. In Figure 10.11 (top plot) the present pulsatility is shown. Although it was very small ($< 1\%$), replacing it with a rotary pump could eliminate the pulses. Nonetheless, the disadvantage of a rotary pump is the required higher effort in cleaning.

The air trap had a manual valve for the case that too much air was trapped in it. This required the user to check it, an automatic air release valve could be considered to relief the user from this task.

The injection system worked well and robustly. Nonetheless, it was manually operated and hence an inter- and intra individual variability was present. Exchanging the manual three-way selector valves by synchronized automated valves would increase the automation of the setup and its standardization. Switching between route A and B provoked a short interruption of flow and the flow needed a small amount of time to recover. In Figure 10.11 a switching process is shown. The switching of the valve led to a sharp pressure drop as the pressure gauge was placed behind the valves and the flow was restricted by the switching. This was visible in the measured pressure profile. Afterwards, an overshoot was visible due to the capacitive behavior of the tubes and devices placed before the valves. The same behavior was visible for the flow but temporally broader. The optical measurement based on the proposed method was exclusively performed after the recovery of the flow after a few seconds (in the shown case, after time points $t > 5154\,\mathrm{s}$). The proposed vessel connector was convenient to use and easy to fit to different vessel diameters and lengths. Attaching the vessel onto the barbed nozzle of the Luer connector held the challenge of aligning them into perfectly concentricity. Otherwise, a disturbance of flow was present at the transition from connector to vessel and vice versa. Figure 10.12 shows a non-concentric alignment at the white arrow and a concentric alignment at the red arrow. The setup used an industrial pressure gauge and flow meter. The flow meter provided the reference flow value. Its accuracy was approved for blood as a medium. Its sampling frequency of $f_{sample} = 100\,\mathrm{Hz}$ showed to be sufficient to measure the reference flow.

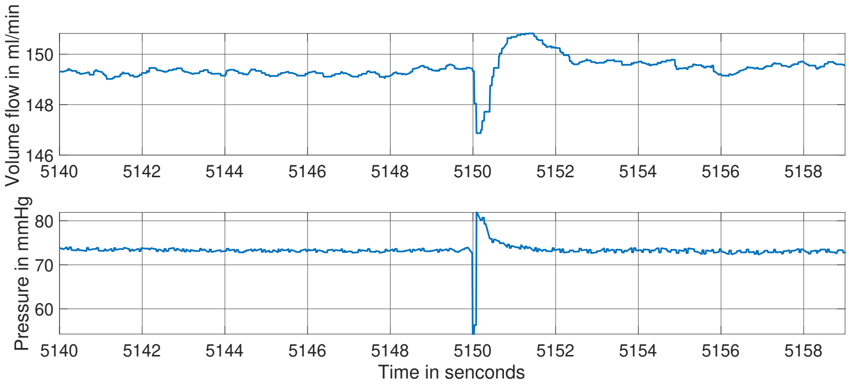

Figure 10.11: Turning the valves to redirect the flow from route A to B and vice versa provokes a short interruption of flow. The top plot shows the volume flow and the bottom plot the pressure in dependence of the time. At approx. $5150\,\mathrm{s}$ valves 1 & 4 were turned and hence the flow redirected. This switching process results in a characteristic timewise morphology of flow and pressure. The flow measurement by the proposed method should only by conducted after the flow has recovered from the interruption ($t > 5154\,\mathrm{s}$).

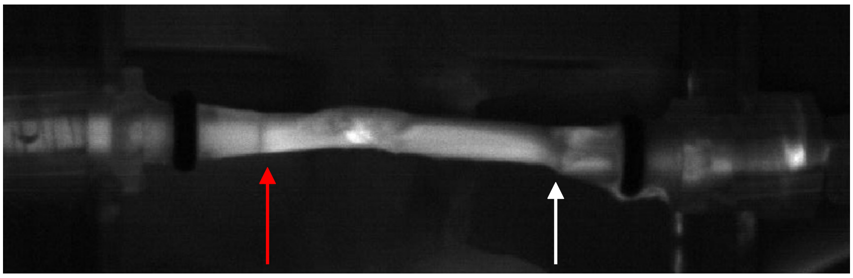

Figure 10.12: The red arrow points at a concentric aligned aorta and connector. The arrow is placed at the end of the connector and no constriction is visible. The white arrow points at a non-concentric aligned aorta and connector. An asymmetrical constriction of the aorta is visible. It affected the flow as seen by the heterogeneous fluorescence.

The settings of the camera (exposure time and gain) were chosen to use the whole 12 bit color depth without going into over saturation at a reasonable frame rate. The gain of 12 dB should be reduced since it amplifies noise as well. Although the cameras chip is NIR enhanced, a more sensitive camera with a larger pixel size (current camera: $5.5\,\mu\mathrm{m} \times 5.5\,\mu\mathrm{m}$) would yield a less noisy image. Having a less noisy image results in a higher accuracy in the time measurement (see Section 8.4.2.2).

Evaluation of flow The results of the *ex vivo* experiment are very promising and serve as a first proof of concept of this type of measurement. So far, no proof of concept of a FA based method of quantifying blood volume flow was published.
The results in Table 10.3 show that the ground truth was very stable throughout all experiments. The resulting flow from the proposed method was corrected for the identified systemic error (see Chapter 9). The determined mean flow values by the proposed method agreed well with the reference for the flow values of $120\,\frac{\mathrm{ml}}{\mathrm{min}}$ and above. For the flow value of $60\,\frac{\mathrm{ml}}{\mathrm{min}}$,

a deviation was observed. This behavior is contradictory to the expected accuracy of the measurement: the propagated relative statistical error is smaller at small flow values and thus the deviation for the flow of 60 $\frac{\text{ml}}{\text{min}}$ was expected to be smaller than for larger flow values.

The first hypothesis is validated for all flows higher than 120 $\frac{\text{ml}}{\text{min}}$. For the flow of 60 $\frac{\text{ml}}{\text{min}}$, the hypothesis cannot be validated.

Compared to the reference, the statistical spread of the flow values determined by the proposed method were much larger. For all flow values, the spread was in a similar order of magnitude. The propagated relative statistical error analyzed in Chapter 8 and given in Table 10.3 matches the observed spread in this experiment well. This emphasizes the validity of the approach and its results. A difference is still present and can be traced back to the fact that the analysis in Chapter 8 did not include some sources of errors such as the segmentation error or projection error (although the latter is not expected in this setting since the vessel was perfectly straight and in the focal plain).

The second hypothesis was validated for four out of five aortas. Table 10.4 shows that the measurement followed the increasing flow at the input for the aortas A1 to A4. Aorta A1 showed a small step for the step from 60 $\frac{\text{ml}}{\text{min}}$ to 120 $\frac{\text{ml}}{\text{min}}$. Aorta A5 showed a difference in the third decimal place for the step from 180 $\frac{\text{ml}}{\text{min}}$ to 200 $\frac{\text{ml}}{\text{min}}$. Taking the propagated relative statistical error (Table 10.2, appox. 30%) and the step sizes into account, there is a high probability of not being able to distinguish small steps as present from 180 $\frac{\text{ml}}{\text{min}}$ to 200 $\frac{\text{ml}}{\text{min}}$ in a singular case. Nonetheless, for all aortas the step from 60 $\frac{\text{ml}}{\text{min}}$ to 120 $\frac{\text{ml}}{\text{min}}$ and to 180 $\frac{\text{ml}}{\text{min}}$ was very clear. Performing a significance analysis for each aorta and step is possible but not trustworthy with so little experiments performed for each step. Nonetheless, using all measurements (on all aorta) proved significant changes for each step size using the Mann-Whitney-U-test ($p<0.05$).

The ratio of increase for any step size across all aortas showed a large range (e.g. 180/60 for A1: 1.75 and for A5: 3.06). A deviation across multiple measurements was expected due to the propagated relative statistical error. A deviation across multiple aortas can be derived from the natural deviations in the anatomy of the vessel and changes of its geometry due to the manipulation of the aorta (sealing it). These characteristic changes of the geometry and hence the flow could have caused the deviations observed.

The systemic error derived and quantified in Chapter 9, assumed a laminar flow with a parabolic flow profile. In Figure 10.13, the single images show the timewise course of the spatial fluorescence intensity. It is visible that the fluorescence intensity was shifting from the left to the right of the artery. As the fluorescence intensity depicted the velocity field in the artery, an asymmetric flow profile has to be assumed. This violates the assumption made to calculate the systemic error (parabolic flow profile). To minimize the influence of the asymmetric flow profile, the first arrival of the bolus was used to extract the bolus' transit time. This improved the measurement, as the first arrival time is less affected by the asymmetric flow profile.

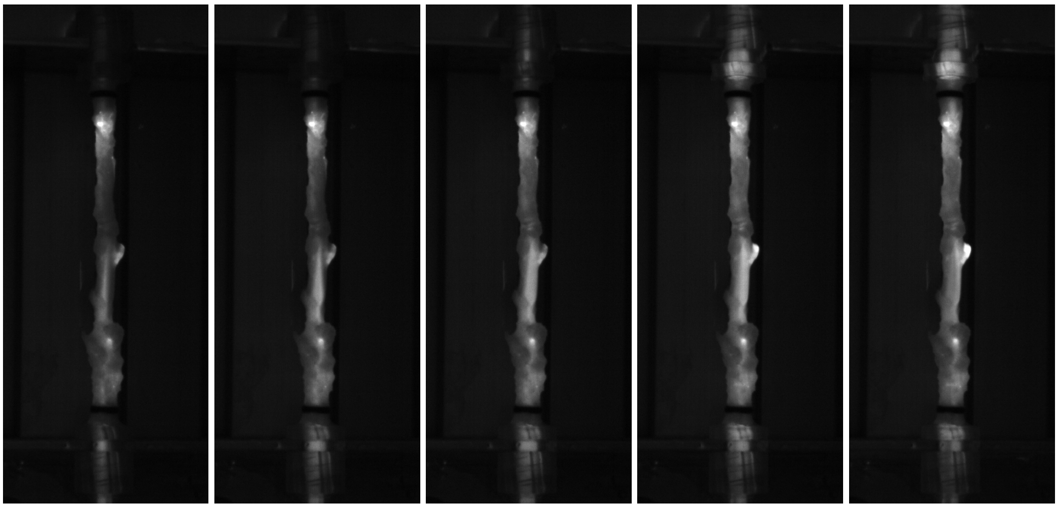

Figure 10.13: An image sequence of the transit of the ICG bolus through a rabbit's aorta. The time is increasing from left to right. The first image shows the first arrival of the bolus. Notice that the fluorescence intensity is high left of the centerline of the vessel. With increasing time the fluorescence intensity shifts to the right side of the centerline. This indicates an asymmetric flow profile and hence a violation of the assumption made in Chapter 9 to calculate the systemic error.

10.5 Outlook

For future *ex vivo* experiments, some possibilities for the improvement of the setup were revealed by the past experiments. A different arterial model should be considered. Thereby, using an artery with less branches is in focus to reduce the manipulations (gluing the artery or installing ligatures). A filter should be placed in front of the intake to prevent clots to enter the system. An automated air release valve in the air trap would reduce and simplify the necessary tasks of the user. Automated three-way selector valves at the injection system would increase the standardization of the setup and ensure the repeatability of the experiments. A temperature management system should be installed to ensure a constant ambient temperature. The current lab is conditionally suitable since it neither has an active climate control nor a window blind. Hence, a structural remodeling of the lab or a closed sub-system with constant temperature is required. The connection of the arteries to the system is currently realized by barbed nozzles. The nozzles are larger than the artery to prevent leakage. This leads to a constriction of the artery right after the transition from connector to artery in case of not perfect concentric alignment. Nozzles with a thinner wall would allow a better match of the connector's to the artery's diameter and hence prevent disturbance of the flow. Furthermore, a camera with a higher sensitivity could increase the SNR of the recording and therefore yield a smaller error in the measurement of the bolus transit time.

The results of the *ex vivo* experiment are very promising and serve as a first proof of concept of this type of measurement. A transition to an *in vivo* study should and was conducted in Chapter 11 to proof its suitability in a clinical environment.

Chapter 11

In vivo study

The overarching goal of this work was to enable an intraoperative and quantitative measurement of blood volume flow via fluorescence angiography (FA). The *ex vivo* experiment in Chapter 10 proved the validity of the proposed approach in a lab setup. In this chapter, the proposed methods and the work flow were utilized to provide a proof of concept of the blood volume flow measurement in an *in vivo* setting. *In vivo* (Latin: "within the living") means that the subjects used in this study were alive. The acquisition of the data was performed by collaborators from the Department of Neurosurgery at the Stanford University School of Medicine.

11.1 Introduction

In vivo studies allow the assessment of a method's performance in a realistic environment. Therefore, recordings from cerebrovascular surgery on humans were obtained. A data set for one subject had to contain a ground truth flow measurement and the FA video data. The requirements on the data were described in Section 6.1.

By comparing the computed blood volume flow by the proposed algorithm and the reference flow, an assessment of the accuracy of the proposed method in its use case situation can be performed. This does not necessarily reflect the clinical relevance of the optical measurement of blood flow via indocyanine green (ICG) FA but its agreement with the current gold standard (US-flow probe, see Section 4.2).

The hypothesis is:

1. The blood volume flow computed by the proposed method is for all subjects within the valid flow range determined by the current gold standard (US-flow probe).

11.2 Materials and methods

11.2.1 Patients & surgical procedure

Patients facing moyamoya disease (MMD) underwent surgical treatment at the Department of Neurosurgery at the Stanford University School of Medicine. MMD is a cerebrovascular disorder characterized by a progressive occlusion of the internal carotid arteries and their branches with the development of an abnormal vascular network in the areas of occlusion [281]. The clinical manifestations are predominantly ischemic although hemorrhagic complications can also occur [282]. Possible treatment involves surgical revascularization of the cerebrum [49, 283, 284]. All patients in this study were treated by a direct artery-to-artery anastomosis with an extracranial-to-intracranial (EC-IC) bypass (see Section 2.3 for details on the procedure).

17 patients underwent EC-IC bypass grafting and were included in this study (8 males with a median age of 48 years and a range from 17 to 54 years / 9 females with a median age of 33 years and a range from 12 to 54 years). Tow separate phases of the surgery were present: before and after bypass grafting. The data sets before installing the EC-IC bypass were analyzed in this study. Specifically, the blood flow in a branch or section of the middle cerebral artery (MCA) was suitable for the investigation since it was exposed and well visible in the video recordings and a reference flow was given.

During surgery, the flow was measured via an US-flow probe and an ICG FA video was recorded as well. Both modalities will be described in the following two sections.

11.2.2 Reference flow measurement

The clinical protocol included the measurement of the donor vessel's (superficial temporal artery (STA)) and recipient vessel's (MCA) size and blood flow value. Both measurements were performed intraoperatively using the following devices:

- Ruler Micro-Scale metric 5mm (minitool Inc., Campbell, CA 95008, USA)
- Surgical flow probe Transonic Intracranial Charbel Micro-Flow Probes® (Transonic Systems Inc., Ithaca, NY 14850, USA)
- Recording device Transonic Optima-Flow QC® (Transonic Systems Inc., Ithaca, NY 14850, USA)

The size of the vessels was used for an additional plausibility test for the automatic diameter measurement included in the proposed method. As the microscope did not output the image's scale, the ruler served as a reference for the scale of the image.

The vessel was placed in the US-flow probe as shown in Figure 11.1 and the flow was recorded for a duration of at least 10 seconds. The flow was saved as a minimum and maximum value. Hence, for each patient a specific range was given which allowed the evaluation of the performance of the proposed method.

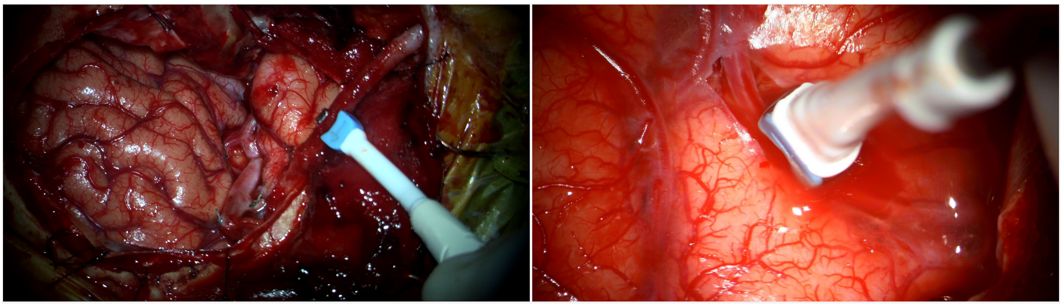

Figure 11.1: Both images show the application of the US-flow probe (white device with a blue tip). It must be placed around the vessel to measure the blood volume flow. Vessel compromise and rupture are possible [5]. Furthermore, by applying the probe the flow can be affected. The usage of the flow probe requires the surgeon to change instruments. **Left**: A flow probe was applied to the STA (extracranial artery). The usage of the flow probe is convenient as long as the vessel fits the probe well. The STA had a diameter of approx. 1.7 mm. **Right**: A flow probe was applied to a section of the MCA (intracranial artery). Generally, the usage of the flow probe is more challenging on the MCA since it is embedded in tissue. The MCA had a diameter of 1.5 mm.

11.2.3 Fluorescence angiography

The FA was performed using the following devices and agents after intravenous administration of ICG:

- Surgical microscope ZEISS KINEVO® 900 (Carl Zeiss Meditec AG, Jena, Germany)
- ICG (Diagnostic Green LLC, Farmington Hills, MI 48331, USA)

The FA was recorded using the FLOW® 800 software of the microscope. The software assists in recording the video and metadata. A recording consisted of a video of the MCA starting before the ICG bolus had arrived in the field of view of the camera and ended during the washout of the ICG. The recordings varied in length between 30 and 60 seconds. During the recording, the surgical microscope was kept still and the setting was not changed. The videos were recorded on a hard disc and the flow was determined retrospectively.

11.2.4 Retrospective evaluation of flow

The flow was extracted from the videos by the workflow described in Chapter 6 which proved to perform well on *ex vivo* data (see Section 10). The single steps of the algorithm will be shortly introduced and necessary details will be given in the following paragraphs.

Pre-processing of the videos In some cases, the recorded video was of excessive length. Temporal pruning was necessary to avoid prolonged processing times in the following steps. The pruning was introduced in Section 6.2. The first arrival of the ICG bolus was determined by the first time point at which the average fluorescence intensity exceeded 0.5% of the maximum of the average fluorescence intensity of each frame. The end of the video was determined manually to exclude the recirculation of the bolus (Figure 6.2).
All videos contained relative motion of the vessel and camera. The proposed motion compensation in Section 6.2 was applied.

Frame selection and segmentation The automatic frame selection presented in Section 6.3 was applied and yielded a frame suitable for segmentation. The segmentation introduced in Section 6.4 needed the user to determine the vessel of interest (using the largest structure or the one in the middle of the frame did not yield good results since the observed *in vivo* variability was large). Moreover, branches appeared frequently at the vessel of interest, so the user needed to decide which branches to include and exclude in the segmentation. Both user interactions were performed sequentially. Figure 11.2 shows the raw frame, its segmentation and the segmentation after user interaction.

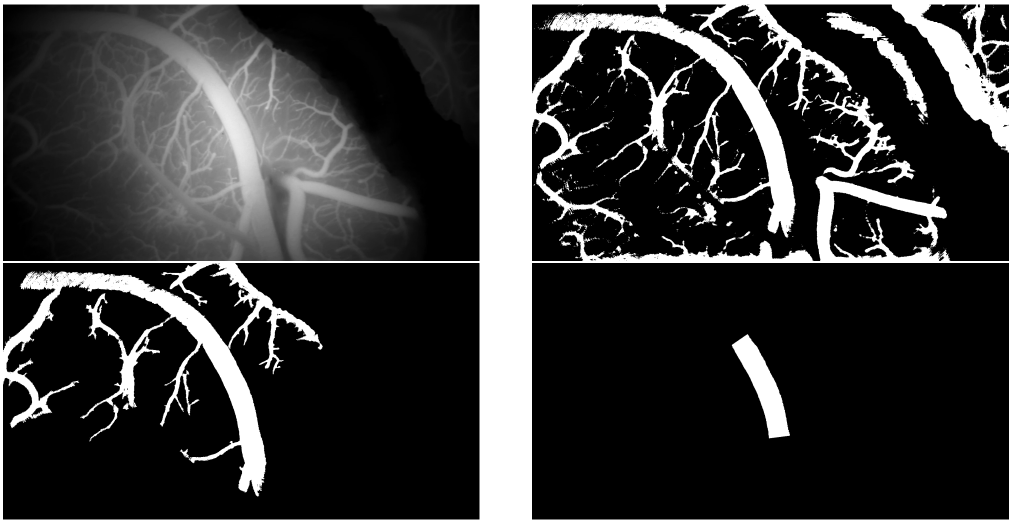

Figure 11.2: Top left: The automatic frame selection identified a frame that was suitable for segmentation. **Top right**: The initial segmentation assigned many vessel to the foreground. **Bottom left**: The user picked the vessel of interest. **Bottom right**: The user picked a section of the vessel which is free of branches. This segmentation mask was used for further analysis.

Length and diameter measurement To measure the length s and diameter d of the vessel a scale was needed. The scale was extracted manually from the recorded ruler (see Figure 6.6 in Section 6.6). It resulted in an individual scale for each case (in mm/pixel). Afterwards, the centerline was extracted by erosion, the diameter determined and the continuous length measured using the piecewise Bézier curve fitting (see Section 8.2.1.2 and Section 8.2.1.3).

The diameter was extracted for each pixel of the centerline and used to obtain the cross sectional area of the vessel. Afterwards, the mean cross sectional area A was calculated and used for the calculation of the blood volume flow.

Bolus transit time measurement Two indicator dilution curve (IDC) were acquired at the ends of the centerline to extract the bolus transit time. The IDC were obtained as the frame-wise average fluorescence signal within a squared region of interest (ROI) that had an edge length of a third of the respective diameter value at this location. The same temporal feature as in the *ex vivo* experiment was used to asses the transit time ($t_{transit}$): mean time difference of the two IDCs at 2%, 3%, 4%, 5%, 7%, 10% of maximum fluorescence intensity. This feature holds the least amount of diameter dependent systemic deviations based on the findings in Chapter 9. The systemic error was set to $\varepsilon_{sys}(d) = -0.120 \cdot d + 1.297$ for $d \in [1\text{mm}, 2\text{mm}]$ according to the findings in Chapter 9 (see Equation 9.16).

Determination of blood volume flow The transit time $t_{transit}$ of the bolus to travel the geodesic distance s and the mean cross sectional area A were obtained as described before. The observed blood volume flow was corrected and calculated as given in Equation 11.1. The determined value for ε_{sys} in Equation 9.16 were used for the correction. Since ε_{sys} depends on the diameter of the vessel, it was calculated for each vessel individually.

$$\dot{V} = \varepsilon_{sys} \cdot A \cdot \frac{s}{t_{transit}}. \tag{11.1}$$

Comparison with the reference blood volume flow value The reference flow was given as a minimum and maximum value. This is due to the time resolved measurement by the US-flow probe and the variability of blood flow over time. The flow value computed by the proposed method yields a single value for each measurement. Hence, the computed value should be within the minimum and maximum flow range of the reference.

11.3 Results

The flow value computed by the proposed method matched the reference flow range in 8 out of 17 subjects (see Figure 11.3). Taking into consideration the determined accuracy of the proposed method (±20%, see Section 8) and the accuracy of the US-flow probe (±10%) another 4 subjects were in this range. For the remaining 5 subjects, the flow deviated from the reference by more than 30%. No correlation was observed to the age or sex of the patients.

11.4 Discussion & conclusion

The quantitative measurement of blood volume flow via intraoperative FA in an *in vivo* setting was performed. The reference yielded a flow range with a maximum and minimum

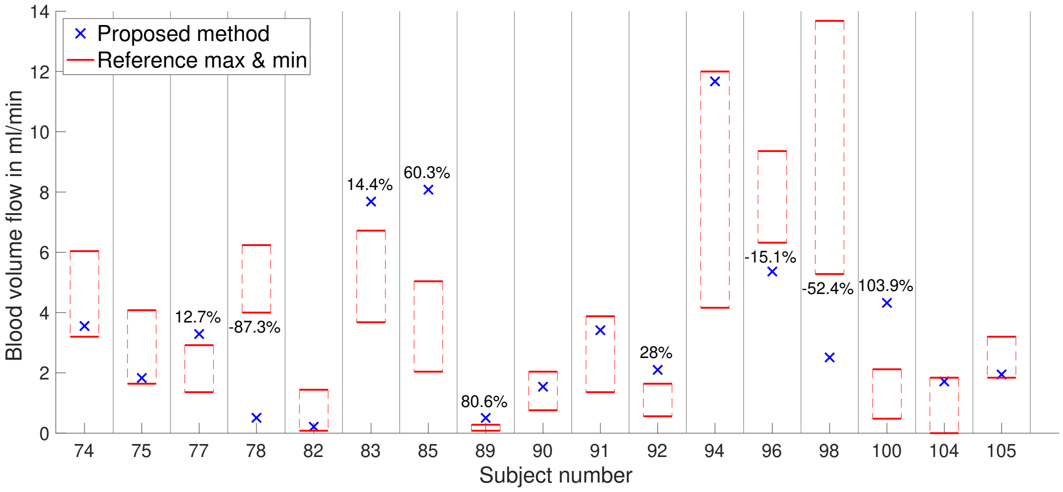

Figure 11.3: The subject numbers are shown on the abscissa and the blood volume flow is shown on the ordinate. A reference flow was given as the minimum and maximum flow measured by the gold standard method and marked by red horizontal lines. The blue crosses indicate the computed flow value for each subject by the proposed method. Whenever the determined flow by the proposed method did not match the reference flow range, the percentage of the deviation is specified.

value, which emerged from measurements taken over multiple heart beats. The cardiac cycle with its systole and diastole yields a pulsatile flow. The computed flow using the FA data yields a single value. Comparing it with a mean value (mean of maximum and minimum) does not make sense, since it was not temporally synchronized to the cardiac cycle. Hence, using the measured flow range of the reference device is valid for the determination of the accuracy of the proposed method.

The hypothesis that the blood volume flow computed by the proposed method lies for all subjects within the flow range determined by the reference was falsified. In 5 cases, the deviation was too large. Nonetheless, the results are in the same order of magnitude and in well agreement with the reference. To put the deviations into a clinical context, the observed relative changes before and after installing the bypass of all subjects was analyzed and are given in Figure 11.4 as box plots. The minimum increase of flow due to the revascularization surgery was 185% and a median value of 381%. This emphasizes that the discussion of the results must be split into a technical view and clinical view which is done in the following.

Technical view on the results The accuracy of the flow measurement by the proposed method was affected negatively by not perfectly fulfilling the requirements upon recording. The ruler is prone to errors. A tilted ruler introduces an error (cosine of the angle). Figure 11.5 shows a ruler with only one end in the focal plane. This indicates that the camera and ruler were not parallel to each other and hence, the extracted scale is overestimated. An erroneous scale affects the diameter and length measurement and thus has a large effect by the error propagation on the flow. The presence of a tilted ruler was ascertained for one

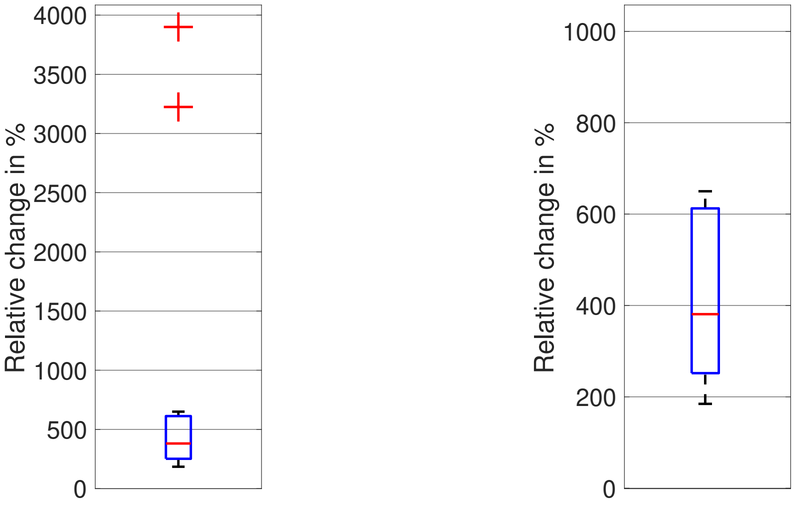

Figure 11.4: The relative increase of the blood volume flow after the installation of the bypass was analyzed and is shown as a box plot. Both plots show the same box plot. The plot to the right shows details of the section from 0 to 1000%. The median is at 381%. The 25th percentile is at 252%, the 75th percentile is at 613%. The minimum is at 185%, the maximum is at 3900%.

subject (subject 85, see Figure 11.5) and it has most probably contributed to the deviation since it is positive (+60.3%).

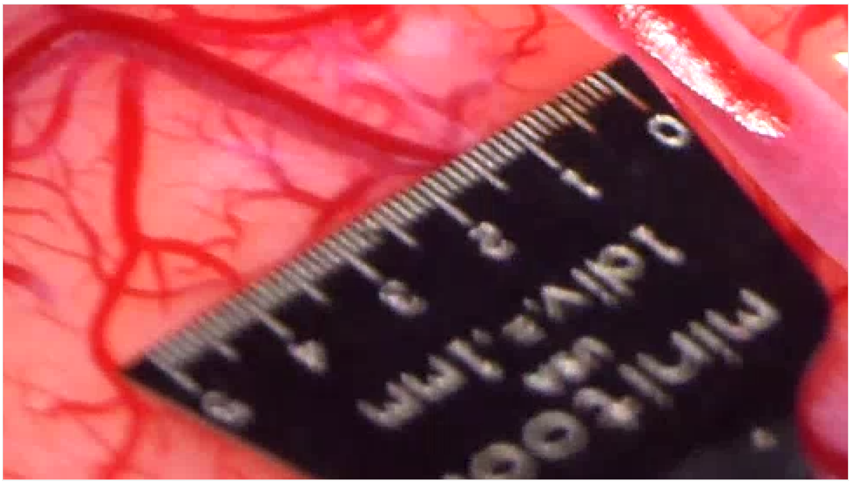

Figure 11.5: The ruler used to extract the scale in subject 85 was tilted. This is indicated by a focused and another defocused end. This introduced an overestimation of the scale and hence of the flow. This is also reflected in the results in Table 11.3

Branches in the measurement area interfere with flow measurement technique. At a branch, a fraction of the flow is lead off (according to the nodal rule). As shown in Figure 11.6, small branches appeared in the middle of the artery and were present for both measurement techniques. The proposed method measured the volume flow along the vessel. An error occurs in case a branch was present between the start and end of this measurement distance. This was avoided by the user partitioning the vessel, so that no large branches are included. Nonetheless, small branches might in inevitable. The presence of excessive branches was observed for 2 subjects (subject 78 and 100, see Figure 11.6). For subject 78, it probably influences the measurement since the deviation is negative. In subject 100, the deviation is positive and cannot be traced back to excessive branches. The influence of a small branch on the measurement error was not investigated. Whether a branch influences the flow measurement by the US-flow probe similarly, is not clear and no publication was found taking small branches into account.

The flow probe was used as reference. Its correct use is important to obtain accurate flow values, which was assumed in this study. Nonetheless, the flow values measured are close the maximum zero offset of the device ($\pm 3\,\frac{\text{ml}}{\text{min}}$ and $\pm 5\,\frac{\text{ml}}{\text{min}}$) [168]. Hence, an inaccurately performed zero offset compensation would have a large relative influence on the measurement.

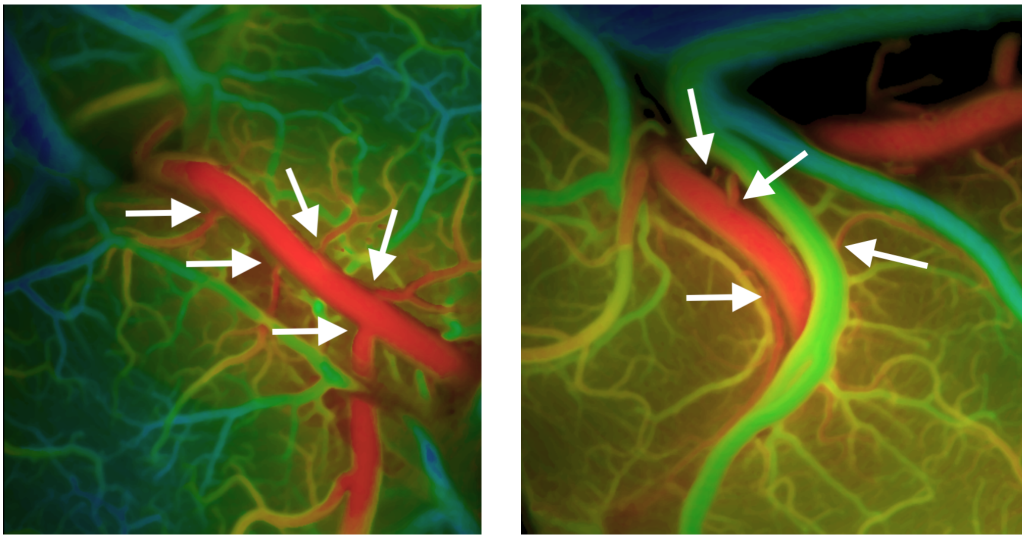

Figure 11.6: Both images show different intracranial arteries before the bypass installation. The color code shows the temporal delay of fluorescence. Red indicates that the fluorescence arrived in the respective spot early and blue indicates a late arrival. Structures of similar color are most likely connected. In both cases, the vessel of interest was the red large vessel in the middle. The white arrows indicate branches that lead off.

Conservation of flow at large branches One advantage of the proposed method is the ability to analyze the volume flow of different vessel in the field of view simultaneously. An US-flow probe needs to get in contact with the vessel for the flow measurement and hence is not capable of measuring the flow at different vessels simultaneously.

The nodal rule states that the sum of the flow in each branch at a junction must add up to zero (conservation of flow). Two cases included large branches in the field of view and an analysis of each branch was performed. The cases are shown in Figure 11.7. The determined flow values for the vessels in the left figure comply perfectly with the nodal rule. The flows determined for the vessels in the right figure comply with the nodal rule only when taking the statistical error into account.

Analyzing multiple vessels at once was not required in this thesis but might be useful in the surgical treatment of complex vascular structures.

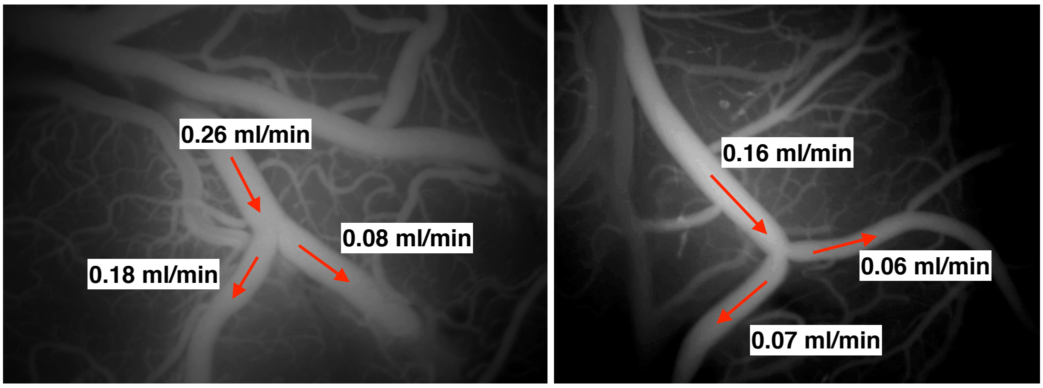

Figure 11.7: Two subjects exhibited a large bifurcation of the artery. The proposed method was used to assess whether the conservation of flow was valid at the junction. Therefore, the blood volume flow of all branches was calculated and is shown in the image. The arrows depict the flow direction. The sum of the flows in the left image was zero and in the right image $0.03\,\frac{\mathrm{ml}}{\mathrm{min}}$ or 18% of the inflow.

Clinical view on the results In subject 98, a clear underestimation of the flow was present. Taking a closer look at the video data revealed that the vessel was in spasm while recording the FA data (see Figure 11.8). Hence, a smaller cross sectional area, a higher resistance and a lower flow were present. The reference was most likely not measured in the presence of a spasm according to the surgeons.

The hypothesis set in Section 11.1 was falsified. Nonetheless, the hypothesis was driven by technical ambition. Whether the requirements to match the reference measurement is clinically relevant, needs to be determined. The goal of a revascularization surgery is to restore the blood flow. Figure 11.4 indicate that the increase in blood flow is significantly higher than the observed deviation of the proposed method to the reference method. Its complementary use besides the US-flow probe or in the cases were US-flow probes yield the risk of vessel compromise or rupture could benefit the surgeon. Hence, the proposed method is very likely suitable for the intraoperative, quantitative, and non-contact analysis of blood volume flow in cerebrovascular surgery. To confirm this thesis a clinical trail with a focus on the patients outcome is needed.

Relation to the state of the art The current use of ICG FA includes the anatomical visualization and qualitative functional imaging of vessels in the field of view of the surgeon [7–11]. Approaches to quantitatively analyze the bloods flow are present but yet do not yield a true quantitative flow measurement (in ml/min) [132, 134, 135, 285–291]. The

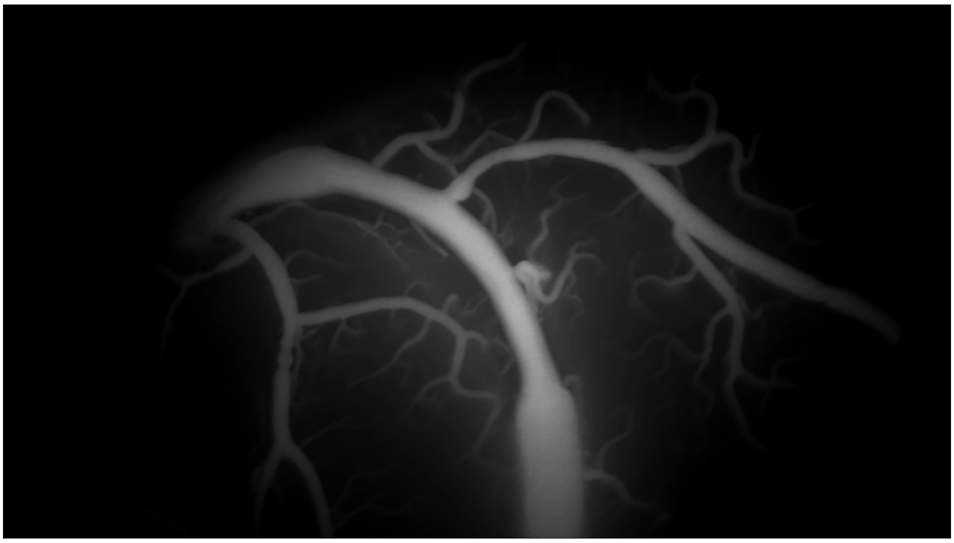

Figure 11.8: The vessel shown in this image has a variable diameter. According to the surgeon, the artery faced spasm (contraction of the arterial muscles) at the beginning of the surgery. Hence, the diameter was reduced. It is not documented whether the reference measurement was taken with or without the spasm. The measured flow by the proposed method was smaller than the reference which makes sense in the case that the reference was recorded without the spasm.

investigations performed by Weichelt et al. have attempted to quantitatively analyze the blood flow via ICG FA [137, 182]. Their results did not yield an accurate measurement on a large set of *in vivo* data. A detailed comparison with their methods is not possible since many details on the used methods were not described in their publications [137, 182].

To my best knowledge, the methods used and results obtained in the *in vivo* analysis performed in this thesis are a novelty to the community and pave the way towards a clinical use of this intraoperative, quantitative, and non-contact measurement of blood volume flow by ICG FA.

The current clinical state-of-the-art device to measure the blood volume flow is the US-flow probe. Its use yields a functional and quantitative assessment of the vascular flow. It is a quick, real-time, and temporally resolved measurement. Its main limitation is that it needs direct contact to the vessel and even needs to be wrapped around it (see Figure 11.1). This holds risks. More importantly, the requirement of contact is troublesome in the analysis of deep or embedded vessels. In contrast, the proposed method overcomes this limitation and does not require contact to the vessel. It requires the visibility of the vessel which is very likely since the surgeon needs to work on the vessel.

11.5 Outlook

The present analysis included 17 EC-IC bypass surgeries from 17 different subjects. The vasculature of the cerebral arteries is complex and unique for each individual [37]. Including more cases is necessary to test the algorithm and ensure its suitability.

Including other vascular surgeries into the analysis might reveal the methods versatility or limitations. For example, in aneurysm clipping surgery the patency of the vessel is of great importance and needs to be ensured. Using a flow probe on deep aneurysms is often not possible due to the narrow and deep working channel. The proposed method would overcome this limitation and can provide quantitative flow values.

The present analysis included only pre-operative cases (before installing the anastomosis). Analyzing the blood flow after installing the anastomosis is of great interest because the difference from pre- to post-operative flow is important to the surgeon. This might also reveal new points for improvement since the post-operative images have different anatomical features to the pre-operative. Figure 11.9 shows a pre- and post-operative image of the same artery.

The present microscope did not provide the image's scale and extracting the scale from a ruler is prone to errors. The microscope should be capable to provide a scale derived from the optical parameters.

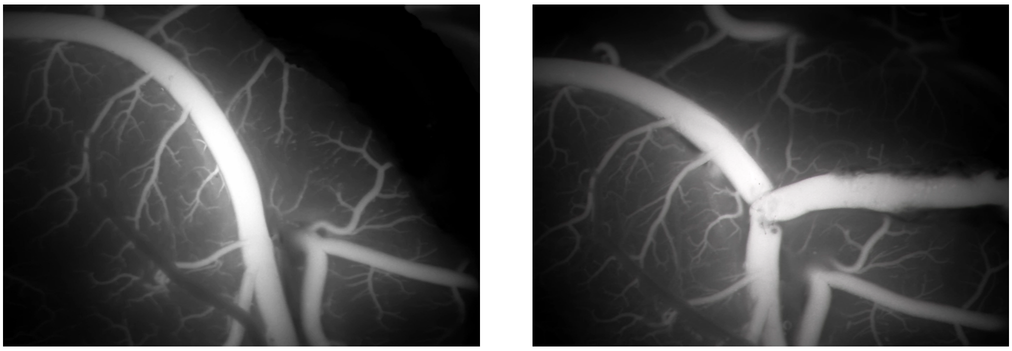

Figure 11.9: **Left**: the recipient artery before the installation of the STA as a donor. **Right**: the STA was sutured onto the recipient. The geometry of the vessel has changed slightly. Moreover, the area at the suture cannot be used for an evaluation of the flow. Hence, the suitable length of the vessel for an analysis is shortened.

So far, the analysis was performed retrospectively after the surgery was performed. Integrating the algorithms into a surgical microscope should be done and introduced to the operating room. The handling of the microscope and the software needs to comply with the physicians' workflow. Problems when applying the software might occur and must be solved to ensure a save and smooth workflow.

PART V

CONCLUSION AND OUTLOOK

Chapter 12

Conclusion

The overarching goal of this research was to develop an intraoperative, quantitative, and non-contact measurement of the blood volume flow using indocyanine green (ICG) fluorescence angiography (FA).

In order to do so, the geodesic length and diameter of the vessel needed to be determined. The proposed method to obtain both parameters needed a thorough validation of their accuracy. Hence, a data set containing the ground truth was required. This ground truth was obtained by creating a model utilizing mathematical functions projected onto a discrete pixel grid. This had the advantage of providing a reliable and precise ground truth of the geodesic length as the arc length of the mathematical functions. The analysis revealed that the ground truth length of the centerline of a vessel was extended by 6.3 % solely due to its discretization (no reconstruction of the centerline was involved). By taking the reconstruction by erosion and Voronoi diagrams into account, the error increased to 7.0 % and 7.9 %, respectively. This findings emphasize the need to develop methods to counteract the discretization error. By re-continualizing the centerline by piecewise fitted Bézier curves, the error was significantly reduced by more than 50 % (see Table 8.4). This validated the first hypothesis formulated in Section 8.1.1 and underlines the effectiveness of the proposed method in reducing the discretization error. Additionally, the dependency of the discretization error on the angular orientation of the structure was significantly reduced (see Table 8.8 & 8.9 and Figure 8.11). This validated the second hypothesis formulated in Section 8.1.1 and underlines the robustness of the proposed method. In fact, the decoupling of the discretization error on the angular orientation of a structure is essential to state a generally valid error margin. Otherwise, an individual orientation needs to be determined which would increase the computational effort. The computed discretization error of straight lines and the angular dependency of the error were also confirmed by an experiment using tubes filled with contrast agent. The mean relative error of the measurement of the diameter was approx. 3 %, which is assumed acceptable. Nonetheless, the diameter has a large influence on the flow calculation because it is squared in the formula (see Equation 7.5). Other methods of determining the diameter should be taken into consideration for future work. A more detailed discussion is given in Section 8.4.1.

Additionally to the length and diameter of the blood vessel, the transit time of the moving ICG bolus inside the vessel had to be determined. Analogously to the analysis of the geometrical parameters, a data set containing a ground truth transit time was generated. For this purpose, a fluid flow simulation was set up and multiple indicator dilution curves (IDCs) were acquired. These IDCs were morphologically similar to the data obtained from an experimental setup and human *in vivo* data. The IDCs were further processed to create the desired data set. The analysis revealed that a re-continualizing of the curves by a mathematical function enhances the accuracy in the transit time measurement drastically for all applied noise levels. This validated the first hypothesis set in Section 8.1.2. Thereby, the local density random walk (LDRW) function together with the gamma variate function proved to perform best. Moreover, the second hypothesis was also validated for a limited range of applied noise levels to the signal. This emphasizes that already at the recording of the data, noise should be attenuated as much as possible. A detailed discussion of the generation of the data sets and their evaluation is given in Section 8.4.2.

The presence of a systemic error in the flow measurement was proven in Section 7.2. Its compensation required a simulation of the photons' propagation in a vessel. To do so, a Fluorescence-Monte-Carlo-Multi-Cylinder (FMCMC) model was developed and validated. Beforehand, a fluid flow simulation was utilized to obtain the distribution of ICG in flowing blood. This distribution is limited to the given diameter and flow settings. A larger variation of input parameters such as the blood's viscosity or geometry is possible, yet time consuming. Regardless, the analysis of the propagation of photons in the vessel using the validated fluorescence FMCMC model revealed that the systemic error was not dependent on the volume flow but dependent on the diameter and the relative time point at which it was extracted, which validated both hypotheses. The dependency of the systemic error on the diameter was smaller at time points closer to the first arrival of the bolus. This finding is very important, since as mentioned before, the simulated diameter and flow settings were limited. The conclusion was drawn that using a temporal feature for obtaining the transit time closer to the first arrival of the bolus yields a more robust determination. This finding is contradictory to the analysis of the previous paragraph, which stated that taking the whole curve into consideration yields the most accurate result (see Section 8.4.2). A detailed discussion of the limitations of the FMCMC simulation are given in Section 9.5.

The conducted *ex vivo* experiments used pig blood and rabbit aortas to provide a proof of concept of the proposed method to measure the blood volume flow. The variability of the size of the aortas was limited and the results cannot reflect a variation in diameter. A variation of the flow was performed and the results showed a good agreement with the reference. The first hypothesis was validated for all flow values except the lowest flow value. A clear reason why this is the case cannot be derived. The statistical spread of the flow values obtained by the analysis of the statistical errors was confirmed in this experiment and underlines the validity of the approaches to obtain the statistical error *in silico*. The stepwise increase of volume flow was reflected in the measurement of the volume flow. It validated the second hypothesis for four out of five aortas. The validation failed in one case because the increase of flow

from 180 $\frac{\text{ml}}{\text{min}}$ to 200 $\frac{\text{ml}}{\text{min}}$ was not detected. Taking the statistical error of the measurement into account, this step size was potentially too small to be identified. Nevertheless, the results showed large deviations for some data sets, which can mostly be traced back to the experimental setup. Especially, the connection of a rabbit's aorta to a barbed nozzle showed to be fragile. An imperfect co-axial positioning of both resulted in disturbances of the flow and hence visible non-physiological changes of the streamlines. Nonetheless, the results are very promising and emphasize the need to apply the developed method for measuring blood flow to *in vivo* data. A detailed discussion of points to improve are given in Section 10.4.
The performed retrospective study on *in vivo* data, acquired by the collaborators, reflected the performance of the developed measurement method in a clinical use case scenario. Although the formulated hypothesis was falsified, the method performed very well and matched the flow reference obtained by the current gold standard method for most subjects. The mismatches are discussed in Section 11.4. Taking into consideration the expected outcome of the surgery in terms of increase in flow (see Figure 11.4), the obtained accuracy is sufficient. The flow at large bifurcations was analyzed and the results complied with the conservation of flow at junctions. This emphasizes an advantage of this method towards the current state of the art: it is capable of acquiring multiple flow values at once.

The current state of the art in commercially available ICG FA systems is limited to the anatomical visualization and qualitative functional imaging of vessels [6–12]. The current state of the art in research on the usage of ICG FA for the true quantitative measurement of blood flow (in ml/min) provide neither a detailed and extensive analysis of the errors nor an *in vivo* (or *ex vivo*) validation of the methods [137, 182, 273]. This work levitates the state of the art to a truly substantial analysis of its performance on simulated and standardized data and on clinical use case data. A comparison with other established "quantitative" measurements of blood flow by ICG FA is not possible since they do not provide a truly quantitative volume flow value. They rather provide a scalar value to quantify the functional condition of a vessel (e.g. using the blood flow index - BFI) [130–135]. Hence, a comparison with this state of the art in research is not expedient. It may be rather performed in a large clinical study focused on the patient outcome than on physical quantities.

The current state of the art in clinical blood flow measurement (US-flow probe) has some limitations mainly due to the fact that it must get in contact with and even be placed around the vessel, which risks harming the patient [5]. The methods developed in this work overcome those limitations. A comparison of the blood flow obtained by the proposed method and the US-flow probe showed good agreement, which makes the presented method very promising.

The given results are a proof of concept of the suitability of the presented intraoperative, quantitative, and non-contact measurement of blood volume flow via ICG FA. This thesis paves the way towards clinical use of this method, complementing the current state of the art.

Chapter 13

Outlook

The utilized *in silico* model to perform the analysis of the accuracy in the length and diameter measurement used multiple mathematical functions to describe the centerline of a vessel. The model was designed to depict an extensive range of vessel geometries and a retrospective containment is possible due to the separate analysis of the functions. Hence, if the vessel can be fit to one of the functions, then an individual error can be assigned. This personalized analysis would increase the reliability of the determined accuracy. A drawback of the model is the missing consideration of any projection errors. Obtaining the topology of the tissue by a microscope is possible and can provide the basis for including the projection error into the length measurement [292–295]. The whole analysis of the length measurement is also applicable to 3D data. Hence, translating the approach to other applications such as computed tomography (CT) or magnetic resonance imaging (MRI) is possible. The diameter measurement of small vessels was prone to large relative errors since the discretization has a considerable influence. Research on the sub-pixel diameter measurement should be broadened. More details are given in Section 8.5.1.

The analysis of the error in the transit time measurement was based on indicator dilution curves (IDCs) computed by a fluid flow simulation, which represent the temporal changes in concentration of the indicator at a certain location. This did not involve the transfer function from the indicator's concentration to its fluorescence emission. Chronologically later in this work, the Fluorescence-Monte-Carlo-Multi-Cylinder (FMCMC) was developed and can provide the transfer from concentration distribution to total fluorescence emission. The results of the performed investigation emphasize the importance of the noise level. Hence, noise reduction techniques should be considered for the analysis of the transit time while keeping a strong focus on maintaining the signals' morphology. Finally, the sampling frequency (for cameras in frames per second) is worth investigating since the accuracy in the transit time measurement is a trade off between the noise and sampling frequency. Operating a system at the optimal frequency increases the accuracy in the transit time measurement.

The systemic error was determined using a fluid flow simulation to obtain the spatio-temporal concentration of indocyanine green (ICG) followed by an optical simulation to obtain the

location of fluorescence events. In the fluid flow simulation, the blood was modeled as a homogeneous liquid in the fluid flow simulation. In contrast, blood is a cell suspension [21]. Especially the red blood cells (RBCs) tend to aggregate at the center of the vessel [22]. This heterogeneous distribution affects the viscosity of blood and thus the flow. Moreover, the RBCs are platelet-like shaped cells. Their orientation has an influence on the optical properties [246, 247]. Deriving the RBCs orientation in the fluid flow simulation and transferring this information to the optical simulation would be beneficial.
The optical simulation was intended to compute the location of fluorescence events. The correctness of the locations was assumed and was based on the validated total fluorescence emission (which did not reflect the location of fluorescence events). The validation of this assumption would increase the trustworthiness of the results.
The FMCMC did not include the self-absorbance and remission of fluorescent photons [101, 102]. Including it would influence the location of the fluorescence event and thus influence the result. Fluorescence provokes a change in the wavelength of the photons. Thus, the optical properties of the tissue need to be adjusted. It was shown that the optical properties in the regarded wavelength range do not change a lot and hence were ignored. In future implementations, a look-up table can be included in the simulation to allow wavelength dependent changes of optical properties of the tissue. The Henyey-Greenstein phase function was used for the scattering of photons. Its suitability for modeling the scattering of blood is not clear in published literature [159–163]. Taking other phase functions into consideration and testing them for blood would clarify the performance and probably identify an ideal phase function for the simulation of the propagation of photons in blood. The implemented detector model in the FMCMC is not a realistic representation of a microscope's optics. Including realistic optics would increase the realism of the model and also yield the ability to obtain an artificial image of the tissue. This can be used with fluorescent phantoms to additionally validate the FMCMC.

The *ex vivo* experiments suffered from clots in the devices and tubes. This was the main reason for a slowdown since a clot needed to be removed with water and a chemical agent. Afterwards, a meticulous flush with water was needed to remove the agent. Preventing clotting would increase the efficiency of the experiments. Some aspects that can be automatized are mentioned in Section 10.5 and would increase the level of standardization of the experiments and convenience for the user.
Some of the recordings showed constrictions at the interface of the artery to the connector. This entails a disturbed flow which was also visible in some cases. A rethinking of the connection can improve the flow of the blood. Finally, using arteries with less branches is favorable (e.g. cerebral arteries from pigs) to prevent glue or suture threads being in the optical path.

The *in vivo* study yielded very promising results on data obtained from extracranial-to-intracranial (EC-IC) bypass surgery on humans. 17 subjects were included and within those, a large variability of the vessel's shape and the blood flow were observable. Including more cases is crucial to increase the reliability of the measurement and identify potential stepping stones. Moreover, including other diseases and surgical interventions would be beneficial to reveal the handicaps of the method. So far, the analysis of the data was limited to the recordings obtained before installing the bypass. The recordings after installing the bypass should be analyzed. Finally, integrating the software into a surgical microscope and applying it not only on use case data but operate it in the use case environment would show whether its intraoperative handling fits the surgeon's need.

PART VI

APPENDIX

Appendix **A**

Appendix for the statistical and systemic error analysis

A.1 Examples of synthetic data sets used to evaluate the measurement of geometrical parameters

The following figures show more examples of the synthetic data set used to assess the accuracy in the measurement of geometrical parameters. Figure A.1 shows examples with only one function in the field of view. Figure A.2 shows examples with bifurcations composed of different mathematical functions.

A.2 Details on the spur removal

Introduction In medical image analysis the extraction of information of a structure is of great interest. The centerline (skeleton) of a binarized structure is a simplified and efficient descriptor of its shape. It was used to measure the length and diameter of a vessel's segmentation. Common centerline (or skeleton) extraction methods, such as erosion, thinning, voronoi diagrams, fast marching distance transform etc., are often sensitive to irregularities on the border of the segmentation and thereby produce spurs [296–298]. Spurs are defined as faulty additional junctions, thus artifacts. They must be differentiated from real branches which are caused by bifurcations of vessels. Otherwise, an analysis would incorrectly interpret the spurs as vessels. Therefore, a method is proposed that takes the spatial orientation of the centerline and of the structure into account to identify and eliminate misfits. Thereby, the spatial dimension of the potential spurs is not of relevance. This holds the assumption that a centerline should always have the same orientation as the structure itself which is very likely to be true for lengthy objects.

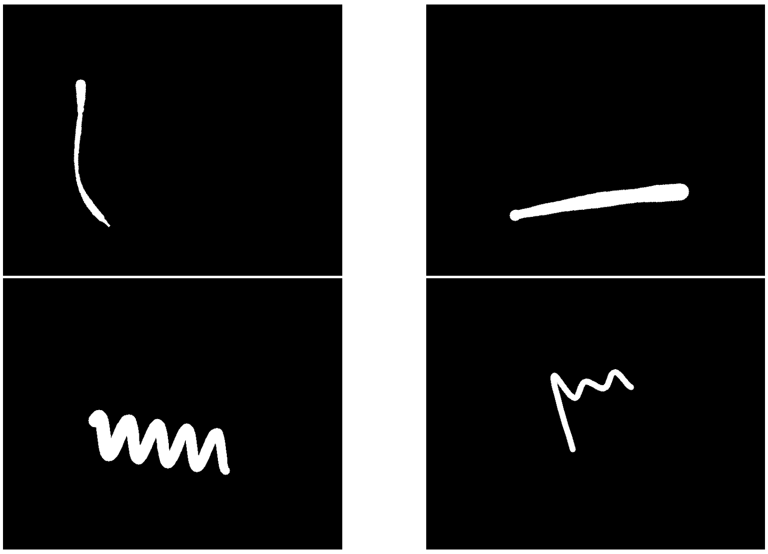

Figure A.1: *In silico* simulation of two vessel segmentations. Please note that the function are rotated arbitrarily and might not appear in their expected shape. **Top-left**: section of a Gaussian bell with variable diameter, **top-right**: section of a parabola with variable diameter, **bottom-left**: section of a sinusoid with decreasing diameter, **bottom-right**: polynomial with constant diameter

Centerline orientation A predefined set of templates for the 3x3 neighborhood of a single pixel were used. This method is straight forward and fast. Three templates are shown in Figure A.3. An orientation is assigned to all centerline pixels in case a particular direction is clear. No orientation can be assigned to the cases that are similar to the template on the right of Figure A.3. Furtheron, no orientation was assigned to branch pixels. In contrast to the given example in the figure, branch pixels are defined as pixel where a bifurcation is present and thus have ambiguous orientation.

Structure orientation via Optimally Oriented Flux The following brief description is based on the publication by Law and Chung [299]. For more details please have a look into their publication. The main difference to their approach is the reduction from 3D to 2D and the invert of definition of the flux's orientation.

The Optimally Oriented Flux (OOF) is a detector of curvilinear structures and was used in here on grayscale image. Generally, the OOF is able to encode direction information of a structure by measuring the amount of projected gradient that flows in or out of a local circular region (centered around the pixel under investigation). It assigns several parameters to each pixel of the image. The so called value (also called amount) of OOF is often referred to as a vesselness measure of the single pixel. The calculation also yields an axis which is referred to the orientation of this vesselness value of the pixel. Here, the orientation of the vessel and therefore the direction of this axis is of interest. Following is a brief description on how to obtain it. The oriented gradient flux of an image is

$$f(\mathbf{x},r,\hat{\rho}) = \frac{1}{2\pi r}\int_{\partial S_r} (\nabla(G*I)(\mathbf{x}+\mathbf{h})\cdot\hat{\rho})\hat{\rho}\cdot\hat{n}\,dA \tag{A.1}$$

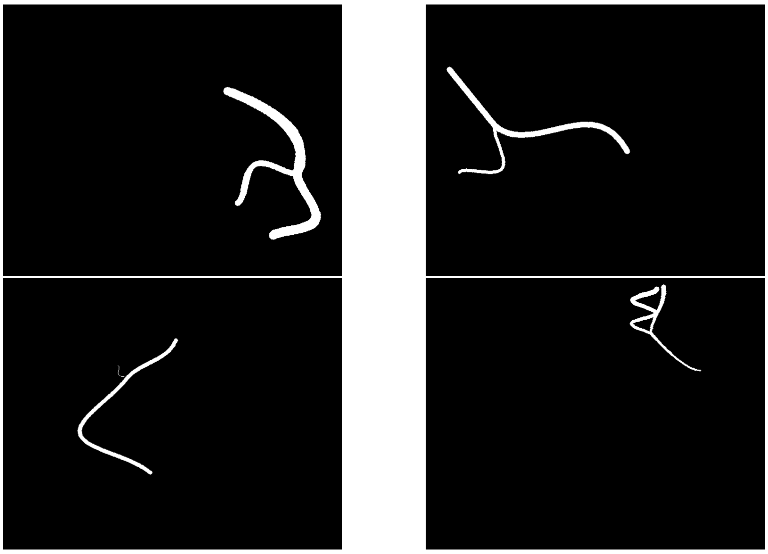

Figure A.2: *In silico* simulation of two vessel segmentations. Please note that the function are rotated arbitrarily and might not appear in their expected shape **Top-left**: a bifurcation including section of two Gaussian bells and a parabola, **top-right**: a bifurcation including section of straight line, sinusoid and Gaussian bell, **bottom-left**: a bifurcation including section of curved wave and two Gaussian bells, **bottom-right**: an invalid bifurcation because the sinusoid branch merges with another branch.

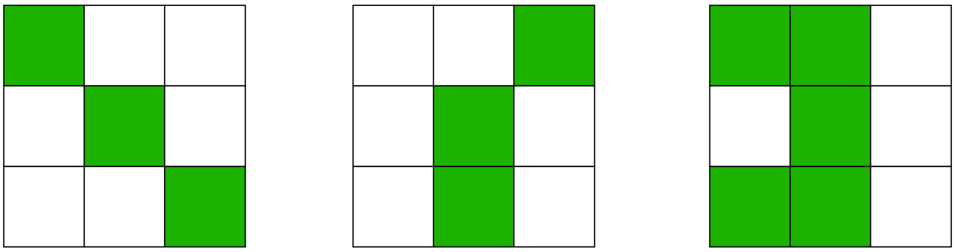

Figure A.3: Three examples of 3x3 templates used to determine the centerlines orientation. Left: an angle of 45°. Middle: an angle of -67.5°. Right: No orientation is determined.

with r as the radius of the circle around the pixel of interest, ∂S_r as the boundary of it, G as the Gaussian function with a scaling factor of 1 used to obtain the image gradient of image I, $\mathbf{h} = \hat{n}r$ is the relative position vector, $\hat{n}$ is the outward unit normal of ∂S_r, $\hat{\rho}$ is the projected direction of outward gradient flux. Equation A.1 can be written in quadratic form matrix $Q_{r,x}$ as

$$f(\mathbf{x}, r, \hat{\rho}) = \hat{\rho}^T \mathbf{Q}_{\mathbf{x},r} \hat{\rho} \tag{A.2}$$

$$\mathbf{Q}_{\mathbf{x},r} = \begin{bmatrix} q^{1,1}_{\mathbf{x},r} & q^{1,2}_{\mathbf{x},r} \\ q^{2,1}_{\mathbf{x},r} & q^{2,2}_{\mathbf{x},r} \end{bmatrix} \tag{A.3}$$

with

$$q^{i,j}_{\mathbf{x},r} = \frac{1}{2\pi r} \int_{\partial S_r} \partial_i (G * I)(\mathbf{x} + \hat{n}r) n_j \, dA. \tag{A.4}$$

OOF tries to find the projection direction $\hat{\rho}$ that maximizes $f(x,r,\hat{\rho})$. This can be solved as a generalized eigenvalue problem. In 2D images it results in two pairs of an eigenvalue and eigenvector (λ_k, ω_k) for each pixel in the image. Thereby, the eigenvalue with the larger absolute value is used as a vesselness measure. The eigenvectors are often neglected but nonetheless they can be interpreted as the orientation of the structure [299].

As Eqs. A.1 to A.4 show the chosen radius r of the circle around the pixel of interest is of great importance for the optimization since the image gradient is measured at its boundary ∂S_r. Choosing the correct radius is key to a correct determination of the OOF.

The binarized structure and the extracted centerline (incl. spurs) are given. A diameter value for each pixel of the centerline was already obtained and will be used here.

Finally, two pairs of eigenvalue and eigenvector are computed for each pixel of the centerline. Thereby, the eigenvectors are orthogonal since the matrix $\mathbf{Q}_{\mathbf{x},r}$ is symmetrical. One eigenvalue will be close to zero and the other negative. The interpretation of both values is as following. The negative eigenvalue is due to the maximization of the $f(x,r,\hat{\rho})$. It is negative since $\hat{n}$ points outwards and the structures gradient always points inwards (assuming we are in a lengthy structure with a white foreground and black background) on the boundary of the circle. Therefore, the outflow is negative. The corresponding eigenvector points towards the gradient, so not in the orientation of the structure. The eigenvector of the eigenvalue which is closer to zero (very little gradient) has the same orientation as the structure. The structure's orientation is defined as the eigenvector which corresponds to the eigenvalue closer to zero.

Detection of spurs The detection of spurs relies on the assumption that the orientation of the centerline and of the structure have little difference. The calculation of the absolute angular difference of the two orientations is needed $|\alpha_{diff}|$ and afterwards compared to a defined angular tolerance α_{tol}. Finally, a binary decision on whether the pixel is an element of a spur is done, therefore a binary flag Y is defined:

$$Y = \begin{cases} true, & |\alpha_{diff}| > \alpha_{tol} \\ false, & |\alpha_{diff}| < \alpha_{tol} \end{cases} \tag{A.5}$$

An angular tolerance of $\alpha_{tol} = 45°$ was used. It should not be chosen too small since the discretization of possible angles in the calculation of the centerline orientation is strong. This discretization can be reduced by increasing the neighborhood used for the calculation of the centerline orientation (current 3x3). The detected spur-pixel are then marked according to Eq. A.5. The determination of the orientation of a centerline pixel might include such a marked pixel. Therefore, a second iteration is performed without taking those marked pixels into account. A third iteration is not necessary as long as the template format for the determination of the orientation of the centerline is kept at 3x3. A larger template format would require more iterations. The OOF is not affected by the exclusion of these marked pixels. A spur is removed in the case it has at least as many elements assigned with $Y = true$ as are assigned with $Y = false$.

Result A subjective comparison with other threshold based spur removal methods showed that the proposed method performs better. Figure A.4 shows an example.

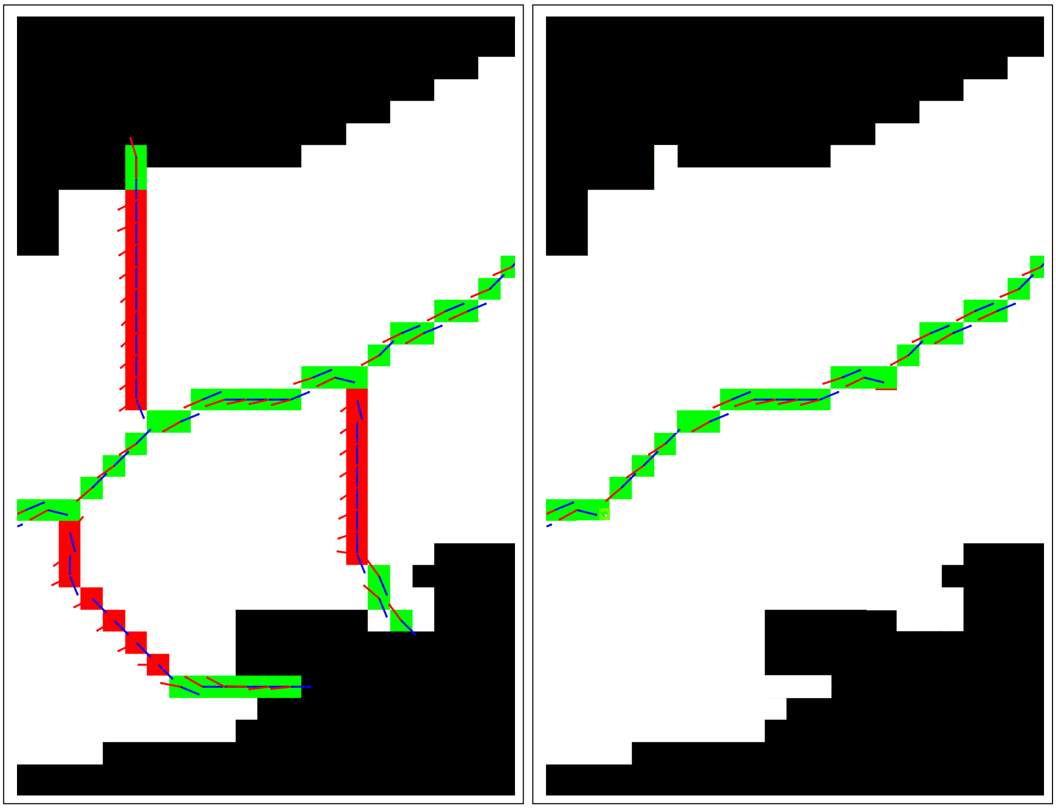

Figure A.4: This image shows in white the segmentation of a vessel and in black the background. The green and red marked pixels were determined as potential centerline pixel. To each non-branch pixel two orientations were extracted: the centerline orientation and the structures orientation, marked by blue and red lines respectively. Pixel which show an $|\alpha_{diff}| < \alpha_{tol}$ are marked green and others in red. All three branches containing red pixels were removed from the centerline. The resulting centerline is shown in the right image.

A.3 Details on the fluid flow simulation setting

The *in silico* computation of the presented raw indicator dilution curve (IDC) is performed in COMSOL Multiphysics V5.4. Describing all settings of the simulation is extensive and not appropriate. The .mph is archived and can be handed out. Following is an overview of the parameters defined in the simulation:

- ◦ Initial indicator concentration $c_{ICG} = 6.4519\,\frac{\mathrm{mmol}}{\mathrm{m}^3}$ $(= 0.005\,\frac{\mathrm{g}}{\mathrm{l}})$
- ◦ Diffusion coefficient D based on [228, 229]:
  - $D_{ICG} = 7.6 \cdot 10^{-11}\,\frac{\mathrm{m}^2}{\mathrm{s}}$
  - $D_{Water} = 2 \cdot 10^{-9}\,\frac{\mathrm{m}^2}{\mathrm{s}}$

  - $D_{Glycerol} = 1.37 \cdot 10^{-12}\,\frac{\text{m}^2}{\text{s}}$
  - $D_{Protein} = 7.6 \cdot 10^{-11}\,\frac{\text{m}^2}{\text{s}}$

- Density ρ
  - $\rho_{Water} = 1009\,\frac{\text{kg}}{\text{m}^3}$
  - $\rho_{Glycerol} = 1263\,\frac{\text{kg}}{\text{m}^3}$
  - $\rho_{Protein} = 1087\,\frac{\text{kg}}{\text{m}^3}$
  - $\rho_{BloodAnalog} = 1157\,\frac{\text{kg}}{\text{m}^3}$

- Molar mass M
  - $M_{ICG} = 0.7496\,\frac{\text{kg}}{\text{mol}}$
  - $M_{Glycerol} = 0.092094\,\frac{\text{kg}}{\text{mol}}$
  - $M_{Water} = 0.018015\,\frac{\text{kg}}{\text{mol}}$

- Reynolds number Re
  - $Re_{BloodAnalog} = 79.613$
  - $Re_{Water} = 808.29$

- Dynamic viscosity η
  - $\eta_{BloodAnalog}(\dot{\gamma}) = 0.00058 \cdot (1 - 0.69)^{-2.5} + \frac{0.625^3 \cdot 0.69^3}{10 \cdot \dot{\gamma}}$ mPa · s, modeled by the Casson-model
  - $\eta_{Water} = 1\,\text{mPa} \cdot \text{s}$

A.4 Details on the results of the temporal error analysis

A.4.1 Cross-correlation of the raw data sets cut by method 3 - Figure 8.14A at 25 fps

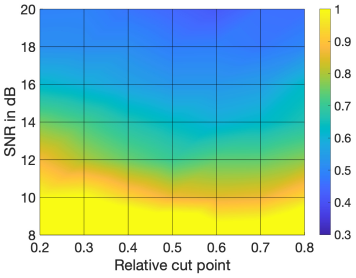

Figure A.5: Figure 8.14A in the manuscript: mean ε_{frames} using the raw data sets ($f_{sampling} = 25\,\mathrm{Hz}$) with no mathematical fits. To obtain the transit time the cross-correlation is computed after applying the cut method 3. This image is adapted from [136] published under the Creative Commons Attribution 4.0 License.

				μ **in frames**			
	Cut level in % of $\mathrm{C_{max}}$						
SNR	**20%**	**30%**	**40%**	**50%**	**60%**	**70%**	**80%**
20 dB	0,49	0,49	0,47	0,44	0,42	0,46	0,46
18 dB	0,52	0,51	0,51	0,48	0,49	0,47	0,50
16 dB	0,62	0,60	0,56	0,53	0,53	0,55	0,63
14 dB	0,76	0,72	0,66	0,63	0,60	0,62	0,66
12 dB	0,87	0,80	0,75	0,70	0,74	0,74	0,77
10 dB	1,00	1,01	0,93	0,87	0,85	0,86	0,94
8 dB	1,31	1,23	1,19	1,19	1,07	1,08	1,20
				σ **in frames**			
20 dB	0,27	0,28	0,26	0,24	0,23	0,25	0,26
18 dB	0,34	0,32	0,31	0,30	0,29	0,28	0,32
16 dB	0,42	0,41	0,35	0,34	0,36	0,36	0,41
14 dB	0,53	0,51	0,44	0,42	0,41	0,43	0,43
12 dB	0,62	0,62	0,55	0,53	0,56	0,56	0,56
10 dB	0,79	0,75	0,65	0,62	0,64	0,68	0,70
8 dB	0,96	0,93	0,89	0,86	0,80	0,81	0,87

Table A.1: Top: calculated mean $\varepsilon_{\mathrm{frame}}$; bottom: calculated standard deviation σ_{frame} for the results presented in Figure A.5 in the supplements and Figure 8.14A in the manuscript.

A.4.2 Cross-correlation of the interpolated data sets cut by method 2 - Figure 8.14B at 25 fps

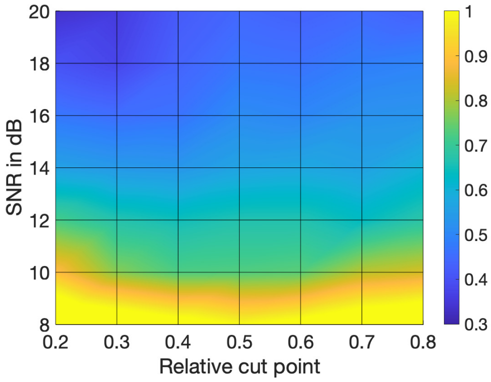

Figure A.6: Figure 8.14B in the manuscript: mean ε_{frames} using the linearly interpolated data sets ($f_{sampling} = 25 \cdot 100\,\mathrm{Hz}$) with no mathematical fits. To obtain the transit time the cross-correlation is computed after applying the cut method 2. This image is adapted from [136] published under the Creative Commons Attribution 4.0 License.

	μ in frames						
	Cut level in % of C_{max}						
SNR	**20%**	**30%**	**40%**	**50%**	**60%**	**70%**	**80%**
20 dB	0,33	0,35	0,42	0,44	0,43	0,45	0,43
18 dB	0,40	0,38	0,44	0,47	0,46	0,48	0,49
16 dB	0,47	0,45	0,46	0,51	0,50	0,52	0,53
14 dB	0,56	0,54	0,53	0,57	0,57	0,56	0,60
12 dB	0,72	0,67	0,65	0,67	0,67	0,64	0,68
10 dB	0,89	0,77	0,72	0,73	0,74	0,81	0,84
8 dB	1,15	1,09	1,04	1,00	1,03	1,09	1,13
	σ in frames						
20 dB	0,23	0,22	0,23	0,24	0,23	0,26	0,25
18 dB	0,27	0,24	0,26	0,28	0,27	0,29	0,29
16 dB	0,35	0,31	0,30	0,34	0,32	0,33	0,32
14 dB	0,44	0,41	0,38	0,36	0,36	0,37	0,41
12 dB	0,55	0,50	0,48	0,48	0,46	0,44	0,51
10 dB	0,69	0,61	0,54	0,51	0,51	0,58	0,62
8 dB	0,86	0,83	0,78	0,72	0,75	0,78	0,83

Table A.2: Top: calculated mean $\varepsilon_{\mathrm{frame}}$; bottom: calculated standard deviation σ_{frame} for the results presented in Figure A.6 in the supplements and Figure 8.14B in the manuscript.

A.4.3 Cross-correlation of the fitted Gamma Variate functions cut by method 3 - Figure 8.15A at 25 fps

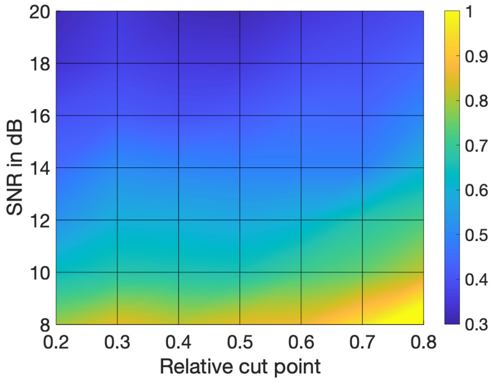

Figure A.7: Figure 8.15A in the manuscript: mean ε_{frames} using the Gamma Variate model on the data sets ($f_{sampling} = 25\,\mathrm{Hz}$). Before fitting the model, cut method 3 is applied to the data set. To obtain the transit time the cross-correlation is computed. This image is adapted from [136] published under the Creative Commons Attribution 4.0 License.

μ in frames							
	Cut level in % of C$_{max}$						
SNR	**20%**	**30%**	**40%**	**50%**	**60%**	**70%**	**80%**
20 dB	0,32	0,35	0,32	0,32	0,34	0,37	0,39
18 dB	0,34	0,37	0,36	0,36	0,39	0,40	0,44
16 dB	0,40	0,42	0,40	0,42	0,45	0,44	0,50
14 dB	0,45	0,51	0,50	0,49	0,49	0,49	0,60
12 dB	0,53	0,60	0,59	0,58	0,60	0,67	0,72
10 dB	0,64	0,67	0,66	0,66	0,71	0,75	0,82
8 dB	0,79	0,85	0,82	0,85	0,87	0,96	1,11
σ in frames							
20 dB	0,19	0,24	0,21	0,21	0,21	0,21	0,24
18 dB	0,22	0,24	0,24	0,23	0,25	0,25	0,28
16 dB	0,27	0,32	0,27	0,27	0,28	0,30	0,35
14 dB	0,32	0,35	0,34	0,33	0,34	0,34	0,40
12 dB	0,39	0,42	0,43	0,41	0,44	0,48	0,53
10 dB	0,48	0,51	0,48	0,50	0,50	0,53	0,63
8 dB	0,56	0,60	0,61	0,62	0,64	0,73	0,84

Table A.3: Top: calculated mean $\varepsilon_{\text{frame}}$; bottom: calculated standard deviation σ_{frame} for the results presented in Figure A.7 in the supplements and Figure 8.15A in the manuscript.

A.4.4 Cross-correlation of the first derivative of the fitted Gamma Variate functions cut by method 1 - Figure 8.15B at 25 fps

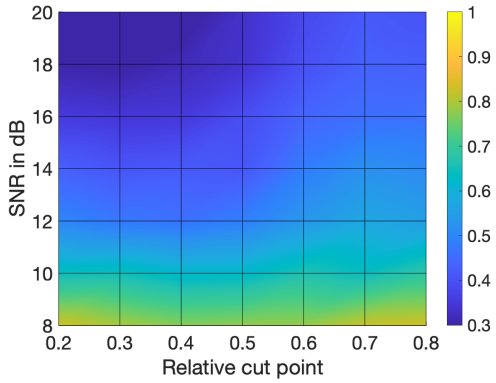

Figure A.8: Figure 8.15B in the manuscript: mean ε_{frames} using the Gamma Variate model on the data sets ($f_{sampling} = 25\,\mathrm{Hz}$). Before fitting the model, cut method 1 is applied to the data set. To obtain the transit time the cross-correlation of the first derivative is computed. This image is adapted from [136] published under the Creative Commons Attribution 4.0 License.

μ in frames							
	Cut level in % of C_{max}						
SNR	**20%**	**30%**	**40%**	**50%**	**60%**	**70%**	**80%**
20 dB	0,27	0,27	0,28	0,33	0,38	0,42	0,40
18 dB	0,30	0,29	0,32	0,34	0,40	0,43	0,43
16 dB	0,35	0,34	0,35	0,39	0,44	0,46	0,46
14 dB	0,43	0,41	0,42	0,41	0,48	0,52	0,51
12 dB	0,50	0,47	0,46	0,48	0,53	0,57	0,55
10 dB	0,64	0,65	0,62	0,62	0,66	0,64	0,68
8 dB	0,83	0,80	0,77	0,78	0,78	0,82	0,83
σ in frames							
20 dB	0,17	0,18	0,17	0,19	0,21	0,24	0,22
18 dB	0,20	0,21	0,22	0,22	0,25	0,27	0,27
16 dB	0,26	0,24	0,24	0,26	0,28	0,30	0,32
14 dB	0,30	0,30	0,29	0,32	0,36	0,37	0,38
12 dB	0,38	0,36	0,36	0,36	0,39	0,41	0,42
10 dB	0,49	0,49	0,45	0,46	0,48	0,46	0,50
8 dB	0,61	0,60	0,57	0,58	0,62	0,63	0,61

Table A.4: Top: calculated mean $\varepsilon_{\mathrm{frame}}$; bottom: calculated standard deviation σ_{frame} for the results presented in Figure A.8 in the supplements and Figure 8.15B in the manuscript.

A.4.5 Cross-correlation of the first derivative of the fitted LDRW functions cut by method 1 - Figure 8.15C at 25 fps

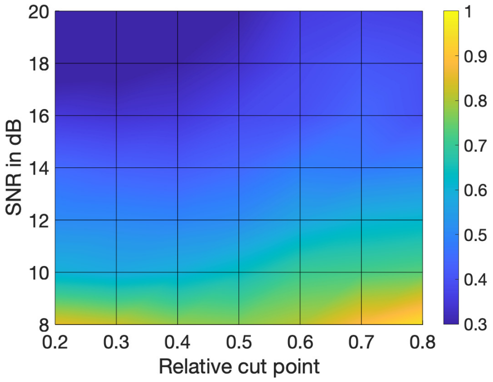

Figure A.9: Figure 8.15C in the manuscript: mean ε_{frames} using the local density random walk (LDRW) model on the data sets ($f_{sampling} = 25\,\mathrm{Hz}$). Before fitting the model, cut method 1 is applied to the data set. To obtain the transit time the cross-correlation of the first derivative is computed. This image is adapted from [136] published under the Creative Commons Attribution 4.0 License.

	μ in frames						
	Cut level in % of C$_{\text{max}}$						
SNR	**20%**	**30%**	**40%**	**50%**	**60%**	**70%**	**80%**
20 dB	0,26	0,25	0,25	0,30	0,36	0,37	0,36
18 dB	0,27	0,28	0,30	0,33	0,38	0,41	0,40
16 dB	0,35	0,34	0,35	0,38	0,40	0,44	0,40
14 dB	0,45	0,43	0,42	0,44	0,48	0,48	0,49
12 dB	0,51	0,50	0,50	0,51	0,57	0,60	0,62
10 dB	0,60	0,58	0,60	0,64	0,71	0,72	0,74
8 dB	0,85	0,83	0,78	0,77	0,81	0,89	0,96
	σ in frames						
20 dB	0,16	0,17	0,18	0,19	0,21	0,23	0,22
18 dB	0,18	0,19	0,20	0,21	0,24	0,27	0,28
16 dB	0,25	0,23	0,24	0,27	0,29	0,30	0,28
14 dB	0,32	0,31	0,30	0,32	0,38	0,39	0,35
12 dB	0,38	0,38	0,38	0,37	0,43	0,45	0,46
10 dB	0,48	0,46	0,46	0,46	0,50	0,51	0,51
8 dB	0,60	0,59	0,57	0,60	0,65	0,66	0,72

Table A.5: Top: calculated mean $\varepsilon_{\text{frame}}$; bottom: calculated standard deviation σ_{frame} for the results presented in Figure A.9 in the supplements and Figure 8.15C in the manuscript.

A.4.6 Cross-correlation of the raw data sets cut by method 3 - Figure 8.16A at 60 fps

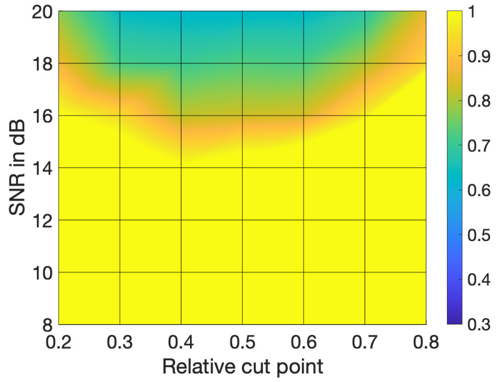

Figure A.10: Figure 8.16A in the manuscript: mean ε_{frames} using the raw data sets ($f_{sampling} = 60\,\mathrm{Hz}$) with no mathematical fits. To obtain the transit time the cross-correlation is computed after applying the cut method 2. This image is adapted from [136] published under the Creative Commons Attribution 4.0 License.

μ in frames							
	Cut level in % of C$_{\text{max}}$						
SNR	**20%**	**30%**	**40%**	**50%**	**60%**	**70%**	**80%**
20 dB	0,78	0,63	0,62	0,62	0,63	0,68	0,85
18 dB	0,87	0,72	0,71	0,73	0,72	0,81	0,93
16 dB	1,01	0,94	0,82	0,83	0,84	0,97	1,30
14 dB	1,17	1,11	1,01	1,07	1,14	1,30	1,62
12 dB	1,56	1,37	1,27	1,25	1,20	1,40	1,78
10 dB	1,78	1,65	1,52	1,42	1,61	1,81	2,31
8 dB	2,19	2,04	1,88	1,86	2,00	2,19	2,78
σ in frames							
20 dB	0,54	0,45	0,40	0,42	0,41	0,47	0,60
18 dB	0,61	0,49	0,48	0,47	0,52	0,55	0,64
16 dB	0,71	0,69	0,59	0,63	0,60	0,74	0,90
14 dB	0,88	0,82	0,78	0,82	0,83	0,93	1,17
12 dB	1,19	1,10	0,98	0,96	0,96	1,11	1,33
10 dB	1,34	1,26	1,17	1,07	1,16	1,30	1,74
8 dB	1,62	1,56	1,48	1,42	1,54	1,64	2,06

Table A.6: Top: calculated mean $\varepsilon_{\text{frame}}$; bottom: calculated standard deviation σ_{frame} for the results presented in Figure A.10 in the supplements and Figure 8.16A in the manuscript.

A.4.7 Cross-correlation of the interpolated data sets cut by method 2 - Figure 8.16B at 60 fps

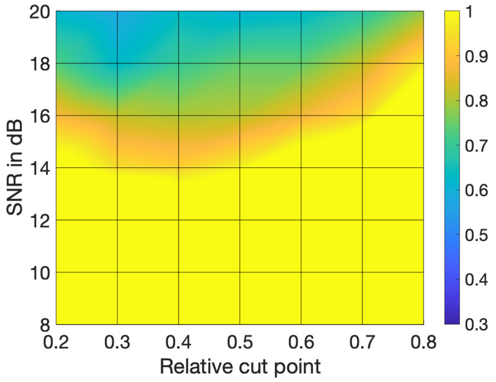

Figure A.11: Figure 8.16B in the manuscript: mean ε_{frames} using the linearly interpolated data sets ($f_{sampling} = 60 \cdot 100\,\mathrm{Hz}$) with no mathematical fits. To obtain the transit time the cross-correlation is computed after applying the cut method 2. This image is adapted from [136] published under the Creative Commons Attribution 4.0 License.

	μ in frames						
	Cut level in % of C_{max}						
SNR	**20%**	**30%**	**40%**	**50%**	**60%**	**70%**	**80%**
20 dB	0,62	0,58	0,63	0,61	0,62	0,68	0,78
18 dB	0,73	0,63	0,70	0,74	0,74	0,82	0,97
16 dB	0,88	0,82	0,80	0,81	0,87	0,93	1,19
14 dB	1,06	0,95	0,92	0,98	1,11	1,25	1,46
12 dB	1,30	1,28	1,16	1,22	1,31	1,46	1,88
10 dB	1,67	1,44	1,39	1,52	1,62	1,85	2,30
8 dB	2,05	1,88	1,74	1,76	1,96	2,28	2,89
	σ in frames						
20 dB	0,43	0,39	0,43	0,41	0,43	0,48	0,56
18 dB	0,55	0,49	0,48	0,50	0,52	0,57	0,68
16 dB	0,64	0,56	0,59	0,57	0,58	0,69	0,88
14 dB	0,83	0,71	0,72	0,75	0,82	0,93	1,14
12 dB	1,03	0,99	0,92	0,96	1,00	1,11	1,37
10 dB	1,26	1,15	1,10	1,14	1,21	1,40	1,73
8 dB	1,61	1,39	1,31	1,32	1,45	1,71	2,17

Table A.7: Top: calculated mean $\varepsilon_{\text{frame}}$; bottom: calculated standard deviation σ_{frame} for the results presented in Figure A.11 in the supplements and Figure 8.16B in the manuscript.

A.4.8 Cross-correlation of the fitted Gamma Variate functions cut by method 3 - Figure 8.17A at 60 fps

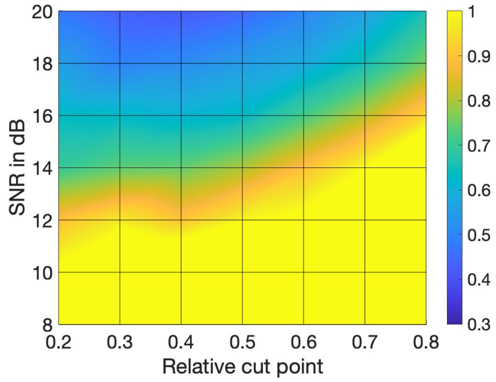

Figure A.12: Figure 8.17A in the manuscript: mean ε_{frames} using the Gamma Variate model on the data sets ($f_{sampling} = 60\,\mathrm{Hz}$). Before fitting the model, cut method 3 is applied to the data set. To obtain the transit time the cross-correlation is computed. This image is adapted from [136] published under the Creative Commons Attribution 4.0 License.

μ in frames							
	Cut level in % of C$_{\mathrm{max}}$						
SNR	**20%**	**30%**	**40%**	**50%**	**60%**	**70%**	**80%**
20 dB	0,47	0,43	0,42	0,44	0,50	0,56	0,66
18 dB	0,55	0,49	0,51	0,55	0,58	0,65	0,76
16 dB	0,63	0,63	0,61	0,63	0,72	0,81	0,94
14 dB	0,70	0,74	0,75	0,80	0,90	1,00	1,20
12 dB	0,90	0,97	0,91	0,99	1,02	1,18	1,48
10 dB	1,02	1,16	1,17	1,24	1,42	1,48	1,83
8 dB	1,34	1,39	1,45	1,58	1,65	1,92	2,33
σ in frames							
20 dB	0,36	0,33	0,30	0,31	0,35	0,40	0,49
18 dB	0,41	0,36	0,36	0,41	0,42	0,47	0,59
16 dB	0,50	0,52	0,51	0,47	0,48	0,60	0,73
14 dB	0,52	0,64	0,54	0,59	0,66	0,75	0,95
12 dB	0,71	0,79	0,69	0,74	0,78	0,93	1,07
10 dB	0,79	0,95	0,85	0,92	1,01	1,10	1,39
8 dB	1,00	1,08	1,17	1,20	1,17	1,44	1,67

Table A.8: Top: calculated mean $\varepsilon_{\mathrm{frame}}$; bottom: calculated standard deviation σ_{frame} for the results presented in Figure A.12 in the supplements and Figure 8.17A in the manuscript.

A.4.9 Cross-correlation of the fitted LDRW functions cut by method 3 - Figure 8.17B at 60 fps

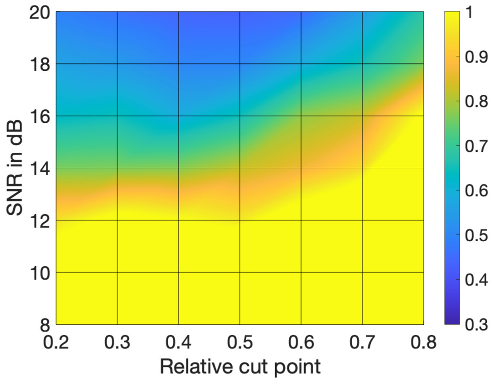

Figure A.13: Figure 8.17B in the manuscript: mean ε_{frames} using the local density random walk (LDRW) model on the data sets ($f_{sampling} = 60\,\mathrm{Hz}$). Before fitting the model, cut method 3 is applied to the data set. To obtain the transit time the cross-correlation is computed. This image is adapted from [136] published under the Creative Commons Attribution 4.0 License.

	μ in frames						
	Cut level in % of C_{max}						
SNR	**20%**	**30%**	**40%**	**50%**	**60%**	**70%**	**80%**
20 dB	0,49	0,46	0,44	0,43	0,45	0,55	0,68
18 dB	0,56	0,54	0,50	0,50	0,58	0,65	0,76
16 dB	0,63	0,65	0,59	0,65	0,78	0,83	1,02
14 dB	0,76	0,77	0,77	0,82	0,87	0,94	1,27
12 dB	0,95	1,04	1,00	0,97	1,08	1,20	1,49
10 dB	1,10	1,15	1,18	1,29	1,48	1,60	1,85
8 dB	1,35	1,42	1,35	1,53	1,64	1,93	2,54
	σ in frames						
20 dB	0,40	0,33	0,33	0,31	0,33	0,42	0,51
18 dB	0,45	0,41	0,37	0,35	0,42	0,46	0,58
16 dB	0,49	0,48	0,44	0,49	0,54	0,62	0,71
14 dB	0,59	0,66	0,61	0,61	0,64	0,71	0,91
12 dB	0,72	0,82	0,74	0,78	0,82	0,89	1,12
10 dB	0,86	0,94	0,91	0,99	1,10	1,23	1,34
8 dB	1,04	1,10	1,06	1,20	1,26	1,46	1,87

Table A.9: Top: calculated mean $\varepsilon_{\mathrm{frame}}$; bottom: calculated standard deviation σ_{frame} for the results presented in Figure A.13 in the supplements and Figure 8.17B in the manuscript.

A.4.10 Cross-correlation of the first derivative of the fitted LDRW functions cut by method 1 - Figure 8.17C at 60 fps

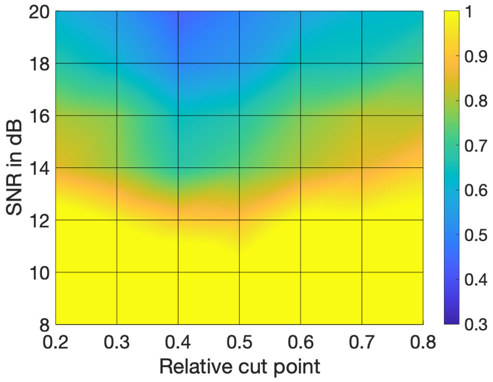

Figure A.14: Figure 8.17C in the manuscript: mean ε_{frames} using the local density random walk (LDRW) model on the data sets ($f_{sampling} = 60\,\mathrm{Hz}$). Before fitting the model, cut method 1 is applied to the data set. To obtain the transit time the cross-correlation of the first derivative is computed. This image is adapted from [136] published under the Creative Commons Attribution 4.0 License.

	μ in frames						
	Cut level in % of C$_{max}$						
SNR	**20%**	**30%**	**40%**	**50%**	**60%**	**70%**	**80%**
20 dB	0,60	0,54	0,43	0,49	0,57	0,61	0,63
18 dB	0,68	0,61	0,50	0,54	0,65	0,66	0,72
16 dB	0,80	0,77	0,64	0,67	0,77	0,81	0,81
14 dB	0,85	0,79	0,68	0,74	0,80	0,86	0,92
12 dB	1,06	0,98	0,92	0,90	1,02	1,01	1,04
10 dB	1,16	1,14	1,11	1,04	1,16	1,20	1,27
8 dB	1,49	1,47	1,41	1,44	1,46	1,49	1,56
	σ in frames						
20 dB	0,37	0,36	0,32	0,33	0,40	0,43	0,42
18 dB	0,44	0,43	0,38	0,39	0,44	0,47	0,51
16 dB	0,54	0,53	0,53	0,52	0,55	0,61	0,61
14 dB	0,59	0,58	0,57	0,58	0,63	0,65	0,67
12 dB	0,80	0,74	0,72	0,76	0,79	0,82	0,84
10 dB	0,86	0,84	0,82	0,86	0,88	0,95	0,92
8 dB	1,09	1,05	1,02	1,08	1,10	1,18	1,25

Table A.10: Top: calculated mean $\varepsilon_{\mathrm{frame}}$; bottom: calculated standard deviation σ_{frame} for the results presented in Figure A.14 in the supplements and Figure 8.17C in the manuscript.

A.5 Expected change in morphology of an IDC in the setup - validation of assumption

The duplication and shifting of the IDCs was justified by assuming a negligible morphological changes between two IDCs measured at two very close points. The *in silico* model was used to clarify on the magnitude of changes and validate the assumptions. In contrast to the distances used in the main manuscript (intention there was to obtain IDCs with different morphology) a distance to be 2 cm was defined here, which is expected in an *in vivo* setting. The obtained curves are shown in Figure A.15. For a comparison of both curves the maximum value and the full width at half maximum (FWHM) were analyzed and are shown in Table A.11. Thereby, the morphological changes measured by the maximum value and FWHM are below 0.5 $\%$.

To put this change in relation to the performed investigation, noise was applied to the signals to check whether the two sets of noisy IDCs can be distinguished. We used 1000 independent applications of white Gaussian noise (WGN) at 20 dB to the IDCs. Using the two sided Mann-Whitney-U test showed no significance to distinguish the two curves ($p > 0.05$). This emphasizes that the morphological changes between the two measurement points are negligible.

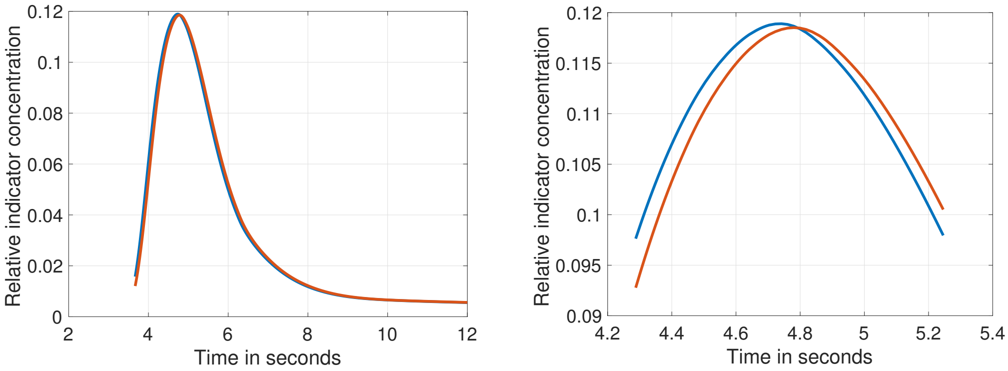

Figure A.15: In blue the IDC at $50\,\mathrm{cm}$; in red the IDC at $52\,\mathrm{cm}$. To the left: the IDCs are shown and differences are barely visible. To the right: the section around the maximum of both IDCs is shown in detail. You can clearly see that the maximum is shifted in time which is expected. Very little differences are visible for the maximum value and the width of the IDCs. Detailed numbers are given in Table A.11. Both images are adapted from [136] published under the Creative Commons Attribution 4.0 License.

Parameter	$\mathrm{IDC}_{50\mathrm{cm}}$	$\mathrm{IDC}_{52\mathrm{cm}}$	Relative deviation
Maximum value	0.1189	0.1185	0.34%
FWHM in seconds	1.8325	1.8367	0.23%

Table A.11: This table shows the maximum of the relative indocyanine green (ICG) concentration, the FWH and the relative deviation of two IDCs that were computed at 50 cm and 52 cm and their deviation.

A.6 Comparison of the simulation with measured IDC

The subjective comparison of the presented *in vivo* and *in silivo* data sets (Figures 8.12 A & B) show strong similarity (Pearson's correlation coefficient of 0.93). To underline this, several *in vitro* data sets were recorded. The used setup strongly relies on the setup in Section 10.2 but has minor differences which are presented in [272].
Thereby, the proposed blood analog is used and pumped through a tube system to an area which is observed by a fluorescence microscope. A peristaltic pump provides the flow rate and an air trap is placed in the pipeline to smooth the peristaltic behavior of the pump. The recorded IDCs are shown in Figures A.16 to A.18. The *in vitro* IDCs are shifted in time so their maximum is at the same position and the fluorescence intensity was scaled, so that the height match's the *in silico* data. They have a strong similarity with the *in silico* data set (Pearson's correlation coefficient of 0.98 - 0.99). Some deviations are present, which is not surprising since external factors (bending of the tube, trapped air bubbles, etc.) affect the experimental results.

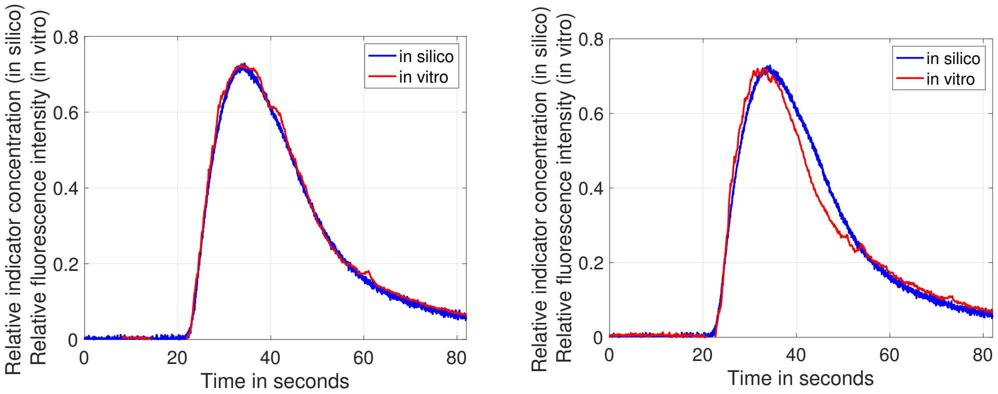

Figure A.16: Comparison of the computed and recorded IDC. Both images are adapted from [136] published under the Creative Commons Attribution 4.0 License.

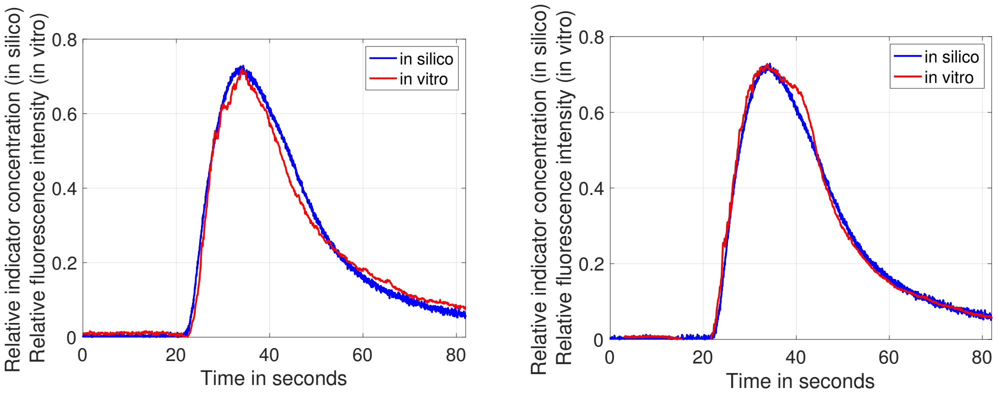

Figure A.17: Comparison of the computed and recorded IDC. Both images are adapted from [136] published under the Creative Commons Attribution 4.0 License.

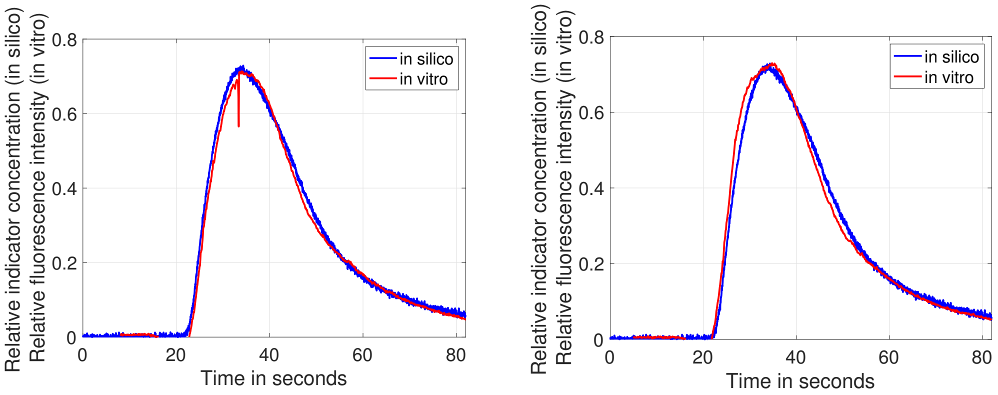

Figure A.18: Comparison of the computed and recorded IDC. Both images are adapted from [136] published under the Creative Commons Attribution 4.0 License.

References

[1] S. Fantini, A. Sassaroli, K. T. Tgavalekos, et al., “Cerebral blood flow and autoregulation: current measurement techniques and prospects for noninvasive optical methods.” *Neurophotonics*, vol. 3, no. 3, p. 031411, 7 2016.

[2] A. Schurr and B. M. Rigor, “Brain anaerobic lactate production: a suicide note or a survival kit?” *Developmental neuroscience*, vol. 20, no. 4-5, pp. 348–357, 1 1998.

[3] T. Kim, C. W. Oh, O.-K. Kwon, et al., “Stroke prevention by direct revascularization for patients with adult-onset moyamoya disease presenting with ischemia.” *Journal of neurosurgery*, vol. 124, no. 6, pp. 1788–1793, 6 2016.

[4] X. Chen, C.-L. Lin, Y.-C. Su, et al., “Risk of subsequent stroke, with or without extracranial-intracranial bypass surgery: a nationwide, retrospective, population-based study.” *Journal of neurosurgery*, pp. 1906–1913, 6 2018.

[5] S. Amin-Hanjani, G. Meglio, R. Gatto, et al., “The utility of intraoperative blood flow measurement during aneurysm surgery using an ultrasonic perivascular flow probe.” *Neurosurgery*, vol. 58, no. 4 Suppl 2, pp. ONS–305–12; discussion ONS–312, 4 2006.

[6] D. A. Hardesty, H. Thind, J. M. Zabramski, et al., “Safety, efficacy, and cost of intraoperative indocyanine green angiography compared to intraoperative catheter angiography in cerebral aneurysm surgery.” *Journal of clinical neuroscience : official journal of the Neurosurgical Society of Australasia*, vol. 21, no. 8, pp. 1377–1382, 8 2014.

[7] A. Raabe, J. Beck, R. Gerlach, et al., “Near-infrared indocyanine green video angiography: a new method for intraoperative assessment of vascular flow.” *Neurosurgery*, vol. 52, no. 1, pp. 132–139, 1 2003.

[8] A. Raabe, J. Beck, and V. Seifert, “Technique and image quality of intraoperative indocyanine green angiography during aneurysm surgery using surgical microscope integrated near-infrared video technology.” *Zentralblatt fur Neurochirurgie*, vol. 66, no. 1, pp. 1–6; discussion 7–8, 2 2005.

[9] A. Feletti, X. Wang, R. Tanaka, et al., “Dual-image videoangiography during intracranial microvascular surgery.” *World neurosurgery*, vol. 99, pp. 572–579, 3 2017.

[10] A. Raabe, P. Nakaji, J. Beck, et al., “Prospective evaluation of surgical microscope-integrated intraoperative near-infrared indocyanine green videoangiography during aneurysm surgery.” *Journal of neurosurgery*, vol. 103, no. 6, pp. 982–9, 12 2005.

[11] J. G. de Oliveira, J. Beck, V. Seifert, et al., “Assessment of flow in perforating arteries during intracranial aneurysm surgery using intraoperative near-infrared indocyanine green videoangiography.” *Neurosurgery*, vol. 62, no. 6 Suppl 3, pp. 1300–10, 6 2008.

[12] J. A. Simal-Julian, P. Miranda-Lloret, R. Evangelista-Zamora, et al., “Indocyanine green videoangiography methodological variations: review.” *Neurosurgical review*, vol. 38, no. 1, pp. 49–57; discussion 57, 1 2015.

[13] M. Riva, S. Amin-Hanjani, C. Giussani, et al., “Indocyanine green videoangiography in aneurysm surgery: Systematic review and meta-analysis.” *Neurosurgery*, vol. 83, no. 2, pp. 166–180, 8 2018.

[14] A. Fick, “Über die messung des blutquantums in den herzventrikeln,” *SB phys-med ges Würzburg*, 7 1870.

[15] P. Meier and K. L. Zierler, “On the theory of the indicator-dilution method for measurement of blood flow and volume.” *Journal of applied physiology*, vol. 6, no. 12, pp. 731–44, 6 1954.

[16] W. Perl, N. Lassen, and R. Effros, “Matrix proof of flow, volume and mean transit time theorems for regional and compartmental systems,” *Bulletin of Mathematical Biology*, vol. 37, pp. 573–588, 1 1975.

[17] M. Belanger, I. Allaman, and P. J. Magistretti, “Brain energy metabolism: focus on astrocyte-neuron metabolic cooperation.” *Cell metabolism*, vol. 14, no. 6, pp. 724–38, 12 2011.

[18] M. Ereci?ska and I. A. Silver, “ATP and brain function.” *Journal of cerebral blood flow and metabolism : official journal of the International Society of Cerebral Blood Flow and Metabolism*, vol. 9, no. 1, pp. 2–19, 2 1989.

[19] M. S. Vavilala, L. A. Lee, and A. M. Lam, “Cerebral blood flow and vascular physiology,” *Anesthesiology Clinics of North America*, vol. 20, no. 2, pp. 247–264, 1 2002.

[20] Y.-C. Tzeng and P. N. Ainslie, “Blood pressure regulation IX: cerebral autoregulation under blood pressure challenges.” *European journal of applied physiology*, vol. 114, no. 3, pp. 545–59, 3 2014.

[21] G. Aumüller, G. Aust, and A. Doll, *Duale reihe: Anatomie*, vol. 2. Stuttgart: Thieme, 1 2010.

[22] A. M. Robertson, A. Sequeira, and R. G. Owens, *Cardiovascular mathematics. modeling and simulation of the circulatory system*, L. Formaggia, A. Veneziani, and A. Quarteroni, Eds. Springer Verlag (Milano), 2009.

[23] N. Willenbacher and K. Georgieva, “Rheology of disperse systems,” pp. 7–49, 1 2013.

[24] K. B. Chandran, A. P. Yoganathan, and S. E. Rittgers, *Biofluid mechanics: The human circulation*. Annual Review of Fluid Mechanics, 2007.

[25] D. Katritsis, L. Kaiktsis, A. Chaniotis, et al., “Wall shear stress: theoretical considerations and methods of measurement.” *Progress in cardiovascular diseases*, vol. 49, no. 5, pp. 307–29, 1 2007.

[26] D. Rubinstein, W. Yin, and M. Frame, “Biofluid mechanics,” 1 2016.

[27] T. V. How, “Advances in hemodynamics and hemorheology,” 1 1996.

[28] D. M. Eckmann, S. Bowers, M. Stecker, et al., “Hematocrit, volume expander, temperature, and shear rate effects on blood viscosity,” *Anesthesia & Analgesia*, vol. 91, pp. 539–45, 2000.

[29] F. Yilmaz and M. Y. Gondugdu, “A critical review on blood flow in large arteries: relevance to blood rheology, viscosity models, and physiologic conditions,” *Korea-Australia Rheology Journal*, vol. 20, no. 4, pp. 197–211, 2008.

[30] D. J. A. Heylings, S. W. Carmichael, S. J. Leinster, et al., *Mcminn’s concise human anatomy*. CRC Press, 2018.

[31] S. Mujagic, “The inner diameter of arteries of the circle of willis regarding gender and age on magnetic resonance angiography,” *Acta Medica Saliniana*, vol. 42, no. 2, pp. 6–12, 2013.

[32] E. Pepic, E. Talovic, A. Voljevica, et al., “Morphometric analysis of willis circle arteries,” *Archives of Pharmacy Practice*, vol. 4, no. 2, p. 77, 1 2013.

[33] M. A. Maaly and A. A. Ismail, “Three dimensional magnetic resonance angiography of the circle of willis: Anatomical variations in general egyptian population,” *The Egyptian Journal of Radiology and Nuclear Medicine*, vol. 42, no. 3-4, pp. 405–412, 1 2011.

[34] K. A. Hafez, N. M. Afifi, and F. Z. Saudi, “Anatomical variations of the circle of willis in males and females on 3d MR angiograms,” *The Egyptian Journal of Hospital Medicine*, vol. 26, no. 1, pp. 106–121, 1 2007.

[35] M. A. Stefani, F. L. Schneider, A. C. H. Marrone, et al., “Influence of the gender on cerebral vascular diameters observed during the magnetic resonance angiographic examination of willis circle,” *Brazilian Archives of Biology and Technology*, vol. 56, no. 1, pp. 45–52, 2013.

[36] H. W. Chen, P. S. Yen, C. C. Lee, et al., “Magnetic resonance angiographic evaluation of circle of willis in general population: A morphologic study in 507 cases,” *Chinese Journal of Radiology*, vol. 29, no. 5, pp. 223–229, 2004.

[37] A. P. Avolio, “Multi-branched model of the human arterial system.” *Medical & biological engineering & computing*, vol. 18, no. 6, pp. 709–718, 11 1980.

[38] L. Zarrinkoob, K. Ambarki, A. Wahlin, et al., “Blood flow distribution in cerebral arteries.” *Journal of cerebral blood flow and metabolism : official journal of the International Society of Cerebral Blood Flow and Metabolism*, vol. 35, no. 4, pp. 648–54, 3 2015.

[39] M. E. MacDonald and R. Frayne, “Phase contrast MR imaging measurements of blood flow in healthy human cerebral vessel segments.” *Physiological measurement*, vol. 36, no. 7, pp. 1517–27, 7 2015.

[40] A. G. Hudetz, G. Mark, A. G. Kovach, et al., “Biomechanical properties of normal and fibrosclerotic human cerebral arteries,” *Atherosclerosis*, vol. 39, no. 3, pp. 353–365, 1 1981.

[41] A. P. Ebrahimi, “Mechanical properties of normal and diseased cerebrovascular system.” *Journal of vascular and interventional neurology*, vol. 2, no. 2, pp. 155–62, 4 2009.

[42] S. Frolov, A. Potlov, S. Proskurin, et al., “Young?s modulus evaluation of the walls of cerebral arteries with aneurysms,” pp. 1–4, 1 2020.

[43] P. J. Blanco, L. O. Müller, and J. D. Spence, “Blood pressure gradients in cerebral arteries: a clue to pathogenesis of cerebral small vessel disease.” *Stroke and vascular neurology*, vol. 2, no. 3, pp. 108–117, 9 2017.

[44] R. G. Gosling and D. H. King, “Arterial assessment by doppler-shift ultrasound.” *Proceedings of the Royal Society of Medicine*, vol. 67, no. 6 Pt 1, pp. 447–449, 6 1974.

[45] L. Zarrinkoob, K. Ambarki, A. Wahlin, et al., “Aging alters the dampening of pulsatile blood flow in cerebral arteries.” *Journal of cerebral blood flow and metabolism : official journal of the International Society of Cerebral Blood Flow and Metabolism*, vol. 36, no. 9, pp. 1519–1527, 9 2016.

[46] P. Deb, S. Sharma, and K. M. Hassan, “Pathophysiologic mechanisms of acute ischemic stroke: An overview with emphasis on therapeutic significance beyond thrombolysis.” *Pathophysiology : the official journal of the International Society for Pathophysiology*, vol. 17, no. 3, pp. 197–218, 6 2010.

[47] J.-H. Park, J.-H. Hong, S.-W. Lee, et al., “The effect of chronic cerebral hypoperfusion on the pathology of alzheimer’s disease: A positron emission tomography study in rats.” *Scientific reports*, vol. 9, no. 1, p. 14102, 10 2019.

[48] B. R. S. Broughton, D. C. Reutens, and C. G. Sobey, “Apoptotic mechanisms after cerebral ischemia.” *Stroke*, vol. 40, no. 5, pp. e331–339, 5 2009.

[49] P. Pandey and G. K. Steinberg, "Neurosurgical advances in the treatment of moyamoya disease." *Stroke*, vol. 42, no. 11, pp. 3304–3310, 11 2011.

[50] J. de la Torre, "Critically attained threshold of cerebral hypoperfusion: the CATCH hypothesis of alzheimer?s pathogenesis," *Neurobiology of Aging*, vol. 21, no. 2, pp. 331–342, 1 2000.

[51] S. Heo, R. S. Prakash, M. W. Voss, et al., "Resting hippocampal blood flow, spatial memory and aging." *Brain research*, vol. 1315, pp. 119–27, 2 2010.

[52] J. C. de la Torre, "Cardiovascular risk factors promote brain hypoperfusion leading to cognitive decline and dementia." *Cardiovascular psychiatry and neurology*, vol. 2012, p. 367516, 1 2012.

[53] F. Arba, G. Mair, T. Carpenter, et al., "Cerebral white matter hypoperfusion increases with small-vessel disease burden. data from the third international stroke trial." *Journal of stroke and cerebrovascular diseases : the official journal of National Stroke Association*, vol. 26, no. 7, pp. 1506–1513, 7 2017.

[54] A. Safouris, A.-S. Hambye, C. Sculier, et al., "Chronic brain hypoperfusion due to multi-vessel extracranial atherosclerotic disease: a potentially reversible cause of cognitive impairment." *Journal of Alzheimer's disease : JAD*, vol. 43, no. 1, pp. 23–27, 1 2015.

[55] W. N. van Mook, R. J. Rennenberg, G. W. Schurink, et al., "Cerebral hyperperfusion syndrome," *The Lancet Neurology*, vol. 4, no. 12, pp. 877–888, 1 2005.

[56] W. Yanagihara, K. Chida, M. Kobayashi, et al., "Impact of cerebral blood flow changes due to arterial bypass surgery on cognitive function in adult patients with symptomatic ischemic moyamoya disease." *Journal of neurosurgery*, vol. 131, no. 6, pp. 1716–1724, 12 2018.

[57] A. R. Naylor, J. Evans, M. M. Thompson, et al., "Seizures after carotid endarterectomy: hyperperfusion, dysautoregulation or hypertensive encephalopathy?" *European journal of vascular and endovascular surgery : the official journal of the European Society for Vascular Surgery*, vol. 26, no. 1, pp. 39–44, 7 2003.

[58] R. C. Heros, R. M. Scott, J. P. Kistler, et al., "Temporary neurological deterioration after extracranial-intracranial bypass." *Neurosurgery*, vol. 15, no. 2, pp. 178–85, 8 1984.

[59] M. G. Yasargil, "A legacy of microneurosurgery: memoirs, lessons, and axioms." *Neurosurgery*, vol. 45, no. 5, pp. 1025–1092, 11 1999.

[60] D. W. Newell, "Superficial temporal artery to middle cerebral artery bypass." *Skull base : official journal of North American Skull Base Society*, vol. 15, no. 2, pp. 133–141, 5 2005.

[61] J. Zhao, H. Lin, R. Summers, et al., "Current treatment strategies for intracranial aneurysms: An overview." *Angiology*, vol. 69, no. 1, pp. 17–30, 1 2018.

[62] *Zeitschrift fuer wissenschaftliche mikroskopie und mikroskopische technik.*, vol. bd. 28 (1911). Stuttgart [etc.]S. Hirzel [etc.], 1911, https://www.biodiversitylibrary.org/bibliography/3927.

[63] M. Renz, "Fluorescence microscopy-a historical and technical perspective." *Cytometry. Part A : the journal of the International Society for Analytical Cytology*, vol. 83, no. 9, pp. 767–779, 9 2013.

[64] F. W. Herschel, "On a case of superficial colour presented by a homogeneous liquid internally colourless," *Abstracts of the Papers Communicated to the Royal Society of London*, vol. 5, pp. 547–547, 1 1845.

[65] G. G. Stokes, "On the change of refrangibility of light," *Philosophical Transactions of the Royal Society of London*, vol. 142, pp. 463–562, 1 1852.

[66] E. Abbe, "Beiträge zur theorie des mikroskops und der mikroskopischen wahrnehmung," *Archiv für mikroskopische Anatomie*, vol. 9, no. 1, pp. 413–468, 1873.

[67] H. Helmholtz and H. Fripp, “On the limits of the optical capacity of the microscope,” *The Monthly Microscopical Journal*, vol. 16, no. 1, pp. 15–39, 1 1876.

[68] S. Kable, *Basic principle of fluorescence*. Jenny Stanford Publishing, 1 2019, vol. 1.

[69] P. Hawkes and J. Spence, “Springer handbook of microscopy,” 1 2019.

[70] J. S. Ploem, “The use of a vertical illuminator with interchangeable dichroic mirrors for fluorescence microscopy with incidental light.” *Zeitschrift fur wissenschaftliche Mikroskopie und mikroskopische Technik*, vol. 68, no. 3, pp. 129–42, 11 1967.

[71] J. T. Alander, I. Kaartinen, A. Laakso, et al., “A review of indocyanine green fluorescent imaging in surgery.” *International journal of biomedical imaging*, vol. 2012, p. 940585, 1 2012.

[72] A. M. Smith, M. C. Mancini, and S. Nie, “Second window for in vivo imaging.” *Nature nanotechnology*, vol. 4, no. 11, pp. 710–712, 11 2009.

[73] FDA. (1959) FDA-approved drugs: ICG/NDA:011525.

[74] S. L. Owens, “Indocyanine green angiography.” *The British journal of ophthalmology*, vol. 80, no. 3, pp. 263–266, 3 1996.

[75] J. V. Frangioni, “In vivo near-infrared fluorescence imaging.” *Current opinion in chemical biology*, vol. 7, no. 5, pp. 626–34, 10 2003.

[76] A. Agarwal, “Fundus fluorescein and indocyanine green angiography,” 1 2007.

[77] L. A. Yannuzzi, “Indocyanine green angiography: a perspective on use in the clinical setting.” *American journal of ophthalmology*, vol. 151, no. 5, pp. 745–751.e1, 5 2011.

[78] C. H. Meyer, R. A Oechsler, and E. B. Rodrigues, “Historical considerations in applying vital dyes in vitreoretinal surgery: from early experiments to advanced chromovitrectomy,” *Expert Review of Ophthalmology*, vol. 2, no. 1, pp. 71–77, 1 2014.

[79] K. Kamisaka, Y. Yatsuji, H. Yamada, et al., “The binding of indocyanine green and other organic anions to serum proteins in liver diseases,” *Clinica Chimica Acta*, vol. 53, no. 2, pp. 255–264, 1 1974.

[80] M. L. Landsman, G. Kwant, G. A. Mook, et al., “Light-absorbing properties, stability, and spectral stabilization of indocyanine green.” *Journal of applied physiology*, vol. 40, no. 4, pp. 575–83, 4 1976.

[81] I. J. FOX and E. H. WOOD, “Indocyanine green: physical and physiologic properties.” *Proceedings of the staff meetings. Mayo Clinic*, vol. 35, pp. 732–744, 12 1960.

[82] K. J. Baker, “Binding of sulfobromophthalein (BSP) sodium and indocyanine green (ICG) by plasma alpha-1 lipoproteins.” *Proceedings of the Society for Experimental Biology and Medicine. Society for Experimental Biology and Medicine (New York, N.Y.)*, vol. 122, no. 4, pp. 957–963, 1 1966.

[83] J. Janecki and J. Krawcy?ski, “Labeling with indocyanine green of serum protein from normal persons and patients with acute viral hepatitis.” *Clinical chemistry*, vol. 16, no. 12, pp. 1008–1011, 12 1970.

[84] K. Hironaka, O. Hiroshi, S. Seigo, et al., “Abnormal binding of indocyanine green with serum proteins in a patient with delayed ICG clearance,” *Clinica Chimica Acta*, vol. 47, no. 1, pp. 39–43, 1 1973.

[85] T. Desmettre, J. M. Devoisselle, and S. Mordon, “Fluorescence properties and metabolic features of indocyanine green (ICG) as related to angiography,” *Survey of Ophthalmology*, vol. 45, no. 1, pp. 15–27, 2000.

[86] G. R. Cherrick, S. W. Stein, C. M. Leevy, et al., "Indocyanine green: observations on its physical properties, plasma decay, and hepatic extraction." *The Journal of clinical investigation*, vol. 39, no. 4, pp. 592–600, 1960.

[87] W. Chu, A. Chennamsetty, R. Toroussian, et al., "Anaphylactic shock after intravenous administration of indocyanine green during robotic partial nephrectomy." *Urology case reports*, vol. 12, pp. 37–38, 5 2017.

[88] S. Mindt, I. Karampinis, M. John, et al., "Stability and degradation of indocyanine green in plasma, aqueous solution and whole blood." *Photochemical & photobiological sciences : Official journal of the European Photochemistry Association and the European Society for Photobiology*, vol. 17, no. 9, pp. 1189–1196, 9 2018.

[89] G. Paumgartner, P. Probst, R. Kraines, et al., "Kinetics of indocyanine green removal from the blood," *Annals of the New York Academy of Sciences*, vol. 170, pp. 134–147, 7 1970.

[90] G. Paumgartner, "Biliary physiology and disease: reflections of a physician-scientist." *Hepatology (Baltimore, Md.)*, vol. 51, no. 4, pp. 1095–1106, 4 2010.

[91] G. A. Lutty, "The acute intravenous toxicity of biological stains, dyes, and other fluorescent substances," *Toxicology and Applied Pharmacology*, vol. 44, no. 2, pp. 225–249, 1 1978.

[92] M. Hope-Ross, L. A. Yannuzzi, E. S. Gragoudas, et al., "Adverse reactions due to indocyanine green," *Ophthalmology*, vol. 101, no. 3, pp. 529–533, 1 1994.

[93] A. Obana, T. Miki, K. Hayashi, et al., "Survey of complications of indocyanine green angiography in japan," *American Journal of Ophthalmology*, vol. 118, no. 6, pp. 749–753, 1 1994.

[94] J. Bjerregaard, M. P. Pandia, and R. A. Jaffe, "Occurrence of severe hypotension after indocyanine green injection during the intraoperative period." *A & A case reports*, vol. 1, no. 1, pp. 26–30, 10 2013.

[95] C. A. Bonte, J. Ceuppens, and A. M. Leys, "Hypotensive shock as a complication of infracyanine green injection." *Retina (Philadelphia, Pa.)*, vol. 18, no. 5, pp. 476–477, 1 1998.

[96] R. Benya, J. Quintana, and B. Brundage, "Adverse reactions to indocyanine green: a case report and a review of the literature." *Catheterization and cardiovascular diagnosis*, vol. 17, no. 4, pp. 231–233, 8 1989.

[97] S. Prahl. (2018) Optical absorption of indocyanine green (ICG).

[98] R. Weissleder, "A clearer vision for in vivo imaging." *Nature biotechnology*, vol. 19, no. 4, pp. 316–317, 4 2001.

[99] R. C. Benson and H. A. Kues, "Fluorescence properties of indocyanine green as related to angiography." *Physics in medicine and biology*, vol. 23, no. 1, pp. 159–63, 1 1978.

[100] A. Raabe, "INFRARED 800 video angiography a practical guide for the surgeon," vol. 3, 8 2010.

[101] G. Ackermann, "Photophysikalische grundlagen zur fluoreszenzdiagnostik von tumoren der haut," 2001.

[102] B. Yuan, N. Chen, and Q. Zhu, "Emission and absorption properties of indocyanine green in intralipid solution." *Journal of biomedical optics*, vol. 9, no. 3, pp. 497–503, 1 2004.

[103] J. D. Briers, "Laser doppler, speckle and related techniques for blood perfusion mapping and imaging." *Physiological measurement*, vol. 22, no. 4, pp. R35–66, 11 2001.

[104] V. Rajan, B. Varghese, T. G. van Leeuwen, et al., "Review of methodological developments in laser doppler flowmetry." *Lasers in medical science*, vol. 24, no. 2, pp. 269–283, 3 2009.

[105] A. N. Obeid, N. J. Barnett, G. Dougherty, et al., “A critical review of laser doppler flowmetry.” *Journal of medical engineering & technology*, vol. 14, no. 5, pp. 178–181, 1 1990.

[106] S. Oyre, W. Paaske, S. Ringgaard, et al., “Automatic accurate non-invasive quantitation of blood flow, cross-sectional vessel area, and wall shear stress by modelling of magnetic resonance velocity data,” *European Journal of Vascular and Endovascular Surgery*, vol. 16, no. 6, pp. 517–524, 1 1998.

[107] A. G. Morgan, M. J. Thrippleton, J. M. Wardlaw, et al., “4d flow MRI for non-invasive measurement of blood flow in the brain: A systematic review.” *Journal of cerebral blood flow and metabolism : official journal of the International Society of Cerebral Blood Flow and Metabolism*, vol. 41, no. 2, pp. 206–218, 2 2021.

[108] M. Wintermark, P. Maeder, J. P. Thiran, et al., “Quantitative assessment of regional cerebral blood flows by perfusion CT studies at low injection rates: a critical review of the underlying theoretical models.” *European radiology*, vol. 11, no. 7, pp. 1220–1230, 1 2001.

[109] R. Tabrizchi and M. K. Pugsley, “Methods of blood flow measurement in the arterial circulatory system,” *Journal of Pharmacological and Toxicological Methods*, vol. 44, no. 2, pp. 375–384, 1 2000.

[110] A. Kolin, “A new approach to electromagnetic blood flow determination by means of catheter in an external magnetic field.” *Proceedings of the National Academy of Sciences of the United States of America*, vol. 65, no. 3, pp. 521–7, 3 1970.

[111] J. D. Folts, “The electromagnetic flowmeter and its use in the operating room,” *J. of ExtraCorporeal Technology*, vol. 6, pp. 127–136, 1974.

[112] M. K. Bevir, “The theory of induced voltage electromagnetic flowmeters,” *Journal of Fluid Mechanics*, vol. 43, pp. 577–590, 1 1970.

[113] K. O’Neill. (2019) Magnetic flow meter basics.

[114] H. Schima, L. Huber, H. Schmallegger, et al., “Flow measurement at the pump head of centrifugal pumps: comparison of ultrasonic transit time and ultrasonic doppler systems.” *Artificial organs*, vol. 21, no. 7, pp. 808–815, 7 1997.

[115] C. DROST, “Vessel diameter-independent volume flow measurements using ultrasound,” *Proc San Diego Biomed*, vol. 17, pp. 299–302, 1978.

[116] N. Nakayama, S. Kuroda, K. Houkin, et al., “Intraoperative measurement of arterial blood flow using a transit time flowmeter: monitoring of hemodynamic changes during cerebrovascular surgery.” *Acta neurochirurgica*, vol. 143, no. 1, pp. 17–24, 1 2001.

[117] O. D. Shekhtman, S. S. Eliava, V. A. Shakhnovich, et al., “[the role of intraoperative flowmetry in surgery of cerebral aneurysms].” *Zhurnal voprosy neirokhirurgii imeni N. N. Burdenko*, vol. 75, no. 3, pp. 39–49; discussion 49, 1 2011.

[118] S. Amin, A.-C. Pinho-Gomes, and D. P. Taggart, “Relationship of intraoperative transit time flowmetry findings to angiographic graft patency at follow-up.” *The Annals of thoracic surgery*, vol. 101, no. 5, pp. 1996–2006, 5 2016.

[119] H. Nakajima, A. Takazawa, A. Yoshitake, et al., “Intraoperative transit-time flowmetry in patients undergoing coronary surgery to determine relationships between graft flow and patency and prior coronary interventions and flow demand: a retrospective study.” *Journal of cardiothoracic surgery*, vol. 13, no. 1, p. 121, 11 2018.

[120] J. Laustsen, E. Pedersen, K. Terp, et al., “Validation of a new transit time ultrasound flowmeter in man,” *European Journal of Vascular and Endovascular Surgery*, vol. 12, no. 1, pp. 91–96, 1 1996.

[121] P. Vikatmaa and A. Albäck, "Intraoperative quality control with transit time flow measurement," *Gefässchirurgie*, vol. 23, no. 8, pp. 580–585, 1 2018.

[122] Transonic. (2021) Reduce intraoperative stroke risk with volume flow measurements.

[123] H. J. Swan, W. Ganz, J. Forrester, et al., "Catheterization of the heart in man with use of a flow-directed balloon-tipped catheter." *The New England journal of medicine*, vol. 283, no. 9, pp. 447–451, 8 1970.

[124] K. B. Saunders, J. I. Hoffman, M. I. Noble, et al., "A source of error in measuring flow with indocyanine green." *Journal of applied physiology*, vol. 28, no. 2, pp. 190–8, 2 1970.

[125] J. B. BASSINGTHWAIGHTE, A. W. EDWARDS, and E. H. WOOD, "Areas of dye-dilution curves sampled simultaneously from central and peripheral sites." *Journal of applied physiology*, vol. 17, pp. 91–8, 1 1962.

[126] P. A. Doriot, P. A. Dorsaz, L. Dorsaz, et al., "Is the indicator dilution theory really the adequate base of many blood flow measurement techniques?" *Medical physics*, vol. 24, no. 12, pp. 1889–1898, 12 1997.

[127] D. F. OPDYKE, "AGREEMENT OF CARDIAC OUTPUTS CALCULATED FROM PAIRED INDICATOR-DILUTION CURVES." *Journal of applied physiology*, vol. 20, pp. 9–15, 1 1965.

[128] J. C. SLEEPER, H. K. THOMPSON, H. D. McINTOSH, et al., "Reproducibility of results obtained with indicatordilution technique for estimating cardiac output in man." *Circulation research*, vol. 11, pp. 712–20, 10 1962.

[129] R. R. Jacobs, U. Schmitz, W. C. Heyden, et al., "Determination of the accuracies of the dye-dilution and electromagnetic flowmeter methods of measuring blood flow." *The Journal of thoracic and cardiovascular surgery*, vol. 58, no. 4, pp. 601–608, 10 1969.

[130] L. Perbeck, D. H. Lewis, L. Thulin, et al., "Correlation between fluorescein flowmetry, 133xenon clearance and electromagnetic flow measurement: a study in the intestine of the pig." *Clinical physiology (Oxford, England)*, vol. 5, no. 3, pp. 293–299, 6 1985.

[131] L. Perbeck, F. Lund, L. Svensson, et al., "Fluorescein flowmetry: a method for measuring relative capillary blood flow in the intestine." *Clinical physiology (Oxford, England)*, vol. 5, no. 3, pp. 281–92, 6 1985.

[132] R. C. Rennert, B. A. Strickland, K. Ravina, et al., "Assessment of ischemic risk following intracranial-to-intracranial and extracranial-to-intracranial bypass for complex aneurysms using intraoperative indocyanine green-based flow analysis." *Journal of Clinical Neuroscience : official journal of the Neurosurgical Society of Australasia*, vol. 67, pp. 191–197, 9 2019.

[133] K. Uda, Y. Araki, S. Muraoka, et al., "Intraoperative evaluation of local cerebral hemodynamic change by indocyanine green videoangiography: prediction of incidence and duration of postoperative transient neurological events in patients with moyamoya disease." *Journal of neurosurgery*, pp. 1–9, 4 2018.

[134] M. Saito, T. Saga, H. Hayashi, et al., "Quantitative blood flow assessment by multiparameter analysis of indocyanine green video angiography." *World neurosurgery*, vol. 116, pp. e187–e193, 8 2018.

[135] W. M. Kuebler, A. Sckell, O. Habler, et al., "Noninvasive measurement of regional cerebral blood flow by near-infrared spectroscopy and indocyanine green." *Journal of cerebral blood flow and metabolism : official journal of the International Society of Cerebral Blood Flow and Metabolism*, vol. 18, no. 4, pp. 445–456, 4 1998.

[136] A. Naber, M. Reiß, and W. Nahm, “Transit time measurement in indicator dilution curves: Overcoming the missing ground truth and quantifying the error,” *Frontiers in Physiology*, vol. 12, pp. 1–16, 1 2021.

[137] C. Weichelt, P. Duscha, R. Steinmeier, et al., “Quantitative fluorescence angiography for neurosurgical interventions.” *Biomedizinische Technik. Biomedical engineering*, vol. 58, no. 3, pp. 269–279, 6 2013.

[138] S. R. Arridge, M. Cope, and D. T. Delpy, “The theoretical basis for determination of optical pathlengths in tissue: temporal and frequency analysis,” *Physics in Medicine and Biology*, vol. 37, no. 7, pp. 1531–1560, 1 1992.

[139] S. R. Arridge, “The forward and inverse problems in time resolved infra-red imaging,” in *Medical optical tomography: functional imaging and monitoring*, G. Mueller, Ed. Bellingham, WA, USA: SPIE Optical Engineering Press, 1 1993, pp. 35–64.

[140] S. R. Arridge and J. C. Hebden, “Optical imaging in medicine: II. modelling and reconstruction.” *Physics in medicine and biology*, vol. 42, no. 5, pp. 841–53, 5 1997.

[141] L. Dagdug, G. H. Weiss, and A. H. Gandjbakhche, “Effects of anisotropic optical properties on photon migration in structured tissues.” *Physics in medicine and biology*, vol. 48, no. 10, pp. 1361–1370, 5 2003.

[142] A. P. Gibson, J. C. Hebden, and S. R. Arridge, “Recent advances in diffuse optical imaging,” *Physics in Medicine and Biology*, vol. 50, no. 4, pp. R1–43, 1 2005.

[143] V. G. Peters, D. R. Wyman, M. S. Patterson, et al., “Optical properties of normal and diseased human breast tissues in the visible and near infrared.” *Physics in medicine and biology*, vol. 35, no. 9, pp. 1317–1334, 9 1990.

[144] J. F. Beek, H. J. van Staveren, P. Posthumus, et al., “The optical properties of lung as a function of respiration.” *Physics in medicine and biology*, vol. 42, no. 11, pp. 2263–2272, 11 1997.

[145] A. Pifferi, P. Taroni, G. Valentini, et al., “Real-time method for fitting time-resolved reflectance and transmittance measurements with a monte carlo model.” *Applied optics*, vol. 37, no. 13, pp. 2774–2780, 5 1998.

[146] C. R. Simpson, M. Kohl, M. Essenpreis, et al., “Near-infrared optical properties of ex vivo human skin and subcutaneous tissues measured using the monte carlo inversion technique.” *Physics in medicine and biology*, vol. 43, no. 9, pp. 2465–2478, 9 1998.

[147] C. K. Hayakawa, J. Spanier, F. Bevilacqua, et al., “Perturbation monte carlo methods to solve inverse photon migration problems in heterogeneous tissues.” *Optics letters*, vol. 26, no. 17, pp. 1335–1347, 9 2001.

[148] G. M. Palmer and N. Ramanujam, “Monte carlo-based inverse model for calculating tissue optical properties. part i: Theory and validation on synthetic phantoms.” *Applied optics*, vol. 45, no. 5, pp. 1062–1071, 2 2006.

[149] T. J. Pfefer, J. K. Barton, D. J. Smithies, et al., “Modeling laser treatment of port wine stains with a computer-reconstructed biopsy.” *Lasers in surgery and medicine*, vol. 24, no. 2, pp. 151–66, 1 1999.

[150] A. Liebert, H. Wabnitz, H. Obrig, et al., “Non-invasive detection of fluorescence from exogenous chromophores in the adult human brain.” *NeuroImage*, vol. 31, no. 2, pp. 600–608, 6 2006.

[151] T. Binzoni, T. S. Leung, R. Giust, et al., “Light transport in tissue by 3d monte carlo: influence of boundary voxelization.” *Computer methods and programs in biomedicine*, vol. 89, no. 1, pp. 14–23, 1 2008.

[152] J. Luu, K. Redmond, W. Lo, et al., "FPGA-based monte carlo computation of light absorption for photodynamic cancer therapy," pp. 157–164, 1 2009.

[153] J. S. Li, T. Pawlicki, J. Deng, et al., "Validation of a monte carlo dose calculation tool for radiotherapy treatment planning." *Physics in medicine and biology*, vol. 45, no. 10, pp. 2969–85, 10 2000.

[154] J. M. Boone, M. H. Buonocore, and V. N. Cooper, "Monte carlo validation in diagnostic radiological imaging." *Medical physics*, vol. 27, no. 6, pp. 1294–304, 6 2000.

[155] B. C. Wilson and G. Adam, "A monte carlo model for the absorption and flux distributions of light in tissue." *Medical physics*, vol. 10, no. 6, pp. 824–830, 1 1983.

[156] L. Wang, S. L. Jacques, and L. Zheng, "MCML-monte carlo modeling of light transport in multi-layered tissues," *Computer Methods and Programs in Biomedicine*, vol. 47, no. 2, pp. 131–146, 1 1995.

[157] A. J. Welch, C. Gardner, R. Richards-Kortum, et al., "Propagation of fluorescent light," *Lasers in Surgery and Medicine*, vol. 21, no. 2, pp. 166–178, 1 1997.

[158] E. Hecht, *Optik*. Muenchen: Oldenbourg, 1 2009.

[159] L. O. Reynolds and N. J. McCormick, "Approximate two-parameter phase function for light scattering," *Journal of the Optical Society of America*, vol. 70, no. 10, p. 1206, 1 1980.

[160] T. Binzoni, T. S. Leung, A. H. Gandjbakhche, et al., "The use of the henyey-greenstein phase function in monte carlo simulations in biomedical optics." *Physics in medicine and biology*, vol. 51, no. 17, pp. N313–22, 9 2006.

[161] L. G. Henyey and J. L. Greenstein, "Diffuse radiation in the galaxy," *Astrophysical Journal*, vol. 93, pp. 70–83, 1 1941.

[162] M. Hammer, A. N. Yaroslavsky, and D. Schweitzer, "A scattering phase function for blood with physiological haematocrit." *Physics in medicine and biology*, vol. 46, no. 3, pp. N65–9, 3 2001.

[163] M. Friebel, A. Roggan, G. Mueller, et al., "Determination of optical properties of human blood in the spectral range 250 to 1100 nm using monte carlo simulations with hematocrit-dependent effective scattering phase functions." *Journal of biomedical optics*, vol. 11, no. 3, p. 34021, 1 2006.

[164] N. Otsu, "A threshold selection method from gray-level histograms," *IEEE Transactions on Systems, Man, and Cybernetics*, vol. 9, no. 1, pp. 62–66, 1 1979.

[165] A. Naber, D. Berwanger, G. K. Steinberg, et al., "Spatial gradient based segmentation of vessels and quantitative measurement of the inner diameter and wall thickness from ICG fluorescence angiographies," in *SPIE Photonics West*, vol. 11229 1122916-2. San Francisco, California, United States: SPIE BiOS, 2020.

[166] "DIN 1319-3:1996-05, grundlagen der messtechnik - teil 3: Auswertung von messungen einer einzelnen messgroesse, messunsicherheit," Tech. Rep., 5 1996.

[167] M. Grabe, *Measurement uncertainties in science and technology*, 1 2014.

[168] Transonic, *Transonic clinical flowprobes*, 6 2019.

[169] F. Durst, "Grundlagen der stroemungsmechanik," 1 2006.

[170] B. Thomas and K. Sumam, "Blood flow in human arterial system-a review," *Procedia Technology*, vol. 24, pp. 339–346, 1 2016.

[171] A. Naber, D. Berwanger, and W. Nahm, "In silico modelling of blood vessel segmentations for estimation of discretization error in spatial measurement and its impact on quantitative

fluorescence angiography," in *41st Annual International Conference of the IEEE Engineering in Medicine and Biology Society (EMBC)*. IEEE, 2019, pp. 4787–4790.

[172] A. Naber, D. Berwanger, and W. Nahm, "Geodesic length measurement in medical images: Effect of the discretization by the camera chip and quantitative assessment of error reduction methods," *Photonics*, vol. 7, no. 3, pp. 1–16, 1 2020.

[173] S. Rieger, S. Klee, and D. Baumgarten, "Experimental characterization and correlation of mayer waves in retinal vessel diameter and arterial blood pressure." *Frontiers in physiology*, vol. 9, p. 892, 1 2018.

[174] L. Johnson Chacko, D. T. Schmidbauer, S. Handschuh, et al., "Analysis of vestibular labyrinthine geometry and variation in the human temporal bone." *Frontiers in neuroscience*, vol. 12, pp. 1–13, 1 2018.

[175] A. B. Cuesta Cuesta, M. D. Martin Rios, M. R. Noguero Meseguer, et al., "Accuracy of tumor size measurements performed by magnetic resonance, ultrasound and mammography, and their correlation with pathological size in primary breast cancer." *Cirugia espanola*, vol. 97, no. 7, pp. 391–396, 1 2019.

[176] F. Long, M. Ozturk, M. Wolff, et al., "Dental imaging using mesoscopic fluorescence molecular tomography: An ex vivo feasibility study," *MDPI Photonics*, vol. 1, no. 4, pp. 488–502, 1 2014.

[177] Y. Takahashi, T. Tsuchitani, N. Kotoura, et al., "Influence of image noise and object size on segmentation accuracy of FDG-PET imaging: a phantom experiment." *Radiological physics and technology*, vol. 12, no. 3, pp. 343–350, 9 2019.

[178] A. Bozzato, T. Struffert, V. Hertel, et al., "Analysis of the accuracy of high-resolution computed tomography techniques for the measurement of stapes prostheses." *European radiology*, vol. 20, no. 3, pp. 566–571, 3 2010.

[179] J. Griebel and W. Dierking, "Impact of sea ice drift retrieval errors, discretization and grid type on calculations of ice deformation," *Remote Sensing*, vol. 10, p. 393, 3 2018.

[180] D. A. Reuter, C. Huang, T. Edrich, et al., "Cardiac output monitoring using indicator-dilution techniques: basics, limits, and perspectives." *Anesthesia and analgesia*, vol. 110, no. 3, pp. 799–811, 3 2010.

[181] E. O. Kung, A. S. Les, C. A. Figueroa, et al., "In vitro validation of finite element analysis of blood flow in deformable models." *Annals of biomedical engineering*, vol. 39, no. 7, pp. 1947–60, 7 2011.

[182] P. Cimalla, D. Graf, P. Duscha, et al., "Methods for determining the blood flow velocity in cerebral vessels using intraoperative indocyanine green fluorescence video angiography," *4th European Conference of the International Federation for Medical and Biological Engineering, IFMBE Proceedings*, vol. 22, pp. 1446–1449, 1 2008.

[183] R. J. Ellis, B. Zhu, J. Koenig, et al., "A careful look at ECG sampling frequency and r-peak interpolation on short-term measures of heart rate variability." *Physiological measurement*, vol. 36, no. 9, pp. 1827–1852, 9 2015.

[184] W. F. Hamilton, J. W. Moore, J. M. Kinsman, et al., "STUDIES ON THE CIRCULATION," *American Journal of Physiology-Legacy Content*, vol. 99, no. 3, pp. 534–551, 1 1932.

[185] K. Zierler, "Indicator dilution methods for measuring blood flow, volume, and other properties of biological systems: a brief history and memoir." *Annals of biomedical engineering*, vol. 28, no. 8, pp. 836–48, 8 2000.

[186] M. Mischi, T. Kalker, and E. Korsten, "Videodensitometric methods for cardiac output measurements," *EURASIP Journal on Advances in Signal Processing*, vol. 2003, pp. 479–489, 12 2003.

[187] M. Mischi, J. A. den Boer, and H. H. M. Korsten, "On the physical and stochastic representation of an indicator dilution curve as a gamma variate." *Physiological measurement*, vol. 29, no. 3, pp. 281–94, 3 2008.

[188] T.-C. Lee and R. L. Kashyap, "Building skeleton models via 3-d medial surface/axis thinning algorithms," *CVGIP: Graphical Models and Image Processing*, vol. 56, no. 6, pp. 462–478, 1 1994.

[189] C. Zeng, S. Bird, J. Luce, et al., "A natural-rule-based-connection (NRBC) method for river network extraction from high-resolution imagery," *Remote Sensing*, vol. 7, pp. 14 055–14 078, 10 2015.

[190] R. C. Gonzalez, R. E. Woods, and S. L. Eddins, *Digital image processing using MATLAB*, 1 2020.

[191] F. Aurenhammer, R. Klein, and D.-T. Lee, *Voronoi diagrams and delaunay triangulations*, 1 2013.

[192] L. Antiga, "Patient-specific modeling of geometry and blood flow in large arteries," PhD thesis, 1 2002.

[193] T. K. Moon, "Mathematical methods and algorithms for signal processing," 1 2000.

[194] H. Prautzsch, W. Boehm, and M. Paluszny, *Bezier and b-spline techniques*, 1 2002.

[195] R. Arieli and A. Marmur, "A biophysical vascular bubble model for devising decompression procedures." *Physiological reports*, vol. 5, no. 6, pp. 1–11, 3 2017.

[196] N. Nakayama, S. Kuroda, K. Houkin, et al., "Intraoperative measurement of arterial blood flow using a transit time flowmeter: monitoring of hemodynamic changes during cerebrovascular surgery." *Acta neurochirurgica*, vol. 143, no. 1, pp. 17–24, 1 2001.

[197] K. Cieslicki and D. Ciesla, "Investigations of flow and pressure distributions in physical model of the circle of willis." *Journal of biomechanics*, vol. 38, no. 11, pp. 2302–10, 11 2005.

[198] F. H. Ebner, J. S. Marquardt, B. Hirt, et al., "Optical requirements on magnification systems for intracranial video microsurgery." *Microsurgery*, vol. 31, no. 7, pp. 559–563, 10 2011.

[199] T. Wohland, R. Rigler, and H. Vogel, "The standard deviation in fluorescence correlation spectroscopy," *Biophysical Journal*, vol. 80, pp. 2987–2999, 6 2001.

[200] M. E. Wise, "Tracer dilution curves in cardiology and random walk and lognormal distributions." *Acta physiologica et pharmacologica Neerlandica*, vol. 14, no. 2, pp. 175–204, 1966.

[201] K. H. Norwich and S. Zelin, "The dispersion of indicator in the cardio-pulmonary system." *The Bulletin of mathematical biophysics*, vol. 32, no. 1, pp. 25–43, 3 1970.

[202] E. J. Schlossmacher, H. Weinstein, S. Lochaya, et al., "Perfect mixers in series model for fitting venoarterial indicator-dilution curves." *Journal of applied physiology*, vol. 22, no. 2, pp. 327–332, 2 1967.

[203] R. Davenport, "The derivation of the gamma-variate relationship for tracer dilution curves." *Journal of nuclear medicine : official publication, Society of Nuclear Medicine*, vol. 24, no. 10, pp. 945–948, 10 1983.

[204] J. B. Borges, F. Suarez-Sipmann, S. H. Bohm, et al., "Regional lung perfusion estimated by electrical impedance tomography in a piglet model of lung collapse." *Journal of applied physiology (Bethesda, Md. : 1985)*, vol. 112, no. 1, pp. 225–236, 1 2012.

[205] J. J. More and D. C. Sorensen, “Computing a trust region step,” *SIAM Journal on Scientific and Statistical Computing*, vol. 4, no. 3, pp. 553–572, 1 1983.

[206] J. M. Bogaard, S. J. Smith, A. Versprille, et al., “Physiological interpretation of the skewness of indicator-dilution curves; theoretical considerations and a practical application.” *Basic research in cardiology*, vol. 79, no. 4, pp. 479–493, 1 1984.

[207] M. T. Madsen, “A simplified formulation of the gamma variate function,” *Physics in Medicine & Biology*, vol. 37, pp. 1597–2000, 1992.

[208] J. Brands, H. Vink, and J. W. G. E. Van Teeffelen, “Comparison of four mathematical models to analyze indicator-dilution curves in the coronary circulation.” *Medical & biological engineering & computing*, vol. 49, no. 12, pp. 1471–1479, 12 2011.

[209] M. Kaschke, K.-H. Donnerhacke, and M. S. Rill, *Optical devices in ophthalmology and optometry : technology, design principles and clinical applications*. Hoboken : Wiley, 1 2014.

[210] B. Mandelbrot, *The fractal geometry of nature*. W. H. Freeman and Co., 1 1982.

[211] G. Mincewicz, A. Aloszko, J. Rumi?ski, et al., “Adjusted subpixel method enables optimisation of bronchial measurements in high-resolution CT.” *The British journal of radiology*, vol. 85, no. 1016, pp. 1093–1097, 8 2012.

[212] F. Da and H. Zhang, “Sub-pixel edge detection based on an improved moment,” *Image and Vision Computing*, vol. 28, no. 12, pp. 1645–1658, 1 2010.

[213] Q. Sun, Y. Hou, Q. Tan, et al., “A robust edge detection method with sub-pixel accuracy,” *Optik - International Journal for Light and Electron Optics*, vol. 125, pp. 3449–3453, 7 2014.

[214] R. Aris, “On the dispersion of a solute in a fluid flowing through a tube,” *Proceedings of the Royal Society of London. Series A*, vol. 235, pp. 67–77, 4 1956.

[215] A. Alizadeh, C. A. Nieto de Castro, and W. A. Wakeham, “The theory of the taylor dispersion technique for liquid diffusivity measurements,” *International Journal of Thermophysics*, vol. 1, pp. 243–284, 9 1980.

[216] R. K. Millard, “Indicator-dilution dispersion models and cardiac output computing methods.” *The American journal of physiology*, vol. 272, no. 4 Pt 2, pp. H2004–H2012, 4 1997.

[217] C. Strouthos, M. Lampaskis, V. Sboros, et al., “Indicator dilution models for the quantification of microvascular blood flow with bolus administration of ultrasound contrast agents.” *IEEE transactions on ultrasonics, ferroelectrics, and frequency control*, vol. 57, no. 6, pp. 1296–1310, 6 2010.

[218] G. Lenis, N. Pilia, A. Loewe, et al., “Comparison of baseline wander removal techniques considering the preservation of ST changes in the ischemic ECG: A simulation study,” *Computational and Mathematical Methods in Medicine*, vol. 2017, no. Article ID 9295029, p. 13, 1 2017.

[219] J. Alastruey, K. H. Parker, J. Peiro, et al., “Modelling the circle of willis to assess the effects of anatomical variations and occlusions on cerebral flows.” *Journal of biomechanics*, vol. 40, no. 8, pp. 1794–1805, 1 2007.

[220] D. R. Enzmann, M. R. Ross, M. P. Marks, et al., “Blood flow in major cerebral arteries measured by phase-contrast cine MR.” *AJNR. American journal of neuroradiology*, vol. 15, no. 1, pp. 123–129, 1 1994.

[221] M. Silvestrini, B. Rizzato, F. Placidi, et al., “Carotid artery wall thickness in patients with obstructive sleep apnea syndrome.” *Stroke*, vol. 33, no. 7, pp. 1782–1785, 7 2002.

[222] F. Durst, S. Ray, B. Unsal, et al., “The development lengths of laminar pipe and channel flows,” *Journal of Fluids Engineering*, vol. 127, no. 6, pp. 1154–1160, 1 2005.

[223] F. J. Walburn and D. J. Schneck, “A constitutive equation for whole human blood.” *Biorheology*, vol. 13, no. 3, pp. 201–210, 6 1976.

[224] P. L. Easthope and D. E. Brooks, “A comparison of rheological constitutive functions for whole human blood.” *Biorheology*, vol. 17, no. 3, pp. 235–247, 1 1980.

[225] P. Neofytou, “Comparison of blood rheological models for physiological flow simulation,” *Biorheology*, vol. 41, no. 6, pp. 693–714, 2004.

[226] T. Kenner, “The measurement of blood density and its meaning.” *Basic research in cardiology*, vol. 84, no. 2, pp. 111–124, 1 1989.

[227] D. J. Vitello, R. M. Ripper, M. R. Fettiplace, et al., “Blood density is nearly equal to water density: A validation study of the gravimetric method of measuring intraoperative blood loss.” *Journal of veterinary medicine*, vol. 2015, p. 152730, 1 2015.

[228] J. E. Kinsella and D. M. Whitehead, “Proteins in whey: Chemical, physical, and functional properties,” *Advances in Food and Nutrition Research*, vol. 33, pp. 343–438, 1989.

[229] M. T. Tyn and T. W. Gusek, “Prediction of diffusion coefficients of proteins,” *Biotechnology and Bioengineering*, vol. 35, no. 4, pp. 327–338, 1990.

[230] Carl Zeiss Meditec AG, *KINEVO 900 von ZEISS*, 1 2018.

[231] J. Swartling, A. Pifferi, A. M. K. Enejder, et al., “Accelerated monte carlo models to simulate fluorescence spectra from layered tissues.” *Journal of the Optical Society of America. A, Optics, image science, and vision*, vol. 20, no. 4, pp. 714–27, 4 2003.

[232] A. Liebert, H. Wabnitz, N. Zo?ek, et al., “Monte carlo algorithm for efficient simulation of time-resolved fluorescence in layered turbid media.” *Optics express*, vol. 16, no. 17, pp. 13 188–202, 8 2008.

[233] N. A. Carbone, D. I. Iriarte, and J. A. Pomarico, “GPU accelerated monte carlo simulation of light propagation in inhomogeneous fluorescent turbid media: application to whole field CW imaging,” *Biomedical Physics & Engineering Express*, vol. 3, no. 4, p. 045012, 1 2017.

[234] R. Philip, A. Penzkofer, W. Baeumler, et al., “Absorption and fluorescence spectroscopic investigation of indocyanine green,” *Journal of Photochemistry and Photobiology A: Chemistry*, vol. 96, no. 1-3, pp. 137–148, 1 1996.

[235] Q. Liu, C. Zhu, and N. Ramanujam, “Experimental validation of monte carlo modeling of fluorescence in tissues in the UV-visible spectrum.” *Journal of biomedical optics*, vol. 8, no. 2, pp. 223–36, 4 2003.

[236] S. L. Jacques, “Corrigendum: Optical properties of biological tissues: a review,” *Physics in Medicine and Biology*, vol. 58, p. 5007, 7 2013.

[237] M. Yahya and M. Z. Saghir, “Empirical modelling to predict the refractive index of human blood.” *Physics in medicine and biology*, vol. 61, no. 4, pp. 1405–1415, 2 2016.

[238] V. Tuchin, D. Zhestkov, A. Bashkatov, et al., “Theoretical study of immersion optical clearing of blood in vessels at local hemolysis.” *Optics express*, vol. 12, no. 13, pp. 2966–2971, 6 2004.

[239] H. Li, L. Lin, and S. Xie, “Refractive index of human whole blood with different types in the visible and near-infrared ranges,” *Proceedings of the SPIE*, vol. 3914, pp. 517–521, 6 2000.

[240] M. Keijzer, S. L. Jacques, S. A. Prahl, et al., “Light distributions in artery tissue: Monte carlo simulations for finite-diameter laser beams,” *Lasers in Surgery and Medicine*, vol. 9, no. 2, pp. 148–154, 1 1989.

[241] M. Keijzer, R. R. Richards-Kortum, S. L. Jacques, et al., “Fluorescence spectroscopy of turbid media: Autofluorescence of the human aorta.” *Applied optics*, vol. 28, no. 20, pp. 4286–92, 10 1989.

[242] A. N. Yaroslavsky, I. V. Yaroslavsky, T. Goldbach, et al., "Optical properties of blood in the near-infrared spectral range," *Proceedings of the SPIE*, vol. 2678, pp. 314–324, 5 1996.

[243] A. I. Chen, M. L. Balter, M. I. Chen, et al., "Multilayered tissue mimicking skin and vessel phantoms with tunable mechanical, optical, and acoustic properties." *Medical physics*, vol. 43, no. 6, pp. 3117–3131, 6 2016.

[244] N. Bosschaart, G. J. Edelman, M. C. G. Aalders, et al., "A literature review and novel theoretical approach on the optical properties of whole blood." *Lasers in medical science*, vol. 29, no. 2, pp. 453–79, 3 2014.

[245] U. M. Noebauer and S. A. Sim, "Monte carlo radiative transfer," *Living Reviews in Computational Astrophysics*, vol. 5, p. 1, 6 2019.

[246] V. S. Lee and L. Tarassenko, "Absorption and multiple scattering by suspensions of aligned red blood cells." *Journal of the Optical Society of America. A, Optics and image science*, vol. 8, no. 7, pp. 1135–1141, 7 1991.

[247] A. M. K. Enejder, J. Swartling, P. Aruna, et al., "Influence of cell shape and aggregate formation on the optical properties of flowing whole blood." *Applied optics*, vol. 42, no. 7, pp. 1384–1394, 3 2003.

[248] M. Koch, P. Symvoulidis, and V. Ntziachristos, "Tackling standardization in fluorescence molecular imaging," *Nature Photonics*, vol. 12, pp. 505–515, 8 2018.

[249] Y. Liu, P. Ghassemi, A. Depkon, et al., "Biomimetic 3d-printed neurovascular phantoms for near-infrared fluorescence imaging." *Biomedical optics express*, vol. 9, no. 6, pp. 2810–2824, 6 2018.

[250] D. Gorpas, M. Koch, M. Anastasopoulou, et al., "Multi-parametric standardization of fluorescence imaging systems based on a composite phantom." *IEEE transactions on bio-medical engineering*, vol. 67, no. 1, pp. 185–192, 1 2020.

[251] A. J. Ruiz, M. Wu, E. P. M. LaRochelle, et al., "Indocyanine green matching phantom for fluorescence-guided surgery imaging system characterization and performance assessment." *Journal of biomedical optics*, vol. 25, no. 5, pp. 1–15, 5 2020.

[252] D. E. Burgos, B. Blumenkopf, and J. Pfefer, "Biomimetic 3d-printed fluorescence angiography phantoms for evaluation of neurosurgical microscopes," pp. 1–12, 1 2021.

[253] M. Meinke, G. Mueller, J. Helfmann, et al., "Optical properties of platelets and blood plasma and their influence on the optical behavior of whole blood in the visible to near infrared wavelength range." *Journal of biomedical optics*, vol. 12, no. 1, p. 014024, 1 2007.

[254] A. Roggan, M. Friebel, K. Doerschel, et al., "Optical properties of circulating human blood in the wavelength range 400-2500 nm." *Journal of biomedical optics*, vol. 4, no. 1, pp. 36–46, 1 1999.

[255] L.-G. Lindberg and P. A. Oberg, "Optical properties of blood in motion," *Optical Engineering 32(02)*, vol. 32, 2 1993.

[256] R. Bayer, S. Caglayan, and B. Guenther, "Discrimination between orientation and elongation of RBC in laminar flow by means of laser diffraction," *Proceedings of the SPIE*, vol. 2136, pp. 105–113, 7 1994.

[257] J. Lademann, H. Richter, W. Sterry, et al., "Diagnostic potential of erythrocytes aggregation and sedimentation measurements in whole blood samples," *Proceedings of the SPIE*, vol. 4263, pp. 106–111, 6 2001.

[258] A. H. Gandjbakhche, P. Mills, P. Snabre, et al., “Aggregation and deformation of red blood cells as probed by a laser light scattering technique in a concentrated suspension: methodology,” *Proceedings of the SPIE*, vol. 2136, pp. 87–96, 7 1994.

[259] A. V. Priezzhev, O. M. Ryaboshapka, N. N. Firsov, et al., “Aggregation and disaggregation of erythrocytes in whole blood: study by backscattering technique.” *Journal of biomedical optics*, vol. 4, no. 1, pp. 76–84, 1 1999.

[260] R. N. Pittman, “In vivo photometric analysis of hemoglobin.” *Annals of biomedical engineering*, vol. 14, no. 2, pp. 119–137, 1 1986.

[261] T. M. Amin and J. A. Sirs, “The blood rheology of man and various animal species.” *Quarterly journal of experimental physiology (Cambridge, England)*, vol. 70, no. 1, pp. 37–49, 1 1985.

[262] E. Nader, S. Skinner, M. Romana, et al., “Blood rheology: Key parameters, impact on blood flow, role in sickle cell disease and effects of exercise.” *Frontiers in physiology*, vol. 10, p. 1329, 1 2019.

[263] U. Windberger, A. Bartholovitsch, R. Plasenzotti, et al., “Whole blood viscosity, plasma viscosity and erythrocyte aggregation in nine mammalian species: reference values and comparison of data.” *Experimental physiology*, vol. 88, no. 3, pp. 431–440, 5 2003.

[264] T. P. C. van Doormaal, J. H. Sluijs, A. Vink, et al., “Comparing five simple vascular storage protocols.” *The Journal of surgical research*, vol. 192, no. 1, pp. 200–205, 11 2014.

[265] J. B. Casals, N. C. G. Pieri, M. L. T. Feitosa, et al., “The use of animal models for stroke research: a review.” *Comparative medicine*, vol. 61, no. 4, pp. 305–313, 8 2011.

[266] H. J. Streefkerk, J. P. Bremmer, M. van Weelden, et al., “The excimer laser-assisted nonocclusive anastomosis practice model: development and application of a tool for practicing microvascular anastomosis techniques.” *Neurosurgery*, vol. 58, no. 1 Suppl, pp. 148–156, 2 2006.

[267] T. P. C. van Doormaal, A. van der Zwan, B. H. Verweij, et al., “Experimental simplification of the excimer laser-assisted nonocclusive anastomosis (ELANA) technique.” *Neurosurgery*, vol. 67, no. 3 Suppl Operative, pp. 283–290, 9 2010.

[268] D. C. Kim, P. G. Hayward, and W. A. Morrison, “Training model for microvessel anastomosis.” *Microsurgery*, vol. 15, no. 11, pp. 820–821, 1 1994.

[269] G. Oelsner, W. Boeckx, H. Verhoeven, et al., “The effect of training in microsurgery,” *American Journal of Obstetrics and Gynecology*, vol. 152, no. 8, pp. 1054–1058, 1 1985.

[270] J. F. Wolfs, L. F. van den Ham, M. P. ter Laak, et al., “Scanning electron microscopic evaluation of nonocclusive excimer laser-assisted anastomosis in rabbits.” *Acta neurochirurgica*, vol. 142, no. 12, pp. 1399–1407, 1 2000.

[271] “VDI 2206 - design methodology for mechatronic systems,” 6 2004.

[272] A. Naber, L. Meyer-Hilberg, and W. Nahm, “Design of a flow phantom for the evaluation of quantitative ICG fluorescence angiography,” in *Current Directions in Biomedical Engineering*, vol. 5, no. 1, 10 2019.

[273] C. Weichelt, J. Kuss, P. Cimalla, et al., “Development of a flow phantom to verify the evaluation of cerebral blood flow by ICG-fluorescence video analysis,” in *IFMBE Proceedings*, vol. 25, no. 4. September 7 - 12, 2009, Munich, Germany.: Springer, Berlin, Heidelberg, 1 2009, pp. 1448–1451.

[274] O. Bonnefous, V. M. Pereira, R. Ouared, et al., “Quantification of arterial flow using digital subtraction angiography.” *Medical physics*, vol. 39, no. 10, pp. 6264–6275, 10 2012.

[275] D. Schetelig, J. Sedlacik, J. Fiehler, et al., “Analysis of the influence of imaging-related uncertainties on cerebral aneurysm deformation quantification using a no-deformation physical flow phantom.” *Scientific reports*, vol. 8, no. 1, p. 11004, 7 2018.

[276] S. Prevrhal, C. H. Forsythe, R. J. Harnish, et al., “CT angiographic measurement of vascular blood flow velocity by using projection data.” *Radiology*, vol. 261, no. 3, pp. 923–929, 12 2011.

[277] M. Qian, L. Niu, K. K. L. Wong, et al., “Pulsatile flow characterization in a vessel phantom with elastic wall using ultrasonic particle image velocimetry technique: the impact of vessel stiffness on flow dynamics.” *IEEE transactions on bio-medical engineering*, vol. 61, no. 9, pp. 2444–2450, 9 2014.

[278] A. Tsukiyama, Y. Murai, F. Matano, et al., “Optical effects on the surrounding structure during quantitative analysis using indocyanine green videoangiography: A phantom vessel study.” *Journal of biophotonics*, vol. 11, no. 4, p. e201700254, 4 2018.

[279] *Data sheet: ALU CLEANER SX WIGOL GmbH*, 12 2016.

[280] M. Stukelj, Z. Valencak, M. Krsnik, et al., “The effect of the combination of acids and tannin in diet on the performance and selected biochemical, haematological and antioxidant enzyme parameters in grower pigs.” *Acta veterinaria Scandinavica*, vol. 52, p. 19, 3 2010.

[281] R. M. Scott and E. R. Smith, “Moyamoya disease and moyamoya syndrome.” *The New England journal of medicine*, vol. 360, no. 12, pp. 1226–1237, 3 2009.

[282] D. Kainth, S. A. Chaudhry, H. Kainth, et al., “Epidemiological and clinical features of moyamoya disease in the USA.” *Neuroepidemiology*, vol. 40, no. 4, pp. 282–287, 1 2013.

[283] A. A. Baaj, S. Agazzi, Z. A. Sayed, et al., “Surgical management of moyamoya disease: a review.” *Neurosurgical focus*, vol. 26, no. 4, p. E7, 4 2009.

[284] M. Lee, R. Guzman, T. Bell-Stephens, et al., “Intraoperative blood flow analysis of direct revascularization procedures in patients with moyamoya disease.” *Journal of cerebral blood flow and metabolism : official journal of the International Society of Cerebral Blood Flow and Metabolism*, vol. 31, no. 1, pp. 262–274, 1 2011.

[285] V. Prinz, N. Hecht, N. Kato, et al., “FLOW 800 allows visualization of hemodynamic changes after extracranial-to-intracranial bypass surgery but not assessment of quantitative perfusion or flow.” *Neurosurgery*, vol. 10 Suppl 2, pp. 231–239, 6 2014.

[286] F. Faber, N. Thon, G. Fesl, et al., “Enhanced analysis of intracerebral arterioveneous malformations by the intraoperative use of analytical indocyanine green videoangiography: technical note.” *Acta neurochirurgica*, vol. 153, no. 11, pp. 2181–2187, 11 2011.

[287] D. Hanggi, N. Etminan, and H.-J. Steiger, “The impact of microscope-integrated intraoperative near-infrared indocyanine green videoangiography on surgery of arteriovenous malformations and dural arteriovenous fistulae.” *Neurosurgery*, vol. 67, no. 4, pp. 1094–1103, 10 2010.

[288] M. A. Kamp, P. Slotty, B. Turowski, et al., “Microscope-integrated quantitative analysis of intraoperative indocyanine green fluorescence angiography for blood flow assessment: first experience in 30 patients.” *Neurosurgery*, vol. 70, no. 1 Suppl Operative, pp. 65–73; discussion 73–4, 3 2012.

[289] J. A. Guenette, W. R. Henderson, P. B. Dominelli, et al., “Blood flow index using near-infrared spectroscopy and indocyanine green as a minimally invasive tool to assess respiratory muscle blood flow in humans.” *American journal of physiology. Regulatory, integrative and comparative physiology*, vol. 300, no. 4, pp. 984–992, 4 2011.

[290] H. Uchino, T. Nakamura, K. Houkin, et al., “Semiquantitative analysis of indocyanine green videoangiography for cortical perfusion assessment in superficial temporal artery to middle cerebral artery anastomosis.” *Acta neurochirurgica*, vol. 155, no. 4, pp. 599–605, 4 2013.

[291] T. Awano, K. Sakatani, N. Yokose, et al., “Intraoperative EC-IC bypass blood flow assessment with indocyanine green angiography in moyamoya and non-moyamoya ischemic stroke.” *World neurosurgery*, vol. 73, no. 6, pp. 668–674, 6 2010.

[292] M. A. Audette, K. Siddiqi, and T. M. Peters, “Level-set surface segmentation and fast cortical range image tracking for computing intrasurgical deformations,” in *Medical Image Computing and Computer-Assisted Intervention – MICCAI’99*, C. Taylor and A. Colchester, Eds. Berlin, Heidelberg: Springer Berlin Heidelberg, 1999, pp. 788–797.

[293] O. Skrinjar, H. Tagare, and J. Duncan, “Surface growing from stereo images,” vol. 2, pp. 571–576, 1 2000.

[294] M. I. Miga, T. K. Sinha, D. M. Cash, et al., “Cortical surface registration for image-guided neurosurgery using laser-range scanning.” *IEEE transactions on medical imaging*, vol. 22, no. 8, pp. 973–85, 8 2003.

[295] H. Sun, D. W. Roberts, H. Farid, et al., “Cortical surface tracking using a stereoscopic operating microscope.” *Neurosurgery*, vol. 56, no. 1 Suppl, pp. 86–97; discussion 86–97, 1 2005.

[296] H. Duan, J. Wang, X. Liu, et al., “A skeleton pruning approach using contour length as the significance measure,” pp. 360–364, 1 2008.

[297] D. Shaked and A. M. Bruckstein, “Pruning medial axes,” *Computer Vision and Image Understanding*, vol. 69, no. 2, pp. 156–169, 1 1998.

[298] W. Shen, X. Bai, X. Yang, et al., “Skeleton pruning as trade-off between skeleton simplicity and reconstruction error,” *Science China Information Sciences*, vol. 56, no. 4, pp. 1–14, 1 2013.

[299] M. W. K. Law and A. C. S. Chung, “Three dimensional curvilinear structure detection using optimally oriented flux,” in *Computer Vision ECCV 2008*, Lecture Notes in Computer Science, vol. 5305. Springer Berlin Heidelberg, 1 2008, pp. 368–382.

List of publications and supervised theses

Journal articles

- **Ady Naber**, Daniel Berwanger, Werner Nahm *Geodesic Length Measurement in Medical Images: Effect of the Discretization by the Camera Chip and Quantitative Assessment of Error Reduction Methods*, MDPI Photonics 2020; 56; 435–443
- **Ady Naber**, Michael Reiß, Werner Nahm, *Transit Time Measurement in Indicator Dilution Curves: Overcoming the Missing Ground Truth and Quantifying the Error*, Frontiers in Physiology 2021; 12 ;491–507

Refereed conference articles

- Michael Fischer, Mike Stubenrauch, **Ady Naber**, Nam Gutzeit, Maren Klett, Sukhdeep Singh, Andreas Schober, Hartmut Witte, Jens Müller *LTCC-Based Micro Plasma Source for the Selective Treatment of Cell Cultures*, 2017 21st European Microelectronics and Packaging Conference (EMPC) & Exhibition, Warsaw, Poland, 2017, pp. 1-5
- **Ady Naber**, Werner Nahm *Video Magnification for Intraoperative Assessment of Vascular Function*, Current Directions in Biomedical Engineering, vol. 3, no. 2, Dresden, Germany, 2017, pp. 175-178
- **Ady Naber**, Werner Nahm *Bi - Domain Intraoperative Registration of Vessels*, Current Directions in Biomedical Engineering, vol. 4, no. 1, Aachen, Germany, 2018, pp. 25-28
- Tamara Wirth, **Ady Naber**, Werner Nahm *Combination of Color and Focus Segmentation for Medical Images with Low Depth-of-Field*, Current Directions in Biomedical Engineering, vol. 4, no. 1, Aachen, Germany, 2018, pp. 345-349
- Konstantin Sieler, **Ady Naber**, Werner Nahm *An Evaluation of Image Feature Detectors Based on Spatial Density and Temporal Robustness in Microsurgical Image Processing*, Current Directions in Biomedical Engineering, vol. 5, no. 1, Frankfurt, Germany, 2019, pp. 273-276

- **Ady Naber**, Daniel Berwanger, Werner Nahm *In Silico Modelling of Blood Vessel Segmentations for Estimation of Discretization Error in Spatial Measurement and its Impact on Quantitative Fluorescence Angiography*, 2019 41st Annual International Conference of the IEEE Engineering in Medicine and Biology Society (EMBC), Berlin, Germany, 2019, pp. 4787-4790
- **Ady Naber**, Daniel Berwanger, Gary Steinberg, Werner Nahm *Spatial Gradient Based Segmentation of Vessels and Quantitative Measurement of the Inner Diameter and Wall Thickness from ICG Fluorescence Angiographies*, Proc. SPIE 11229, Advanced Biomedical and Clinical Diagnostic and Surgical Guidance Systems XVIII, San Francisco, USA, 2020, 1122916
- **Ady Naber**, Jayson Chaykowski, Jesvin Jimmy, Werner Nahm *Diffuse Reflectance Monte Carlo Simulation to Assess the Transit Time Error in Intraoperative Fluorescence Angiography*, Proc. SPIE 11363, Tissue Optics and Photonics, Strasbourg, France 2020, 1136313
- **Ady Naber**, Werner Nahm *Assessing the Systematic Error in Quantitative Fluorescence Angiography using a Diffuse Reflectance Monte Carlo Model*, Nordic Baltic Conference on Biomedical Engineering and Medical Physics 2020 IFMBE Proceedings, Reykjavik, Iceland, 2020
- Michael Reiß, **Ady Naber**, Werner Nahm *Simulating a Ground Truth for Transit Time Analysis of Indicator Dilution Curves*, Current Directions in Biomedical Engineering, vol. 6, no. 3, Leipzig, Germany, 2020, pp. 268-271
- Simon A. Hoffmann, **Ady Naber**, Werner Nahm *Towards Quantitative ICG Angiography: Fluorescence Monte Carlo Multi Cylinder*, 55th DGBMT annual conference on biomedical engineering, Hannover, Germany ,2021, submitted
- Amr Abuzer, **Ady Naber**, Simon A. Hoffmann, Lucy Kessler, Ramin Khoramnia, Werner Nahm *Investigation on Non-Segmentation Based Algorithms for Microvasculature Quantification in Retinal OCTA Images*, 2021, 55th DGBMT annual conference on biomedical engineering, Hannover, Germany, 2021, in preparation
- Bernhard K. J. Viertel, **Ady Naber**, Simon A. Hoffmann, Daniel Berwanger, Lucy Kessler, Ramin Khoramnia, Werner Nahm *Automated Vessel Centerline Extraction and Diameter Measurement in OCT Angiography*, 2021, 55th DGBMT annual conference on biomedical engineering, Hannover, Germany, 2021, submitted

Refereed conference abstracts

- **Ady Naber**, Leila Meyer-Hilberg, Werner Nahm *Design of a Flow Phantom for the Evaluation of Quantitative ICG Fluorescence Angiography*, Current Directions in Biomedical Engineering, vol. 5, no. 1, Frankfurt, Germany, 2019, pp. 25-28
- Mike Stubenrauch, Michael Fischer, **Ady Naber**, Cornelia Wiegand, Uta-Christine Hipler, Hartmut Witte, Jens Muüller *Micro Plasma Source for the Selective Treatment of Cell*

Cultures, Current Directions in Biomedical Engineering, vol. 5, no. 1, Dresden, Germany, 2017, pp. 25-28

Conference presentations

- **Ady Naber**, Werner Nahm *Video Magnification for Intraoperative Assessment of Vascular Function*, Current Directions in Biomedical Engineering, vol. 3, no. 2, Dresden, Germany, 2017, pp. 175-178
- **Ady Naber**, Werner Nahm *Bi - Domain Intraoperative Registration of Vessels*, Current Directions in Biomedical Engineering, vol. 4, no. 1, Aachen, Germany, 2018, pp. 25-28
- **Ady Naber**, Daniel Berwanger, Werner Nahm *In Silico Modelling of Blood Vessel Segmentations for Estimation of Discretization Error in Spatial Measurement and its Impact on Quantitative Fluorescence Angiography*, 2019 41st Annual International Conference of the IEEE Engineering in Medicine and Biology Society (EMBC), Berlin, Germany, 2019, pp. 4787-4790
- **Ady Naber**, Daniel Berwanger, Gary Steinberg, Werner Nahm *Spatial Gradient Based Segmentation of Vessels and Quantitative Measurement of the Inner Diameter and Wall Thickness from ICG Fluorescence Angiographies*, Proc. SPIE 11229, Advanced Biomedical and Clinical Diagnostic and Surgical Guidance Systems XVIII, San Francisco, USA, 2020, 1122916
- **Ady Naber**, Jayson Chaykowski, Jesvin Jimmy, Werner Nahm *Diffuse reflectance Monte Carlo simulation to assess the transit time error in intraoperative fluorescence angiography*, Proc. SPIE 11363, Tissue Optics and Photonics, Strasbourg, France, 2020, 1136313
- **Ady Naber**, Werner Nahm *Assessing the Systematic Error in Quantitative Fluorescence Angiography using a Diffuse Reflectance Monte Carlo Model*, 2020, Nordic Baltic Conference on Biomedical Engineering and Medical Physics 2020 IFMBE Proceedings

Patents

- **Ady Naber**, Werner Nahm, Daniel Berwanger, Christoph Hauger, Roland Guckler *Computerimplementiertes Verfahren, Computerprogramm und Diagnosesystem, insbesondere zur Bestimmung wenigstens eines Geometriemerkmals eines Abschnitts eines Blutgefäßes*, filed on February 3, 2020 under the official file number (Amtsaktenzeichen) DE102020102683.8
- **Ady Naber**, Werner Nahm, Daniel Berwanger, Christoph Hauger, Roland Guckler *Computer-implemented method, computer program and diagnostic system, in particular for determining at least one geometric feature of a section of a blood vessel*, filed on February 3, 2020 with the serial number no. US17/166,945

- **Ady Naber**, Werner Nahm, Christoph Hauger, Roland Guckler *Computerimplementiertes Verfahren, Computerprogramm und Operationssystem zur Bestimmung des Blutvolumenflusses durch einen Abschnitt eines Blutgefäßes in einem Operationsbereich*, filed on February 3, 2020 under the official file number (Amtsaktenzeichen) DE102020102681.1 and internationally prioritized under the official file number PCT/EP2021/052449

Reports and theses

- **Ady Naber**, *In vitro Untersuchung des Zertrümmerungsverhaltens der Phakoemulsifikation*, Bachelor Thesis, Institute of Biomedical Engineering and Informatics, Ilmenau University of Technology, 2014
- **Ady Naber**, *Aufbau einer miniaturisierten Atmosphären-Plasmaquelle für biologisch-medizintechnische Anwendungen*, Master Thesis, Department of Electronics Technology & Department of Biomechatronics, Ilmenau University of Technology, 2016

Supervised student theses

- Maximilian Sachs, *Study and Analysis of the Pulse Signal Morphology Extracted by PPG and cbPPG*, Bachelor Thesis, Institute of Biomedical Engineering, Karlsruhe Institute of Technology (KIT), 2018
- Gregor Stein, *Analysis and Optimization of Non-Contact Tissue Activity Measurement based on Color Changes*, Master Thesis, Institute of Biomedical Engineering, Karlsruhe Institute of Technology (KIT), 2018
- Tamara Wirth, *Optical Detection of Regions of No Interest in Medical Sceneries*, Master Thesis, Institute of Biomedical Engineering, Karlsruhe Institute of Technology (KIT), 2018
- Daniel O. Baumann, *Frame Selective and Automatic Information Transfer for Bi-Domain Registration of Vessel in Surgical Video Data*, Bachelor Thesis, Institute of Biomedical Engineering, Karlsruhe Institute of Technology (KIT), 2018
- Daniel Berwanger, *Automatic Optical Estimation of Vessel Length and Diameter Based on Preprocessed Segmentations*, Bachelor Thesis, Institute of Biomedical Engineering & Humanoids and Intelligence Systems Lab, Karlsruhe Institute of Technology (KIT), 2018
- Jimmy Jesvin, *Monte Carlo Simulation of Light Propagation in Fluorescent Turbid Media*, DAAD exchange student, Institute of Biomedical Engineering, Karlsruhe Institute of Technology (KIT), 2018
- Jayson Chaykowski, *The Propagation of a Photon Through a Turbid Medium*, DAAD exchange student, Institute of Biomedical Engineering, Karlsruhe Institute of Technology (KIT), 2019

- Leila Meyer-Hilberg, *Modeling of the Flow Behavior of a Bolus in a Flow Phantom for Intraoperative ICG Fluorescence Angiography*, Master Thesis, Institute of Biomedical Engineering, Karlsruhe Institute of Technology (KIT), 2019
- Felix P. Katz, *Design, Aufbau und Durchführung einer Studie zur Untersuchung des Volumenstroms eines Blutanalogs in einem Flussphantom*, Master Thesis, Institute of Biomedical Engineering, Karlsruhe Institute of Technology (KIT), 2020
- Simon A. Hoffmann, *Tiefenverteilung der Fluoreszenzereignisse in der quantitativen Fluoreszenzangiographie*, Master Thesis, Institute of Biomedical Engineering, Karlsruhe Institute of Technology (KIT), 2020
- Michael Reiß, *Enhancing Accuracy Ascertaining the Time Difference between two Indicator Dilution Curves in Quantitative Fluorescence Angiography using Mathematical Models*, Bachelor Thesis, Institute of Biomedical Engineering, Karlsruhe Institute of Technology (KIT), 2020
- Roen Thanasaj, *Simulation of Heterogeneous Indicator Distribution in Laminar Flow in Quantitative Fluorescence Angiography*, Bachelor Thesis, Institute of Biomedical Engineering, Karlsruhe Institute of Technology (KIT), 2020
- Amr N. Abuzer, *Investigation of Non-Segmentation Based Algorithms for Microvasculature Quantification in OCTA Images*, Bachelor Thesis, Institute of Biomedical Engineering, Karlsruhe Institute of Technology (KIT), 2021
- Bernhard K. J. Viertel, *Segmentierung und Durchmessermessung von Gefäßen in OCT-Angiographie Aufnahmen*, Bachelor Thesis, Institute of Biomedical Engineering, Karlsruhe Institute of Technology (KIT), 2021